EAST EUROPEAN JOURNAL OF PHYSICS. 2. 304-308 (2024)
DOI:10.26565/2312-4334-2024-2-34 ISSN 2312-4334

# MORPHOLOGY OF THE SURFACE OF SILICON DOPED WITH LUTETIUM

**Khodjakbar S. Daliev[a], Sharifa B. Utamuradova[b], Jonibek J. Khamdamov[b], Zavkiddin E. Bahronkulov[b]***

*[a]Branch of the Federal State Budgetary Educational Institution of Higher Education "National Research University MPEI", 1 Yogdu st., Tashkent, Uzbekistan*
*[b]Institute of Semiconductor Physics and Microelectronics at the National University of Uzbekistan, 20 Yangi Almazar st., Tashkent, 100057, Uzbekistan*
**Corresponding Author e-mail: zbakhronkulov@inbox.ru*
Received February 22, 2024; revised March 29, 2024; accepted April 2, 2024

In this paper, using a scanning electron microscope (SEM) and atomic analysis, the location map of microcomposites formed on the surface of n-Si, p-Si, n-Si<Lu> and p-Si<Lu> samples was studied. Force microscope (AFM) research devices. The atomic fractions of inclusions of carbon, oxygen and lutetium formed on the surface of the samples were studied. Also, using the ASM device, the sizes, relief and topographic appearance of defects formed on the surface of the samples were determined. In silicon samples doped with Lu, a decrease in the size of surface defects and the formation of nano-sized structures were found, which makes it possible to obtain materials with a more perfect crystal structure. Using a ZEISS GeminiSEM 300 scanning electron microscope, the structural structure, chemical composition and images of their arrangement of n-Si, p-Si, n-Si<Lu> and p-Si<Lu> samples were obtained. In this case, the electron accelerating voltage was 20 kV, and the pressure in the sample chamber was ($10^{-3}$ mmHg). Research results show that the structural structure of micro- and nanocomposites formed in silicon mainly depends on the diffusion time and cooling rate of the samples after diffusion annealing.
**Keywords:** *Silicon; Lutetium; Access; Doping; Defect; Diffusion; Oxygen; Carbon; SEM; AFM*
**PACS:** 33.20.Ea, 33.20.Fb

## INTRODUCTION

As you know, silicon is the main semiconductor material used in electronics [1,17]. These are micro-nano compounds important optical, electrophysical and photoelectric to the properties of k e. Therefore, the study of the structure, size and surface morphology of such compounds is one of the urgent problems of modern physics.

Silicon-based microstructures have a wide range of potential properties that can enhance the capabilities of micro-nanoelectronic devices. Many scientific works note that of particular importance is the study of processes occurring as a result of the interaction of alloying and technological impurities of atoms of their sizes, as well as specific defects, and the determination of the stages of their formation. impurity atoms during the diffusion of various impurity atoms into a silicon single crystal at high temperatures [3,6,9,13,15]. In the photoconductivity region, they can increase light absorption and reduce recombination losses. Silicon single crystals can also serve as an active element in LEDs and other optoelectronic devices [10,11, 14,16]. By analyzing changes in surface topography, researchers have conducted a number of studies to develop new technologies in areas such as microelectronics, optoelectronics and photovoltaics [9,12,16].

Electronic processes in semiconductor materials are determined mainly by volumetric and surface defects of the semiconductor. Studying these defects and reducing their formation is one of the main tasks of modern semiconductor electronics. In recent years, interest in the development of methods for monitoring defects in silicon single crystals and their interaction by doping with rare earth elements (REEs) has increased significantly [2,5,8].

## MATERIALS AND METHODS

In the manufacture of silicon structures based on rare earth elements (REE), the diffusion method was used [7,15]. In the research work, n-type (ρ=0.3÷150 Ω×cm) and p-type (ρ =0.3÷20 Ω×cm) silicon single crystals grown by the Czochralski method were used. At the input, the element lutetium with a purity of 99.999% was obtained.

Before diffusion, silicon single crystals were subjected to mechanical and chemical treatment. Using a VUP-4 setup, lutetium atoms were deposited onto the surface of a silicon sample under high vacuum conditions ($10^{-6}$ mm Hg). A high-vacuum ampoule was prepared using quartz glass. Diffusion was carried out in a SUOL oven at a temperature of 1250°C for 30 hours. After diffusion, the samples were quickly cooled. After diffusion annealing, the samples were quickly cooled. Before measurements, 10 µm was removed from the surface of the prepared samples using micropowder. After mechanical and chemical treatment, the morphology of the samples was measured using SEM, and the surface composition structure was measured using SEM.

## RESULTS AND DISCUSSION

Using a ZEISS GeminiSEM 300 scanning electron microscope, the structural structure, chemical composition and images of their arrangement of n-Si, p-Si, n-Si<Lu> and p-Si<Lu> samples were obtained.

*Cite as:* Kh.S. Daliev, Sh.B. Utamuradova, J.J. Khamdamov, Z.E. Bahronkulov, East Eur. J. Phys. 2, 304 (2024), https://doi.org/10.26565/2312-4334-2024-2-34
© Kh.S. Daliev, Sh.B. Utamuradova, J.J. Khamdamov, Z.E. Bahronkulov, 2024; CC BY 4.0 license

In this case, the electron accelerating voltage was 20 kV, and the pressure in the sample chamber was ($10^{-3}$ mmHg). Research results show that the structural structure of micro- and nanocomposites formed in silicon mainly depends on the diffusion time and cooling rate of the samples after diffusion annealing.

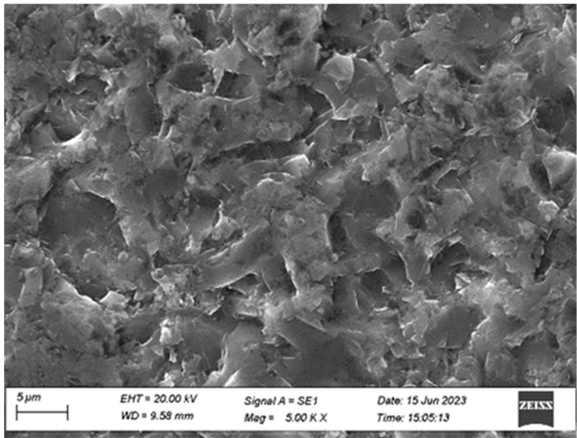


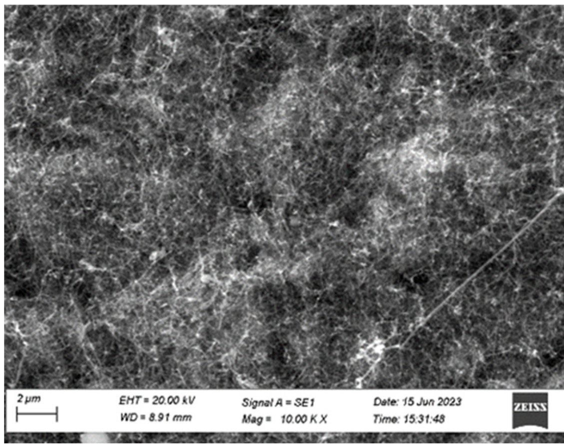


**Figure 1.** p – Si (control) and SEM image of samples p - Si <Lu>

In Figure 1 shows an SEM image of lutetium-doped silicon. As can be seen in the figure, for the first time the fibrous arrangement of lutetium atoms on the surface of single-crystalline silicon doped with lutetium has been experimentally established. As a result of the research, quantitative indicators of atoms of technological raw materials, such as O and C, as well as Si and Lu atoms in this microcomposite were determined.

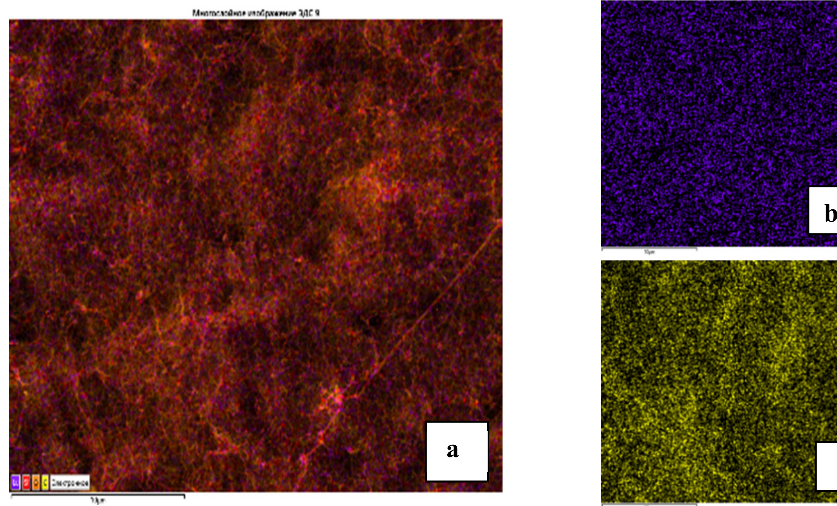


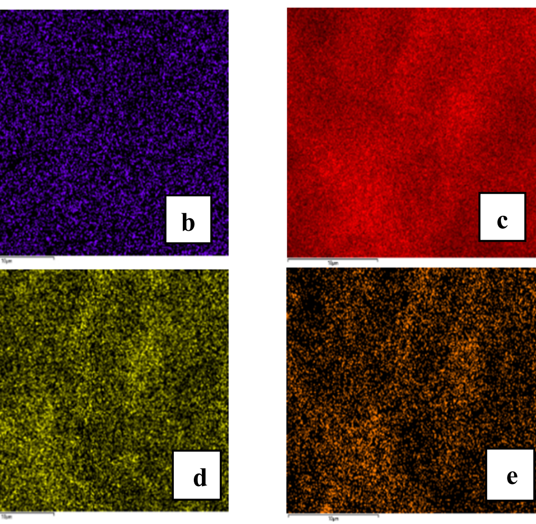


**Figure 2.** Arrangement of elemental atoms in a lutetium-doped silicon sample (p-Si<Lu>).
a) p- Si<Lu>, b) Lu, c) Si, e) C, d) O

Figure 2 with lutetium doped in silicon elements concentration for elemental spectrum mapping shown. In the mapping image, the elements Si, Lu, O and C (red, violet, green and yellow) are arranged correctly without any gaps, and the atomic percentages of the sample are 25.24%, 0.96%, 7.08% and 66 .72% respectively. These quantitative values were obtained from SEM analysis. The results of the analysis of the chemical composition of these microgranules in their central part are presented in the Table below.

**Table.** Total spectrum of the card

| Element | Line type | Conditional concentration | Weight. % | Atom % |
|---|---|---|---|---|
| | | n-Si | | |
| C | series K | 9.51 | 44.74 | 66.72 |
| O | series K | 5.03 | 6.32 | 7.08 |
| Si | series K | 65.99 | 39.57 | 25.24 |
| | | p-S<Lu> | | |
| C | series K | 9.51 | 44.74 | 66.72 |
| O | series K | 5.03 | 6.32 | 7.08 |
| Si | series K | 65.99 | 39.57 | 25.24 |

| Element | Line type | Conditional concentration | Weight. % | Atom % |
|---|---|---|---|---|
| Lu | L series | 10.89 | 9.36 | 0.96 |
| | | **n-S<Lu>** | | |
| C | series K | 1.55 | 13.07 | 24.75 |
| O | series K | 17.26 | 20.79 | 29.56 |
| Si | series K | 65.56 | 54.59 | 44.19 |
| Lu | L series | 10.34 | 11.55 | 1.50 |

When the finished samples are measured, no peaks are observed. The Si peak obtained at 1.8 keV confirms the correctness of the technological process in the prepared samples. Figure 3-a, b confirm the absence of any impurities other than natural additives. Works [1,5,7] confirm the formation of additional growing technological impurities (defects) formed during sample preparation.An unknown Si peak obtained at an energy of 1.8 keV confirms the correctness of the technological process in the prepared samples. The results obtained confirm the absence of any additions other than preformed defects. Works [1,5,7] confirm the formation of additional growing technological impurities (defects) formed during sample preparation.

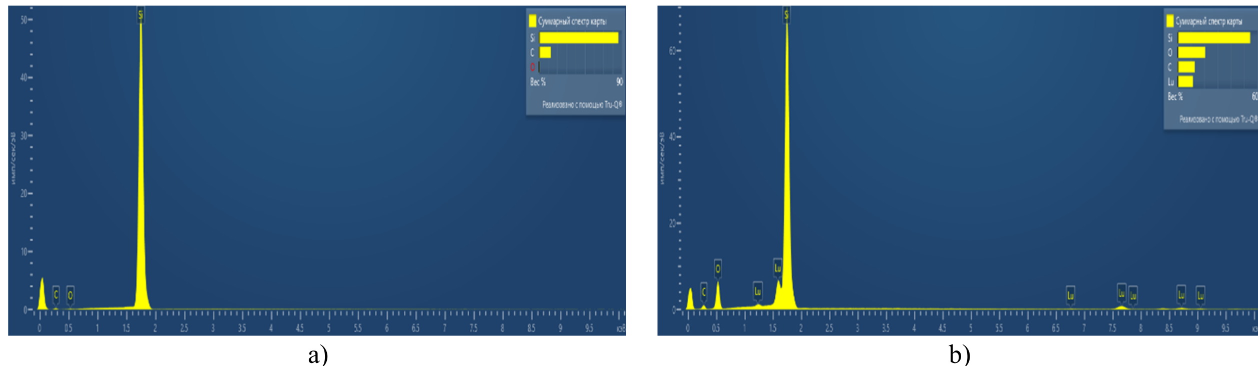

a) b)

**Figure 3.** SEM spectrum of n-Si(a) and n-Si<Lu>(b) samples

A single crystal of silicon is an optional element with doping its surface morphology changes [3-5]. In our studies, changes in surface properties can be seen when doped with lutetium. However, these surface changes may be associated not with the concentration of lutetium atoms, but with technological factors of sample preparation. In general, in a number of works it was believed that the addition of a foreign substance to a silicon single crystal leads to a change in the surface topography [11,12,15].

Changes in surface morphology may depend on the sputtering time during the deposition process, the heating temperature of the crucible and the diffusion time during the diffusion process in the VUP-4 installation.

The AFM image was obtained at different points on the sample surface. On the surface of the sample there are pits in the form of protrusions up to 1 µm wide, the appearance of which is directly related to mechanical processing. Small rounded peaks were observed on the surface of the silicon single crystal; a transverse peak height profile with a diameter of 2 to 14 nm is shown (Fig. 3). The surface relief heights of the silicon monolith differ from each other by 31.5 nm.

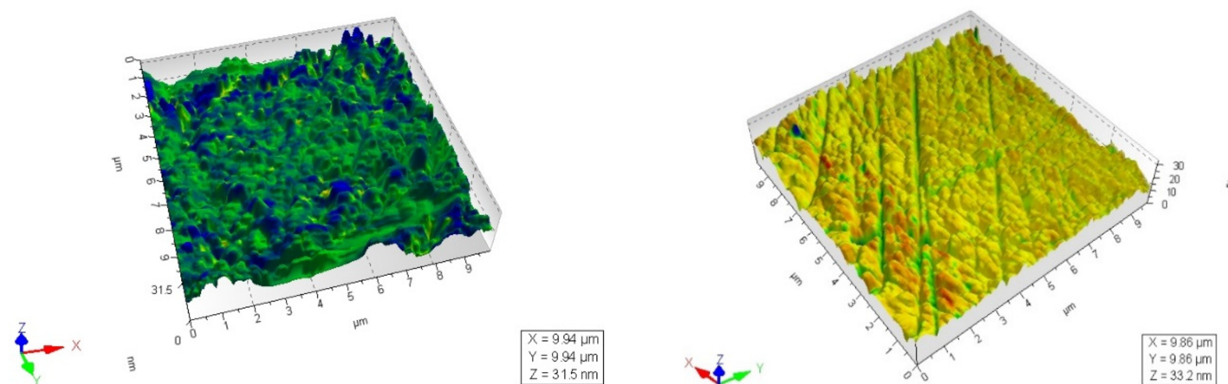


**Figure 4.** SEM images of n-Si and n-Si<Lu> samples

Doping single-crystal silicon with lutetium led to a significant change in the morphology of the sample surface (Fig. 5.1). But the relief height was 33.15 nm. If the initial relief height of a silicon single crystal was 31.15 nm, then the change in relief can be associated with the diffusion process. Grooves up to 1 µm wide were observed on the surface of samples in the initial state of a single crystal of silicon and on the surface of samples doped with lutetium. These pits are explained by the removal of a 10 µm thick layer from the surface of the sample after a diffusion process followed by mechanical processing.

Judging by the obtained image profiles, the dimensions of the resulting grooves can vary from hundreds of nanometers to several microns. Analysis of the 3D image shows that the overall structure (n-Si<Lu>) shows that the structure formed on the surface of the sample is very small. However, this is not visible in the cross-sectional profile of the AKM image of the surface (Fig. 5.2), which is due to the visualization of the gaps due to the nanometry and shape of its structural elements.

Several factors have been found to influence the surface morphology of lutetium-doped silicon.

1. Firstly, it fills the irregularities on the surface of the silicon single crystal, that is, the voids, and reduces lumps on the surface.

2. Secondly, the protrusions in the glaze led to a decrease in the growth of crystalline phases.

As a result of the diffusion of lutetium atoms onto the surface of a single crystal of silicon, the morphology of the silicon surface changes; probably, the collision of lutetium ions with the surface of the crystal during diffusion at 1250°C leads to the formation of structural defects on the silicon surface. sample. This, in turn, leads to an increase in the number of quantum islands on the surface of the sample.

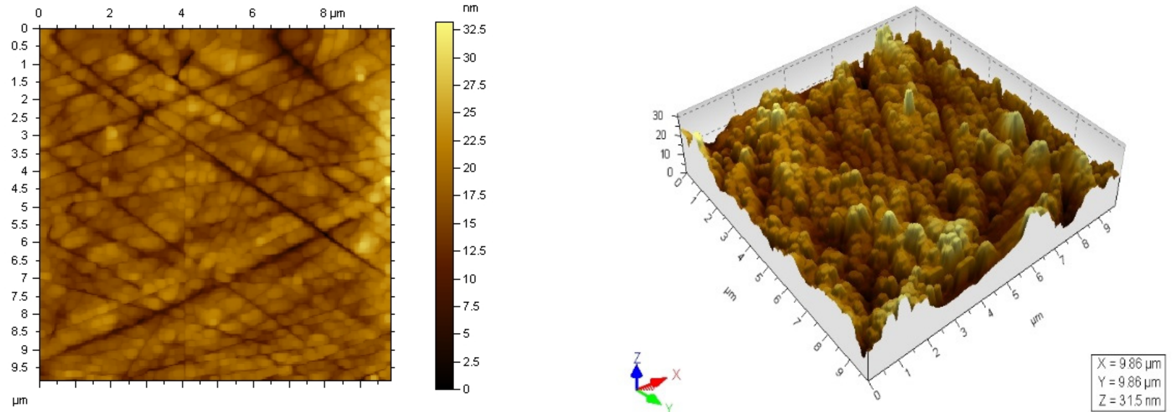


**Figure 5.1** Raw monocrystalline silicon (n - Si) state AKM received description

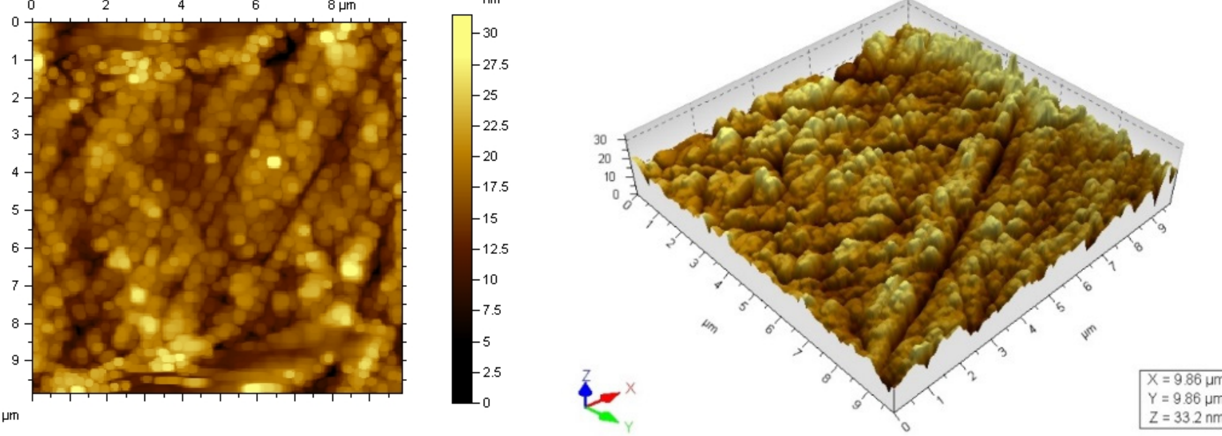


**Figure 5.2** Lutetium with An AFM of doped silicon single crystal was obtained. description

## CONCLUSION

Based on the results of the experiments, the following conclusions were made. The structural structure, chemical composition and their description of n-Si, p-Si, p-Si<Lu> and nS<Lu> samples were studied for the first time. Research results have shown that the structural structure of micro- and nanocompounds formed in silicon mainly depends on the diffusion time and cooling rate of the samples after diffusion annealing. For the first time, the fibrous arrangement of lutetium atoms on the surface of single-crystalline silicon doped with lutetium has been experimentally established. As a result of the studies carried out, the quantitative indicators of atoms of technological raw materials, such as O and C, as well as Si and Lu atoms, were determined in this microcomposite. In our studies, a significant change in the morphology of the sample surface was observed when single-crystal silicon was doped with lutetium. Grooves up to 1 µm wide were observed on the surface of samples in the initial state of a single crystal of silicon and on the surface of samples doped with lutetium. It was concluded that the grooves formed on the surface are associated with mechanical processing. If the initial relief height of a silicon single crystal was 31.15 nm, then the change in relief can be associated with the diffusion process. Grooves up to 1 µm wide were observed on the surface of samples in the initial state of a single crystal of silicon and on the surface of samples doped with lutetium.

**ORCID**
**Khodjakbar S. Daliev,** https://orcid.org/0000-0002-2164-6797; **Sharifa B. Utamuradova,** https://orcid.org/0000-0002-1718-1122
**Jonibek J. Khamdamov,** https://orcid.org/0000-0003-2728-3832; **Zavkiddin E. Bahronkulov,** https://orcid.org/0009-0002-9843-8344

## REFERENCES

[1] K.V. Ravi, *Imperfections and impurities in semiconductor silicon*, (Wiley, New York, 1981).
[2] H. Wang, Y. Nyu, H. Lin, J. Qiao, Y. Zhang, W. Zhong, and S. Qiu, "Modification of rare earth Ce by inclusions in non-oriented silicon steel W 350," Metals, **13**, 453 (2023). https://doi.org/10.3390/met13030453
[3] Sh.B. Utamuradova, A.V. Stanchik, and D.A. Rakhmanov, "X-Ray Structural Investigations Of n-Si<Pt> Irradiated with Protons," East Eur. J. Phys. 2, 201 (2023). https://doi.org/10.26565/2312-4334-2023-2-21
[4] Sh.B. Utamuradova, H.J. Matchonov, Zh.J. Khamdamov, and H.Yu. Utemuratova, "X-ray diffraction study of the phase state of silicon single crystals doped with manganese," New Materials, Connections Oath Applications, **7**(2), 93-99 (2023). http://jomardpublishing.com/UploadFiles/Files/journals/NMCA/v7n2/Utamuradova_et_al.pdf
[5] N.M. Bogatov, L.R. Grigoryan, A.Y. Kovalenko, M.S. Kovalenko, F.A. Kolokolov, and L.S. Lunin, FTP, **54**, 144-148 (2020). https://doi.org/10.21883/FTP.2020.02.48909.9255
[6] Kh.S. Daliev, Sh.B. Utamuradova, J.J. Khamdamov, and Z.E. Bahronkulov, "Electrophysical properties of silicon doped with lutetium," Advanced Physical Research, **6**(1), 42-49 (2024). https://doi.org/10.62476/apr61.49
[7] B.I. Boltax, *Diffusion in semiconductors*, (Moscow, State Publishing House of Physical and Mathematical Literature, 1971). (in Russian)
[8] S.B. Utamuradova, Z.T. Azamatov, M.A. Yuldoshev, N.N. Bazarbayev, and A.B. Bakhromov, "Investigations of Nonlinear Optical Properties of Lithium Niobate Crystals," East Eur. J. Phys. (4), 147 (2023). https://doi.org/10.26565/2312-4334-2023-4-15
[9] Sh.B. Utamuradova, S.A. Muzafarova, A.M. Abdugofurov, K.M. Faizullaev, E.M. Naurzalieva, and D.A. Rakhmanov, Applied Physics, **4**, 90 (2021). https://applphys.orion-ir.ru/appl-21/21-4/PF-21-4-81.pdf
[10] Daliev, K.S., Utamuradova, S.B., Khamdamov, J.J., Structural properties of silicon doped rare earth elements ytterbium. East European Journal of Physics, (1), 375–379 (2024). https://doi.org/10.26565/2312-4334-2024-1-37
[11] Yu.S. Katarria, S. Kumar, F. Singh, J.K. Pivin, and D. Kanjilal, "Synthesis of buried SiC using an energetic ion beam," J. Phys. D: Adj. Phys. **39**, 3969–3973 (2006). http://dx.doi.org/10.1088/0022-3727/39/18/007
[12] I.S. Smirnov, I.G. Dyachkovan, and E.G. Novoselova, "High resolution X-ray diffraction study of proton irradiated silicon crystals," Modern electronic materials, **2**, 29–32 (2016). http://dx.doi.org/10.1016/j.moem.2016.08.005
[13] Kh.S. Daliev, Z.E. Bahronkulov, and J.J. Hamdamov, "Investigation of the Magnetic Properties of Silicon Doped with Rare-Earth Elements," East Eur. J. Phys. (4), 167 (2023). https://doi.org/10.26565/2312-4334-2023-4-18
[14] O.V. Skalyaukh, "Defect formation in silicon when irradiated with alpha particles with an energy of 5.4 MeV," Ph.D. thesis, Ulyanovsk, 2000. (in Russian)
[15] Kh.S. Daliev, Sh.B. Utamuradova, Z.E. Bahronkulov, A.Kh. Khaitbaev, and J.J. Hamdamov, East Eur. J. Phys. (4), 193 (2023). https://doi.org/10.26565/2312-4334-2023-4-23
[16] V.A. Zinoviev, Ph.D. Thesis, "Processes on the silicon surface under the influence of low-energy ions under molecular beam epitaxy conditions," Siberian Branch of the Russian Academy of Sciences, Institute of Semiconductor Physics, Novosibirsk 2004. (in Russian)
[17] S.M. Osadchiy, A. Petukhov, and V.B. Dunin, "Application of silicon detectors with differential discriminators in X-ray diffractometers," Journal of Surface Investigation X-ray Synchrotron and Neutron Techniques, **8**, 25–29 (2019). (in Russian)

## МОРФОЛОГІЯ ПОВЕРХНІ КРЕМНІЮ, ЛЕГОВАНОГО ЛЮТЕЦІЄМ

**Ходжакбар С. Далієв[a], Шаріфа Б. Утамурадова[b], Джонібек Дж. Хамдамов[b], Завкіддін Е. Бахронкулов[b]**
[a]*Філія ФДБУ «Національний дослідницький університет МПЕІ», Йогду, 1, Ташкент, Узбекистан*
[b]*Інститут фізики напівпровідників та мікроелектроніки Національного університету Узбекистану, вул. Янгі Алмазара, 20, Ташкент, 100057, Узбекистан*

У цій роботі за допомогою скануючого електронного мікроскопа (SEM) та атомного аналізу досліджено карту розташування мікрокомпозитів, сформованих на поверхні зразків n-Si, p-Si, n-Si<Lu> та p-Si<Lu>. Дослідницькі прилади силового мікроскопа (АСМ). Досліджено атомні частки включень вуглецю, кисню та лютецію, що утворюються на поверхні зразків. Також за допомогою приладу АСМ визначали розміри, рельєф і топографічний вигляд дефектів, утворених на поверхні зразків. У зразках кремнію, легованих Lu, виявлено зменшення розмірів поверхневих дефектів і утворення нанорозмірних структур, що дозволяє отримувати матеріали з більш досконалою кристалічною структурою. За допомогою скануючого електронного мікроскопа ZEISS GeminiSEM 300 отримано структурну будову, хімічний склад та зображення їх розташування зразків n-Si, p-Si, n-Si<Lu> та p-Si<Lu>. У цьому випадку прискорювальна напруга електронів становила 20 кВ, а тиск у камері зразка становив (10-3 мм рт. ст.). Результати досліджень показують, що структурна структура мікро- та нанокомпозитів, сформованих у кремнії, в основному залежить від часу дифузії та швидкості охолодження зразків після дифузійного відпалу.
**Ключові слова:** *кремній; лютецій; доступ; допінг; дефект; дифузія; кисень; карбон; SEM; ACM*

East European Journal of Physics. 2. 309-314 (2024)
DOI:10.26565/2312-4334-2024-2-35 ISSN 2312-4334

# NANOCRYSTALLINE ZnO FILMS ON VARIOUS SUBSTRATES: A STUDY ON THEIR STRUCTURAL, OPTICAL, AND ELECTRICAL CHARACTERISTICS

**Numonjon A. Sultanov, Zokirjon X. Mirzajonov, Fakhriddin T. Yusupov*, Tokhirbek I. Rakhmonov**
*Fergana Polytechnic Institute, Fergana, Uzbekistan*
**Corresponding Author e-mail: yusupov.fizika@gmail.com*
Received March 23, 2024; revised April 10, 2024; accepted April 30, 2024

Zinc oxide (ZnO), characterized by its wide bandgap and substantial exciton binding energy, is extensively utilized in optoelectronic applications, including blue and ultraviolet light-emitting diodes (LEDs) and lasers. In this study, the deposition of ZnO films on various substrates (Si, sapphire, GaAs, GaP) through thermal oxidation is investigated as a cost-effective alternative to molecular beam epitaxy (MBE) and chemical vapor deposition (CVD). A thorough analysis of the structural, optical, and electrical properties of these films is presented, with a focus on their suitability for heterojunction diodes. The methodology employed involved the thermal evaporation of Zn films in a vacuum chamber, followed by oxidation in a pure oxygen atmosphere. The conditions for deposition were optimized to yield nanocrystalline ZnO films with a preferential orientation, as confirmed by X-ray diffraction (XRD) analysis. An increase in the optical bandgap was indicated by optical transmittance measurements, while photoluminescence (PL) spectra exhibited uniform and enhanced crystalline integrity across the samples. The electrical characterization of ZnO-based heterojunction diodes on different substrates revealed distinct electrical characteristics, with variations in leakage current and ideality factor observed. The specific resistances of the Zinc Oxide (ZnO) films were determined by analyzing the linear portions of the current-voltage (I-V) curves.
**Keywords:** *Zinc oxide (ZnO); Zinc oxide (ZnO); Heterojunction diodes; Optoelectronic applications; Nanocrystalline structure; Optical bandgap; Electrical properties; Current-voltage (I-V) characteristics; Substrate temperature; Photoluminescence spectra*
**PACS:** 78.20.-e, 73.61.Ga, 85.60.-q, 68.55.-a

## INTRODUCTION

Zinc oxide (ZnO) has attracted significant attention from various research groups worldwide due to its direct wide bandgap (Eg ~ 3.3 eV at 300 K) and large exciton binding energy of ~60 meV, making ZnO a promising material for manufacturing blue and ultraviolet LEDs and lasers operating at high temperatures and under extreme radiation conditions [3,4]. It involves the oxidation of metallic zinc films in a controlled atmosphere, offering a cost-effective alternative to techniques like MBE and CVD. In addition, ZnO is widely used in electroacoustic applications because of its large electromechanical coupling constant, in the manufacturing of varistors, and as transparent electrodes for solar cells. Despite significant interest in this area and progress in depositing high-quality undoped and doped zinc oxide, several issues remain, such as the development of a reproducible technology to achieve low-resistive p-type conductivity. There are many methods currently used for growing low-impurity ZnO, such as molecular beam epitaxy (MBE) [4], and chemical deposition [5]. Despite the substantial interest in ZnO deposition, thermal oxidation is one of the methods that receive very little attention, despite its apparent simplicity. However, there are only a few reports in the literature dedicated to the deposition of ZnO by thermal oxidation [6,10-12].

## EXPERIMENTAL METHODOLOGY

The fabrication of ZnO thin films was conducted in a high-vacuum chamber, where a controlled environment was established by evacuating air and subsequently introducing a mixture of argon and oxygen gases. The focus of this study is on the thermal oxidation process, where zinc films, deposited via thermal evaporation, undergo oxidation in a pure oxygen atmosphere to form ZnO films. This process was applied to various substrates, including silicon, sapphire, GaAs, and GaP, to assess the versatility of the method in producing heterostructures for optoelectronic applications. The deposition parameters were carefully optimized to ensure the formation of nanocrystalline ZnO films with a preferential c-axis orientation, a key factor for enhancing the optoelectronic properties of the films. The substrate temperature was maintained at 200°C, and the working pressure of the gas mixture ($Ar+O_2$) was regulated at $2.3\times10^{-2}$ Pa. The thickness control of the ZnO films, which ranged from 1,5-2 μm, was achieved using a quartz crystal thickness monitor (IC5). After deposition, the samples underwent an annealing process at 600°C in an ambient air atmosphere for one hour to improve the crystallinity and electrical properties of the ZnO films. The characterization of the ZnO-based heterojunction diodes was conducted under dark conditions at room temperature, employing current-voltage (I-V) measurements to evaluate the diode parameters such as leakage current and ideality factor, which are critical for assessing the performance of the heterostructures in optoelectronic devices. To ensure accurate I-V measurements, a shielded measurement cell was employed, and the samples were placed in a temperature-controlled thermostat that allowed for temperature stability ranging from room temperature to 300°C. The electrical connections to the samples were established using a precision

***Cite as:*** N.A. Sultanov, Z.X. Mirzajonov, F.T. Yusupov, T.I. Rakhmonov, East Eur. J. Phys. 2, 309 (2024), https://doi.org/10.26565/2312-4334-2024-2-35
© N.A. Sultanov, Z.X. Mirzajonov, F.T. Yusupov, T.I. Rakhmonov, 2024; CC BY 4.0 license

microprobe connected to a micromanipulator within the thermal enclosure. The applied voltage to the samples and the temperature within the thermal enclosure were regulated by a central control unit, while a dedicated measurement apparatus was used to monitor these parameters. The exploration of the conduction mechanism in ZnO and the development of film-based devices with Ni-ZnO-pSi-Ni, Ni-ZnO-GaAs-Ni, and Ni-ZnO-GaP-Ni structures were facilitated by examining the I-V characteristics. The ZnO films were deposited onto p-Si, GaAs, and GaP substrates using thermal evaporation, with substrate temperatures varying between 80 and 350°C, and the deposition rate was maintained at 10-15 Å/s to ensure uniform film growth [12-15].

## RESULTS AND DISCUSSION

**Electrical Properties and Heterojunction Diodes.** In optoelectronic applications, the significance of the electrical properties of ZnO films, particularly within the context of heterojunction diodes, cannot be overstated. The optimization of conductivity and the elucidation of charge transport mechanisms have been the focus of rigorous investigation [17,18]. Through the employment of electron diffraction techniques, the amorphous nature of the films, as deposited, was ascertained. A transition to crystalline phases, characterized by hexagonal lattice parameters (a=3.249 Å and c=5.206 Å), was observed following annealing at temperatures ranging from 350-400°C for a duration of no less than 3 hours. The bandgap energies of the amorphous and crystalline films, as derived from the temperature dependence of electrical conductivity, were found to be 3.2 eV and 3.6 eV, respectively. The specific resistances of the ZnO films, deduced from the linear regions of the I-V curves, spanned from $10^3$ to $10^5$ ohm·cm, indicating their aptitude as dielectric coatings. Symmetrical behavior in both forward and reverse bias directions was exhibited by the I-V characteristics of the Ni-ZnO-pSi-Ni, Ni-ZnO-GaAs-Ni, and Ni-ZnO-GaP-Ni structures, with three distinct regions being observed: ohmic, quadratic, and cubic. The deposition of ZnO films was conducted in a vacuum environment maintained at no less than 10-5 mmHg, followed by the application of aluminum or nickel films serving as ohmic contacts. For the analysis of the current-voltage (I-V) characteristics, the fabricated structures were positioned within a shielded measurement cell. A microprobe, mounted on a micromanipulator, was utilized to establish electrical contact with the upper aluminum films. Subsequently, the cell was situated inside a thermostat, ensuring a stable temperature range spanning from room temperature to 470 Kelvin.The study of the electrical conductivity mechanism in thin polycrystalline films was facilitated by the analysis of transverse conductivity in film sandwich structures. In the scenario where a transverse current traverses a film, the impact exerted by intergranular regions diminishes when the thickness of the film is comparable to the size of the crystals. This condition results in the experimental conditions approaching the ideal case, where the current flow is akin to that in a single crystal, as illustrated in Figure 1. This phenomenon is critical for understanding the electrical behavior of thin films in semiconductor physics.

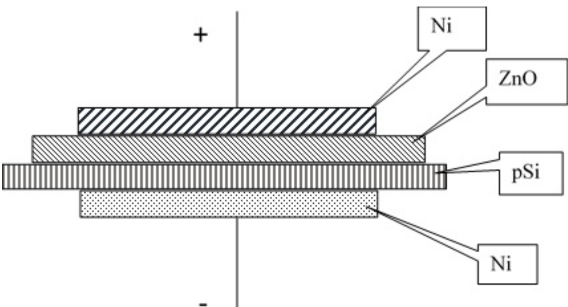


**Figure 1**. Schematic of the Ni-ZnO-pSi-Ni structure type.

The temperature-dependent I-V characteristics of thin ZnO films were measured over a wide temperature range (296-470 K) to investigate the current transport mechanism. The diode equation, enhanced with series and shunt resistances, is paramount in characterizing the electrical performance of heterojunction diodes.

In the analysis of the I-V characteristics of the Ni-ZnO-p-Si-Ni structure, the theoretical models governing the behavior of charge carriers within the semiconductor junction were considered. The Shockley ideal diode equation was employed to describe the I-V relationship under forward and reverse bias conditions [21]:

$$\mathrm{I} = I_S\left(e^{\frac{qV}{nkT}} - 1\right). \tag{1}$$

In the equation, the current passing through the diode is denoted by *I*, while $I_s$ represents the saturation current. The voltage applied across the diode is indicated by *V*, and *q* symbolizes the charge of an electron. The ideality factor, generally approximating 1 for an ideal diode, is expressed by n. The Boltzmann constant is given by k, and the temperature in Kelvin is represented by T. To accommodate for real-world non-idealities, the equation can be modified to include series resistance $R_S$ and shunt resistance $R_{SH}$, which account for the voltage drop due to the internal resistance of the diode and the leakage current paths, respectively:

$$I = \frac{V - IR_S}{R_{SH}} + I_S(e^{\frac{q(V - IR_S)}{nkT}} - 1). \tag{2}$$

Moreover, the current transport mechanism in the diode under high electric fields can be described by the space-charge-limited current (SCLC) model when the injected charge carrier density exceeds the intrinsic charge carrier density of the semiconductor:

$$J = \frac{9}{8}\varepsilon\varepsilon_0\mu\frac{V^2}{d^3}, \tag{3}$$

where $J$ is the current density, $\varepsilon$ is the relative permittivity of the material, $\varepsilon_0$ is the vacuum permittivity, $\mu$ is the charge carrier mobility, and $d$ is the thickness of the semiconductor layer.

The temperature dependence of the saturation current can be expressed using the Arrhenius equation:

$$I_S(T) = I_S(T_0)e^{\frac{-E_a}{k}(\frac{1}{T}-\frac{1}{T_0})}. \tag{4}$$

In the expression, $E_a$ denotes the activation energy required for conduction, while $T_0$ signifies a reference temperature [22].

These equations provide a framework for understanding the electronic properties of the Ni-ZnO-p-Si-Ni heterostructure and can be used to calculate the expected I-V behavior, allowing for a comparison with experimental data. The agreement or discrepancy between the theoretical predictions and experimental results will yield insights into the quality of the heterojunction, the presence of interface states, and the predominant charge transport mechanisms.

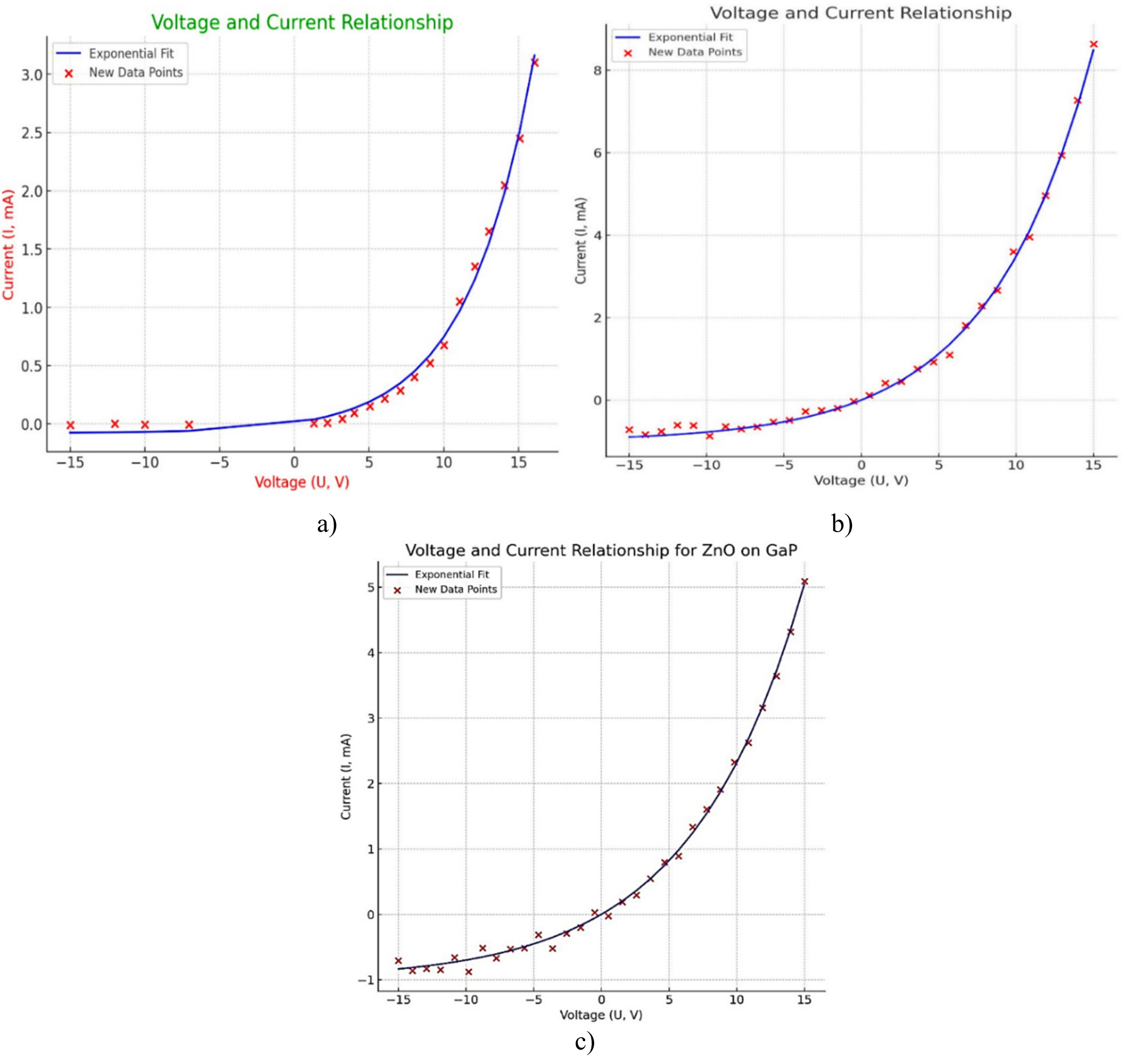


**Figure 2**. (a) I-V characteristics of the Ni-ZnO-pSi-Ni structure for the crystalline film in forward and reverse current directions, (b) I-V characteristics of the Ni-ZnO-GaAS-Ni structure for the crystalline film in forward and reverse current directions. (c) I-V characteristics of the Ni-ZnO-GaP-Ni structure for the crystalline film in forward and reverse current directions.

Figure 2. a,b,c are characteristic current-voltage (I-V) curves for semiconductor junctions, specifically for structures incorporating nickel (Ni), zinc oxide (ZnO), and doped silicon (Si), as well as one with gallium phosphide (GaP). These curves are paramount in semiconductor physics for analyzing the electrical properties of the materials and junctions within the device. Each graph presents the I-V characteristics for different semiconductor structures under forward and reverse

bias conditions, showing how the current (in mA) varies with the applied voltage (in V). The red 'X' marks indicate experimental data points, and the blue line represents an exponential fitting of these points, likely obtained through a process like least squares fitting, to model the expected behavior of the semiconductor structure. For the Ni-ZnO-p-Si-Ni structure, the curve demonstrates the typical exponential increase in current with the applied forward voltage, indicative of diode-like behavior. The same applies to the Ni-ZnO-GaP-Ni structure. The saturation of current at reverse biases (negative voltage values) is typical for a diode, representing a minimal leakage current until breakdown occurs, which is not shown here.

The last graph also includes the label "Figure 2c. I-V characteristics of the Ni-ZnO-GaP-Ni structure for the crystalline film in forward and reverse current gyul;directions," which specifies the materials used in the heterojunction and indicates that the measurements are likely taken at room temperature, as is standard unless otherwise noted.

**Structural Properties of ZnO Films.** The structural quality of ZnO films, including crystallinity and orientation, is crucial for device performance. X-ray diffraction (XRD) is commonly used to assess these properties, with a preferential c-axis orientation being desirable for many applications [9,12].

Figure 3 is a simulated Scanning Electron Microscope (SEM) micrograph of a ZnO thin film, showing a variety of features likely representing different aspects of the film's surface morphology. In an image produced by Scanning Electron Microscopy (SEM) such as this, the variations in grayscale tones are indicative of the quantity of secondary electrons released from the surface upon bombardment by the primary electron beam. Bright areas typically indicate surfaces perpendicular to the electron beam that are emitting more electrons, while darker areas indicate surfaces that are angled away, emit fewer electrons, or are of a different material composition. The image displays a heterogeneous surface with features of varying sizes and shapes, suggesting a complex surface topology. The presence of spherical and irregular particulates could indicate the film's granular nature or the presence of clusters or aggregations on the film's surface. The variation in feature size and the distribution of particles might inform us about the deposition conditions, such as temperature, the presence of impurities, or the atmosphere in which the film was grown. Given the marked contrast between different regions, we can infer that the material has areas with distinct topographies or compositional contrasts. However, without additional context or analytical data, it is challenging to draw concrete conclusions about the material's electrical, optical, or structural properties. In AFM imaging (Figure 4), a cantilever with a sharp tip is scanned across the sample surface. The tip's interaction with the surface forces is measured, and these forces are used to construct a topographic map of the surface at the nanoscale. The grayscale contrast in an AFM image corresponds to height variation, with lighter areas indicating higher regions and darker areas indicating lower regions. The micrograph shows a highly textured and anisotropic surface, indicating a crystalline structure with pronounced ridges and valleys. This could be indicative of a preferred orientation in crystal growth, likely influenced by the substrate preparation, deposition parameters, or post-deposition treatments. The distinct high-aspect-ratio features suggest a columnar growth pattern, which is common in thin films grown by methods such as vapor transport or sputtering under certain conditions. The uniformity of these features across the image implies a well-controlled growth process. Considering the application of ZnO in optoelectronics, such as UV lasers and LEDs, the morphology observed here could affect the optical properties of the film. High-aspect-ratio structures can enhance light extraction efficiency, which is beneficial for LED applications.

Figure 5 illustrates the photoluminescence (PL) spectra at five distinct points on a sputtered ZnO thin film deposited on a sapphire substrate. The PL spectra reveal that the predominant emission occurs at an average peak wavelength of 386.4 nm, corresponding to a bandgap energy of 3.421 eV. Notably, the PL intensity for the sputtered sample annealed at 350 °C surpasses that of samples synthesized via a homemade metal-organic chemical vapor deposition (MOCVD) system, even at an elevated temperature of 450 °C, as referenced in [9]. This enhanced PL intensity is indicative of superior crystalline quality of the film. Furthermore, the standard deviation among the peak wavelengths at various locations on the ZnO sample prepared by RF sputtering was determined to be 3.4 nm. The average full width at half maximum (FWHM) was measured to be 26.5 nm (equivalent to 0.195 eV), with the standard deviation of the FWHM for the ZnO sample being 0.75 nm. Photoluminescence (PL) is a process in which a substance absorbs photons (light energy) and then re-emits them. The absorbed energy transitions the material to an excited state, and when it returns to the ground state, it releases energy in the form of light [7,10]. This emitted light is detected as the PL spectrum. The PL intensity equation with temperature considerations reflects the thermal quenching of PL. At higher temperatures, the non-radiative recombination processes become more pronounced, diminishing the PL intensity. This behavior is critical in determining the efficiency of light emission in optoelectronic applications. In the graph, the x-axis denotes the wavelength of the emitted light in nanometers (nm), and the y-axis shows the PL intensity in arbitrary units (a.u.). Each line corresponds to a different spatial point on the sample, suggesting that the PL measurement was taken at multiple locations, perhaps to assess the uniformity of the photoluminescent properties across the sample. The sharp peak observed at around 380 nm indicates a strong PL emission in the ultraviolet range. The similarity of the spectra at different spatial points suggests that the material exhibits consistent photoluminescent behavior across these points. The augmented photoluminescence intensity is indicative of an enhanced crystalline integrity within the film's matrix. Upon meticulous analysis of the ZnO specimen, which was synthesized via the RF sputtering technique, the spatial inhomogeneity was quantitatively assessed through the standard deviation of the peak emission wavelengths across multiple loci, revealing a value of 3.2 nm. Moreover, the spectral width of the emission profile, as characterized by the full width at half maximum (FWHM), displayed an average value of 1.8 nm. This value corresponds to an energy dispersion of approximately 0.14 electron

volts (eV).The dispersion in the FWHM values across the sample was determined to be 1.6 nm, denoting a relative uniformity in the energetic profile of the photoluminescent phenomena intrinsic to the ZnO structure under examination.

**Figure 3**. SEM images of n-ZnO grown on sapphire with the scale bar is 2 μm in each figure.

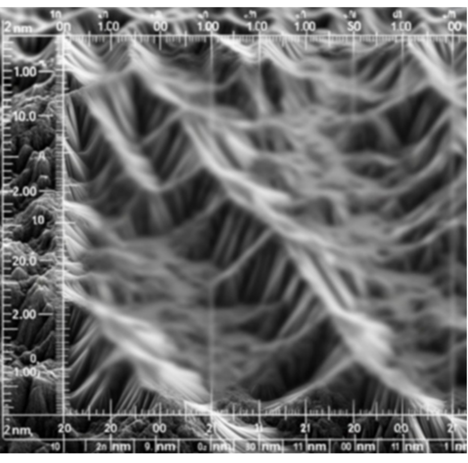

**Figure 4**. An image captured by Atomic Force Microscopy (AFM) depicts the growth of n-type Zinc Oxide (n-ZnO) on a sapphire substrate.

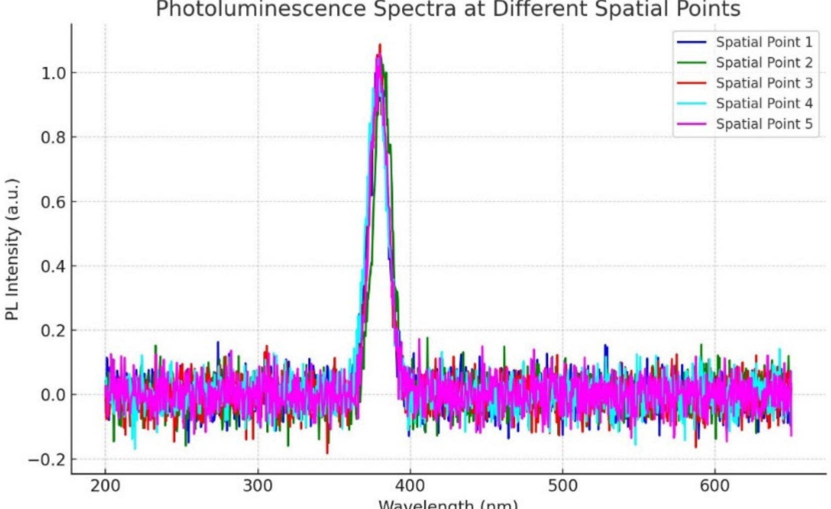


**Figure 5.** Photoluminescence spectra measured at different points on a ZnO thin film deposited on sapphire.

## CONCLUSIONS

In conclusion, this study has successfully demonstrated the deposition of ZnO films on Si, sapphire, GaAs, and GaP substrates using thermal oxidation. X-ray diffraction analysis revealed that the films exhibited a nanocrystalline structure with a preferential orientation. Optical transmittance measurements indicated an increase in the optical bandgap, while photoluminescence spectra revealed uniform and enhanced crystalline integrity. Electrical characterization of ZnO-based heterojunction diodes on different substrates showed distinct electrical characteristics, with variations in leakage current and ideality factor. The specific resistances of the Zinc Oxide (ZnO) films, determined from the linear portions of the current-voltage (I-V) curves, varied between $10^7$ and $10^9$ ohm·cm. This range highlights their potential as dielectric coatings. Furthermore, the temperature-dependent I-V characteristics of thin ZnO films, assessed over a wide temperature range (296-470 K), provided insights into the current transport mechanism, revealing that the currents were limited by space charges (SCL3). The photoluminescence spectra exhibited a sharp peak at around 380 nm, indicating strong PL emission in the ultraviolet range, with a standard deviation of peak emission wavelengths across multiple loci revealing a value of 1.8 nm. These findings highlight the potential of thermal oxidation-deposited ZnO films for applications in optoelectronic devices. Future research should focus on optimizing the deposition parameters and exploring the performance of these films in specific optoelectronic devices, with an emphasis on enhancing the uniformity and crystalline integrity of the films to further improve their optoelectronic properties.

**ORCID**
**Numonjon A. Sultanov,** https://orcid.org/0000-0002-4420-836X; **Zokirjon X. Mirzajonov,** https://orcid.org/0000-0002-4881-2994
**Fakhriddin T. Yusupov,** https://orcid.org/0000-0001-8937-7944; **Tokhirbek I. Rakhmonov,** https://orcid.org/0000-0002-6080-6159

## REFERENCES

[1] N. Sultanov, Z. Mirzajonov, and F. Yusupov, "Technology of production and photoelectric characteristics of AlB 10 heterojunctions based on silicon," E3S Web of Conferences, **458**, 01013 (2023). https://doi.org/10.1051/e3sconf/202345801013
[2] M.A. Ahmed, L. Coetsee, W.E. Meyer, J.M. Nel, "Influence (Ce and Sm) co-doping ZnO nanorods on the structural, optical and electrical properties of the fabricated Schottky diode using chemical bath deposition," J. Alloys Compd. **810**, 151929 (2019). https://doi.org/10.1016/j.jallcom.2019.151929
[3] Y. Deng, F. Peng, Y. Lu, X. Zhu, W. Jin, J. Qiu, J. Dong, et al., "Solution-processed green and blue quantum-dot light-emitting diodes with eliminated charge leakage," Nat. Photon. **16**, 505–511 (2022). https://doi.org/10.1038/s41566-022-00999-9
[4] Y.H. Won, O. Cho, T. Kim, D.-Y. Chung, T. Kim, H. Chung, H. Jang, et al., "Highly efficient and stable InP/ZnSe/ZnS quantum dot light-emitting diodes," Nature, **575**, 634–638 (2019). https://doi.org/10.1038/s41586-019-1771-5
[5] J.D. Ye, S.L. Gu, S.M. Zhu, S.M. Liu, Y.D. Zheng, R. Zhang, Y. Shi, et al., "Gallium doping dependence of single-crystal n-type ZnO grown by metal organic chemical vapor deposition," Journal of Crystal Growth, **283**(3-4), 279-285 (2005). https://doi.org/10.1016/j.jcrysgro.2005.06.030
[6] B.H. Kong, D.C. Kim, S.K. Mohanta, and H.K. Cho, "Influence of VI/II ratios on the growth of ZnO thin films on sapphire substrates by low temperature MOCVD," Thin Solid Films, **518**(11), 2975-2979 (2010). https://doi.org/10.1016/j.tsf.2009.10.124
[7] R. Pietruszka, R. Schifano, T.A. Krajewski, B.S. Witkowski, K. Kopalko, L. Wachnicki, and E. Zielony, "Improved efficiency of n-ZnO/p-Si based photovoltaic cells by band offset engineering," Solar Energy Materials and Solar Cells, **147**, 164-170 (2016). https://doi.org/10.1016/j.solmat.2015.12.018
[8] M. Volkova, R. Sondors, L. Bugovecka, A. Kons, L. Avotina, and J. Andzane, "Enhanced thermoelectric properties of self-assembling ZnO nanowire networks encapsulated in nonconductive polymers," Scientific Reports, **13**(1), 21061 (2023). https://doi.org/10.1038/s41598-023-30019-x
[9] P. Mishra, B. Monroe, B. Hussain, and I. Ferguson, "Temperature optimization for MOCVD-based growth of ZnO thin films," in: *2014 11th Annual High-Capacity Optical Networks and Emerging/Enabling Technologies (Photonics for Energy),* (Charlotte, NC, USA, 2014). https://doi.org/10.1109/HONET.2014.7029400
[10] E. Widyastuti, J.L. Hsu, and Y.C. Lee, "Insight on photocatalytic and photoinduced antimicrobial properties of ZnO thin films deposited by HiPIMS through thermal oxidation," Nanomaterials, **12**(3), 463 (2022). https://doi.org/10.3390/nano12030463
[11] A.P. Rambu, V. Tiron, V. Nica, and N. Iftimie, "Functional properties of ZnO films prepared by thermal oxidation of metallic films," Journal of Applied Physics, **113**(23), 234506 (2013). https://doi.org/10.1063/1.4811357
[12] O. Sánchez-Dena, S. Hernández-López, M.A. Camacho-López, P.E. Acuña-Ávila, J.A. Reyes-Esqueda, and E. Vigueras-Santiago, "ZnO Films from Thermal Oxidation of Zn Films: Effect of the Thickness of the Precursor Films on the Structural, Morphological, and Optical Properties of the Products," Crystals, **12**(4), 528 (2022). https://doi.org/10.3390/cryst12040528
[13] Q. Yang, X. Zhang, X. Zhou, and S. Liang, "Growth of Ga-doped ZnO films by thermal oxidation with gallium and their optical properties," AIP advances, **7**(5), 528 (2017). https://doi.org/10.3390/cryst12040528
[14] Y.G. Wang, S.P. Lau, H.W. Lee, S.F. Yu, B.K. Tay, X.H. Zhang, and H.H. Hng, "Photoluminescence study of ZnO films prepared by thermal oxidation of Zn metallic films in air," Journal of Applied Physics, **94**(1), 354-358 (2003). https://doi.org/10.1063/1.1577819
[15] N. Srivastava, and W. Bolse, "Stress-driven growth of ZnO nanowires through thermal oxidation of Zinc thin films over silicon substrate," Journal of Materials Science: Materials in Electronics, **34**(7), 616 (2023). https://doi.org/10.1007/s10854-023-10059-9
[16] I. Mihailova, V. Gerbreders, E. Tamanis, E. Sledevskis, R. Viter, and P. Sarajevs, "Synthesis of ZnO nanoneedles by thermal oxidation of Zn thin films," Journal of Non-Crystalline Solids, **377**, 212-216 (2013). https://doi.org/10.1016/j.jnoncrysol.2013.05.003
[17] R. Kumar, Jyotsna, and A. Kumar, "Barrier Height Calculation of Ag/n-ZnO/p-Si/Al Heterojunction Diode," Asian J. Adv. Basic Sci. **8**, 47–52 (2020). https://doi.org/10.33980/ajabs.2020.v08i01.006
[18] M.R. Khanlary, V. Vahedi, and A. Reyhani, "Synthesis and characterization of ZnO nanowires by thermal oxidation of Zn thin films at various temperatures," Molecules, **17**(5), 5021-5029 (2012). https://doi.org/10.3390/molecules17055021
[19] S.J. Chen, Y.C. Liu, J.G. Ma, D.X. Zhao, Z.Z. Zhi, Y.M. Lu, et al., "High-quality ZnO thin films prepared by two-step thermal oxidation of the metallic Zn," Journal of Crystal Growth, **240**(3-4), 467-472 (2002). https://doi.org/10.1016/S0022-0248(02)00925-9
[20] I. Bouanane, A. Kabir, D. Boulainine, S. Zerkout, G. Schmerber, and B. Boudjema, "Characterization of ZnO thin films prepared by thermal oxidation of Zn," Journal of Electronic Materials, **45**, 3307-3313 (2016). https://doi.org/10.1007/s11664-016-4469-6
[21] D.A. Neamen, *Semiconductor Physics and Devices: Basic Principles*, 4th ed. (McGraw-Hill Education, 2012).
[22] S.M. Sze, and K.K. Ng, *Physics of Semiconductor Devices*, 3rd ed. (John Wiley & Sons, 2006).

## НАНОКРИСТАЛІЧНІ ПЛІВКИ ZNO НА РІЗНИХ ПІДКЛАДКАХ: ДОСЛІДЖЕННЯ ЇХ СТРУКТУРНИХ, ОПТИЧНИХ ТА ЕЛЕКТРИЧНИХ ХАРАКТЕРИСТИК

**Нумонджон А. Султанов, Зокірджон Х. Мірзаджонов, Фахріддін Т. Юсупов, Тохирбек I. Рахмонов**
*Ферганський політехнічний інститут, Фергана, Узбекистан*

Оксид цинку (ZnO) – це універсальний напівпровідниковий матеріал із широкою забороненою зоною та великою енергією зв'язку екситонів, що робить його придатним для цілого ряду оптоелектронних застосувань, у тому числі синіх і ультрафіолетових світлодіодів (світлодіодів) і лазерів. У цьому дослідженні ми досліджуємо осадження плівок ZnO на різних підкладках (Si, сапфір, GaAs, GaP) за допомогою термічного окислення, економічно ефективної альтернативи молекулярно-променевої епітаксії (MBE) і хімічного осадження з газової фази (CVD). Ми представляємо комплексний аналіз структурних, оптичних і електричних властивостей цих плівок, зосереджуючись на їх потенціалі для використання в гетеропереходних діодах. Експериментальна методика передбачала термічне випаровування плівок Zn у вакуумній камері з подальшим окисленням в атмосфері чистого кисню. Умови осадження були оптимізовані для отримання нанокристалічних плівок ZnO з переважною орієнтацією, що підтверджено рентгенівським дифракційним аналізом (XRD). Вимірювання оптичного пропускання показало збільшення ширини забороненої зони, тоді як спектри фотолюмінесценції (PL) виявили рівномірну та підвищену цілісність кристалів у зразках. Електричні характеристики гетеропереходних діодів на основі ZnO на різних підкладках показали відмінні електричні характеристики з варіаціями струму витоку та коефіцієнта ідеальності [1-4]. Питомі опори плівок ZnO, розраховані за лінійними відрізками вольт-амперних кривих.

**Ключові слова**: *оксид цинку (ZnO); термічне окислення; гетеропереходні діоди; оптоелектронні застосування; нанокристалічна структура; оптична заборонена зона; електричні властивості; вольт-амперні (ВАХ); температура підкладки; спектри фотолюмінесценції*

East European Journal of Physics. **2.** 315-320 (2024)
DOI:10.26565/2312-4334-2024-2-36 ISSN 2312-4334

# INVESTIGATION OF STRUCTURAL, MAGNETIC AND OPTICAL PROPERTIES FOR DYSPROSIUM DOPED ZINC NANOFERRITES BY SOL-GEL AUTOCOMBUTION TECHNIQUES

**Sanchita V. Chavan[a], Vyankati R. Jadhav[a], Sunanda H. Pisal[b], Ramesh B. Bhise[c]*, Mahendra S. Shinde[d]*, Vishal H. Goswami[e], Pradip B. Sarawade[f]**

*[a]PG Department of Physics, PDEA's Annasaheb Magar College, Hadpsar, Pune-28, MS, India*
*[b]PG Department of Physics, RSS's S. M. Joshi College, Hadpsar, Pune-28, MS, India*
*[c]PG Department of Physics, Balasaheb Jadhav Arts, Commerce and Science College, Ale (Junnar), Pune-412411, MS, India*
*[d]Department of Physics, M.J.M. Arts, Commerce and Science College, Karanjali (Peth) Nashik-422208, MS, India*
*[e]Department of Physics, Chikitsak Samuha's Sir Sitaram and Lady Shantabai Patkar College of Arts & Science and V.P. Varde College of Commerce & Economics, Goregaon West, Mumbai, Maharashtra 400061, India*
*[f]Department of Physics, University of Mumbai, Kalina, Mumbai, India*
**Corresponding Authors' e-mail: bhiseramesh@gmail.com, mahen3569@rediffmail.com*
Received March 9, 2024; revised April 2, 2024; accepted April 18, 2024

Using the auto combustion sol-gel method, nanoferrite crystalline aligns of $Dy^{3+}$ replaced Zn-Fe spinel ferrite with the chemical formula $Dy_xZn_{1-x}Fe_{2-x}O_4$ (x= 0.00, 0.05) were successfully synthesized. In this process, citric acid was utilized as energy (fuel) in a 3:1 ratio to metal nitrate. Using XRD and FT-IR, the crystal structure and phase of dysprosium zinc was examined. Using the XRD method, the crystal size, lattice constant, cation distribution, and porosity were ascertained. FT-IR spectroscopy is used to infer structural study and the redistribution of cations between octahederal (A) and tetrahederal (B) site of Zn material. According to morphological research, the temperature during sintering is what causes grain to form and grow. Utilizing the Hysteresis Loop Technique, saturation magnetism and magneton number are determined. In Zn-Fe ferrite, the saturation magnetization rises with increasing density x, utilizing the Sol-gel auto-combustion method at a comparatively low temperature. Using nitrate citrate, the nanocrystallite $Dy_xZn_{1-x}Fe_{2-x}O_4$ was created. The combustion process and chemical gelation are unique. Using citric acid as a catalyst, their metal nitrates nanoferrites underwent a successful chemical reaction and were obtained as a dried gel. FT-IR, UV-Visible, VSM and XRD were used to characterize the produced nanoferrite powders. Magnetization and hysteresis were measured using the VSM technique. The FT-IR verifies that the synthesized substance is ferrite. The size of the nanocrystalline ferrite material, $Dy_xZn_{1-x}Fe_{2-x}O_4$, was determined by X-ray using the Scherrer method to be between 16.86 to 12.72 nm average crystallite size. Magnetization and hysteresis were measured using the VSM technique.
**Keywords:** *Autocombustion technique; VSM technique; FT-IR spectroscopy; UV-Visible Spectroscopy; XRD method*
**PACS:** 75.50.Gg, 75.75.+a, 76.60.Es

## 1. INTRODUCTION

Substituted rare earth materials with different ferrites are emerging as promising materials with a range of uses. Depending on the kind and quantity of rare earth element utilized, the addition of a small amount of rare earth to iron oxide samples changes their electrical, magnetic, and structural properties. Two categories exist for rare earth ions: one has a radius that is similar to that of iron ions, while the other has a radius that is larger [1]. This variation in ionic radii will cause micro strain, which could cause the spine's structure to deform [2]. Because of their large ionic radii, rare earth ions replaced $Fe^{3+}$ in the ferritin mixture, resulting in limited soluble in the spinel lattice [3]. It is discovered that the rare earth ions are a promising addition to enhance ferrites' magnetic characteristics [4–5]. $Sm^{3+}$ doped Cu–Zn ferrite [6] and $La^{3+}$ doped Ni–Cu–Zn ferrite [5] are two examples of rare earth doped ferrites.

Researchers used a variety of techniques to create zinc ferrite nanoparticles, such as hydrothermal, solgel auto-combustion, combination, sonochemical, the microemulsion, reverse micelle, and high energy ball milling [7-10]. Due to its low cost, heat at low temperatures treatment, and ease of handling in comparison to other methods, sol-gel autocombustion is one of the most widely used methods for preparing nano-scale ferrite powder [11]. The physical properties of zinc ferrite nanoparticles are influenced by grain size and cation distribution at A- and B-sites in the spinel ferrite lattice. Doping spinel ferrite nanoparticles with different rare earth ions in small amounts has recently emerged as a promising strategy for improving their physical properties [12].

In the current study, dysprosium-doped Zinc ferrite was synthesized using the sol-gel auto combustion method [13]. The following techniques were used to characterize these ferrite materials: electrical resistivity, magnetic hysteresis, TGA-DTA, XRD, FT-IR. This dysprosium doped Zn ferrite material's catalytic activity was investigated for the breakdown of hydrogen peroxide. It had demonstrated that the rate constant increases as the amount of Dy in $ZnFe_2O_4$ [x=0.0, 0.050] increases.

***Cite as:*** S.V. Chavan, V.R. Jadhav, S.H. Pisal, R.B. Bhise, M.S. Shinde, V.H. Goswami, P.B. Sarawade, East Eur. J. Phys. 2, 315 (2024), https://doi.org/10.26565/2312-4334-2024-2-36
© S.V. Chavan, V.R. Jadhav, S.H. Pisal, R.B. Bhise, M.S. Shinde, V.H. Goswami, P. B. Sarawade, 2024; CC BY 4.0 license

## 2. MATERIALS AND METHODS

### 2.1 Materials

Chemicals of reagent grade purity were used. We prepared solutions of zinc nitrate, iron nitrate, dysprosium nitrate, and ammonia in deionized water. The added to a beaker containing 0.25 M zinc nitrate solution. Added to it after that were solutions of dysprosium nitrate and 0.25 M iron nitrate. This mixture was mixed with citric acid solution, and ammonia solution was added while stirring continuously to bring the pH to 7. To create gel, this mixture was agitated and heated to 80°C for three hours. To get Dy-Zn ferrite powder, this gel was heated on a hot plate between 300°C. This powder was used for characterization after being calcined for 4-5 hours at 500 $^0$C.

### 2.2 Characterization techniques

The structural characterization and phase identification were examined using X-Ray Diffraction (XRD), (Rigaku miniflex 600), fitted with a high-intensity Cu-k radiation source (λ = 1.5406) in the 2θ range (20°–80°) with a step size of 0.0260 at room temperature. FTIR (Thermo Nicolet, Avatar 370) recorded the room temperature Fourier transform infrared spectra in the wavenumber range of 4000-400 $cm^{-1}$. A Vibrating Sample Magnetometer (VSM) with a maximum applied magnetic field range was used to measure the magnetic characteristics of the sample at room temperature.

## 3. RESULT AND DISCUSSION

### 3.1 XRD Analysis

The X-ray diffraction structure for $ZnDy_xFe_{2-x}O_4$ (x= 0.00, 0.05) spinel ferrite nano particles that were synthesized using the sol-gel method. The samples of Zn composites were sintered for five hours at 500 °C. The XRD was used to determine the structure of the crystal and crystalline phase pattern. This is an extremely useful method for calculating crystalline parameters.

Fig. 1(a). The diffraction peaks observed in the XRD pattern of prepared samples corresponded to the crystal planes (311), (400), (332), (530), (631) and (643) respectively. The presence of all diffraction peaks of nanoparticles that have been synthesized makes certain the formation of the cubic inverse spinel structure, the sign denotes the mixed impurity phase of $DyFeO_3$. Because of its larger ionic radius, the substitution of $Fe^{3+}$ions by $Dy^{3+}$ ions have a solubility limit. As a result, the amount of $Fe^{3+}$ ions that can be replaced by $Dy^{3+}$ ions are limited. Because of its larger ionic radius, the substitution of $Fe^{3+}$ ions by $Dy^{3+}$ions have a solubility limit. As a result, the amount of $Fe^{3+}$ ions that will be replaced by $Dy^{3+}$ ions are limited. As a result of an excess substitute of $Dy^{3+}$ ions, it is expected that $DyFeO_3$ phase will develop together the grain boundaries, as observed [14].

The crystallite sizes were determined using equations 1 are shown in Table 1, and the W-H plots βcosθ versus 4 sin θ for samples that were synthesized are shown in Fig. 1(b). The intercept used to determine the crystal size (D) was calculated was provided by a linear plot, and the strain value was computed by a straight line fitting of the slope. The crystallite sizes of Zn $Dy_xFe_{2-x}O_4$ are smaller than those of pure zinc ferrite due to differences in the ionic radii of doped ions and substituted ions from the interstitial sites, and the results are consistent with ref. [15,16,17].

Figure 1 depicts an XRD pattern. The average size of the crystallite (Dm) was calculated using the Debye Scherrer formula, which is given as:

$$D = k\lambda/\beta\cos\theta \tag{1}$$

Where, k is 0.9 for spinel ferrites; λ is the1.54 indicates the x-ray wavelength; β is the FWHM of the most intense peak, and is the diffraction angle of the most intense peak.

The average lattice parameter 'a' can be calculated using the formula:

$$a = \sqrt{h^2 + k^2 + 1^2} \tag{2}$$

Where, d is the crystal plane spacing; hkl is the miller index value

The average lattice constant for all samples was found to be in the range of 8.44 to 8.33. The ionic radiuses. The average lattice parameter 'a' was explained using the ions Dy $^{3+}$ and $Fe^{3+}$. The average lattice parameter was found to decrease as the $Dy^{3+}$ doping content increased. The following formula can be used to calculate X-ray density $\rho_x$:

$$\rho_x = \frac{8M}{Na^3}, \tag{3}$$

where,
M is the molecular weight of the composition Z=8 for spinel structure represents the number of molecules per unit cell, N is the Avogadro number ($6.0221\times10^{23}$), and $a^3$ is the volume of the unit cell.

The X-ray density was calculated to be between 7.48 and 21.23 g/$cm^3$. Because $Dy^{3+}$ has a higher molar weight than $Fe^{3+}$, the relationship between X-ray density and quantity is almost linear [12]. This means that the X-ray density increases as the amount of $Dy^{3+}$ doping increases.

The Micro-strain calculated by using this formula

$$\text{Micro-strain} = \frac{\beta\cos\theta}{4}(10^{15}) \tag{4}$$

Micro-strain was calculated to be between 0,0021 and 0.0029. As the concentration of $Dy^{3+}$ doping increases, the micro-strain decreases. At x = 0.00, 0.05 the highest value of micro-strain was observed. The dislocation density of the nanoparticles that can be calculated using the following equation:

$$\delta = \frac{1}{D^{z}}(10^{15}) \quad (5)$$

Where, D is the crystalline size.

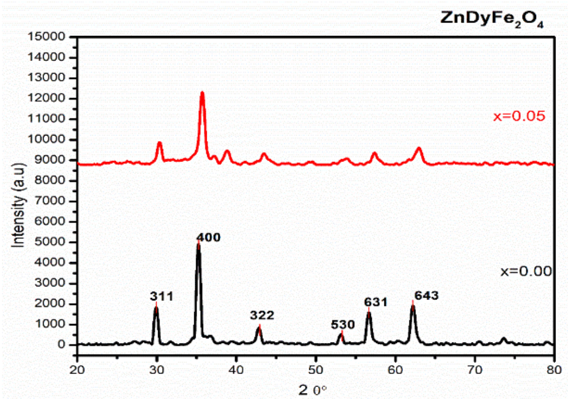


**Figure 1(a).** XRD Analysis of Dy $^{3+}$ Zn ferrite (x=0.00,0.05)

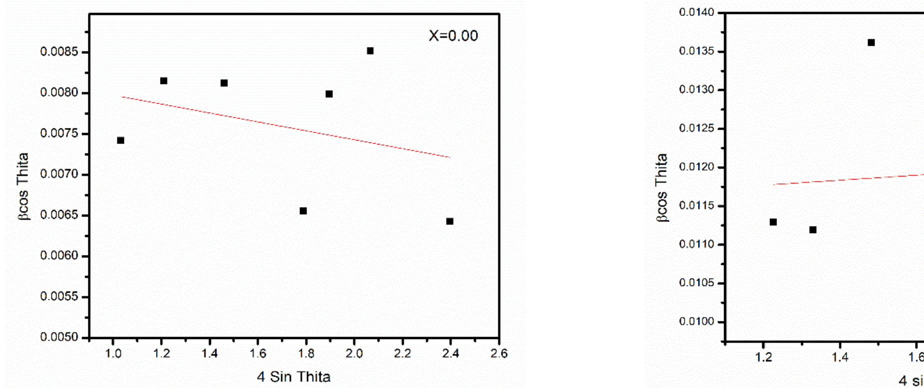


**Figure 1(b).** Hall – Williamson plots of $ZnDyFe_2O_4$ (x=0.00, 0.05)

**Table 1.** Measurement of Lattice Constat, Density and Micro-strain, etc.

| Content x | Interplanar distance | Lattice parameter (A°) | X ray Density | Crystalline size (nm) | Micro-strain | Dislocation Density ($\times10^{14}$) line/m$^2$ |
|---|---|---|---|---|---|---|
| 0.00 | 2.5465 | 8.4469 | 4.2597 | 17.77 | 0.0021 | 0.0084 |
| 0.05 | 2.5120 | 8.3323 | 4.4378 | 12.83 | 0.0029 | 0.0237 |

### 3.2 FT-IR Analysis

As shown in Fig. 2, the FT-IR spectra of the$ZnDy_xFe_{2-x}O_4$ samples are obtained in the 4000 to 500 cm$^{-1}$ range.

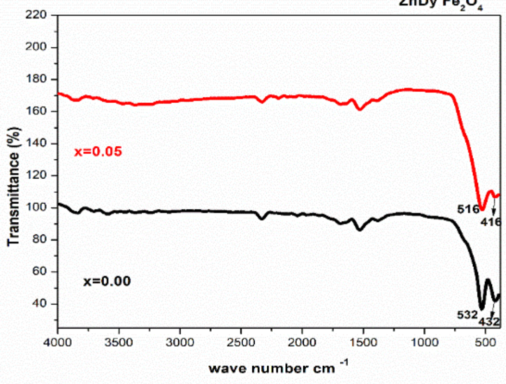


**Figure 2.** FT-IR spectra of $Dy^{3+}$doped Zn ferrite (x=0.00,0.05)

Ferrite exhibits two prominent oxygen-metal frequencies [18]. The tetrahedral (A) and octahedral (B) metal stretching, which are thought to be the typical bands of spinel structure, were associated with the higher frequency band (υ1) and lower frequency band (υ2) which were observed in the range of 532-516 $cm^{-1}$ and 432-416 $cm^{-1}$ [19].

The absorption frequency values, $n_1$ and $n_2$ that as the $Dy^{3+}$content increased, the absorption frequency $\upsilon_2$ was slightly moved towards a higher frequency and $\upsilon_1$ towards a lower frequency side. This is explained by the $Fe^{3+}$ions on the tetrahedral site shifting in the direction of the oxygen ions, which reduces with the $Fe^{3+}$-$O^2$ distance. The basic frequency and central frequency decrease as the site radius increases, which changes to the underside Literature has documented similar reports [20-21].

### 3.3 VSM Analysis

For VSM analysis Figure 3 shows Hysteresis loop of Zn Dy3+doped Zn ferrite(x=0.00,0.05). The Saturation Magnetization (Ms), Coercivity (Hc), and Remnant ratio (R=Mr/Ms) of each sample are listed in Table 2. The values of Ms and Mr for pure zinc ferrite have decreased from 1248.0914 to 041.0400 emu/g and 301.2114 to 301.2114emu/g, respectively, while the coercivity has increased from 058.8889 to 050.5556 Oe. The decrease in Ms with Dy content is in line with the findings of ferrites doped with rare earth elements [22]. Tables show that there is a direct correlation between the size of the nanoferrite particles and the value of $M_S$ [23].

Table 2 shows that when $Dy^{3+}$ is substituted, the magnetization values decrease. The site use of the cations and the changes in the exchange effects brought about by the adding of dysprosium can be used to explain the trend. The primary source of magnetic properties is $Fe^{3+}$ on the cubic spinal B-sites. Due to its strong octahedral preference, the dysprosium ion takes up residence at the B-site, causing the $Fe^{3+}$ ion to migrate to the A-site.

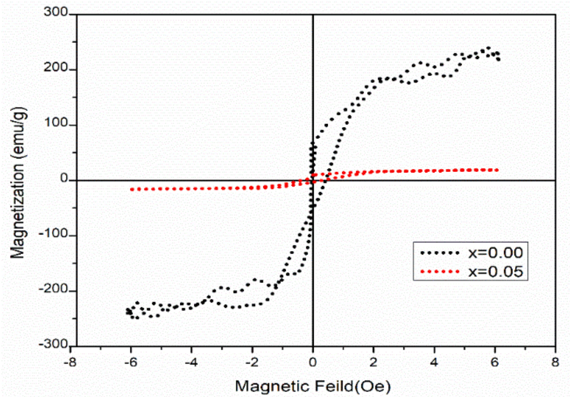


**Figure 3.** Hysteresis loop of Zn $Dy^{3+}$doped Zn ferrite(x=0.00,0.05)

**Table 2.** Measurement of Saturation Magnetization (Ms), Coercivity (Hc), and Remnant ratio

| Composition (x) | Hc (Oe) | Mr (emu/gm) | Ms (emu/gm |
|---|---|---|---|
| 0.00 | 050.5556 | 301.2114 | 1248.0914 |
| 0.05 | 058.8889 | 301.2114 | 041.0400 |

### 3.4 UV-Visible analysis

The Diffuse Reflectance Spectroscopy (DRS) optical absorption spectra in the absorption mode for $ZnDyFe_2O_4$ nanoparticles (where x = 0.00, 0.05) within the UV-visible range are shown in Figure 4.

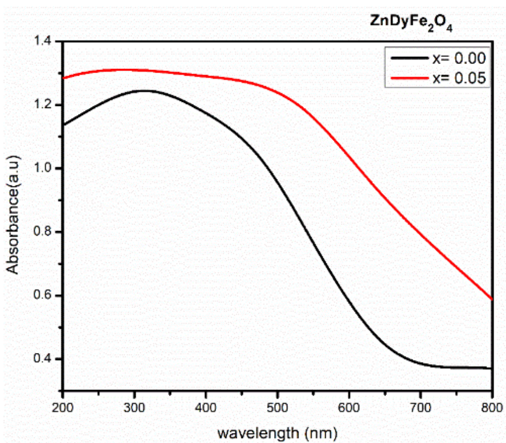


**Figure 4.** Absorbance spectra of $ZnDyFe_2O_4$ system (x=0.00,0.05)

These samples were prepared at room temperature and sintered at 500°C. Three absorption bands are observed at 416 nm and 518 nm, which is in line with the XRD findings. The composition and heat treatment of the samples influence the nature of this absorption, as shown in Figure 4. Three different types of electronic transitions are seen in the optical absorption of $ZnDyFe_2O_4$ samples. Specifically, for the x = 0 composition sample, electronic transitions related to charge carriers are observed in the wavelength range of 200 to 800 nm within the optical region.

The calculated band gap energy decreases from 2.9807 to 2.3938 eV for samples sintered at 500°C [24].

$$\text{Energy band gap}=1240/\pi(\text{nm}) \quad (6)$$

## 4. CONCLUSION

Spinel ferrites nanoparticles have an important role in our daily lives and are used in a variety of applications including medical sectors, nano electronics, and the treatment of waste water, among others. Dysprosium ($Dy^{3+}$) substituted Zn nanoferrites with the general formula $ZnDy_xFe_{2-x}O_4$ (x = 0.00, 0.05) were successfully synthesized using the sol-gel autocombustion method, which is the simplest method for producing such nano ferrites. The decrease in average crystalline size from 16.86 to 12.72 nm is the result of $Dy^{3+}$ substitution on the structural characteristics of zinc ferrite.

FT-IR was used to confirm the spinel phase structure. The characteristics of spinel structure are divided into two primary frequency bands: the higher frequency band $\upsilon_1$ (approx. 532 $cm^{-1}$) and the lower frequency band $\upsilon_2$ (approx. 432 $cm^{-1}$). The absorption peaks are referred to as higher frequency bands $\upsilon_1$ due to the tetrahedral site of inherent increasing vibration. Lower frequency bands $\upsilon_2$ are referred to as octahedral stretching bands.

**ORCID**
**Mahendra S. Shinde,** https://orcid.org/0000-0001-9141-5049; **Vishal H. Goswami,** https://orcid.org/0000-0001-9782-2737

**REFERENCES**

[1] N. Rezlescu, E.C. Rezlescu, and M.L. Craus, “Effects of the rare-earth ions on some properties of a nickel-zinc ferrite,” J. Phys. Condens. Matter. **6**, 5707 (1994). https://doi.org/10.1088/0953-8984/6/29/013
[2] S. Solyman, “Transport properties of La-doped Mn–Zn ferrite,” Ceram. Int. **32,** 755-760 (2006). https://doi.org/10.1016/j.ceramint.2005.05.018
[3] A.A. Sattar, and K.M. EI-Shokrofy, “Rare Earth Doping Effect on the Electrical Properties of Cu-Zn Ferrites,” J. Phys. **7**(1), C1-245-C1-246 (1997). https://doi.org/10.1051/jp4:1997194
[4] N. Rezlescu, E. Rezlescu, P.D. Mangeron, L. Rezlescu, and C. Pasnicu, “The Influence of $R_2O_3$ (R = Yb, Er, Dy, Tb, Gd, Sm and Ce) on the Electric and Mechanical Properties of a Nickel–Zinc Ferrite,” J. Phys. C: State Solid, **162**, 673-678 (1997). https://doi.org/10.1002/1521-396X(199708)162:2%3C673::AID-PSSA673%3E3.0.CO;2-A
[5] P.K. Roy, B.B. Nayak, and J. Bera, “Study on electro-magnetic properties of La substituted Ni–Cu–Zn ferrite synthesized by auto-combustion method,” J. Magn. Magn. Mater. **320**, 1128-1132 (2008). https://doi.org/10.1016/j.jmmm.2007.10.025
[6] A.A. Sattar, A.H. Wafik, K.M. EI-Shokrofy, and M.M. EI-Tabby, “Magnetic Properties of Cu–Zn Ferrites Doped with Rare Earth Oxides,” Status Solidi a, **171**, 563-569 (1999). https://doi.org/10.1002/(SICI)1521-396X(199902)171:2%3C563::AID-PSSA563%3E3.0.CO;2-K
[7] B. Azhdar, B. Stenberg, and L. Kari, “Polymer–nanofiller prepared by high-energy ball milling and high velocity cold compaction,” Polymer Composites, **29**, 252-261 (2008). https://doi.org/10.1002/pc.20353
[8] N. Javerberg, H. Edin, P. Nordell, S. Nawaz, B. Azhdar, and U.W. Gedde, “Dielectric properties of alumina-filled poly (ethylene-co-butyl acrylate) nanocomposites. Part I-dry studies,” IEEE Trans. Dielectr. Electr. Insul. **19**(2), 383-390 (2012). https://doi.org/10.1109/TDEI.2012.6180229
[9] J. Peng, M. Hojamberdiev, Y. Xu, B. Cao, J. Wang, and H. Wu, “Hydrothermal synthesis and magnetic properties of gadolinium-doped $CoFe_2O_4$ nanoparticles,” J. Magn. Magn. Mater. **323**(1), 133-137 (2011). https://doi.org/10.1016/j.jmmm.2010.08.048
[10] M.A. Almessiere, Y. Slimani, S. Guner, M. Sertkol, A. Demir Korkmaz, S.E. Shirsath, and A. Baykal, “Sonochemical synthesis and physical properties of $Co_{0.3}Ni_{0.5}Mn_{0.2}Eu_xFe_{2-x}O_4$ nano-spinel ferrites,” Ultrasonics Sonochemistry, **58**, 104654 (2019). https://doi.org/10.1016/j.ultsonch.2019.104654
[11] V.S. Rizi, F. Sharifianjazi, H. Jafarikhorami, N. Parvin, L.S. Fard, M. Irani, and A. Esmaeilkhanian, “Sol–gel derived $SnO_2/Ag_2O$ ceramic nanocomposite for $H_2$ gas sensing applications,” Materials Research Express, **6**, 1150g-1152g (2019); https://doi.org/10.1088/2053-1591/ab511e
[12] R.S. Yadav, I. Kuřitka, J. Vilcakova, J. Havlica, L. Kalina, P. Urbánek, M. Machovsky, et al., “Sonochemical synthesis of $Gd^{3+}$ doped $CoFe_2O_4$ spinel ferrite nanoparticles and its physical properties,” Ultrason. Sonochem. **40**, 773-783 (2018). https://doi.org/10.1016/j.ultsonch.2017.08.024
[13] P. Ravindranathan, and K.C. Patil, “A low temperature path to the preparation of ultrafine ferrites,” Ceram. Bull. **66**, 688-692 (1987). http://eprints.iisc.ac.in/id/eprint/13867
[14] I.K. Punithavathy, A. Rajeshwari, S.J. Jeyakumar, N. Lenin, B. Vigneshwaran, M. Jothibas, and B. Arunkumar, “Impact of lanthanum ions on magnetic and dielectric properties of Zinc nanoferrites,” J. Mater. Sci. Mater. Electron. **31**, 9783–9795 (2020). https://doi.org/10.1007/s10854-020-03523-3
[15] K.L. Routray, S. Saha, and D. Behera, “Rare-earth ($La^{3+}$) substitution induced changes in the structural, dielectric and magnetic properties of nano- $CoFe_2O_4$ for highfrequencyand magneto-recording devices,” Appl. Phys. A, **125**, 328 (2019). https://doi.org/10.1007/s00339-019-2615-8
[16] S.B. Das, R.K. Singh, V. Kumar, N. Kumar, P. Singh, and N.K. Naik, “Structural, magnetic, optical and ferroelectric properties of $Y^{3+}$ substituted zinc ferrite nanomaterials prepared by a cost-effective sol-gel route,” Mater. Sci. Semicond. Process. **145**, 106632 (2022). https://doi.org/10.1016/j.mssp.2022.106632

[17] S.S. Satpute, S.R. Wadgane, K. Desai, D.R. Msne, and R.H. Kadam, "Substitution effect of $Y^{+3}$ ions on the structural, magnetic and electrical properties of zinc ferrite nanoparticles," Ceramica, **66**, 43–49 (2020). https://doi.org/10.1590/0366-69132020663772734
[18] K.V. Kumar, "Tunable optical bandgap of gadolinium substituted nickel-zinc ferrite nanoparticles-effect of calcination temperature on its optical parameters," Advances in Materials Physics and Chemistry, **12**, 33–45 (2022). https://doi.org/10.4236/ampc.2022.123003
[19] M. Rashad, R. Mohamed, and H. El-Shall, "Magnetic properties of nanocrystalline Sm-substituted $CoFe_2O_4$ synthesized by citrate precursor method," J. Mater. Process. Technol. **198**, 139-146 (2008). https://doi.org/10.1016/j.jmatprotec.2007.07.012
[20] F.-X. Cheng, J.-T. Jia, Z.-G. Xu, B. Zhou, C.-S. Liao, C.-H. Yan, L.-Y. Chen, and H.- B. Zhao, "Microstructure, magnetic, and magneto-optical properties of chemical synthesized Co-RE (RE¼ Ho, Er, Tm, Yb, Lu) ferrite nanocrystalline films," J. Appl. Phys. **86**, 2727-2732 (1999). https://doi.org/10.1063/1.371117
[21] A. Gadkari, T. Shinde, and P. Vasambekar, "Structural analysis of $Y^{3+}$-doped Mg-Cd ferrites prepared by oxalate co-precipitation method," Mater. Chem. Phys. **114**, 505-510 (2009). https://doi.org/10.1016/j.matchemphys.2008.11.011
[22] J. Peng, M. Hojamberdiev, Y. Xu, B. Cao, J. Wang, and H. Wu, "Hydrothermal synthesis and magnetic properties of gadolinium-doped $CoFe_2O_4$ nanoparticles," J. Magn. Magn. Mater. **323**, 133-137 (2011). https://doi.org/10.1016/j.jmmm.2010.08.048
[23] A. Goldman, *Modern Ferrite Technology*, 2nd ed. (Springer, Pittsburgh, 2006).
[24] V. Awati, K. Badave, and D. Bobade, "Effect of $Tb^{3+}$ substitution on structural, optical and magnetic properties of $NiCuZnFe_2O_4$ prepared by sol-gel route," Indian J. of Physics, **96**(1), 89–101 (2022). https://doi.org/10.1007/s12648-020-01955-5

## ДОСЛІДЖЕННЯ СТРУКТУРНИХ, МАГНІТНИХ ТА ОПТИЧНИХ ВЛАСТИВОСТЕЙ НАНОФЕРИТІВ ЦИНКУ, ЛЕГОВАНИХ ДИСПРОЗІЄМ ШЛЯХОМ ЗОЛ-ГЕЛЬ АВТОЗГОРЯННЯ

**Санчіта В. Чаван[a], В'янкаті Р. Джадхав[a], Сунанда Х. Пісал[b], Рамеш Б. Бхісе[c], Махендра С. Шінде[d], Вішал Х. Ґосвамі[e], Прадіп Б. Сараваде[f]**
*[a]PG Департамент фізики, Коледж Аннасахеба Магара PDEA, Хадпсар, Пуна-28, MS, Індія*
*[b]Департамент фізики, Коледж С. М. Джоші RSS, Хадпсар, Пуна-28, MS, Індія*
*[c]PG Департамент фізики, Коледж мистецтв, торгівлі та науки Баласахеба Джадхава, Але (Джуннар), Пуна, MS, Індія*
*[d]Департамент фізики, M.J.M. Коледж мистецтв, торгівлі та науки, Каранджалі (Пет) Нашік-422208, MS, Індія*
*[e]Департамент фізики, коледж мистецтв та наук сера Сітарама та леді Шантабай Паткар Чикітсак Самуха та коледж торгівлі та економіки Варде, Західний Горегаон, Мумбаї, Махараштра 400061, Індія*
*[f]Департамент фізики, Університет Мумбаї, Каліна, Мумбаї, Індія*

Використовуючи золь-гель метод автоматичного спалювання, було успішно синтезовано кристалічні угруповання нанофериту $Dy^{3+}$, заміненого шпінельним феритом Zn-Fe з хімічною формулою $Dy_xZn_{1-x}Fe_{2-x}O_4$ (x= 0,00, 0,05). У цьому процесі лимонна кислота використовувалася як енергія (паливо) у співвідношенні 3:1 до нітрату металу. За допомогою XRD та FT-IR досліджено кристалічну структуру та фазу диспрозію цинку. Методом XRD встановлено розмір кристалів, постійну ґратки, розподіл катіонів і пористість. FT-IR спектроскопія використовується для висновку про структурне дослідження та перерозподіл катіонів між октаедральним (A) і тетраедральним (B) матеріалом Zn. Згідно з морфологічними дослідженнями, температура під час спікання є причиною формування та росту зерна. Використовуючи методику петлі гістерезису, визначають магнетизм насичення та число магнетонів. У фериті Zn-Fe намагніченість насичення зростає зі збільшенням щільності x, з використанням методу золь-гель автоспалювання при порівняно низькій температурі. Використовуючи цитрат нітрату, створено нанокристалліт $Dy_xZn_{1-x}Fe_{2-x}O_4$. Процес горіння і хімічне гелеутворення унікальні. Використовуючи лимонну кислоту як каталізатор, їхні наноферити з нітратів металів пройшли успішну хімічну реакцію та були отримані у вигляді висушеного гелю. FT-IR, UV-Visible, VSM та XRD були використані для характеристики отриманих наноферитових порошків. Намагніченість і гістерезис вимірювали за допомогою методу VSM. FT-IR підтверджує, що синтезована речовина є феритом. Розмір нанокристалічного феритового матеріалу, $Dy_xZn_{1-x}Fe_{2-x}O_4$, був визначений рентгенівським методом за допомогою методу Шеррера, коли середній розмір кристалітів становить від 16,86 до 12,72 нм. Намагніченість і гістерезис вимірювали за допомогою методу VSM.

**Ключові слова:** *техніка автозгоряння; техніка VSM; FT-IR спектроскопія; УФ-видима спектроскопія; метод XRD*

EAST EUROPEAN JOURNAL OF PHYSICS. **2.** 321-326 (2024)
DOI:10.26565/2312-4334-2024-2-37 ISSN 2312-4334

# EFFECT OF γ-IRRADIATION ON STRUCTURE AND ELECTROPHYSICAL PROPERTIES OF S-DOPED ZnO FILMS

**Sirajidin S. Zainabidinov**[a], **Akramjon Y. Boboev**[a,b]*, **Nuritdin Y. Yunusaliyev**[a]
[a]*Andijan state university named after Z.M. Babur, Andijan, Uzbekistan*
[b]*Institute of Semiconductor Physics and Microelectronics at the National University of Uzbekistan, 20 Yangi Almazar st., Tashkent, 100057, Uzbekistan*
**Corresponding Author e-mail: aboboevscp@gmail.com*
Received March 11, 2024; revised April 8, 2024; accepted April 26, 2024

The produced *ZnO<S>* films were characterized with the crystallographic orientation (*001*) and lattice parameters $a = b = 0.3265$ nm and $c = 0.5212$ nm. $ZnO_{1-x}S_x$ nano-crystallites on the surface of the film had characteristic sizes ranging from 50 nm to 200 nm. The lattice parameter of $ZnO_{1-x}S_x$ nano-crystallites was experimentally determined to be $a_{ZnO<S>} = 0.7598$ nm. The study has shed light on what occurs to lattice parameters of the *ZnO* film and the geometric dimensions of $ZnO_{1-x}S_x$ nano-crystallites on the surface of the film under the influence of gamma-irradiation. It has been determined that the crystal structure of $ZnO_{1-x}S_x$ nanocrystallites represents a cubic lattice and belongs to the space group *F43m*. It has been determined that after γ-irradiation at doses $5 \cdot 10^6$ *rad*, the resistivity of *ZnO<S>* films reduced to $\rho = 12{,}7\ \Omega \cdot cm$ and the mobility of the majority charge carriers ($\mu$) became $0.18\ cm^2/V \cdot s$, whereas their concentration ($N$) had increased and equaled $2.64 \cdot 10^{18}\ cm^{-3}$. The study of the current-voltage characteristics of *p- ZnO<S>/n-Si* heterostructures before and after *γ*-irradiation at doses of $5 \cdot 10^6$ *rad* revealed that the dependence of the current on voltage obeys an exponential law which is consistent with the theory of the injection depletion phenomenon. It was determined that under the influence of *γ*-irradiation at doses of $5 \cdot 10^6$ *rad*, the capacitance of the *p-ZnO<S>/n-Si* heterostructure at negative voltages increases and the shelved curve sections and peaks are observed on the curve due to the presence of a monoenergetic level of fast surface states at the heterojunction.
**Keywords:** *Film; Ultrasonic spray pyrolysis; Nano-crystallite; γ-irradiation; Crystallographic orientation; Lattice parameter; Charge carriers; Injection depletion*
**PACS:** 78.30.Am

## INTRODUCTION

*ZnO* metal oxide layers represent semiconductors with a band gap of *3.3eV* and *n*-type conductivity due to oxygen deficiency [1]. The layers are conventionally engineered by three most promising techniques such as, synthesis and doping of zinc oxide under substantially non-equilibrium conditions; thermal annealing under a film of substance with inadequate solubility of the components of compounds; annealing of crystals in an atmosphere of atomic chalcogen [2,3]. In the present experimental case, to a certain extent, all three of these approaches have been implemented. Thus, in the process of pyrolysis of ultrathin films of zinc nitrates and/or acetates solutions, significantly non-equilibrium thermodynamic conditions occur on the surface of the substrate leading to the formation of atomic oxygen and sulfur, as well as *O-S, Zn-O-S* groups, etc., that further line up in a growing film [4]. By applying (choosing) substrates with various solubilities (or different diffusion coefficients) of *Zn, O* and *S* atoms, it would be possible, during post-growth annealing, to optimize the relative rates of "healing" of various defects. In addition, as was revealed earlier, doping metal oxide layers with various elements [5] and their subsequent exposure to *γ*-irradiation [6,7] leads to a reduction in size of crystallite grains and boosts functional properties of nanostructured films.

In this regard, the paper presents the results of experimental studies of *XRD* (X-ray diffraction analysis) and electrophysical properties of *ZnO* metal oxide films doped with *S*, as well as the effect of *γ*-irradiation on their structural parameters.

## MATERIALS AND METHODS

To deposit *S*-doped *ZnO* metal oxide films on silicon substrates, we used the technique of ultrasonic spray pyrolysis.

X-ray diffraction analysis of the resulting thin *ZnO<S>* films and silicon substrates were performed by a third-generation Empyrean Malvern-multipurpose X-ray diffractometer. OriginPro2019 package was used to analyze the correspondent spectra. X-ray diffraction measurements were carried out in the Bragg–Brentano beam geometry in the range $2\theta_B$ = from *15°* to *120°* continuously with a scanning speed of *1 degree/min*.

To determine the resistivity, concentration and the mobility of the majority charge carriers in the grown films, the Van der Pauw method was used on a *HMS-7000* Hall effect measurement unit.

## RESULTS AND DISCUSSION

Figure 1-a shows an XRD pattern of the received *ZnO<S>* metal oxide layer. It is clear from the X-ray diffraction patterns of *ZnO<S>* films that their surface corresponds to the crystallographic orientation *(001)* and differs significantly from the X-ray diffraction pattern of the silicon substrate.

***Cite as:*** S.S. Zainabidinov, A.Y. Boboev, N.Y. Yunusaliyev, East Eur. J. Phys. 2, 321 (2024), https://doi.org/10.26565/2312-4334-2024-2-37
© S.S. Zainabidinov, A.Y. Boboev, N.Y. Yunusaliyev, 2024; CC BY 4.0 license

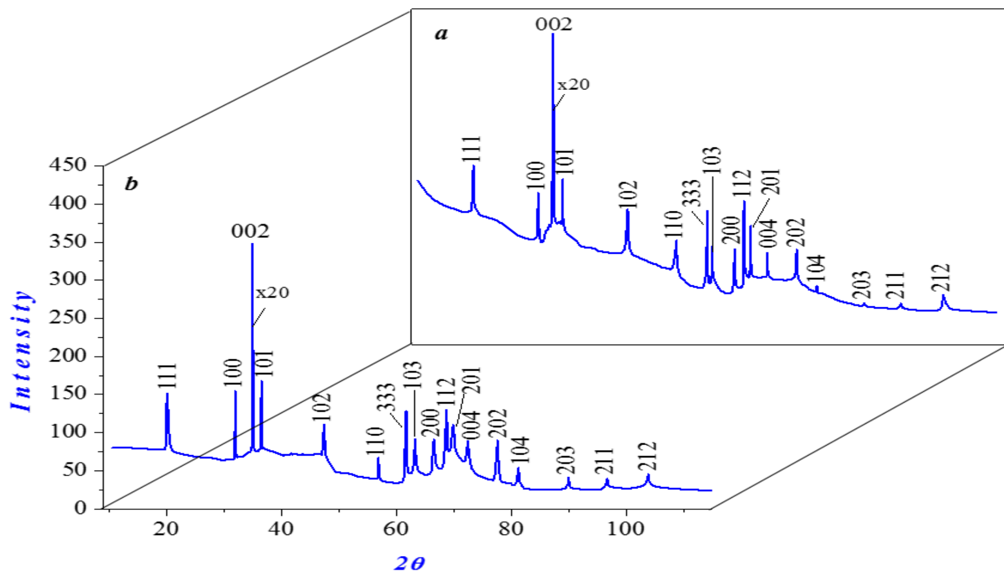


**Figure 1.** X-ray diffraction patterns of ZnO<S> films before (*a*) and after gamma irradiation (*b*)

The above results are indicative of change in the crystal lattice of the matrix layer. The values of the lattice parameters from these reflections (002) were determined to be following: $a = b = 0.3265$ nm and $c = 0.5212$ nm. Tentative analysis and the study of this reflection showed that it most probably belongs to the space group $P6_3mc$ and has a hexagonal system in the crystal lattice. In addition, other structural reflections with different orientations were observed in the *XRD* pattern (Fig. *1-a*.), and their diffraction characteristics are presented hereunder in Table 1.

**Table 1.** Diffraction characteristics of the ZnO-S/Si system before and after γ-irradiation at doses of $5 \cdot 10^6$ rad

| № | Reflection [2] | ZnO-S/Si | | γ-ZnO-S/Si | | ΔΘ |
|---|---|---|---|---|---|---|
| | | I | 2Θ, | I | 2Θ, | |
| 1 | 111 | 239 | 20.081 | 150.9 | 20.1 | 0.019 |
| 2 | 100 | 203 | 31.86 | 72 | 31.79 | 0.07 |
| 3 | 002 | 416.63 | 34.19 | 264 | 34.29 | 0.1 |
| 4 | 101 | 214.15 | 35.93 | 168.3 | 36 | 0.07 |
| 5 | 102 | 181.45 | 47.45 | 103.6 | 47.47 | 0.02 |
| 6 | 110 | 124.8 | 56.79 | 66.6 | 56.87 | 0.08 |
| 7 | 333 | 179 | 61.61 | 128.9 | 61.68 | 0.07 |
| 8 | 103 | 131 | 62.53 | 91.6 | 62.64 | 0.11 |
| 9 | 200 | 117.6 | 66.42 | 90.6 | 66.49 | 0.07 |
| 10 | 112 | 192 | 68.59 | 109.5 | 68.68 | 0.09 |
| 11 | 201 | 159 | 69.31 | 110 | 69.37 | 0.06 |
| 12 | 004 | 123 | 72.28 | 88.5 | 72.31 | 0.03 |
| 13 | 202 | 127.7 | 77.5 | 89.4 | 77.6 | 0.1 |
| 14 | 104 | 79 | 81.2 | 54 | 81.23 | 0.03 |
| 15 | 203 | 55.8 | 89.49 | 41 | 89.59 | 0.1 |
| 16 | 211 | 55.3 | 96.35 | 39.7 | 96.4 | 0.05 |
| 17 | 212 | 66 | 103.56 | 45.2 | 103.66 | 0.1 |

Also, at smaller and medium scattering angles of *XRD* pattern, an inelastic background reflection was observed, associated with the appearance of micro size distortions of the crystal lattice of the film, caused by the mismatch of lattice constants of the matrix layer and the substrate, determined from the following expression [8, 9]:

$$\xi = 2\left|a_{M.C} - a_{\Pi}\right| / (a_{M.C} + a_{\Pi}), \quad (1)$$

In this case, the mismatch of lattice constants was equal to 0.02, i.e. the lattice mismatch of the *ZnO-S/Si (100)* system happens to be 2%. The existence of various type of micro-size distortions of the crystal lattice leads to the formation of nanoobjects in the near-surface regions of the film [10, 11].

That nanosized assemblies are being shaped in the crystal lattice is proven by the appearance of structural lines (*111*) and (*333*). They belong to $ZnO_{1-x}S_x$ nano-crystallites. The sizes of nano-crystallites were determined from the half-width of these reflections using the following expression [12,13]:

---

Reflection (X-ray structural analysis) is a peak in an X-ray pattern corresponding to Bragg reflection from one of the crystallographic planes. Characterized by Miller indices.

$$D = K\lambda / (\beta \cos\theta) \,, \quad (2)$$

where $\lambda$ is irradiation wavelength, ($\lambda = 0.154\ nm$), $\theta$ is the scattering angle (half the diffraction angle $2\theta_Б$), $\beta$ - physical broadening of the line in the diffraction pattern (reflection width at half maximum intensity) in radians, coefficient $K \approx 0.94$ [8].

$$\beta = \frac{1}{2}(B - b + \sqrt{B(B-b)} \,, \quad (3)$$

where $B$ represents true broadening of the reflection, $b$ is the true geometric broadening of the reflection [8].

Calculations of $D$ values using the given formula (2) showed that the size of $ZnO_{1-x}S_x$ nano-crystallites ranges from 50 nm to 200 nm. The lattice parameter $a_{ZnO<S>}$ of $ZnO_{1-x}S_x$ nano-crystallites was experimentally determined 0.7598 nm.

Figure 1-*b* shows an *XRD* pattern of a *ZnO<S>* film after *γ*-irradiation at doses of $5{\cdot}10^6\ rad$. It differs from *XRD* pattern of the *ZnO<S>* film before irradiation; in it one can see that the level of inelastic background reflection decreases by 72% at smaller and medium angles, as well as a decrease in the intensity of the main reflection (*002*) by 13.8% as well as its further shift towards large scattering angles (Fig. 1-*b*). In addition, the authors determined the values of the lattice parameters of the *ZnO<S>* film based on the experimental data of the main reflection (*002*), which were $a = b = 0.3246$ nm and $c = 0.5187$ nm, i.e. slightly less than the lattice parameter of the *ZnO<S>* film before irradiation ($a = b = 0.3265$ nm and $c = 0.5256$ nm). These observed effects indicate that nano-crystallites of $ZnO_{1-x}S_x$-type gather locally and might be associated with a uniform distribution on the surface of the film and prove the presence of several diffraction reflections on the X-ray diffraction pattern, given in Table 1.

As Table 1 and Fig. 1*b* clearly show, the X-ray diffraction pattern demonstrates a decrease in intensities and half-widths of other diffraction reflections and a shift towards larger scattering angles. This is indicative of a decrease in the lattice parameters of the *ZnO* film and the geometric dimensions of $ZnO_{1-x}S_x$ nano-crystallites on the film surface. The authors analyzed the experimental results of these reflections and determined that the crystal structure of $ZnO_{1-x}S_x$ nano-crystallites corresponds to a cubic lattice belonging to the space group *F43m*. The cubic lattice parameter of the nano-crystallites was also determined from the observed reflections, which is approximately 0.7692 nm. The average size of $ZnO_{1-x}S_x$ nano-crystallites ($D$) was calculated in formula (2) using X-ray diffraction data, which were in the range of 10÷150 nm.

The results show that the electrical properties of *p-ZnO<S>* films do indeed improve after irradiation. Before irradiation, these parameters were as follows: resistivity $\rho = 16.2\ \Omega{\cdot}cm$, concentration $N = 1.83{\cdot}10^{18}\ cm^{-3}$ and the mobility of the majority charge carriers at room temperature $\mu = 0.31\ cm^2/V{\cdot}s$. After *γ*-irradiation at doses of $5{\cdot}10^6\ rad$, resistivity $\rho$ of the samples turned out to be $12.7\ \Omega{\cdot}cm$ whereas the mobility of the majority charge carriers $\mu = 0.18\ cm^2/V{\cdot}s$ of *ZnO<S>* films had decreased, while their concentration appeared to increase $N = 2.64{\cdot}10^{18}\ cm^{-3}$. In [14] the authors claim they have witnessed a decrease in the size of nano-crystallites of *ZnO* films with *Al* atoms and a decrease in the mobility of the majority charge carriers. According to X-ray diffraction and electron microscopy analysis of *ZnO<S>* films, after *γ*-irradiation, the size of nano-crystallites used to decrease. A decrease in the size of nano-crystallites leads to an increase in the number of boundaries (edges) in them and thus, to a further decrease in the electron mean free path [15]. This, in turn, leads to a decrease in the mobility of the majority charge carriers.

The current-voltage characteristic was measured using a standard method using a probe at room temperature. We used a DC Power Supply stabilized voltage source *HY3005*, a *MASTECH M3900* digital multimeter in ammeter and voltmeter modes.

To understand the mechanism of the transfer of electric current, the current-voltage (CV) and capacitance-voltage (CV) curves of the fabricated *p-ZnO<S>/n-Si* heterostructures were studied before and after γ-irradiation. Figure 2 shows the forward bias of current-voltage characteristics of *p-ZnO<S>/n-Si* heterostructures consisting of two sections. From Figure *2a* it can be seen that the dependence of current on voltage obeys an exponential law, regardless of irradiation, described in [16-18]:

$$I = I_o \exp\,(eU/ckT), \quad (4)$$

where $I_0$ is the pre-exponential factor ($I_0 = 2.6{\cdot}10^{-6}$ A), $e$-elementary charge (~$1.6{\cdot}10^{-19}$ C), $U$-the voltage applied, $k$ - Boltzmann constant, $T$-temperature. The coefficient $c$ in the denominator of the exponent is determined using the following expression based on two consecutive experimental results:

$$c = e(U_2 - U_1)/kTln(I_2/I_1), \quad (5)$$

which was 7.84.

The next ascending trend in the «*current versus voltage*» curve is observed in sublinear region of the current-voltage characteristic of *p-ZnO<S>/n-Si* heterostructure (Fig. *2b*) which is explained by the phenomenon of injection depletion [19] and is expressed by the following analytical relationship:

$$U \approx U_0 \exp(jad), \quad (6)$$

here $U_0$ is the voltage of the beginning of the sublinear section of the current-voltage curve, $j$ is the current density, $d$ is the length of the base region, $a$ is the constant determined by the following expression [20]:

$$a = \left(2eD_pN_t\right)^{-1}, \quad (7)$$

here $D_p$ is the diffusion coefficient of the majority charge carriers, $N_t$ is the concentration of deep level impurities. Also, the $a$ is the constant is determined from experimental data ($I_1$, $V_1$), ($I_2$, $V_2$) of the sections of injection depletion of the current-voltage curve.

$$a = Sln(U_2/U_1)/d(I_2 - I_1), \quad (8)$$

where $S$ is the cross-sectional area. Authors of the research [19] contend that this happens when the exponent in expression (6) is greater than two ($J_{ad} > 2$). In this case $J_{ad}=9.27$ and the requirement is completely satisfied.

According to the authors of the research [20], such a section of the current-voltage characteristic is mainly observed as a result of ambipolar diffusion and drift migration of charge carriers. Ambipolar diffusion and drift processes often manifest themselves at higher concentrations of defects in deep levels inside the crystal lattice.

The above *XRD* and electron microscopy results suggest that the $ZnO_{1-x}S_x$ nanocrystals formed in *p-ZnO<S>/n-Si* heterostructures differ from substitutions of impurity atoms. These $ZnO_{1-x}S_x$ nanocrystals at the interface of blocks and near-surface regions represent deep impurities and are responsible for the observed part of the current-voltage characteristic.

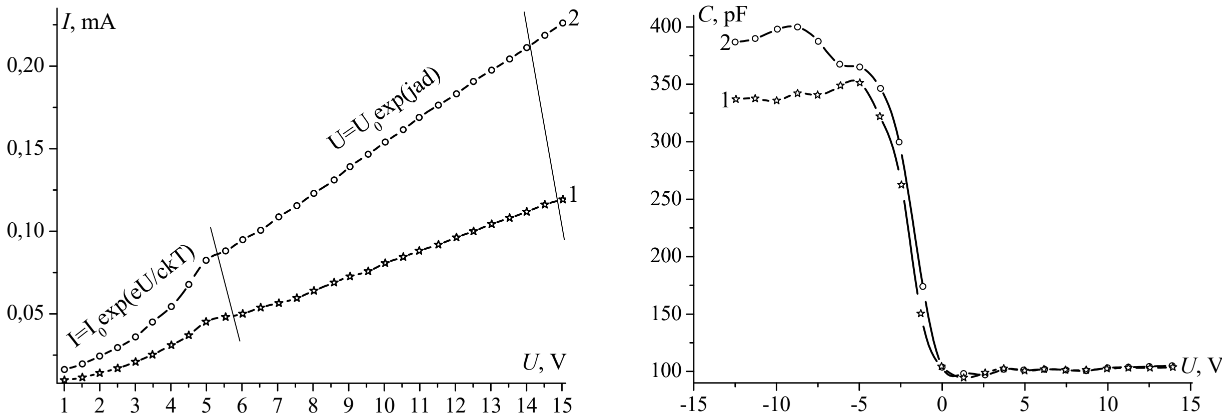


**Figure 2.** Current-voltage and capacitance-voltage characteristics of the *n-ZnO/p-Si* heterostructure before and after γ-irradiation

Capacitance-voltage characteristics were measured using a laboratory *CV*-meter, which had a source of adjustable *DC* bias voltage and a high-frequency (*500 kHz*) measuring signal of both polarities. The *CV* characteristics of the *p-ZnO<S>/n-Si* heterostructure before and after γ-irradiation were subsequently studied. The peak capacitance occurs in the region of negative voltages, which corresponds to the *p*-type conductivity of *ZnO<S>* films. Under the influence of γ-irradiation at doses of $5{\cdot}10^6$ *rad*, the capacitance of the heterostructure at negative voltages does increase, while at positive voltages, the capacitance of the heterostructure practically remains constant and negligent (*~110 pF*). The *CV* curve of the heterostructure exhibits shelves and peaks along the *U* voltage axis. Such a behavior of high-frequency *CV* characteristics is indicative of the presence of a monoenergetic level of fast surface states at the heterointerface.

## CONCLUSION

Thus, metal oxide layers of *p-ZnO<S>* were engineered on silicon substrates using the ultrasonic spray pyrolysis technique.

The resulting *ZnO<S>* films on silicon substrates had crystallographic orientations (*001*) and crystal lattice parameters $a = b = 0.3265$ nm and $c = 0.5212$ nm. $ZnO_{1-x}S_x$ nanocrystals on the film surface had sizes ranging from 57 nm to 200 nm. The lattice parameter of $ZnO_{1-x}S_x$ nano-crystallites was found experimentally to be $a_{ZnO<S>}= 0.7598$ nm.

It has been established that the lattice parameters of the *ZnO<S>* film and the geometric dimensions of $ZnO_{1-x}S_x$ nano-crystallites on the film surface decrease under the influence of $\gamma$-irradiation. It was also determined that the crystal structure of $ZnO_{1-x}S_x$ nano-crystallites corresponds to a cubic lattice and belongs to the space group *F43m.* The medium size of $ZnO_{1-x}S_x$ nano-crystallites were calculated and were found to be in the range of 10÷150 nm.

It was determined that after $\gamma$-irradiation at doses of $5{\cdot}10^6$ *rad*, the values of resistivity $\rho = 12.7$ Ω·cm and the mobility of the majority charge carriers $\mu = 0.18\ cm^2/V{\cdot}s$ of *ZnO<S>* films had actually decreased, whereas their concentration had increased up to $N = 2{,}64{\cdot}10^{18}\ cm^{-3}$.

The study of the current-voltage characteristics of *p-ZnO<S>/n-Si* heterostructures before and after *γ*-irradiation at doses of $5\cdot10^6$ *rad* had shown that the dependence of the current on voltage obeys an exponential law, which was described in the theory of the injection depletion phenomenon.

It has been determined that under the influence of *γ*-irradiation at doses of $5\cdot10^6$ *rad*, the capacitance of the *p-ZnO<S>/n-Si* heterostructure at negative voltages increases and the shelves and peaks are observed on the curve that might be associated with the presence of a monoenergetic level of fast surface states at the heterointerface.

**Conflict of Interests**

The authors declare that they have no conflict of interests

**Funding**

The present research work was financed under the project FZ-292154210 granted by the Ministry of Innovative Development of the Republic of Uzbekistan

**ORCID**

**Sirajidin S. Zainabidinov**, https://orcid.org/0000-0003-2943-5844; **Akramjon Y. Boboev**, https://orcid.org/0000-0002-3963-708X
**Nuritdin Y. Yunusaliyev**, https://orcid.org/0000-0003-3766-5420

**REFERENCES**

[1] M. Staszuk, D. Pakuła, Ł. Reimann, M. Król, M. Basiaga, D. Mysłek, and A. Kříž, "Structure and Properties of ZnO Coatings Obtained by Atomic Layer Deposition (ALD) Method on a Cr-Ni-Mo Steel Substrate Type," Materials (Basel), **13**(19), 4223 (2020). https://doi.org/10.3390%2Fma13194223

[2] A.N. Georgobiani, A.N. Gruzintsev, V.T. Volkov, and M.O. Vorobev, "Effect of annealing in oxygen radicals on the luminescence and electrical conductivity of ZnO:H films," Semiconductors, **36**(3), 284-288 (2002). https://doi.org/10.1134/1.1461400

[3] M. Li, Y. Liu, Y. Zhang, X. Han, T. Zhang, Y. Zuo, C. Xie, et al., "Effect of the Annealing Atmosphere on Crystal Phase and Thermoelectric Properties of Copper Sulfide," ACS Nano, **15**(3), 4967-4978 (2021). https://doi.org/10.1021/acsnano.0c09866

[4] Sh. Yuldashev, S. Zainabidinov, and N. Yunusaliev, "Ultrasonic production technology and properties of ZnO<S> films," Scientific Bulletin Physical and Mathematical Research, 2, 60-64 (2022). (in Russian)

[5] S. Zainabidinov, S. Rembeza, E. Rembeza, et al., "Prospects for the use of metal-oxide semiconductors in energy converters," Applied Solar Energy, **55**(1), 5–7 (2019). https://doi:10.3103/S0003701X1901014

[6] H. Beigli, M. Shaddoust, M.H. Ahmadi, and A. Khatibani, "Effect of low and relatively long-term gamma irradiation on physical properties of ZnO and ZnO:Co thin films," **108**, 798–808 (2023). https://doi.org/10.1007/s10971-023-06229-0

[7] M. Duinong et al., "Effect of Gamma Radiation on Structural and Optical Properties of ZnO and Mg-Doped ZnO Films Paired with Monte Carlo Simulation," Coatings. **12**(10), 1590 (2022). https://doi.org/10.3390/coatings12101590

[8] S. Zainabidinov, Sh. Utamuradova, and A. Boboev, "Structural Peculiarities of the $(ZnSe)_{1-x-y}(Ge_2)_x(GaAs_{1-\delta}Bi_\delta)_y$ Solid Solution with Various Nanoinclusions," Journal of Surface Investigation: X-ray, Synchrotron and Neutron Techniques, **16**, 1130-1134 (2022). https://doi.org/10.1134/S1027451022060593

[9] S.K. Guba, and V.N. Yuzevich, "Calculation of surface characteristics and pressure of InAs quantum dots in the GaAs matrix," Semiconductors, **48**(7), 932-937 (2014).

[10] Kimberly A Dick et al. "Control of III–V nanowire crystal structure by growth parameter tuning," Semicond. Sci. Technol. **25**, 024009 (2010). https://doi.org/10.1088/0268-1242/25/2/024009

[11] S. Zainabidinov, A. Saidov, A. Boboev, and J. Usmonov, "Features of the Properties of the Surface of $(GaAs)_{1-x-y}(Ge2)_x(ZnSe)_y$ Semiconductor Solid Solution with ZnSe Quantum Dots," Journal of Surface Investigation: X-ray, Synchrotron and Neutron Techniques, **15**(1), 94–99 (2021). https://doi.org/10.1134/S102745102101016X

[12] P. Abraham, S. Shaji, D. Avellaneda, J.A. Aguilar-Martínez, and B. Krishnan, "(002) oriented ZnO and ZnO:S thin films by direct ultrasonic spray pyrolysis: A comparative analysis of structure, morphology and physical properties," Materials Today Communications, **35**, 105909 (2023). https://doi.org/10.1016/j.mtcomm.2023.105909

[13] H. Kim, A. Piqué, J. Horwitz, H. Murata, Z. Kafafi, C. Gilmore, and D. Chrisey, "Effect of aluminum doping on zinc oxide thin films grown by pulsed laser deposition for organic light-emitting devices," Thin Solid Films, **377–378**, 798–802 (2000). https://doi.org/10.1016/S0040-6090(00)01290-6

[14] X. Zi-qiang, D. Hong, L. Yan, and C. Hang, "Al-doping effects on structure, electrical and optical properties of c-axis-orientated ZnO:Al thin films," Mater. Sci. Semicond. Proc. **9**, 132 (2006). https://doi.org/10.1016/j.mssp.2006.01.082

[15] P.K. Khabibullaev, Sh.U. Yuldashev, and R.A. Nusretov, "Electroluminescence of ZnO-based p-i-n structures fabricated by the ultrasound-spraying method," Doklady Physics, **52**, 300-302 (2007). https://doi.org/10.1134/S102833580706002X

[16] D. Oeba, J. Bodunrin, and S. Moloi, "The electrical characteristics and conduction mechanisms of Zn doped silicon-based Schottky barrier diode," Heliyon, **9**(12), 3-4 (2023). https://doi.org/10.1016/j.heliyon.2023.e22793

[17] I. Sapaev, and D. Babajanov, "Current-voltage characteristic of the injection photodetector based on M(In)–nCdS–pSi–M(In) structure". Semiconductor physics, **22**(2), 188-192 (2019). https://doi.org/10.15407/spqeo22.02.188

[18] J. Yan, Y. Chen, X. Wang, Y. Fu, J. Wang, J. Sun, G. Dai, Sh. Tao, and Y. Gao, "High-performance ultraviolet photodetectors based on $CdS/CdS:SnS_2$ superlattice nanowires," Nanoscale, **8**(30), 14580–14586 (2016). https://doi.org/10.1039/c6nr02915a

[19] A. Leiderman, S. Zainabidinov, and A. Boboev, "Current-voltage (I-V) characteristics of n-GaAs-p-$(GaAs)_{1-x-y}(ZnSe)_x(Ge_2)_y$ heterostructures," in: *The International Symposium "New Tendencies of Developing Fundamental and Applied Physics: Problems, Achievements, Prospectives*" (Tashkent, 2016), pp. 176-178.

[20] S.Z. Zainabidinov, and A.Y. Boboev, "Photoelectric Properties of n-ZnO/p-Si Heterostructures," Applied Solar Energy, **57(**6) 475-479 (2021). https://doi.org/10.3103/S0003701X21060177

**ВПЛИВ γ-ОПРОМІНЮВАННЯ НА СТРУКТУРУ ТА ЕЛЕКТРОФІЗИЧНІ ВЛАСТИВОСТІ ПЛІВОК ZnO, ЛЕГОВАНИХ S**

**Сіражідін С. Зайнабідінов[a], Акрамжон Ю. Бобоєв[a,b], Нурітдін Ю. Юнусалієв[a]**
*[a]Андижанський державний університет імені З.М. Бабур, Андижан, Узбекистан*
*[b] Інститут фізики напівпровідників та мікроелектроніки Національного університету Узбекистану, 100057, Ташкент, Узбекистан, вул. Янги Алмазар, 20*

Отримані плівки ZnO<S> характеризували кристалографічною орієнтацією (001) і параметрами ґратки a = b = 0,3265 нм і c = 0,5212 нм. Нанокристаліти $ZnO_{1-x}S_x$ на поверхні плівки мали характерні розміри від 50 нм до 200 нм. Параметр ґратки нанокристалітів $ZnO_{1-x}S_x$ експериментально визначено aZnO<S> = 0,7598 нм. Дослідження пролило світло на те, що відбувається з параметрами ґратки плівки ZnO та геометричними розмірами нанокристалітів $ZnO_{1-x}S_x$ на поверхні плівки під впливом гамма-опромінення. Встановлено, що кристалічна структура нанокристалітів $ZnO_{1-x}S_x$ являє собою кубічну решітку і належить до просторової групи F43m. Встановлено, що після γ-опромінення в дозах 5·106 рад питомий опір плівок ZnO<S> знижується до ρ = 12,7 *Ω*·см, а рухливість основних носіїв заряду (μ) стає 0,18 см$^2$/В. ·s, а їх концентрація (N) зросла і становила 2,64·1018 см$^{-3}$. Дослідження вольт-амперних характеристик гетероструктур p-ZnO<S>/n-Si до та після γ-опромінення в дозах $5·10^6$ рад показало, що залежність струму від напруги має експоненціальний закон, який узгоджується з теорія явища виснаження ін'єкції. Встановлено, що під дією γ-опромінення в дозах $5·10^6$ рад ємність гетероструктури p-ZnO<S>/n-Si при від'ємних напругах збільшується і на кривій спостерігаються поличкові ділянки та піки. завдяки наявності моноенергетичного рівня швидких поверхневих станів на гетеропереході.

**Ключові слова:** *плівка; ультразвуковий розпилювальний піроліз; нанокристаліт; γ-опромінення; кристалографічна орієнтація; параметр решітки; носії заряду; ін'єкційне виснаження*

EAST EUROPEAN JOURNAL OF PHYSICS. 2. 327-335 (2024)
DOI:10.26565/2312-4334-2024-2-38 ISSN 2312-4334

# INFLUENCE OF GOLD ON STRUCTURAL DEFECTS OF SILICON

Sharifa B. Utamuradova[a], Shakhrukh Kh. Daliev[a], Alisher Khaitbaev[a], Jonibek J. Khamdamov[a]*, Ulugbek M. Yuldoshev[a], Anifa D. Paluanova[b]
[a]*Institute of Semiconductor Physics and Microelectronics at the National University of Uzbekistan, 20 Yangi Almazar st., Tashkent, 100057, Uzbekistan*
[b]*Nukus State Pedagogical Institute named after Ajiniyaz, Nukus, Uzbekistan*
**Corresponding Author e-mail: jonibek.uzmu@gmail.com*
Received April 8, 2024; revised April 28, 2024; accepted May 15, 2024

In this research, a comprehensive study of the effect of doping silicon with gold on the optical properties and morphology of silicon layers was carried out. For this purpose, the methods of Raman spectroscopy, Fourier transform infrared spectroscopy (FTIR), and scanning electron microscopy (SEM) were used. The results of the study showed that the transition from original silicon to gold-doped silicon leads to significant changes in the optical properties and morphology of the layers. Raman spectra showed characteristic peaks in the regions of 144, 304, 402, 464, 522, 948 and 973 cm$^{-1}$, associated with the violation of long-range order of the crystal lattice and the interaction of gold with silicon. The intensity and position of the peaks in the spectra allowed us to draw conclusions about structural changes, including a decrease in crystallinity and the formation of amorphous and nanocrystalline structures in the samples after treatment at 1373 K. New peaks in the Raman spectra associated with Au-Au stretching and the formation of new bonds Si-Au, confirm the processes in silicon layers when alloyed with gold. SEM studies provided information on the structure, chemical composition and arrangement of n-Si-Au and p-Si-Au samples. The spherical arrangement of gold atoms on the surface of single-crystalline silicon was experimentally established, which indicates the diffusion of gold and the formation of gold silicate, which introduces a positive charge to the interface. Morphological changes included an increase in the number of agglomerates with nanocrystals smaller than 7–9 nm and an increase in the transparency of the layer. These results indicate the possibility of improving the photosensitivity of heterostructures with a Si–Au composite layer due to the quantum-size and plasmonic effects of inclusions containing silicon and gold nanoparticles.
**Keywords:** *Silicon; Gold; Raman spectroscopy; Infrared spectroscopy; Diffusion; Scanning electron microscopy; Heat treatment; Temperature; Compound*
**PACS:** 33.20.Ea, 33.20.Fb

## INTRODUCTION

In recent years, structured silicon has attracted significant interest, since silicon itself is a promising material not only for the field of electronics, but also for optoelectronics and solar cells [1-9]. Atoms of III-V elements (boron, arsenic, phosphorus and others) are widely used for doping silicon with fast-diffusing impurities, while gold is a typical slow-diffusing (deeply impurity) material. When an amphoteric gold atom diffuses into silicon via the Kick-out and Frank-Tranbull mechanisms, the ionized gold atom recombines with an n-type (or p-type) silicon electron (or hole). Diffusion gold atoms compensate for donors (or acceptors), which leads to an increase in silicon resistivity. Maximum resistance (Fig. 1.) can be achieved when the concentration of gold atoms compensates for the concentration of donors (or acceptors) [2].

Cold diffusion from the backside of the silicon device plays a crucial role in forming negative charge centers.

These centers compensate for the inherent positive surface charge at the silicon/silicon dioxide interface. Gold, interacting with silicon, forms an intermetallic compound characterized by the presence of an electrovalent bond (Fig. 2a.). This bond is less stable compared to the covalent bond between silicon atoms. Diffusion of gold from the front side of the silicon device leads to the formation of a gold silicate compound, introducing a positive charge at the interface [2-3]. One of the proposed models explaining the effects of gold centers at the silicon/silicon dioxide interface is based on a three-layer structure of the actual surface (Fig. 2b.). This model suggests the presence of different layers, including silicon, silicon dioxide, and a layer of gold silicate compound [3]. Interaction between these layers and the emerging charge centers plays a key role in the electrochemical and physical properties at the material interface.

The purpose of this work is to study the defect structure of silicon doped with gold, as well as the synthesis of composites on the Si-Au silicon surface by thermal firing at 1373 K. To study the structural and optical characteristics of the samples, methods of scanning electron microscopy (SEM image) and Raman spectroscopy (Raman spectrum) and Fourier transform infrared (FTIR) spectroscopy are used.

Raman spectroscopy is used to examine samples that are irradiated with monochromatic light, usually a laser. This technique allows the study of vibrational states that are the same as those observed in infrared spectroscopy (FTIR). Raman spectroscopy and infrared spectroscopy complement each other, since vibrations that are strong in the infrared spectrum are usually weak in the Raman spectrum, and vice versa. This allows for a more complete analysis of chemical

***Cite as:*** Sh.B. Utamuradova, Sh.Kh. Daliev, A. Khaitbaev, J.J. Khamdamov, U.M. Yuldoshev, A.D. Paluanova, East Eur. J. Phys. 2, 327 (2024), https://doi.org/10.26565/2312-4334-2024-2-38
© Sh.B. Utamuradova, Sh.Kh. Daliev, A. Khaitbaev, J.J. Khamdamov, U.M. Yuldoshev, A.D. Paluanova, 2024; CC BY 4.0 license

components and intramolecular interactions in samples. Raman spectroscopy is a non-destructive analysis method that allows you to study the physical properties of samples without changing their structure or composition. It also operates over a wide range from ultraviolet to near-infrared, making it a convenient and powerful tool for researchers.

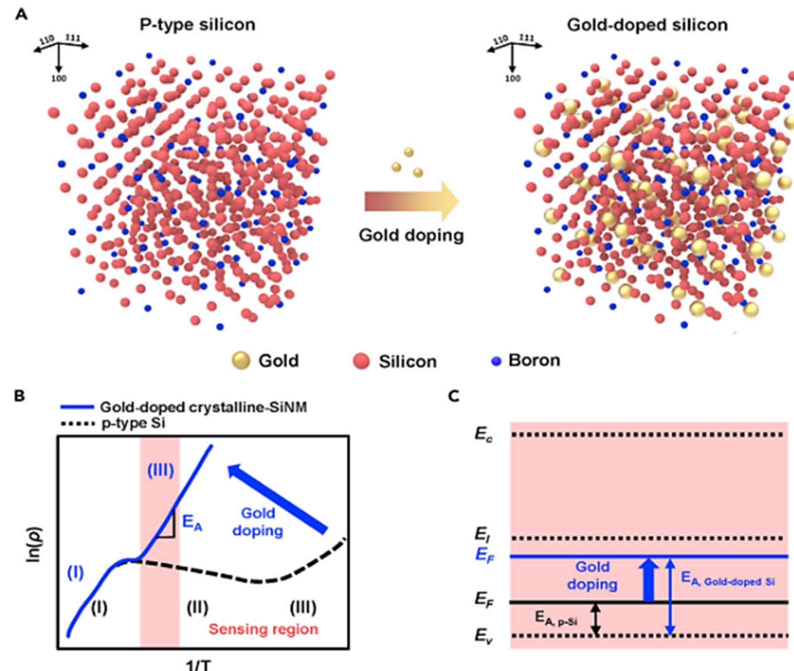


**Figure 1.** Changes in the properties of silicon after alloying with gold [2]
(A) Schematic illustration before and after doping silicon with gold; (B) Shift of resistivity curve after gold alloying process (I: inner region, II: outer region, III: freezing region); (C) Energy diagram of silicon after the gold doping process

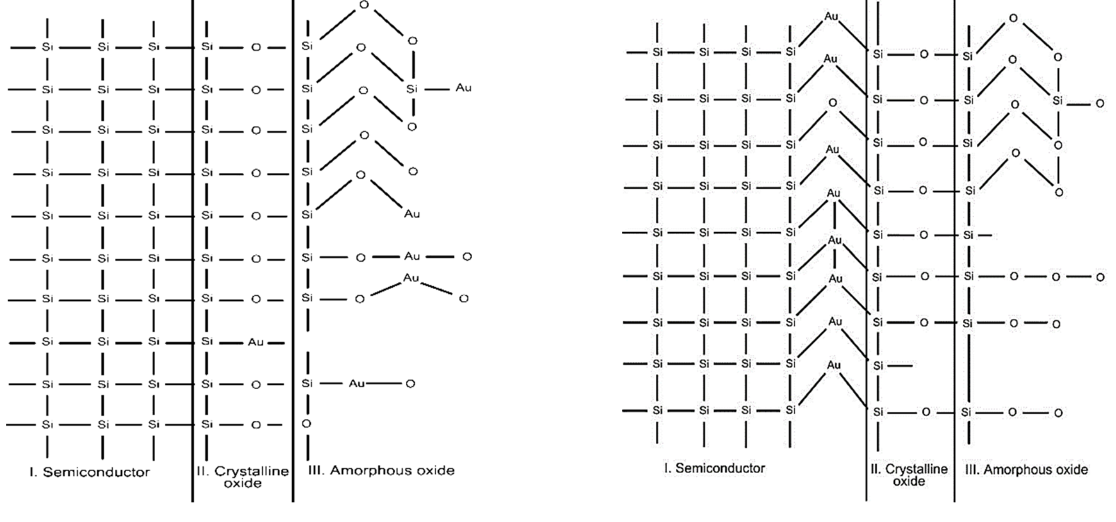


***a)*** *Lattice structure of gold diffusion from the front of the silicon device.*

***b)*** *Lattice structure of gold diffusion into silicon from the back of the substrate*

**Figure 2.** Lattice structure of gold diffusion into silicon [3]

## MATERIALS AND METHODS

Studies using a ZEISS Gemini SEM 300 scanning electron microscope made it possible to obtain information about the structure, chemical composition and arrangement of n-Si-Au and p-Si-Au samples. The electron accelerating voltage was 20 kV, and the pressure in the sample chamber was $10^{-5}$ mmHg.

Raman spectra (Raman) and Fourier transform infrared spectroscopy (FTIR) were performed on six samples, including both types of pristine (n-Si and p-Si) doped with gold (n-Si<Au> и p-Si<Au>), as well as the resulting composites (n-Si-Au and p-Si-Au). The obtained spectroscopic data further confirmed the presence of amorphous and nanocrystalline structures on films annealed at 1373 K. Photoluminescence in the visible and near-infrared regions was observed in films containing both amorphous and crystalline particles.

To conduct the study, n-Si and p-Si silicon samples with an initial resistance of 0.3 Ohm·cm were selected. The process of doping with gold (Au) impurities was carried out sequentially using the thermal diffusion method. The samples were preliminarily chemically cleaned and etched with an HF solution to remove oxide layers from the surface. Then, films of high-purity gold were deposited onto a clean silicon surface by vacuum deposition in evacuated quartz ampoules at a vacuum level of $10^{-6} \div 10^{-8}$ Torr using an oil-free vacuum pumping system.

Diffusion annealing of the samples was carried out at a temperature of 1373 K for 2 hours, followed by fast and slow cooling to uniformly dope the material and maximize the impurity concentration in silicon. Raman spectra were studied using a Confotec MR350 3D scanning laser Raman spectrometer using a 532 nm laser in the wavenumber range from 60 to 9500 cm$^{-1}$, as well as using a Bruker Senterra II Raman microscope using a 532 nm laser, in the wavenumber range from 50 to 4265 cm$^{-1}$, at room temperature. Infrared (IR) spectra were obtained using an FSM-2201 Fourier transform infrared spectrometer in the wavenumber range from 370 to 7800 cm$^{-1}$ using FSpec software.

## RESULTS AND DISCUSSION

Figure 3 shows an SEM image of gold-doped silicon. The spherical arrangement of gold atoms on the surface of monocrystalline p-type silicon doped with gold was experimentally established.

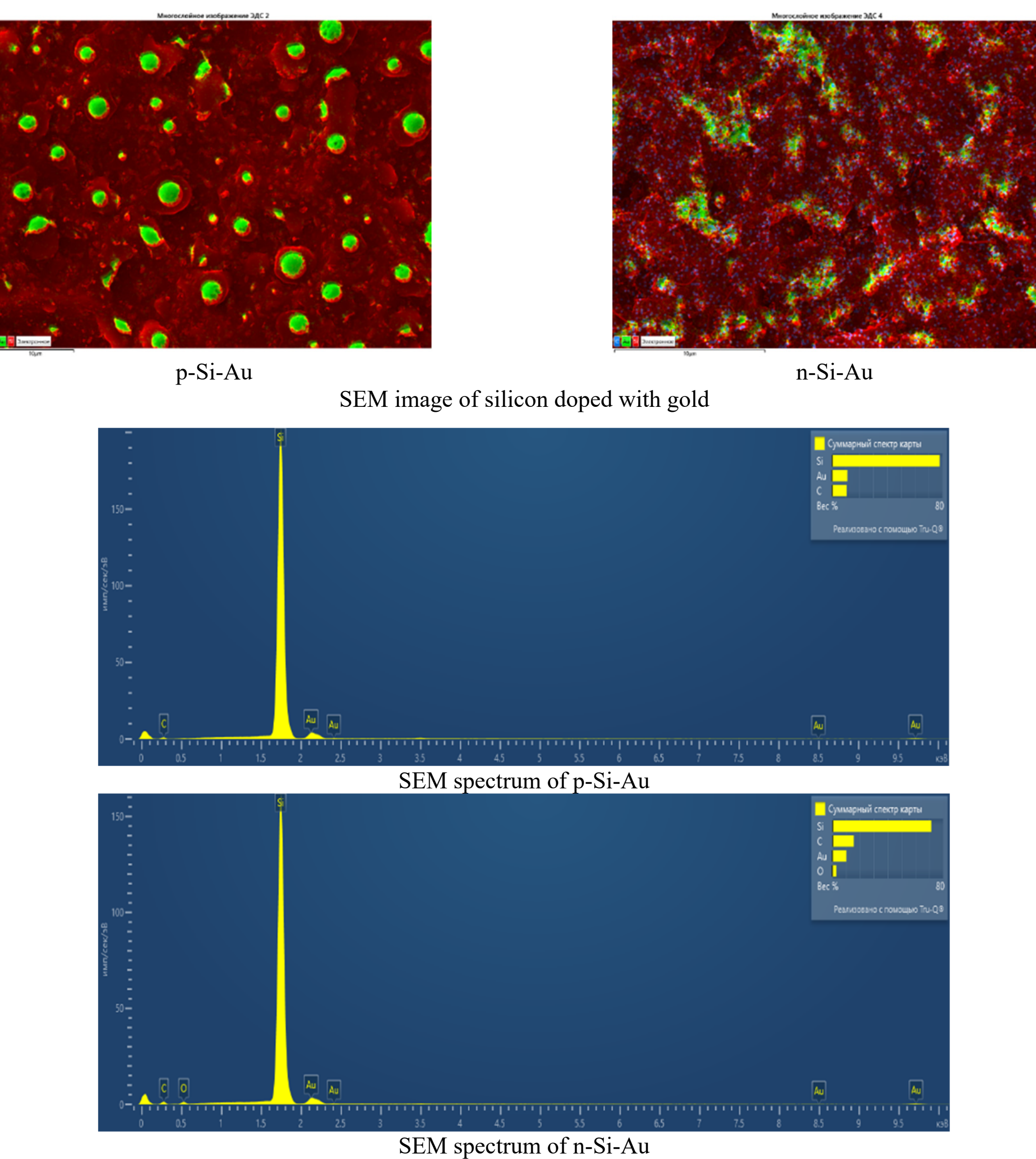


p-Si-Au n-Si-Au

SEM image of silicon doped with gold

SEM spectrum of p-Si-Au

SEM spectrum of n-Si-Au

**Figure 3.** Surface properties of monocrystalline silicon doped with gold and subjected to heat treatment

Research results show that the structure of micro- and nanocomposites formed in silicon mainly depends on the diffusion time and cooling rate of the samples after diffusion annealing. The results of the study showed that thin films of gold with high silicon content were successfully prepared by thermal calcination, and n-Si-Au and p-Si-Au composites were prepared by thermal calcination at 1373 K. The obtained scanning electron microscopy data and Raman spectra were confirmed formation of both amorphous and nanocrystalline structures in films annealed at 1373 K.

Photoluminescence was observed and interpreted as interband recombination in nanoparticles larger than 2.5 nm, as well as carrier recombination through defect states in smaller nanoparticles.

Raman spectra for silicon samples doped with gold n-Si<Au> and p-Si<Au>, as well as composites obtained on their basis n-Si-Au and p-Si-Au, are presented in Figure 4.

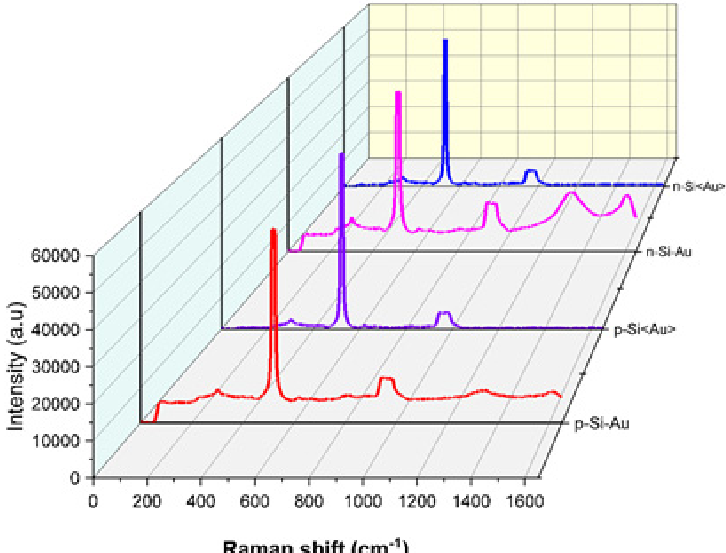


**Figure 4.** Raman spectrum of two types of gold-doped n-Si<Au> and p-Si<Au>, and n-Si-Au and p-Si-Au composites

The Raman spectrum of the sample (Fig. 4) includes bands with maxima in the regions of 144, 304, 402, 464, 522, 948 and 973 cm$^{-1}$. The appearance of such bands in Raman spectra is explained by the violation of long-range order (translation symmetry) of the crystal lattice, which removes the limitation imposed by the quasi-momentum conservation law (q=0). Therefore, in Raman spectra, phonons with all wave vectors q are allowed, which ultimately reproduce the density of vibrational states of the crystal lattice of the material under study [8-15].

The results show that the characteristic peaks of all four spectra examined are at the same spectral positions and the peak intensities are essentially identical. Similarly, to characterize the homogeneity of n-Si and the resulting n-Si-Au composites, we examined the most significant spectral regions (Fig. 5).

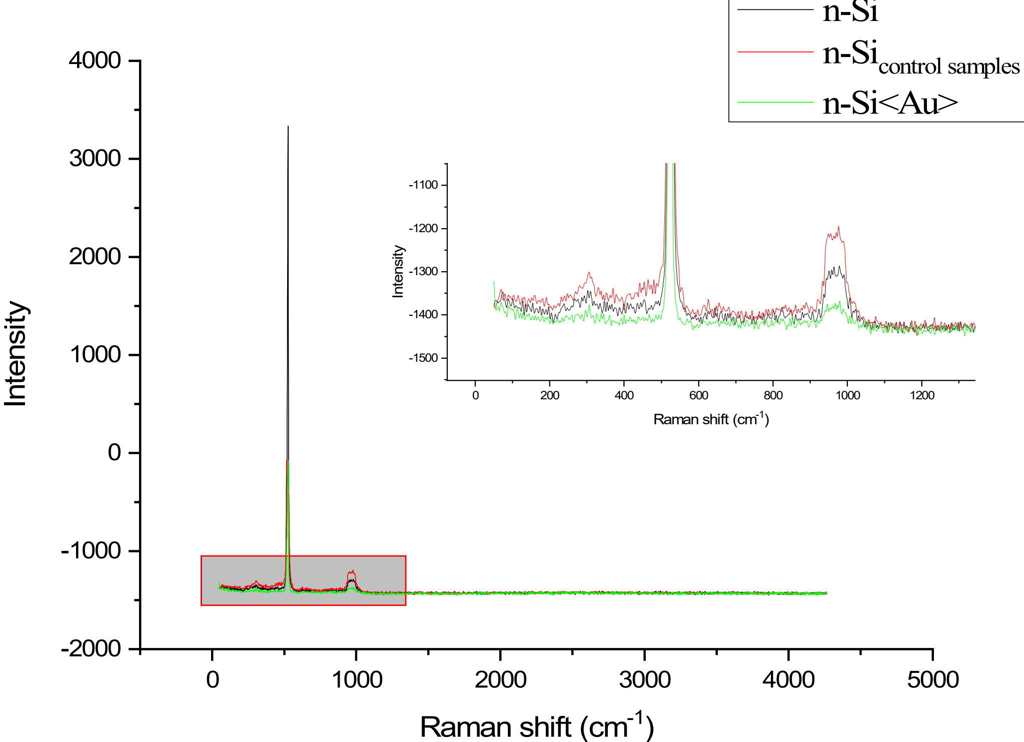


**Figure 5.** Comparative analysis of the Raman spectra of n-Si and gold-doped n-Si<Au>

Then we used the same method to analyze the Raman spectra of the most significant regions of the spectrum of p-Si and p-Si-Au composites obtained on their basis (Fig. 6). It was determined that in the studied spectra the main peaks appear at 566, 628, 674, 796, 948, 973, 1087, 1225, 1463, 1558, 1678, 1784, 2002, 2140 and 2325 $cm^{-1}$, which are consistent with literature data [11].

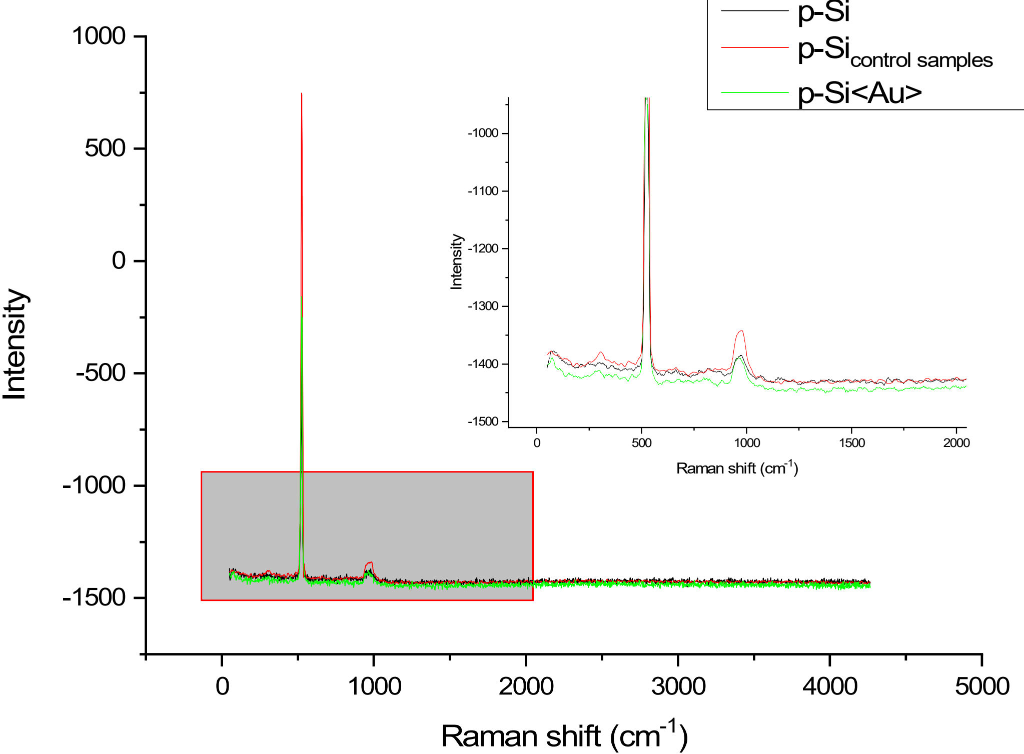


**Figure 6.** Comparative analysis of the Raman spectra of p-Si and gold-doped p-Si<Au>

From the data given in Fig. 5. and Fig.6. it is clear that, when moving from the original n-Si, p-Si to gold-doped n-Si<Au>, p-Si<Au>, the signals in the regions of 304 and 948 $cm^{-1}$ undergo some changes, such as the intensity increases, they expand and will be mixed relative to the signals of the original n-Si, p-Si. It should be also pointed out that the main intense signal manifested in the region of 522 $cm^{-1}$ upon transition from the original n-Si and p-Si to gold-doped n-Si<Au>, p-Si<Au> noticeably broadens. This, in turn, indicates a decrease in the crystallinity of the original n-Si and p-Si.

When studying the obtained spectra, accurate determination of the band of nanocrystals is extremely important, especially for films grown on n-Si and p-Si substrates. In nanocrystalline silicon films, the scattered light from the film is quite intense, but the scattering from the substrate is significantly reduced due to absorption in the film. This means that the shape and position of the band emanating from the nanocrystals should not be distorted when scattered on the substrate. However, in the resulting n-Si-Au, p-Si-Au composites, the filling factor is relatively small, which can be about 10%. The intensity of the scattered light from the Si nanocrystals is quite low, while the Raman line remains strong due to the n-Si substrate. From the given Fig. 5. and Fig.6, it can be seen that the strong band in all spectra has a maximum at 522 $cm^{-1}$ and a width at half maximum of 4.3 $cm^{-1}$. It is necessary to take into account the fact that scattering from Si nanocrystals is quite weak and does not have a noticeable effect on the shape and position of the substrate strip. Since the exact intensity level of the scattered light from the n-Si and p-Si substrate cannot be determined, we conclude that it is impossible to correctly determine the size of Si nanocrystallites from the Raman spectra of the resulting low filling coefficient n-Si-Au, p-Si-Au composites.

Fourier transform infrared spectroscopy (FTIR) was used to further study the changes in gold-doped n-Si<Au> silicon from pristine n-Si. IR spectra in the region from 380 to 600 $cm^{-1}$ were carefully studied to identify structural changes in n-Si and gold-doped silicon n-Si<Au>. The IR spectra of both the original n-Si and gold-doped silicon n-Si<Au> are presented in Figure 7a.

When analyzing using IR spectrometry both n-Si itself, as well as silicon doped with gold n-Si<Au>, in addition to the absorption of light by the atoms of the crystal lattice, there was also an absorption process associated with defects and present impurities. When studying the obtained IR spectra, the following patterns were revealed: absorption bands at 1107 and 513 $cm^{-1}$ of crystalline silicon are associated with oxygen (one must take into account the fact that oxygen in crystalline silicon is located between the nodes and is an electrically neutral interstitial impurity) present in silicon, carbon in crystalline silicon exhibits one antisymmetry typical stretching ($\nu_{as}$) vibration, the frequency of which is 609 $cm^{-1}$. n-Si doped with Au exhibits additional peaks in its IR spectra due to the presence of vacancies and defects in n-Si<Au>. The peaks at 513 $cm^{-1}$ arise from the Si-Si stretching mode, and at 818 $cm^{-1}$ from the wagging mode of hydrogen.

To consider changes in the IR spectra in the original n-Si and doped n-Si<Au> composition, we subsequently studied in detail the regions from 400 to 1650 $cm^{-1}$ (Figure 7b). The resulting spectra clearly show all the changes that occur during the transition from n-Si to doped n-Si<Au>.

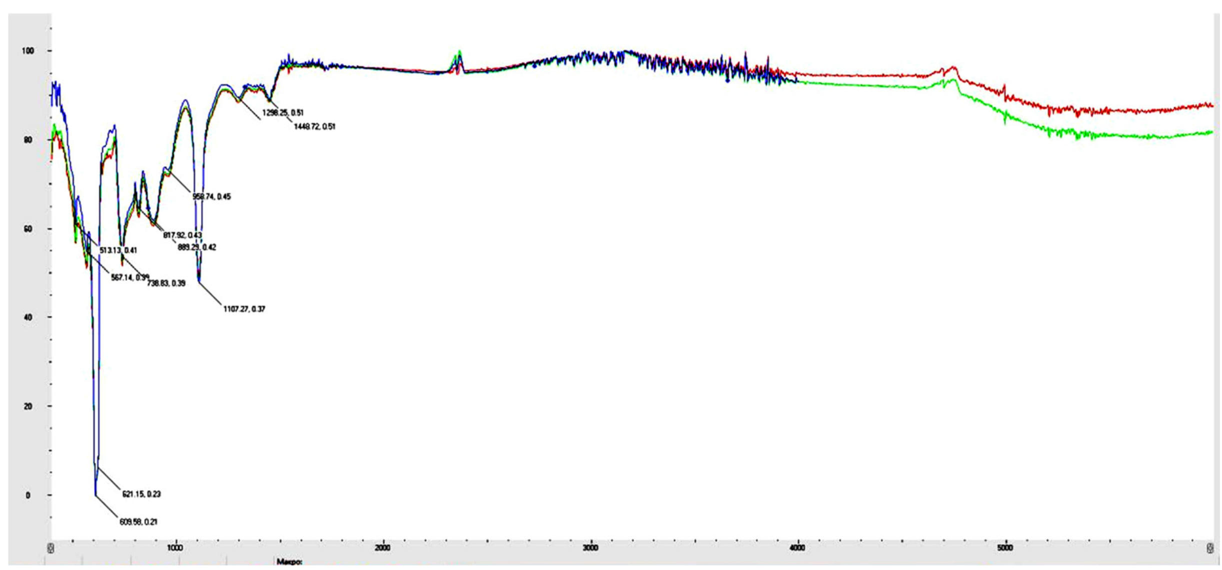


**Figure 7a.** IR spectrum of n-Si:
*(red) n-Si; (green) n-Si$_{control}$ ; (blue) n-Si<Au>*

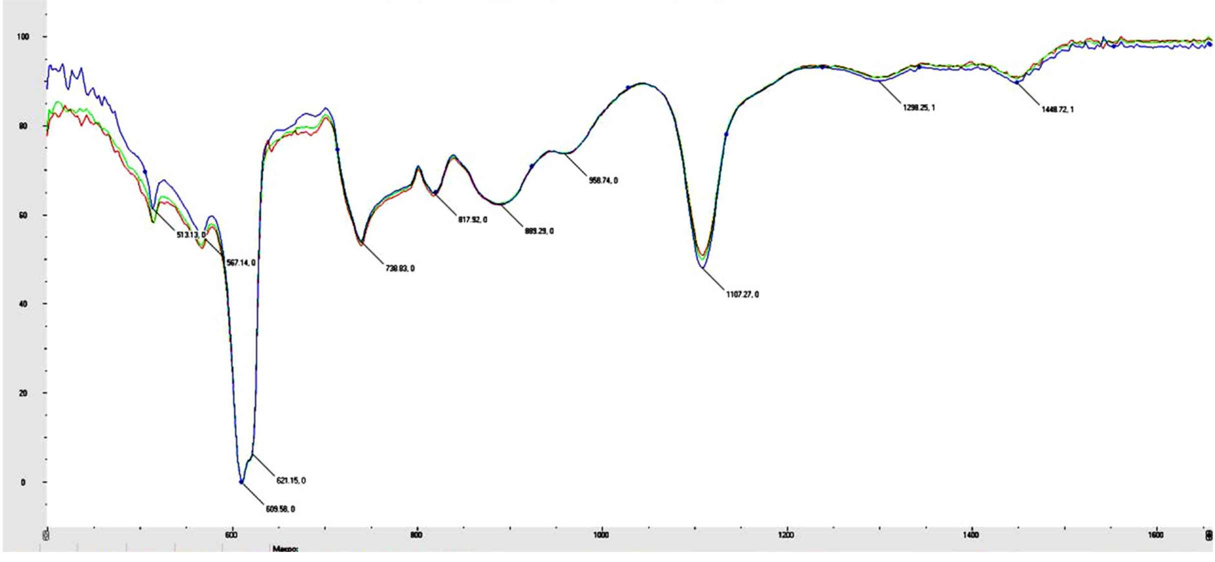


**Figure 7b**. IR spectrum of n-Si (region from 400 to 1650 $cm^{-1}$):
*(red) n-Si; (green) n-Si$_{control}$; (blue) n-Si<Au>*

A detailed study of the obtained IR spectra of n-Si, thermally treated n-Si and doped n-Si<Au> composition revealed the following patterns:

1) when moving from n-Si to thermally treated n-Si, some signals are relatively smoothed out (for example, the region from 400 to 500 $cm^{-1}$) and new signals appear, which can be explained by a mixing of characteristic frequencies;
2) upon transition from both types of n-Si (plain and control samples) to doped n-Si<Au> composition, for some characteristic frequencies (513, 609, 739 and 1107 $cm^{-1}$) the intensity noticeably increases and new signals associated with Au-Au stretching located between 2210 $cm^{-1}$ and 2350 $cm^{-1}$. New signals at 2110 and 2124 $cm^{-1}$ indicate the interaction of gold with silicon by the formation of new Si-Au bonds.

The same method was then used to analyze p-Si and doped p-Si<Au>. At the same time, it was determined that in the studied spectra the main peaks appear at 513, 609, 619, 739, 891, 1107, 1302, 1449 $cm^{-1}$, etc. The IR spectra of both the original p-Si and the doped p-Si<Au> are presented in Figure 8a.

To consider changes in the IR spectra in the original p-Si and doped p-Si<Au> composition, we subsequently studied in detail the regions from 400 to 1750 $cm^{-1}$ (Fig. 8b). The resulting spectra clearly show all the changes that occur during the transition from p-Si to p-Si<Au> doping.

When comparing the obtained spectra of both types n-Si and p-Si, as well as n-Si<Au> and p-Si<Au> obtained on their basis, it should be noted that when going from n-Si<Au> to p-Si<Au> all peaks almost coincide but at the same time the intensity of the signals increases noticeably (comparison of Fig. 7b and Fig. 8b) [16-21].

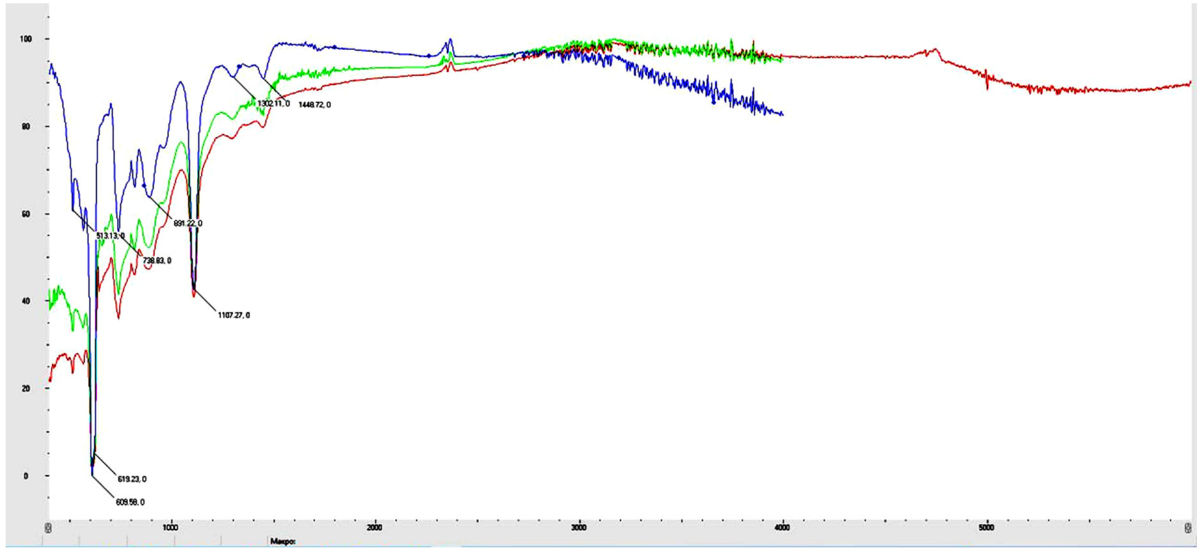


**Figure 8a.** IR spectrum of p-Si:
*(red) p-Si; (green) p-Si$_{control}$; (blue) p-Si<Au>*

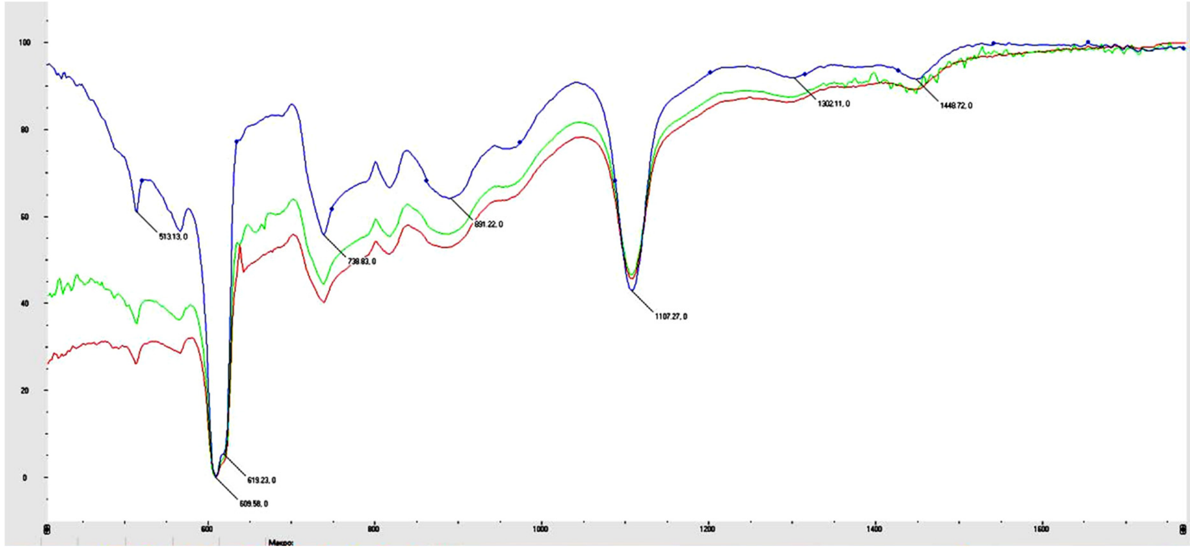


**Figure 8b.** IR spectrum of p-Si (region from 400 to 1750 cm$^{-1}$):
*(red) p-Si; (green) p-Si$_{control}$; (blue) p-Si<Au>*

## CONCLUSIONS

The comprehensive analysis of silicon doped with gold and the subsequent synthesis of Si-Au composites have provided a wealth of insights into their structural and optical characteristics. Utilizing advanced analytical techniques such as scanning electron microscopy (SEM), Raman spectroscopy, and Fourier transform infrared spectroscopy (FTIR), we have uncovered significant transformations in the materials' properties. SEM imaging has offered a detailed view of the surface properties of monocrystalline silicon doped with gold, revealing a distinct spherical arrangement of gold atoms. This arrangement not only confirms successful doping but also hints at potential surface interactions and structural modifications induced by gold. Raman spectroscopy has been instrumental in identifying structural changes at the molecular level. The Raman spectra of gold-doped silicon samples and their resulting composites exhibited characteristic peaks indicative of altered vibrational states. Notably, the broadening and intensification of certain signals suggest the disruption of long-range order and the introduction of new vibrational modes due to gold doping. Further insights were gained through FTIR spectroscopy, which revealed shifts and enhancements in absorption bands associated with the interaction of gold with silicon. The emergence of new Si-Au bonds, as evidenced by specific peaks in the IR spectra, highlights the chemical modifications occurring upon gold doping.

The detailed analysis of these spectroscopic data underscores the intricate interplay between gold and silicon, leading to profound changes in the materials' structural, vibrational, and chemical properties. These findings are of significant importance for understanding the fundamental mechanisms underlying gold doping in silicon and have promising implications for the development of advanced optoelectronic devices and materials with tailored properties. In conclusion, this study contributes valuable insights into the complex behavior of gold-doped silicon and paves the way for future research aimed at harnessing these materials for a wide range of applications in electronics, photonics, and nanotechnology.

**ORCID**

**Sharifa B. Utamuradova**, https://orcid.org/0000-0002-1718-1122
**Shakhrukh Kh. Daliev,** https://orcid.org/0000-0001-7853-2777
**Alisher Khaitbaev,** https://orcid.org/0000-0001-9892-8189
**Jonibek J. Khamdamov**, https://orcid.org/0000-0003-2728-3832
**Ulugbek M. Yuldoshev,** https://orcid.org/0009-0003-7575-7497
**Anifa D. Paluanova,** https://orcid.org/0009-0007-7283-5604

**REFERENCES**

[1] A. Herz, D. Wang, R. Müller, and P. Schaaf, "Formation of supersaturated Au–Ni nanoparticles via dewetting of an Au/Ni bilayer," Mater. Lett. **102-103***,* 22–25 (2013). https://doi.org/10.1016/j.matlet.2013.03.096
[2] M. Sang, K. Kang, Y. Zhang, H. Zhang, K. Kim, M. Cho, J. Shin, J.H. Hong, T. Kim, Sh.K. Lee, W.H. Yeo, J.W. Lee, T. Lee, B. Xu, and K.J. Yu, "Ultrahigh Sensitive Au-Doped Silicon Nanomembrane Based Wearable Sensor Arrays for Continuous Skin Temperature Monitoring with High Precision," Adv. Mater. **34**(4), 2105865 (2022). https://doi.org/10.1002/adma.202105865
[3] G.R. Moghal, "Chemical-bond model for gold surface states in gold doped silicon/silicon dioxide structures," Int. J. Electronics, **53**(3), 271-279 (1982). https://doi.org/10.1080/00207218208901509
[4] W.R. Thurber, D.C. Lewis, and W.M. Buillis, "Resistivity and carrier life time in gold - doped silicon," Electronic Technology Division Institute for Applied Technology National Bureau of Standards Washington, D.C. 20234, (1973**)**. https://nvlpubs.nist.gov/nistpubs/Legacy/IR/nbsir73-128.pdf
[5] S.O. Konorov, H.G. Schulze, M.W. Blades, and R.F.B. Turner, "Silicon−Gold−Silica Lamellar Structures for Sample Substrates That Provide an Internal Standard for Raman Microspectroscopy," Anal. Chem. **86**(19), 9399–9404 (2014). https://doi.org/10.1021/ac501922a
[6] M. Aono, M. Takahashi, H. Takiguchi, Y. Okamoto, N. Kitazawa, and Y. Watanabe, "Thermal annealing of a-Si/Au superlattice thin films," Journal of Non-Crystalline Solids, **358**(17), 2150-2153 (2014). https://doi.org/10.1016/j.jnoncrysol.2011.12.088
[7] K. Fukami, M.L. Chourou, R. Miyagawa, A.M. Noval, T. Sakka, M. Manso-Silván, R.J. Martin-Palma, and Y.H. Ogata, "Gold Nanostructures for Surface-Enhanced Raman Spectroscopy, Prepared by Electrodeposition in Porous Silicon," Materials, **4**, 791-800 (2011). https://doi:10.3390/ma4040791
[8] D. Beeman, R. Tsu, and M.F. Thorpe, "Structural information from the Raman spectrum of amorphous silicon," Phys. Rev. B, **32**, 874 (1985). https://doi.org/10.1103/PhysRevB.32.874
[9] P. Danesh, B. Pantchev, K. Antonova, E. Liarokapis, B. Schmidt, D. Grambole, and J. Baran, "Hydrogen bonding and structural order in hydrogenated amorphous silicon prepared with hydrogen-diluted silane," J. Phys. D, **37**, 249 (2004). https://doi.org/10.1088/0022-3727/37/2/013
[10] R. Tsu, J.G. Hernandez, and F.H. Pollak, "Determination of energy barrier for structural relaxation in a-Si and a-Ge by Raman scattering," J. NonCryst. Solids, **66**, 109 (1984). https://doi.org/10.1016/0022-3093(84)90307-7
[11] Z.Q. Cheng, H.Q. Shi, P. Yu, and Z.M. Liu, 'Surface - enhanced Raman scattering effect of silver nanoparticles array," Acta Phys. Sin. **67**(19), 197302 (2018). https://doi.org/10.7498/aps.67.20180650
[12] F. Huisken, H. Hofmeister, B. Kohn, M.A. Laguna, and V. Paillard, "Laser production and deposition of light-emitting silicon nanoparticles," Appl. Surf. Sci. **154–155**, 305 (2000). https://doi.org/10.1016/s0169-4332(99)00476-6
[13] V. Vinciguerra, G. Franzo, F. Priolo, F. Iacona, and C. Spinella, "Quantum confinement and recombination dynamics in silicon nanocrystals embedded in Si/$SiO_2$ superlattices," J. Appl. Phys. **87**, 8165 (2000). https://doi.org/10.1063/1.373513
[14] Zh. Ma, X. Liao, J. He, W. Cheng, G. Yue, Y. Wang, and G. Kong, "Annealing behaviors of photoluminescence from $SiO_x$:H," J. Appl. Phys. **83**, 7934 (1998). https://doi.org/10.1063/1.367973
[15] S. Zhang, W. Zhang, and J. Yuan, "The preparation of photoluminescent Si nanocrystal–$SiO_x$ films by reactive evaporation," Thin Solid Films, **326**, 92 (1998). https://doi.org/10.1016/S0040-6090(98)00532-X
[16] J. Zi, H. Buscher, C. Falter, W. Ludwig, K. Zhang, and X. Xie, "Raman shifts in Si nanocrystals," Appl. Phys. Lett. **69**, 200 (1996). https://doi.org/10.1063/1.117371
[17] Kh.S. Daliev, Z.E. Bahronkulov, and J.J. Hamdamov, "Investigation of the Magnetic Properties of Silicon Doped with Rare-Earth Elements," East Eur. J. Phys. **(4),** 167 (2023). https://doi.org/10.26565/2312-4334-2023-4-18
[18] Kh.S. Daliev, Sh.B. Utamuradova, Z.E. Bahronkulov, A.Kh. Khaitbaev, and J.J. Hamdamov, "Structure Determination and Defect Analysis n-Si<Lu>, p-Si<Lu> Raman Spectrometer Methods," East Eur. J. Phys. (4), 193 (2023). https://doi.org/10.26565/2312-4334-2023-4-23
[19] K.J. Kingma, and R.J. Hemley, "Raman spectroscopic study of microcrystalline silica," American Mineralogist, **79**(3-4), 269-273 (1994). https://pubs.geoscienceworld.org/msa/ammin/article-pdf/79/3-4/269/4209223/am79_269.pdf
[20] Sh.B. Utamuradova, H.J. Matchonov, Zh.J. Khamdamov, and H.Yu. Utemuratova, "X-ray diffraction study of the phase state of silicon single crystals doped with manganese," New Materials, Connections Oath Applications, **7**(2), 93-99 (2023). http://jomardpublishing.com/UploadFiles/Files/journals/NMCA/v7n2/Utamuradova_et_al.pdf
[21] Kh.S. Daliev, Sh.B. Utamuradova, J.J. Khamdamov, and M.B. Bekmuratov, "Structural Properties of Silicon Doped Rare Earth Elements Ytterbium," East Eur. J. Phys. (1), 375-379 (2024). https://doi.org/10.26565/2312-4334-2024-1-37

**ВПЛИВ ЗОЛОТА НА СТРУКТУРНІ ДЕФЕКТИ КРЕМНІЮ**

**Шаріфа Б. Утамурадова[a], Шахрух Х. Далієв[a], Алішер Хайтбаєв[a], Джонібек Дж. Хамдамов[a], Улугбек М. Юлдошев[a], Аніфа Д. Палуанова[b]**
*[a]Інститут фізики напівпровідників та мікроелектроніки Національного університету Узбекистану, Ташкент, вул. Янгі Алмазара, 20, Узбекистан*
*[b]Нукуський державний педагогічний інститут імені Аджиніяза, Нукус, Узбекистан*

У цьому дослідженні було проведено комплексне дослідження впливу легування кремнію золотом на оптичні властивості та морфологію шарів кремнію. Для цього використовували методи раманівської спектроскопії, інфрачервоної спектроскопії з перетворенням Фур'є (FTIR) та скануючої електронної мікроскопії (SEM). Результати дослідження показали, що перехід від вихідного кремнію до легованого золотом кремнію призводить до значних змін оптичних властивостей і морфології шарів. Спектри КРС показали характерні піки в областях 144, 304, 402, 464, 522, 948 і 973 см–1, пов'язані з порушенням дальнього порядку кристалічної решітки та взаємодією золота з кремнієм. Інтенсивність і положення піків у спектрах дозволили зробити висновки про структурні зміни, включаючи зниження кристалічності та утворення аморфних і нанокристалічних структур у зразках після обробки при 1373 К. Нові піки в спектрах КРС, пов'язані з Au Розтягування -Au і утворення нових зв'язків Si - Au, підтверджують процеси в шарах кремнію при сплаві золотом. Дослідження СЕМ дали інформацію про структуру, хімічний склад і розташування зразків n-Si-Au і p-Si-Au. Експериментально встановлено сферичне розташування атомів золота на поверхні монокристалічного кремнію, що свідчить про дифузію золота та утворення силікату золота, який вносить позитивний заряд на поверхню розділу. Морфологічні зміни включали збільшення кількості агломератів з розміром нанокристалів менше 7–9 нм та збільшення прозорості шару. Ці результати вказують на можливість покращення фоточутливості гетероструктур із композитним шаром Si–Au за рахунок квантово-розмірного та плазмонного ефектів включень, що містять наночастинки кремнію та золота.

**Ключові слова:** *кремній; золото; раманівська спектроскопія; інфрачервона спектроскопія; дифузія; скануюча електронна мікроскопія; термічна обробка; температура; компаунд*

East European Journal of Physics. 2. 336-340 (2024)
DOI:10.26565/2312-4334-2024-2-39 ISSN 2312-4334

# X-RAY STRUCTURAL AND PHOTOELECTRIC PROPERTIES OF $SnO_2$, ZnO, AND $Zn_2SnO_4$ METAL OXIDE FILMS

**Khotamjon J. Mansurov[a], Akramjon Y. Boboev[a,b]*, Jakhongir A. Urinboyev[a]**
[a]*Andijan State University named after Z.M. Babur, Andijan, Uzbekistan*
[b]*Institute of Semiconductor Physics and Microelectronics, National University of Uzbekistan, Tashkent, Uzbekistan*
**Corresponding Author e-mail: aboboevscp@gmail.com*
Received March 9, 2024; revised April 22, 2024; accepted April 23, 2024

The conditions and parameters for the synthesis of metal oxide films (ZnO, $SnO_2$, and $Zn_2SnO_4$) by spray pyrolysis have been determined. The films were synthesized from aqueous solutions; the main differences between the methods were in the composition of the precursors, in the modes and time of deposition. The crystal structure of the $Zn_2SnO_4$ film corresponds to the cubic lattice, which belongs to the space group Fd3m with blocks 53 nm in size and lattice parameters a = 6.238 Å. Films of $SnO_2$ and ZnO nanocrystallites 28 and 31 nm in size coherently arranged with lattices in the volume of thin $Zn_2SnO_4$ films can exhibit quantum size effects, which is of interest for modern nanotechnology. The crystals of the obtained $SnO_2$ films have a tetragonal Bravais lattice with the space group P4 2/mnm with lattice parameters $a = b = 4.836$ Å and $c = 3.245$ Å, and the size of the $SnO_2$ film subcrystals is 61 nm. The resulting ZnO films belong to the C6/mmc space group and the crystal lattice has a hexagonal syngony with the wurtzite structure with parameters $a = b = 0.3265$ nm and $c = 0.5212$ nm. It has been determined that, on the surface of the thin film grown, zinc oxide bumps with sizes $L_{ZnO} \approx 84$ nm appear, which affect the unique properties of the samples. It is shown that the resulting thin $Zn_2SnO_4$, $SnO_2$, and ZnO films can be used in a wide range of applications from sensitive sensor elements to coatings in transparent electronics in terms of their optical parameters.
**Keywords:** *Film; Space group; Subcrystal; Nanocrystal; Quantum size effect; Lattice parameter; Transparent electronics; Band gap*
**PACS:** 78.30.Am

## 1. Introduction

Semiconductor metal oxides have been used in photovoltaic technology for many years. The versatility of their properties and the possibility of using the simplest, inexpensive, and easily reproducible manufacturing methods make them promising materials for the manufacture of photovoltaic devices [1, 2] Metal oxides (Sn, Zn) are semiconductors with a band gap from 3 to 3.6 eV. Wide-gap semiconductors (ZnO, $SnO_2$, $Zn_2SnO_4$) [3–5] have n-type conductivity due to oxygen vacancy and deviations from stoichiometry, and are transparent in the visible region of the optical spectrum. Thin films of metal oxides are widely used in optoelectronics, gas sensors, and transparent electronics. The electrical properties of metal oxides depend not only on their elemental composition, but also on the method of their synthesis. Thin films of metal oxides can be obtained by sol-gel technology [6], magnetron sputtering [7], electron beam evaporation [8], and other methods. In this work, the spray pyrolysis method was used in a way, which is not laborious and allows obtaining the required materials with the necessary characteristics and a minimum number of technological operations. Spray pyrolysis is a method that based on spraying an aerosol into a heated substrate. The aerosol, forming the necessary substance in the course of a chemical reaction is obtained from a solution of metal salts; it evaporates and then after hitting the substrate, sprayed under pressure [9,10].

The purpose of this work is to determine the optimal parameters for the production of metal oxide films by spray pyrolysis, as well as to study the structural and optical parameters of the fabricated ZnO, $SnO_2$, and $Zn_2SnO_4$ films.

## 2. EXPERIMENTAL TECHNIQUE

The synthesis of $SnO_2$ and ZnO was carried out from aqueous solutions of the corresponding metal salts. To synthesize a tin oxide film, tin chloride [$SnCl_2 \cdot 2H_2O$] was used as a precursor; a zinc oxide solution was synthesized from zinc acetate [$Zn(CH_3COO)_2 \cdot 2H_2O$]. water in a volume of 200 ml. In order to avoid hydrolysis of the tin chloride salt in water, hydrochloric acid was added in an amount of 1 ml. To synthesize a zinc stannate film, zinc acetate ($Zn(CH_3COO)_2 \cdot 2H_2O$] and tin chloride [$SnCl_2 \cdot 2H_20$] were chosen as precursors. Zinc acetate ($Zn(CH_3COO)_2 \cdot 2H_2O$] was used as a source of zinc oxide, and tin chloride [$SnCl_2 \cdot 2H_2O$] as a source of tin oxide in the synthesis of the compound $Zn_2SnO_2$. The molar ratio of zinc acetate and tin chloride in the solution was selected as 2:1. The calculated amount of tin chloride and zinc acetate was dissolved in distilled water to form two solutions. Hydrochloric acid HCl was added to prevent hydrolysis of the salt, then the two solutions were mixed and a precipitate formed in the final solution, and more hydrochloric acid was added.

The ZnO, $SnO_2$, and $Zn_2SnO_4$ films were deposited at an air pressure of 2 bar at a rate of 8 ml/min. The distance from the spray head to the preheated glass slide was 85 cm. The film of ZnO, $SnO_2$, and $Zn_2SnO_4$ was deposited in one layer for 18 minutes. Multilayer deposition of the ZnO film took place for 1 min with a subsequent break of 30 seconds to restore the substrate temperature.

*Cite as*: Kh.J. Mansurov, A.Y. Boboev, J.A. Urinboyev, East Eur. J. Phys. 2, 336 (2024), https://doi.org/10.26565/2312-4334-2024-2-39
© Kh.J. Mansurov, A.Y. Boboev, J.A. Urinboyev, 2024; CC BY 4.0 license

Structural studies of thin metal oxide films of $SnO_2$, ZnO, and $Zn_2SnO_4$ were performed on an XRD-6100 X-ray diffractometer. X-ray voltage 40.0 kV, current 30.0 mA. The scanning range is 8.0-9.0, the scanning speed is 2 deg/min, the sampling step is 0.02 degrees. The experimental results obtained with the XRD-6100 were processed by the Rietveld method using the Fullprof program.

## 3. RESULTS AND DISCUSSION

On Fig. 1*a* shows X-ray patterns of the $Zn_2SnO_4$ films and shown that a well-crystallized $Zn_2SnO$ film is obtained, as indicated by clear peaks of reflections from different crystal planes, which can all be attributed to the zinc-stannate phase. This indicates sufficient crystallization immediately after spray pyrolysis application. The X-ray pattern of the $Zn_2SnO$ film has the following reflections, which are presented in Table 1.

**Table 1.** Diffraction positions observed in X-ray spectra of $Zn_2SnO_4$ metal oxide films (HKL – crystallographic orientations, d - interplanar spacing, 2θ – angle)

| | *2θ* | *hkl* | *d, Å* | Composition |
|---|---|---|---|---|
| 1 | 16.077 | 002 | 5.3954 | $SnO_2$ |
| 2 | 18.867 | 111 | 4.6513 | $Zn_2SnO_4$ |
| 3 | 22.23 | 110 | 3.9871 | ZnO |
| 4 | 28.8 | 220 | 3.1258 | $Zn_2SnO_4$ |
| 5 | 33.91 | 311 | 2.6417 | $Zn_2SnO_4$ |
| 6 | 35.46 | 222 | 2.5313 | $Zn_2SnO_4$ |
| 7 | 41.183 | 400 | 2.1921 | $Zn_2SnO_4$ |
| 8 | 46.408 | 211 | 1.9572 | ZnO |
| 9 | 51.03 | 422 | 1.7918 | $Zn_2SnO_4$ |
| 10 | 54.372 | 511 | 1.6872 | $Zn_2SnO_4$ |
| 11 | 59.65 | 440 | 1.5523 | $Zn_2SnO_4$ |
| 12 | 67.57 | 620 | 1.3865 | $Zn_2SnO_4$ |
| 13 | 70.42 | 533 | 1.3374 | $Zn_2SnO_4$ |
| 14 | 71.357 | 622 | 1.3221 | $Zn_2SnO_4$ |
| 15 | 76.82 | 444 | 0.8812 | $Zn_2SnO_4$ |

Table 1 and the diffraction pattern show that the main high-intensity ($5\times10^3$ pulses$^{-1}$) reflection is present at d/n = 0.46513 nm (18.867) and this indicates that the film surface corresponds to the crystallographic plane (111). We analyzed the experimental results of this reflection using the Fullprof program, and determined the crystal structure of the $Zn_2SnO_4$ film corresponds to the cubic lattice, which belongs to the space group Fd3m (Fig. 1*a*). Also using the Nelson-Riley extrapolation function [11]

$$\xi = (1/2)\cdot[(\mathrm{Cos}^2\theta/\theta + (\mathrm{Cos}^2\theta/\mathrm{Sin}\theta)], \quad (1)$$

the cubic lattice parameter of the $Zn_2SnO_4$ film was determined from reflections – (111), which amounted to about 6.238 Å.

The average subcrystal size of the $Zn_2SnO_4$ film (*D*) was calculated by the Solyakov-Scherrer formula [11] using X-ray data, which was 53 nm. The formula is given in the ratio, and the calculated values are given in table 1:

$$D = \frac{k\lambda}{\omega cos\theta}, \quad (2)$$

where *k* is a constant (0.94), *D* is the size of subcrystals (blocks in nm), λ is the length

X-ray wavelength (1.5406 Å), ω is the full width at half maximum (FWHM in radians) and θ is the Bragg diffraction angle

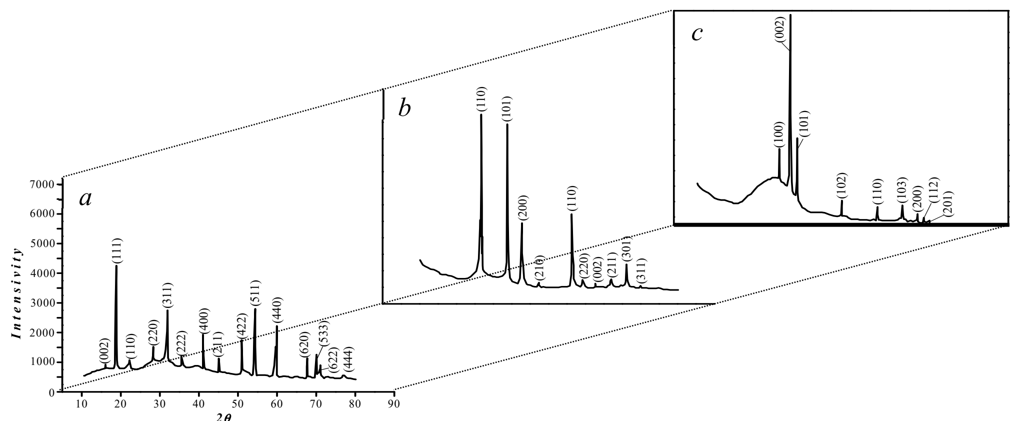


**Figure 1.** X-ray diffraction pattern of thin metal oxide films of $Zn_2SnO_4$ (*a*), $SnO_2$ (*b*), and ZnO (*c*)

However, films of $SnO_2$ and ZnO nanocrystallites 28 and 31 nm in size coherently arranged with lattices in the volume of thin $Zn_2SnO_4$ films can exhibit quantum size effects, which is of interest for modern nanotechnology.

The experimental data obtained using the X-ray diffraction method for thin layers of metal oxide $SnO_2$ are shown in Fig. 1*b*. An analysis of the X-ray diffraction pattern of the $SnO_2$ film shows that several structural reflections (Fig. 1*b*) of a selective nature with different intensities are observed in the diffraction pattern. The observed diffraction reflection from $SnO_2$ films with an intense reflection of (110) $SnO_2$ at $2\theta = 26.8°$ and its other order of (101) $SnO_2$ at $2\theta = 34.1°$, their FWHM(110) $\approx 6.1\times10^{-3}$ rad and FWHM(101) $\simeq 4.33\times10^{-3}$ rad) indicates the perfection of crystalline tin dioxide. Intense reflections from different crystal planes and their analysis of experimental results show that $SnO_2$ crystals have a Bravais tetragonal lattice with space group P4_2/mnm with lattice parameters $a = b = 4.836$ Å and $c = 3.245$ Å.

In addition, new structural reflections with different intensities appeared which are presented in Table 1.

**Table 1.** Diffraction positions observed in X-ray spectra of $SnO_2$ metal oxide films (HKL – crystallographic orientations, d – interplanar distance, θ, 2θ – angle, I – intensity)

| No. | HKL | d, Å | *θ*, deg | 2 *θ*, deg | I |
|---|---|---|---|---|---|
| 1 | 110 | 3.333 | 13° 23′ | 26° 46′ | 100 |
| 2 | 101 | 2.631 | 17° 03′ | 34° 06′ | 80 |
| 3 | 200 | 2.359 | 19° 05′ | 38° 10′ | 30 |
| 4 | 210 | 2.012 | 21° 10′ | 42° 20′ | 7 |
| 5 | 211 | 1.758 | 26° 00′ | 52° 00′ | 40 |
| 6 | 220 | 1.612 | 27° 09′ | 54° 18′ | 20 |
| 7 | 002 | 1.584 | 29° 04′ | 58° 08′ | 5 |
| 8 | 310 | 1.495 | 31° 02′ | 62° 04′ | 10 |
| 9 | 301 | 1.410 | 33° 10′ | 66° 20′ | 20 |
| 10 | 202 | 1.320 | 35° 44′ | 71° 28′ | 5 |

The average size of subcrystals of the $SnO_2$ film (*D*) was calculated by formula (2), which is 61 nm.

Fig. 1*c* shows an X-ray diffraction pattern of a thin film and, at low angle scattering, a broad diffuse reflection with selective crystallographic orientation reflections is observed at d/n = 0.2774 nm ($2\theta = 31.7°$) (100), d/n = 0 .2723 nm ($2\theta = 32.97°$) at (002) and d/n = 0.249 nm ($2\theta = 36.34°$) (101). Structural line (002), observed at d/n = 0.2723 nm ($2\theta = 32.97°$) on the diffraction pattern, shows that it is high intensity ($\sim10^5$ pulses$^{-1}$) and thin width (FWHM = $2.62\cdot10^{-3}$ rad). This testifies to the high perfection of the lattice of the thin-layer crystalline film [12]. An analysis of the experimental results of this reflection showed that it belongs to the C6/mmc space group and has a hexagonal syngony with the wurtzite structure in the crystal lattice (due to the bond between zinc-oxygen atoms). The sizes of subcrystals determined from the half-width of this structural peak were 67 nm.

In addition, another diffuse reflection was observed in the X-ray diffraction pattern of a thin ZnO layer at a maximum average angular scattering of $2\theta \approx 42.12°$ (FWHM = $3.03\times10^{-1}$ rad). At the same time, in diffusion reflection of low intensity at d/n = 0.1911 nm ($2\theta = 47.63°$); at $(102)_{ZnO}$, at $(103)_{ZnO}$ d/n = 0.1630 nm ($2\theta = 56.67°$), and d/n = 0.1481 nm ($2\theta = 62.93°$) $(110)_{ZnO}$ - selective reflections were also observed. Theoretical calculations presented in [12,13,14] and obtained on the basis of the analysis of experimental data of X-ray diffraction patterns of a thin layer confirm that these structural reflections arise on the surface of a thin layer due to the formation of ZnO nanocrystallites, while their average size is ZnO at d/n = 0.1911 nm ($2\theta = 47.63°$) $(102)_{ZnO}$, at d/n = 0.1630 nm ($2\theta = 56.67°$) $(103)_{ZnO}$ and d/n = 0.1481 nm ($2\theta = 62.93$)° $(110)_{ZnO}$ which is determined to be 84 nm using experimental results of selective reflections.

Optical data on the films were obtained on a SPECS SSP-715 M spectrophotometer. The transmission spectra of ZnO, $SnO_2$, and $Zn_2SnO_4$ are shown in Fig. 2. The transmission spectra for films $SnO_2$, ZnO, $Zn_2SnO_4$ have a transparency of more than 80% in the visible and infrared parts of the spectrum. The transparency threshold is in the ultraviolet range. This makes them suitable for use in transparent electronics and solar energy. In accordance with the literature data [15-18], all synthesized metal oxides had a direct band structure.

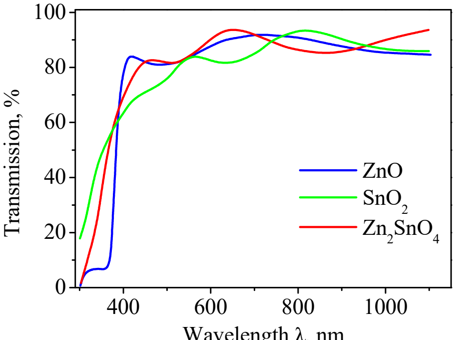


**Figure 2.** Transmission spectrum (transparency) of ZnO, $SnO_2$, and $Zn_2SnO_4$ films

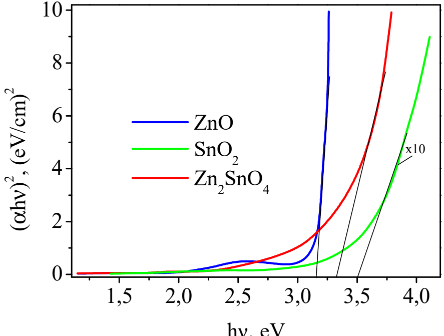


**Figure 3.** Dependences of $(\alpha h\nu)^2$ on the light energy for ZnO, $SnO_2$, and $Zn_2SnO_4$ films

From the absorption thresholds, one can determine the absorption coefficient and band gap of the film in the coordinates $(\alpha h\nu)^2 = f(h\nu)$. The calculation data for the band gap are shown in Fig. 3. The band gap was determined by straightening the graph $(\alpha h\nu)^2 = f(h\nu)$ and amounted to 3.5 eV for $Zn_2SnO_4$, 3.3 eV for $SnO_2$ and 3.2 eV for ZnO.

## 4. CONCLUSION

Thus, based on the analysis of the technological modes of synthesis and the results of the studies of metal oxide films (ZnO, $SnO_2$ and $Zn_2SnO_4$), the following conclusions can be drawn:

- the conditions and parameters for the synthesis of $Zn_2SnO_4$, $SnO_2$ and ZnO films using spray pyrolysis were determined. The films were synthesized from aqueous solutions; the main differences between the methods were in the composition of the precursors, in the modes and time of deposition;

-crystal structure of the $Zn_2SnO_4$ film corresponds to the cubic lattice, which belongs to the space group Fd3m with blocks sized 53 nm and lattice parameters $a$ = 6.238 Å. Films of $SnO_2$ and ZnO nanocrystallites 28 and 31 nm in size coherently arranged with lattices in the volume of thin $Zn_2SnO_4$ films can exhibit quantum size effects, which is of interest for modern nanotechnology.

-crystals of the resulting $SnO_2$ films have a tetragonal Bravais lattice with space group P4_2/mnm with lattice parameters $a = b$ = 4.836 Å and $c$ = 3.245 Å, and the subcrystal size of the $SnO_2$ film is 61 nm.

The resulting ZnO films belong to the C6/mmc space group and the crystal lattice has a hexagonal syngony with the wurtzite structure with parameters $a = b$ = 0.3265 nm and $c$ = 0.5212 nm. It has been determined that, on the surface of the thin film grown, zinc oxide bumps with sizes $L_{ZnO} \approx 84$ nm appear, which affect the unique properties of the samples.

- studies of the parameters of films $Zn_2SnO_4$, $SnO_2$ and ZnO were carried out to assess the possibility of using them as structural elements of a thin-film solar cell. The band gap was determined from the light absorption spectra and was in the range of 3.2 – 3.5 eV for oxides based on Zn and Sn.

**ORCID**
**Xhotamjon J. Mansurov**, https://orcid.org/0009-0006-4571-7795; **Akramjon Y. Boboev**, https://orcid.org/0000-0002-3963-708X
**Jakhondir A. Urinboyev**, https://orcid.org/0009-0003-4903-4164

**REFERENCES**

[1] A. Pérez-Tomás, A. Mingorance, D. Tanenbaum, and M. Lira-Cantu, "Metal oxides in photovoltaics: all-oxide, ferroic, and perovskite solar cells," The Future of Semiconductor Oxides in Next-Generation Solar Cells, **8**(1), 267-356 (2018). https://doi.org/10.1016/B978-0-12-811165-9.00008-9

[2] S.Z. Zainabidinov, S.I. Rembeza, E.S. Rembeza, and Sh.Kh. Yulchiev, "Prospects for the Use of Metal-Oxide Semiconductors in Energy Converters," Applied Solar Energy, **55**(1), 5–7 (2019). https://doi.org/10.3103/S0003701X19010146

[3] H. Hosono, "Ionic amorphous oxide semiconductors: Material design, carrier transport, and device application," Journal of Non-Crystalline Solids, **352**(1), 851-858 (2006). https://doi.org/10.1016/j.jnoncrysol.2006.01.073

[4] M Batzill, and U. Diebold, "The surface and materials science of tin oxide," Progress in Surface Science, **79**, 47–154 (2005). https://doi.org/10.1016/j.progsurf.2005.09.002

[5] O. Ishchenko, V. Roge, G. Lamblin, D. Lenoble, and I. Fechete, "$TiO_2$, ZnO, and $SnO_2$-based metal oxides for photocatalytic applications: principles and development," Comptes Rendus Chimie, **24**,103-124 (2021). https://doi.org/10.5802/crchim.64

[6] B. Stjerna, and C. Granqvist, "Optical and electrical properties of $SnO_x$ thin films made by reactive R.F. magnetron sputtering," Thin Solid Films, **193**, 704-711 (1990). https://doi.org/10.1016/0040-6090(90)90222-Y

[7] X. Wen, Q. Zhang, and Z. Shao, "Magnetron Sputtering for ZnO: Scintillation film production and its application research status in nuclear detection," *C*rystals, **9**(5), 263 (2019). https://doi.org/10.3390/cryst9050263

[8] R. Kumar, M. Sekhar, Raghvendra, R. Laha, and S. Pandey, "Comparative studies of ZnO thin films grown by electron beam evaporation, pulsed laser and RF sputtering technique for optoelectronics applications," Applied Physics, **126**, 859 (2020). https://doi.org/10.1007/s00339-020-04046-8

[9] M. Chitra, "$ZnO/SnO_2/Zn_2SnO_4$ nanocomposite: preparation and characterization for gas sensing applications," Nanosystems: physics, chemistry, mathematics, **7**(4), 707-710 (2016). http://dx.doi.org/10.17586/2220-8054-2016-7-4-707-710

[10] S.Z. Zainabidinov, A.Y. Boboev, Kh.A. Makhmudov, and V.A. Abduazimov, "Photoelectric Properties of n-ZnO/p-Si Heterostructures. X," Applied Solar Energy, **57**(6), 475-479 (2021). https://doi.org/10.3103/S0003701X21060177

[11] S. Zainabidinov, Sh. Utamuradova, and A. Boboev, "Structural Peculiarities of the $(ZnSe)_{1-x-y}(Ge_2)_x(GaAs_{1-\delta}Bi_\delta)_y$ Solid Solution with Various Nanoinclusions," Journal of Surface Investigation X-ray Synchrotron and Neutron Techniques, **16**(6), 1130-1134 (2022). https://doi.org/10.1134/S1027451022060593

[12] S. Zaynabidinov, Sh. Yuldashev, A. Boboev, and N. Yunusaliyev, "X-ray diffraction and electron microscopic studies of the ZnO(S) metal oxide films obtained by the ultrasonic spray pyrolysis method," Herald of the Bauman Moscow State Technical University, Series Natural Sciences, **1**(112), 78-92 (2024). https://doi.org/10.18698/1812-3368-2024-1-78-92

[13] D. Elmurotova, N. Nishonova, F. Kuluyeva, and T. Muxtarova, Photoconductivity of gamma-irradiated Znse (Te)/ZnO:O and ZnSe(Te)/ZnO:O,Zn nanogeterojuctions. E3S Web of Conferences **383**, 04051 (2023). https://doi.org/10.1051/e3sconf/202338304051

[14] Sh. Shahzad, S. Javed, and M. Usman, "A Review on Synthesis and Optoelectronic Applications of Nanostructured ZnO" Front. Mater, **8**, 613825 (2021) | https://doi.org/10.3389/fmats.2021.613825

[15] Sh. Matussin, A. Rahman, and M. Khan, "REVIEW article: Role of Anions in the Synthesis and Crystal Growth of Selected Semiconductors," Front. Chem. **10**, 881518 (2022). https://doi.org/10.3389/fchem.2022.8815

[16] N. Kamarulzaman, M.F. Kasim, and R. Rusdi, "Band Gap Narrowing and Widening of ZnO Nanostructures and Doped Materials," Nanoscale Res. Lett. **10**, 346 (2015). https://doi.org/10.1186/s11671-015-1034-9
[17] O. Mounkachi, E. Salmani, M. Lakhal, H. Ez-Zahraouy, M. Hamedoun, M. Benaissa, A. Kara, et al., "Band-gap engineering of $SnO_2$," Solar Energy Materials and Solar Cells, **148**, 34-38 (2016). https://doi.org/10.1016/j.solmat.2015.09.062
[18] T. Mabate, N. Maqunga, S. Ntshibongo, M. Maumela, and N. Bingwa, "Metal oxides and their roles in heterogeneous catalysis: special emphasis on synthesis protocols, intrinsic properties, and their infuence in transfer hydrogenation reactions," SN Applied Sciences, **5**(196), 1-25 (2023). https://doi.org/10.1007/s42452-023-05416-6

## РЕНТГЕНОСТРУКТУРНІ ТА ФОТОЕЛЕКТРИЧНІ ВЛАСТИВОСТІ $SnO_2$, ZnO, ТА $Zn_2SnO_4$ МЕТАЛООКСИДНИХ ПЛІВОК

**Хотамджон Дж. Мансуров[a], Акрамжон Ю. Бобоєв[a,b], Джахонгір А. Урінбоєв[a]**
*[a]Андижанський державний університет імені З.М. Бабур, Андижан, Узбекистан*
*[b]Інститут фізики напівпровідників та мікроелектроніки Національного університету Узбекистану, Ташкент, Узбекистан*

Визначено умови та параметри синтезу плівок оксидів металів (ZnO, $SnO_2$, $Zn_2SnO_4$) методом розпилювального піролізу. Плівки синтезовано з водних розчинів; основні відмінності методів полягали в складі прекурсорів, режимах і часу осадження. Кристалічна структура плівки $Zn_2SnO_4$ відповідає кубічній ґратці, що належить до просторової групи Fd3m з розміром блоків 53 нм і параметрами ґратки a = 6,238 Å. Плівки нанокристалітів $SnO_2$ і ZnO розміром 28 і 31 нм, когерентно розташовані з ґратками в об'ємі тонких плівок $Zn_2SnO_4$, можуть проявляти квантово-розмірні ефекти, що становить інтерес для сучасних нанотехнологій. Кристали отриманих плівок $SnO_2$ мають тетрагональну ґратку Браве з просторовою групою P4 2/mnm з параметрами ґратки a = b = 4,836 Å та c = 3,245 Å, розмір субкристалів плівки $SnO_2$ становить 61 нм. Отримані плівки ZnO належать до просторової групи C6/mmc, а кристалічна решітка має гексагональну сингонію зі структурою вюрциту з параметрами a = b = 0,3265 нм і c = 0,5212 нм. Встановлено, що на поверхні вирощеної тонкої плівки виникають горбки оксиду цинку з розмірами $L_{ZnO} \approx 84$ нм, які впливають на унікальні властивості зразків. Показано, що отримані тонкі плівки $Zn_2SnO_4$, $SnO_2$ і ZnO можуть бути використані в широкому діапазоні застосувань від чутливих сенсорних елементів до покриттів в прозорій електроніці з точки зору їх оптичних параметрів.

**Ключові слова:** *плівка; просторова група; субкристал; нанокристал; ефект квантового розміру; параметр решітки; прозора електроніка; заборонена зона*

East European Journal of Physics. **2.** 341-344 (2024)
DOI:10.26565/2312-4334-2024-2-40 ISSN 2312-4334

# STUDY OF THE INHOMOGENEITIES OF OVERCOMPENSED SILICON SAMPLES DOPED WITH MANGANESE

**M.Sh. Isaev[a]*, U.T. Asatov[b], M.A. Tulametov[b], S.R. Kodirov[c], A.E. Rajabov[d]**
*[a]National University of Uzbekistan, Tashkent, Uzbekistan*
*[b]Tashkent Institute of Chemical Technology, Tashkent, Uzbekistan*
*[c]Urgench State University, Urgench, Uzbekistan*
*[d]Urgench branch of Tashkent University of Information Technologies named after Muhammad al-Khwarizmi*
**Corresponding Author e-mail: isayevmahmd02@gmail.com*
Received April 9, 2024; revised April 30, 2024; accepted May 11, 2024

Inhomogeneities in the near-surface region of diffusion-doped silicon with manganese atoms were studied using the local photo-EMF method and photovoltage and photoconductivity signals were detected. It has been established that the inhomogeneous region is located at a depth of 3÷35 µm from the surface of the crystal. The magnitude of photo-EMF in these layers does not change monotonically from point to point. It was revealed that the photo-EMF spectra depend on the wavelength of the irradiated light, while the shape of the areas and their shift are related to the penetration depth of laser radiation. The photo-EMF signal increases to a depth of ~25 µm from the surface, then saturates and from ~30 µm smoothly decreases and completely disappears at a depth of ~40 µm. The magnitude of the internal electric field was determined using the Tauc method. A model of the structure of the near-surface region of diffusion-doped silicon with manganese is proposed.
**Key words:** *Diffusion; Inclusion; Heat Treatment; Inhomogeneity; Photo-EMF; Photoprobe; Scattering; Gradient; Twin*
**PACS:** 33.20.Ea, 33.20.Fb

## INTRODUCTION

In recent years, for the controlled formation of the defect structure of silicon, so-called unconventional impurities have been used - impurities of T-ions (transition elements), which create a number of deep levels in the band gap of silicon. These specially introduced impurities interact with various uncontrolled impurities during technological treatments [1-5].

This work presents the results of a study of the inhomogeneity of the surface layer of silicon formed during its diffusion doping with manganese atoms. It was revealed that high-temperature heat treatment contributes to the formation of an anomalous profile of the distribution of current carrier concentration, characterized by a sharp decrease in the latter to a depth of 30-50 µm from the surface of the crystal. This layer requires comprehensive studies of the mechanism of impurity entry into the crystal volume and their interaction with both the matrix (main) atoms of the crystal and with technological (background) impurities, as well as with structural defects [6-10].

## EXPERIMENTAL PART

To determine the inhomogeneity, the local photoprobe method and the method of small-angle laser radiation scattering were used. These methods make it possible to identify heterogeneous areas with high accuracy, especially areas with large conductivity gradients.

Using the local photovoltage method, inhomogeneities were studied in the original, heat-treated and control silicon crystals and doped Si <Mn> crystals having the shape of a rectangular parallelepiped of various sizes: (0.3÷0.5)×(0.3÷1.6)×(0, 5÷1.6) $cm^3$.

The study was carried out on a sample with different surface conditions after each layer removal. There were basically two types of surface: 1-surface obtained after mechanical processing with M14, M7 and M4 powders, after etching for 40-60 seconds, in boiling alkaline etchant ($H_2O_2$:NaOH = 1:3) followed by washing in double-distilled water [10].

Due to the fact that the formation of twins in the original single-crystal silicon leads to a change in the orientation of the crystal, a method was used to determine surface defects when it was illuminated. It is known that a twin is a region of a crystal whose orientation is a mirror image of the main crystal (twin orientation). A characteristic feature of a twin is the presence of a flat boundary, which on the side surface of the crystal is the line of intersection of the twin plane with the surface. On the cut plane, the twin boundary appears as a straight line.

Crystals that had no grain boundaries, twins, or twin lamellas were selected for the study.

Photoconductivity and photovoltage measurements [12,13] were carried out at room temperature on Si <Mn> samples in which the bulk part of the crystal was overcompensated, i.e. n -type. The dimensions of the samples were as follows: after doping with metal atoms - 0.3×0.4×0.5 $cm^3$ and 0.4×1.6×1.6 $cm^3$, after cutting to study the photovoltage - 0.15×0,3×0.5 $cm^3$ and 0.3×1.5×1.6 $cm^3$.

***Cite as:*** M.Sh. Isaev, U.T. Asatov, M.A. Tulametov, S.R. Kodirov, A.E. Rajabov, East Eur. J. Phys. 2, 341 (2024), https://doi.org/10.26565/2312-4334-2024-2-40
© M.Sh. Isaev, U.T. Asatov, M.A. Tulametov, S.R. Kodirov, A.E. Rajabov, 2024; CC BY 4.0 license

To determine the heterogeneous areas, these samples were cut out as shown by the dashed lines in Fig. 1. Samples cut in this way made it possible to compare the photoconductivity and photovoltage both from the cut surface of the samples.

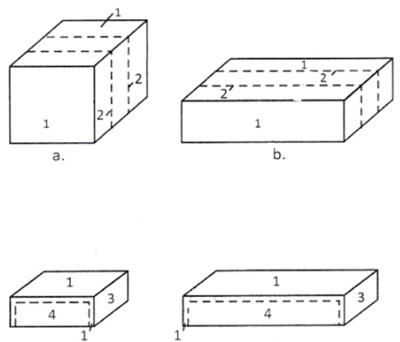


**Figure 1.** Type of sample Si <Mn>, Si<Co>, Si<Cr> for studying photovoltage and photoconductivity:
a - sample 1 (initial); b – sample 2 (initial); c, d – samples after removal of 50 µm from three faces;
1 - near-surface area 2 - cut line; 3 - ohm contact; 4 - volume area.

## RESULTS AND DISCUSSION

Figure 2 shows the results of light scanning for typical Si < Mn > samples when irradiated with light with a wavelength of 0.63 µm, after removing a layer 3-5 µm thick from the surface. It is clear from the figures that the photo-signal does not change monotonically from point to point. Changes in signal magnitude are highly localized. The average value of the photo-signal changes slightly, while in some areas the photo-signal changes greatly. This behavior is associated with a change in the lifetime of current carriers in individual local areas, caused by the inhomogeneity of the crystal.

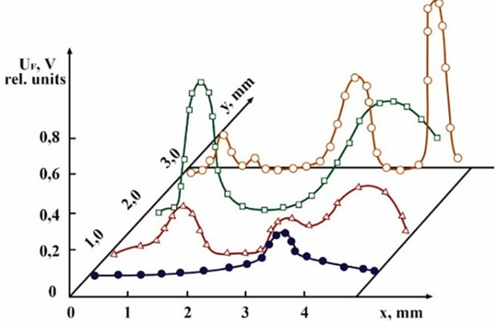


**Figure 2.** Light scanning results for one sample n-Si<Mn> when irradiated with light with $\lambda = 0.63$ µm

In Fig. 3. The results of light scanning are presented for one of the typical Si<Mn> samples at light wavelengths $\lambda$equal to 0.63 µm, 1.15 µm and 3.39 µm after removing a 5 µm thick layer from the surface. From figure it can be seen that the amplitude of the photovoltage increases with decreasing wavelength of the irradiating light.

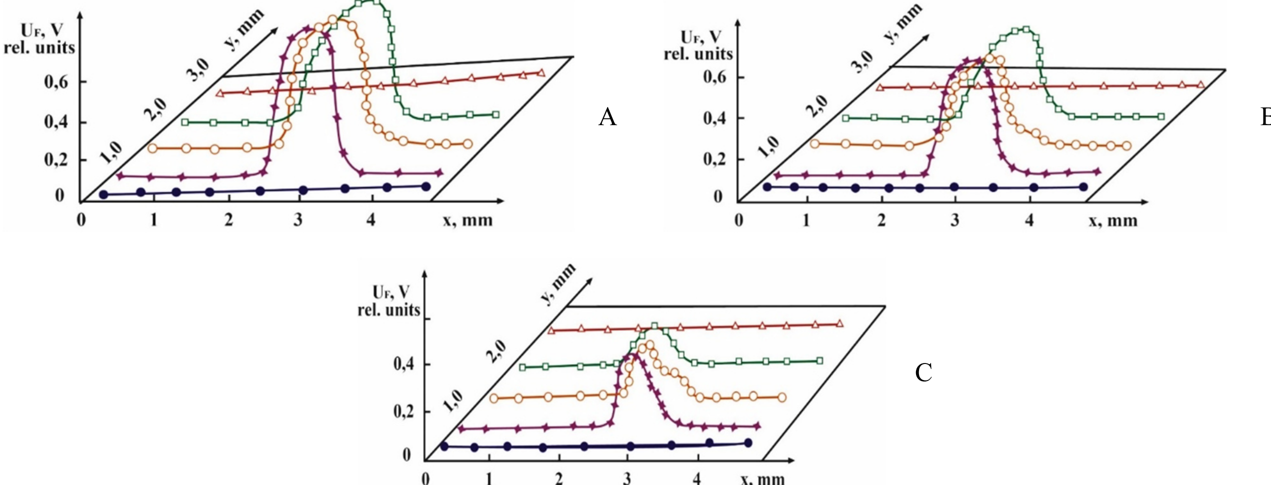


**Figure 3.** Light scanning results for one sample p - Si < Mn > when irradiated with light of different wavelengths:
A) $\lambda = 63\,\mu m$; B) $\lambda = 1.15\,\mu m$; C) $\lambda = 3.39\,\mu m$.

The dependence of the photovoltage on the thickness of the near-surface layer is shown in Fig. 4. It can be seen that the photovoltage signal increases as the layer is removed to a depth of ~25 μm, and then in a narrow region it saturates and from ~30 μm smoothly decreases and completely disappears after removal above 45÷50 μm.

To determine the internal electric field of the inhomogeneous region of the crystal, an external electric field of $E_i$ polarity, inverse to the internal electric field Ei, was applied to it. Studies have shown that at E = 0.9-1.2 V/cm, the volumetric photovoltage current when illuminated with modulated light is zero. In this case, $E_i$ can be determined according to the expression:

$$E_i \to \frac{1+b}{2} \cdot \frac{i}{s}, \tag{1}$$

where $s$ is the cross section of the crystal, $b$is the ratio of electron and hole mobilities, $i$ is the compensating direct current, $\rho$ and is the resistivity of the crystal.

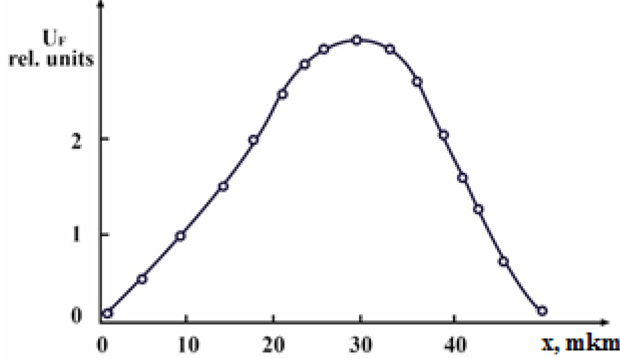


**Figure 4.** Dependence of the photovoltage on the thickness of the surface layer n - Si < Mn >, T = 300 K, $\lambda$ = 0.63 μm

When substituting the values into (1) $b = \mu_n/\mu_p = 3, p = 1.3 \cdot 10^4\ Om \cdot cm,\ i = 1.39 \cdot 10^{-6} A,\ s = 2 \cdot 10^{-2} cm^2$ are obtained $E_i$ = 0.8 V/cm.

Based on the results of complex studies, a model of the structure of the near-surface region of diffusion-doped silicon with manganese is proposed. The near-surface region of compensated silicon is a large number of Schottky diodes (pairs), connected in opposite directions, with a layer of silicon compensated by metal atoms between them, connected in parallel and in series (Fig. 5).

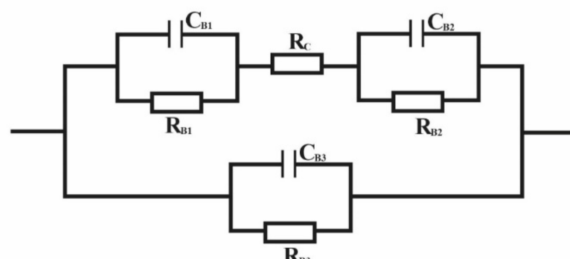


**Figure 5.** Model of the structure of the near-surface region of diffusion -doped silicon with manganese, chromium and cobalt atoms. $R_C$ – resistance of the compensated area, $C_B$, $R_B$ – capacitance and resistance of the Schottky barrier, respectively.

This model is determined by the island nature of the inclusions of the second phase, located at a depth of ~3-45 μm from the surface. This is also confirmed by the maximum value of the photovoltage at a depth of ~25-30 μm (Fig. 4), where, apparently, there is an optimal ratio between the number of islands (inclusions) and their surface, giving the maximum total surface area of the silicon-second phase inclusions boundary.

## CONCLUSIONS

1. It has been established that photovoltage spectra depend on the wavelength of light, and the area shifts and their shape are related to the penetration depth of laser radiation. It has been shown that when using infrared radiation in the near-infrared spectrum, it is possible to determine inhomogeneities in the crystal volume using the local photovoltage method.
2. A study of the dependence of the photovoltage on the thickness of the near-surface layer of doped crystals showed that the photovoltage signal increases as the layer is removed to a depth of ~25 μm, and then in a narrow region it saturates and from ~30 μm smoothly decreases and completely disappears after removing 40 μm.
3. The possibility of determining the internal electric field in an inhomogeneous region of a doped crystal using the Tauc method has been demonstrated. It was established that in the n-Si <Mn> crystal, when an external electric field $E_e$ = 0.9-1.2 V/cm was applied, the internal electric field had a value of $E_i$ = 0.8 V/cm.

4. A model of the structure of the near-surface region of diffusion-doped silicon with manganese is proposed. The near-surface region of compensated silicon is a large number of Schottky diodes (pairs) connected in parallel-series, with a layer of compensated silicon between them.

**ORCID**
**Makhmudkhodja Sh. Isaev,** https://orcid.org/0009-0007-9559-5834

**REFERENCES**

[1] B.A. Lombo, "Deep levels in semiconductors," S. Can. J. Chem. **63,** 1666 (1985). http://dx.doi.org/10.1139/v85-279
[2] A.A. Lebedev, "Deep level centers in silicon carbide: A review," Semiconductors, **33(2),** 107-130 (1999). https://doi.org/10.1134/1.1187657
[3] K.P. Abdurakhmanov, Sh.B. Utamuradova, Kh.S. Daliev, S.G. Tadjy-Aglaeva, and R.M. Érgashev, "Defect-formation processes in silicon doped with manganese and germanium," Semiconductors, **32**(6), 606–607 (1998). https://doi.org/10.1134/1.1187448
[4] Kh.S. Daliev, Sh.B. Utamuradova, O.A. Bozorova, and Sh.Kh. Daliev, "Joint effect of Ni and Gf impurity atoms on the silicon solar cell photosensitivity," Applied Solar Energy (English translation of Geliotekhnika), **41**(1), 80–81 (2005). https://www.researchgate.net/publication/294234192_Joint_effect_of_Ni_and_Gf_impurity_atoms_on_the_silicon_solar_cell_photosensitivity
[5] K.S. Daliev, S.B. Utamuradova, J.J. Khamdamov, and M.B. Bekmuratov, "Structural properties of silicon doped rare earth elements ytterbium," East European Journal of Physics, (1), 375–379 (2024). https://doi.org/10.26565/2312-4334-2024-1-37
[6] S.B. Utamuradova, S.Kh. Daliev, E.M. Naurzalieva, and X.Yu. Utemuratova, "Investigation of defect formation in silicon doped with silver and gadolinium impurities by raman scattering spectroscopy," East European Journal of Physics, (3), 430–433 (2023). https://doi.org/10.26565/2312-4334-2023-3-47
[7] Kh.S. Daliev, Sh.B. Utamuradova, O.A. Bozorova, and Sh.Kh. Daliev, "Joint influence of impurity atoms of nickel and hafnium on photosensitivity of silicon solar cells," Applied Solar Energy (English translation of Geliotekhnika), **1,** 85–87 (2005). https://www.researchgate.net/publication/294234192_Joint_effect_of_Ni_and_Gf_impurity_atoms_on_the_silicon_solar_cell_photosensitivity
[8] M.Sh. Isaev, I.T. Bozarov, and A.I. Tursunov, "Investigation of thermally stimulated conductivity of cobalt silicide," E3S Web of Conferences, **402,** 14019 (2023). https://doi.org/10.1051/e3sconf/202340214019
[9] M.Sh. Isaev, T.U. Atamirzaev, M.N. Mamatkulov, U.T. Asatov, and M.A. Tulametov, "Study of the mobility and electrical conductivity of chromium silicide," East European Journal of Physics, (4), 189–192 (2023). https://doi.org/10.26565/2312-4334-2023-4-22
[10] Sh.B. Utamuradova, Z.T. Azamatov, and M.A. Yuldoshev, "Optical Properties of $ZnO–LiNbO_3$ and $ZnO–LiNbO_3$:Fe Structures," Russian Microelectronics, **52**(Suppl. 1), S99–S103 (2023). https://doi.org/10.1134/S106373972360022X
[11] N.A. Turgunov, E.Kh. Berkinov, and R.M. Turmanova, "The effect of thermal annealing on the electrophysical properties of samples n-Si<Ni,Cu>," East European Journal of Physics, (3), 287–290 (2023). https://doi.org/10.26565/2312-4334-2023-3-26
[12] P.R. Berger, G. Gulyamov, M.G. Dadamirzaev, M.K. Uktamova, and S.R. Boidedaev, "Influence of microwave and magnetic fields on the electrophysical parameters of a tunnel diode," Romanian journal of physics, **69**, 609 (2024). (Accepted Manuscripts)
[13] J.J. Liou, "Non-quasi-static capacitance of p/n junction space-charge regions," Solid-State Electronics, **31**(1), 81-86 (1998). http://dx.doi.org/10.1016/0038-1101(88)90088-3

**ДОСЛІДЖЕННЯ НЕОДНОРІДНОСТЕ НАД КОМПЕНСОВАНИХ ЗРАЗКІВ КРЕМНІЮ, ЛЕГОВАНИХ МАРГАНЦЕМ**

**М.Ш. Ісаєв[a], У.Т. Асатов[b], М.А. Туламетов[b], С.Р. Кодиров[c], А.Е. Раджабов[d]**
[a]*Національний університет Узбекистану, Ташкент, Узбекистан*
[b]*Ташкентський хіміко-технологічний інститут, Ташкент, Узбекистан*
[c]*Ургенчський державний університет, Ургент, Узбекистан*
[d]*Філія Ташкентського університету інформаційних технологій імені Мухаммеда аль-Хорезмі, Ургент, Узбекистан*

Методом локальної фото-ЕРС досліджено неоднорідності приповерхневої області дифузійно-легованого атомами марганцю кремнію та зареєстровано сигнали фотоелектричної напруги та фотопровідності. Встановлено, що неоднорідна область розташована на глибині 3÷35 мкм від поверхні кристала. Величина фото-ЕРС в цих шарах не змінюється монотонно від точки до точки. Виявлено, що спектри фото-ЕРС залежать від довжини хвилі опромінюваного світла, а форма ділянок і їх зсув пов'язані з глибиною проникнення лазерного випромінювання. Сигнал фото-ЕРС зростає до глибини ~25 мкм від поверхні, потім насичується і від ~30 мкм плавно спадає і повністю зникає на глибині ~40 мкм. Величину внутрішнього електричного поля визначали методом Таука. Запропоновано модель структури приповерхневої області дифузійно легованого кремнію марганцем.

**Ключові слова:** *дифузія; включення; термообробка; неоднорідність; фото-ЕРС; фотозонд; розсіювання; градієнт; двійник*

East European Journal of Physics. **2.** 345-352 (2024)
DOI:10.26565/2312-4334-2024-2-41 ISSN 2312-4334

# EFFECT OF STRUCTURAL DEFECTS ON PARAMETERS OF SILICON FOUR-QUADRANT *p-i-n* PHOTODIODES

**Mykola S. Kukurudziak**[a,b]
[a]*Rhythm Optoelectronics Shareholding Company, Holovna str. 244, 58032, Chernivtsi, Ukraine*
[b]*Yuriy Fedkovych Chernivtsi National University, Kotsyubyns'kogo str. 2, 58012, Chernivtsi, Ukraine*
*Corresponding Author e-mail: mykola.kukurudzyak@gmail.com*
Received April 1, 2024; revised April 26, 2024; accepted May 10, 2024

The article examines the influence of structural defects, in particular dislocations, on the electrical and photovoltaic properties of silicon four-quadrant *p-i-n* photodiodes. It was established that growth defects and defects formed during mechanical processing of plates can cross the entire substrate and deteriorate the parameters of photodiodes. This phenomenon is particularly negative due to the placement of defects in the space charge region. In this case, due to the presence of recombination centers in the space charge region, the life time of minor charge carriers decreases and the dark current and responsivity of photodiodes deteriorate. Often, the placement of defects is uneven, which provokes unevenness of parameters on responsive elements. It was also seen that the dislocation lines crossing the responsive elements and the guard ring worsen the insulation resistance of the specified active elements. A method of determining the final resistivity of silicon and the diffusion length of minor charge carriers by studying the pulse shape of the output signal is proposed.
**Keywords**: *Silicon; Photodiode; Point Defects; Dislocations; Dark Current; Sensitivity*
**PACS:** 61.72. Ji, 61.72. Lk, 85.60.Dw

Due to the dominance of silicon as the main electronics material, the issue of defect formation in single-crystal Si and the influence of structural defects on the parameters of electronics elements made on its basis is still open.

There are two possible approaches to the problem of the influence of crystallographic defects on the electrical properties of materials and devices. The first is to study the interaction of defects and impurities interacting with them and with each other on the charge transfer properties in a semiconductor. The second approach is to study the influence of impurities and defects on the performance of devices. The use of the second, more direct approach is an obligatory stage in the development of the so-called "defect-free" technology for manufacturing devices [1]. It is the second approach that will be the basis for this article.

It is known [2-4] that in the process of growing and processing, various crystallographic defects often occur in silicon wafers, the presence of which can have a significant impact on electrical phenomena in devices manufactured on the basis of such material. There are many so-called "gettering" methods that can reduce the harmful effects of crystallographic defects in silicon. These methods include the technology for obtaining defect-free material [5-7], the production of defect-free devices [8, 9], the "deactivation" of electrically active defects [10], and the structural use of defects deliberately introduced into certain areas of crystals [11], etc.

Despite the considerable number of works devoted to the influence of structural defects on the electrical properties of electronics elements in various fields of microelectronics, this problem remains relevant due to the wide variety of devices whose parameters can be affected by defects in different ways. Thus, in this work, we investigated the effect of dislocations on the electrical and photoelectric properties of four-quadrant silicon *p-i-n* photodiodes (PD). It should be noted that in [12] and [13] we investigated the mechanisms of defect formation on the surface of silicon wafers during the diffusion of phosphorus from planar solid-state sources and the liquid-phase diffuser $PCl_3$, and the effect of these defects on the dark currents of *p-i-n* photodiodes; in [14] we proposed a method for reducing the density of dislocations on the surface of photodiode responsive elements (RE). In [15], we also describe the effect of the chemical dynamic polishing on the structural perfection of the surface of silicon wafers and [16] indicates possible causes of the formation of point defects in the package during oxidation, the clusters of which can be the centres of generation of dislocation loops during subsequent thermal operations. However, in this work, we will not discuss the mechanisms of defect formation, but will focus on the effect of growth and acquired defects (in particular, dislocations) on the responsivity of the PD ($S_{pulse}$) (in particular, responsivity spread), the insulation resistance between the RE and guard ring (GR) ($R_{con}$), the dark currents of the RE ($I_d$) and their spread, the barrier capacity of the RE ($C_{RE}$), etc. The study of the effect of dislocations on the PD parameters is the purpose of this article. The information provided on the nature of the influence of these structural defects on certain parameters may be useful to specialists and technologists in the field of *p-i-n* photodiodes to determine the causes of degradation of certain parameters or failure of devices.

## EXPERIMENTAL

The research was carried out in the manufacture of silicon 4Q *p-i-n* PDs with GR for operation at wavelength $\lambda_{op}$ = 1.064 μm. PDs were made on the basis of single-crystal *p*-type silicon with resistivity $\rho \approx$ 18-22 kΩ·cm and [111]

***Cite as:*** M.S. Kukurudziak, East Eur. J. Phys. 2, 345 (2024). https://doi.org/10.26565/2312-4334-2024-0-41
© M.S. Kukurudziak, 2024; CC BY 4.0 license

orientation. The samples were made by diffusion-planar technology according to the technological regimes given in [12]. The thickness of the crystals reached 500-510 μm.

During the serial production of photodiodes, it was found that dislocation lines and grids appear in certain areas of the used wafers (most often on the periphery), which can be seen with the naked eye and without selective etching (Fig. 1). These formations are not observed on the surface of the wafers before thermal operations, but become apparent after thermal operations. The resulting dislocation complexes are characterized by uneven distribution and localization (increased density in certain areas of the wafer). There may be several reasons for the formation of the indicated structural defects. The first is the relaxation of mechanical stresses in silicon during heat treatment. These stresses could be formed during ingot growth or machining. The other is the accumulation of point structural defects and microdefects, which are zones of dislocation loop generation during thermal operations [1, 17].

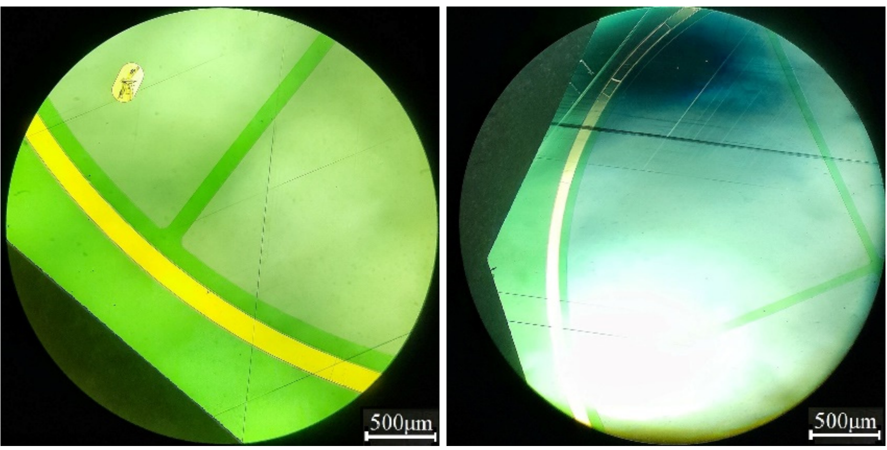


**Figure. 1.** Image of dislocation lines on the photodiode surface before selective etching

The crystals with the described surface formations had deteriorated parameters. A number of such crystals from different series were selected for the study.

The *I–V* characteristics of PDs were measured using a hardware-software complex implemented on the basis of the Arduino platform, an Agilent 34410A digital multimeter and a Siglent SPD3303X programmable power source, which were controlled by a personal computer using software created by the authors in the LabView environment.

Determination of $R_{con}$ and was carried out according to the method shown in [18].

Monitoring of current monochromatic pulse responsitivity was carried out by method of comparing responsitivity of the investigated PD with a reference photodiode certified by the respective metrological service of the company. Measurements were performed when illuminating the PD with a radiation flux of a power of not over $1 \cdot 10^{-3}$ W; load resistance across the responsive element $R_l$= 10 kΩ,

To investigate the defective structure of the substrates chemical treatment was performed in selective Sirtle`s etchant [19] with the following composition: HF – 100 cm$^3$, $CrO_3$ – 50 g, $H_2O$ – 120 cm$^3$. Then the surface was examined in microscopes of different magnifications.

## RESULTS OF THE RESEARCH AND THEIR DISCUSSION

### A) Influence of dislocations on the dark currents of photodiodes

The volt-ampere characteristics of each RE of the studied photodiodes were obtained (Fig. 2). For comparison, the *I-V* characteristics of one serial standard sample are given ($PD_6$).

As can be seen from Figure 2, the studied photodiodes had a significant variation in the dark currents of the RE. To determine the causes of the $I_d$ unevenness, the PD crystals were processed in a Sirtle selective etchant (Fig. 3).

As can be seen from Figure 3, the photoiodines with a scatter of dark currents had an uneven density of dislocations on the surface of RE. In $PD_1$ and $PD_2$, in the areas of increased defectivity, the density of dislocations reached $N_{dis} \approx 10^{11}$-$10^{13}$cm$^{-2}$ (Fig. 4a). In $PD_3$-$PD_5$, in the areas of increased defectivity, the density of dislocations reached $N_{dis} \approx 10^8$-$10^9$ cm$^{-2}$ (Fig. 4b). In serial $PD_6$ $N_{dis} \approx 10^2$-$10^3$ cm$^{-2}$ (Fig. 4c). However, we want to note that the dark current of a photodiode does not depend on the actual density of dislocations on the surface of RE, since the determining component of the dark current of a PD is the volumetric generation-recombination component ($I_d^G$)[1], which is much larger than the surface generation component [12]. Accordingly, the location of dislocations is crucial. And a significant influence on the value of the recombination current will be made by defects located in the space charge region (SCR).

$$\mathrm{I}_d^G = \mathrm{e}\frac{n_i}{2\tau} W_i A_{\mathrm{RE}}, \tag{1}$$

where *e* is electron charge; $n_i$ is intrinsic concentration of charge carriers in the substrate; τ is lifetime of the minor charge carriers; $W_i$ is width of the space charge region, $A_{RE}$ is the area of responsive elements.

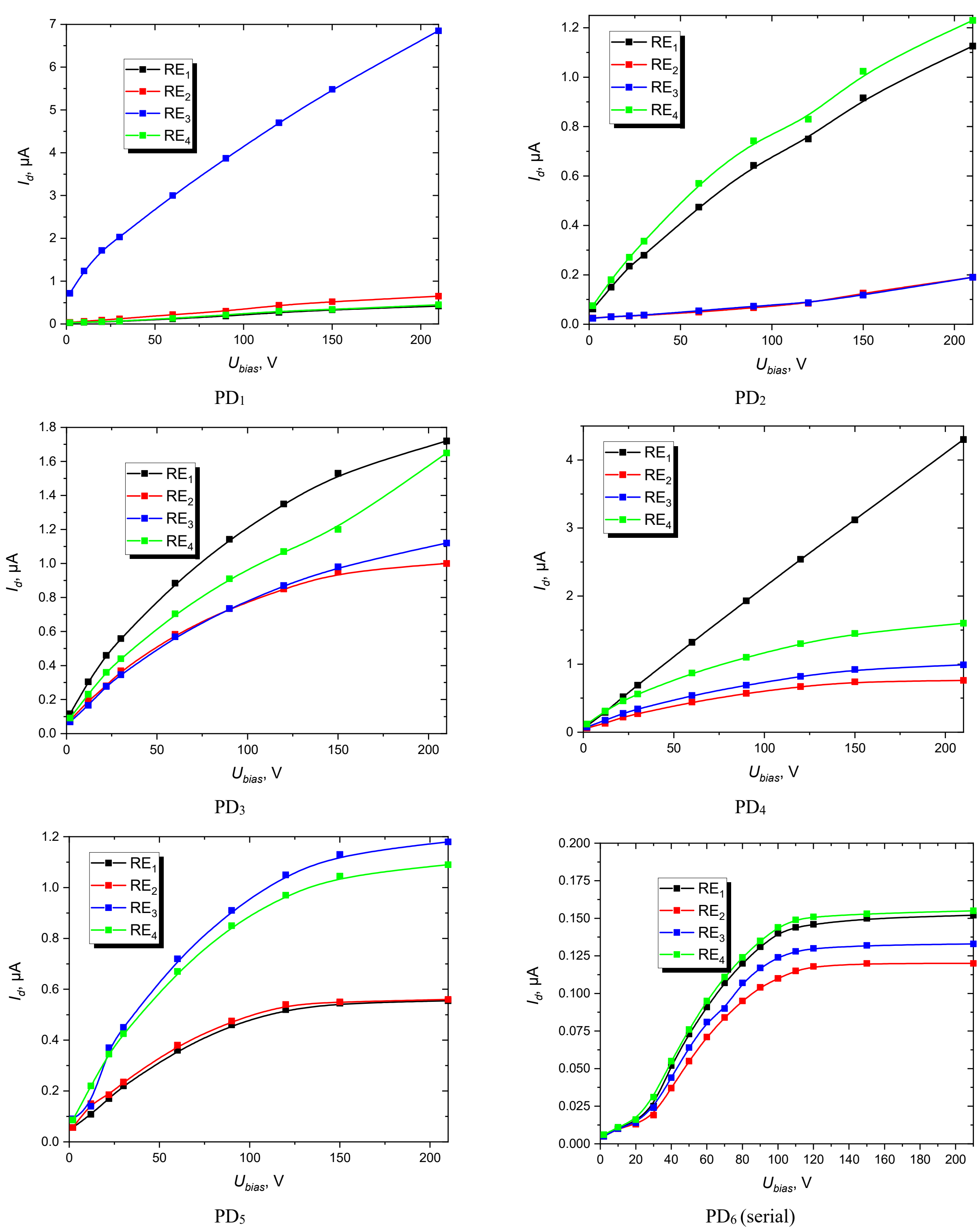


**Figure 2.** *I–V* characteristics of PDs

The depth of the dislocations can be determined by layer-by-layer silicon etching followed by selective etching. However, we found that the vast majority of dislocations formed as a result of phosphorus diffusion from planar solid-state sources are located in the diffusion layer. When doping substrates from liquid-phase phosphorus sources, dislocations may also be generated at some distance from the diffusion layer due to higher mechanical stresses caused by the high concentration of phosphorus atoms in the interstices of the silicon crystal lattice [13]. However, it is worth noting that dislocations formed as a result of growth defects or defects introduced during machining can cross the entire wafer and make a significant contribution to the value of dark currents by reducing the lifetime of minor charge carriers. In order to detect dislocations that cross the entire thickness of the silicon wafer, we also examined the reverse sides of the photodiode crystals under study (Fig. 5).

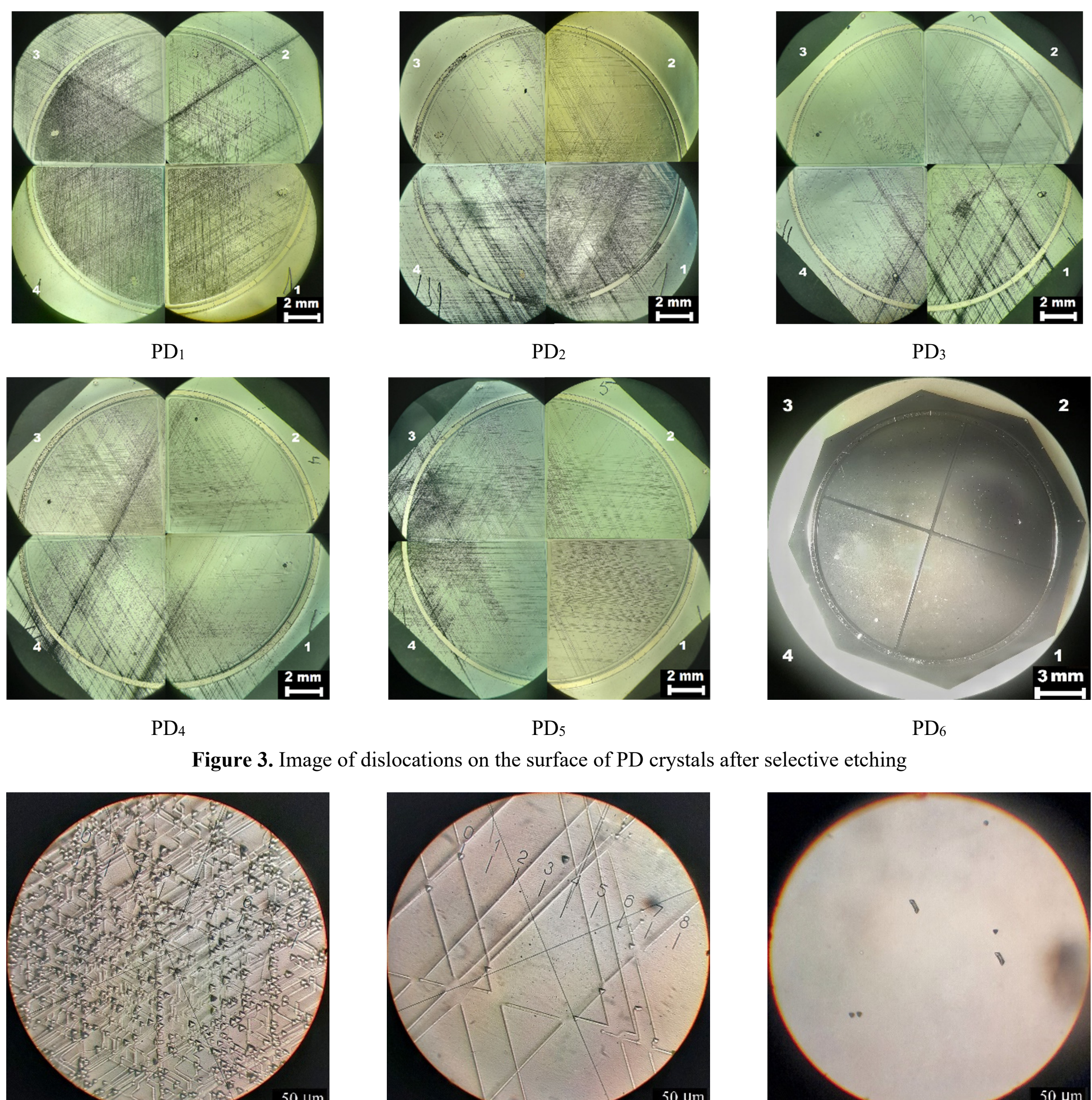


PD1 PD2 PD3

PD4 PD5 PD6

**Figure 3.** Image of dislocations on the surface of PD crystals after selective etching

**a** **b** **c**

**Figure 4.** Zones of increased density of dislocations at a magnification of x500 for: a) $PD_1$ and $PD_2$; b) $PD_3$-$PD_5$; c) $PD_6$

As can be seen from Fig. 5, RE with high dark currents had dislocation grids of increased density in the projections to the back side of wafers. This indicated the presence of dislocations in the entire thickness of the SCR of the RE with increased $I_d$. The REs of the studied PDs, which were not characterised by increased dark currents, also had some dislocation density on the front side, but given the absence of these defects on the back side of these REs, it can be assumed that they are not distributed over the entire thickness of the SCR and are located in the diffusion zone or near it.

In the case of the serial $PD_6$, only a small density of dislocations was found on the reverse side ($N_{dis} \leq 10^2$ $cm^{-2}$), which is typical for silicon after technological treatments. The spread of the dark currents of the serial photodiode was up to 20%, in contrast to the defective samples under study, where the spread could reach 2 or more times.

The effect of dislocations on the electrical parameters of photodiodes and the properties of p-n junctions can be manifested in two ways: first, the presence of dislocations can lead to the appearance of band gap levels due to the elastic stress fields associated with dislocations. Dislocations can serve as areas of charge carrier recombination, and accordingly, the presence of recombination centers in the depleted region of the *p-n* junction will be manifested in an increase in the generation currents with a reverse shift of the *p-n* junction. Secondly, a more important effect is the influence of dislocations on the properties of *p-n* junctions due to the accumulation of impurities on and around dislocations, since dislocations can accumulate impurities due to their elastic fields, a dislocation decorated with impurities crossing a *p-n* junction will lead to the penetration of a high density of generation-recombination centers in the space charge region of the *p-n* junction, which again leads to an increase in the generation currents in the SCR at the reverse bias [1].

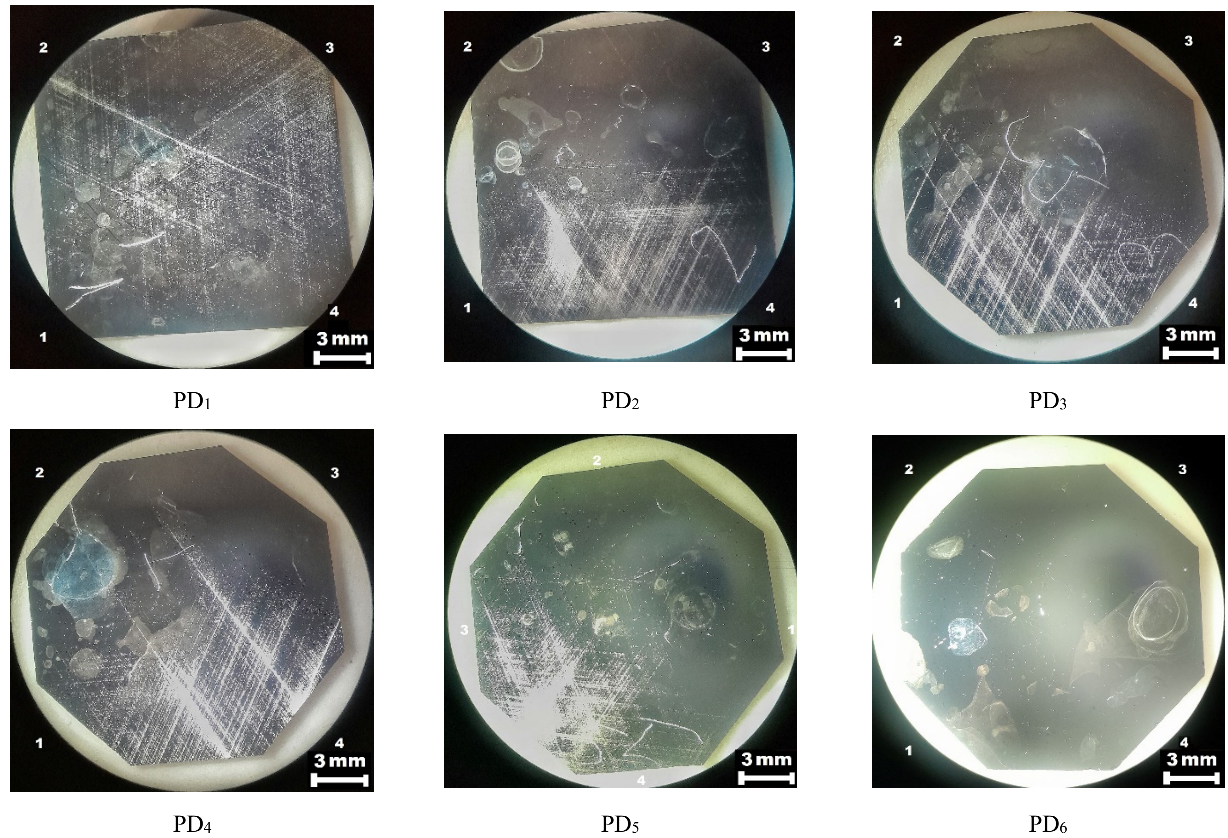


**Figure 5.** Dislocation structure of the back side of PD crystals

### B) The influence of dislocations on the insulation resistance between REs and the GR

A table of the insulation resistance of each REs of the studied PDs and the GR was obtained (Table 1).

**Table 1**. Values of $R_{con}$ of the studied PDs

| | $R_{con}$, MΩ | | | |
|---|---|---|---|---|
| | $RE_1$ | $RE_2$ | $RE_3$ | $RE_4$ |
| $PD_1$ | 30.8 | 2.5 | 20 | 31.7 |
| $PD_2$ | 20 | 40 | 26.7 | 12.5 |
| $PD_3$ | 1.5 | 6.9 | 7.4 | 2.8 |
| $PD_4$ | 3.6 | 6.7 | 6.7 | 1.4 |
| $PD_5$ | 4.8 | 3.7 | 1.4 | 2.8 |
| $PD_6$ | 8 | 6.7 | 7.1 | 8.3 |

As can be seen from Table 1, the $PD_1$-$PD_5$ had a certain scattering in the $R_{con.}$ It was found that the RE "connected" to the GR by dislocation lines have a reduced insulation resistance. No scattering of $R_{con.}$ was observed in the serial $PD_6$, since there are no dislocation lines crossing the RE and GR.

### C) The influence of dislocations on the responsivity of PD

When measuring the responsivity of the photodiodes, we also observed some unevenness of this parameter across the REs. This phenomenon will be studied in more detail on the example of $PD_5$ and $PD_6$.The dependence of the responsivity of each photodiode RE on the bias voltage is shown at Fig. 6.

As can be seen from Figure 6, the $S_{pulse}$ of each RE at a fixed voltage is different. It can also be seen that each curve reaches saturation at a different $U_{bias}$, although the maximum responsivity of the REs is approximately the same. Differences in responsivity values can be caused by differences in the lifetime of minor charge carriers due to different dislocation densities of each responsive element.

Note that the difference in the saturation voltage of responsivity can also be caused by the difference in the collection coefficient of minor charge carriers ($\gamma$) (2), which depends on the SCR width, which in turn depends on the material resistivity. The responsivity of the PD reaches saturation when the collection coefficient of the charge carriers reaches its maximum value, i.e. when all photogenerated charge carriers in the photodiode base are distributed by a *p-n* junction (3) [20].

$$\gamma = 1 - e^{-\alpha(W_i + L_n)}, \tag{2}$$

where $\alpha$ is the absorption index, $L_n$ is diffusion length of electrons

$$S_\lambda = (1 - R)TQ\sum\gamma\frac{\lambda_{op}}{1.24}, \tag{3}$$

where $R$ is the reflection coefficient, $T$ is the transmission coefficient of the input window or optical filter; $Q$ is the quantum output of the internal photo effect.

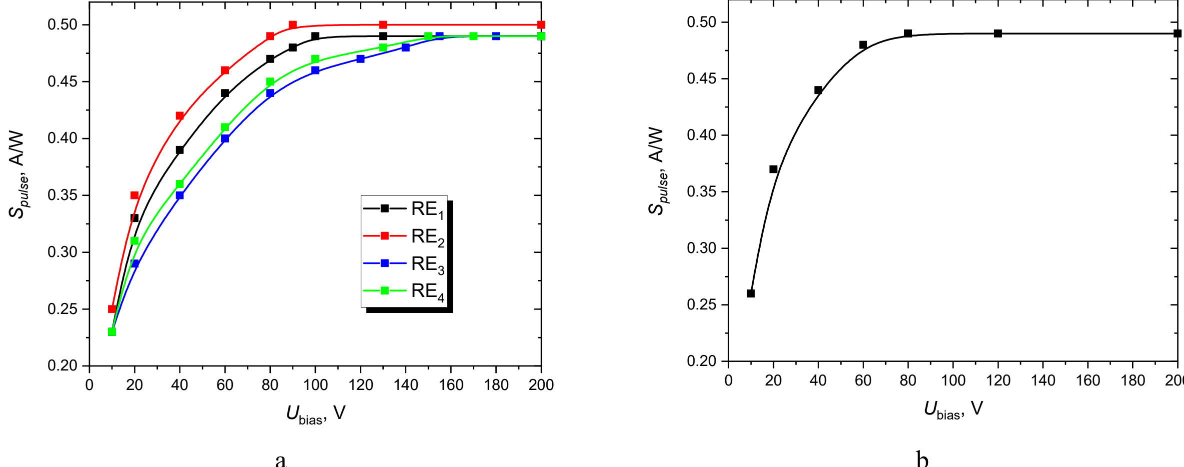


**Figure 6**. Dependence of the responsivity of RE on the bias voltage: a) $PD_5$; b) $PD_6$

The acquisition of the collection coefficient, and, accordingly, the responsivity, is possible when one of two conditions is met (4):

$$\begin{cases} X = L_n + W_i & (4.1) \\ X = W_i & (4.2) \end{cases}$$

where $X$ is the thickness of the high-resistance region of the photodiode (base).

To be able to differentiate between these two cases, it is necessary to consider the impulse characteristic of the PD (Fig. 7). In the case (4.2), when the $W_i$ is extended over the entire high-resistance region of the photodiode, the performance and inertial properties are determined by the drift mechanism of charge carrier transfer and the impulse characteristic will take the form shown in Fig. 7a.

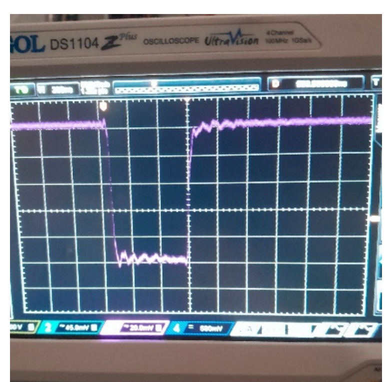


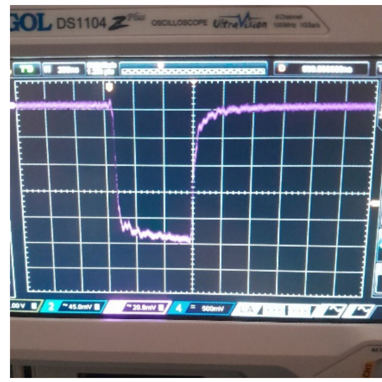


**Figure 7.** The pulse shape of the PD output signal: a) the case when the SCR occupies the entire high resistivity region of the PD; b) the case when the sum of the width of the SCR and $L_n$ is is equal to the $i$-region of the photodiode

Figure 7a shows the $S_{pulse}$ characteristic of $PD_5$ $RE_2$ at $U_{bias}$=130 V. With a decrease in the reverse $U_{bias}$, the $W_i$ decreases, but the responsivity does not decrease, since the diffusion mechanism of charge carrier transport begins to operate. The $S_{pulse}$ will start to decrease when $W_i$+$L_n$ is smaller than the $i$-region of the PD. In this case, the 4.1 condition is met at $U_{bias}$=90 V (Fig. 7b).

Knowing the thickness of the high-resistance region of the PD, which is $W_i$, formula (5)[21] can be used to determine the concentration of acceptors ($N_A$) in the $i$-region:

$$W_i = \left(\frac{2\varepsilon\varepsilon_0\,(\phi_c - U_{bias})}{eN_A}\right)^{\frac{1}{2}}, \tag{5}$$

where $\varepsilon$, $\varepsilon_0$ are dielectric constants for silicon and vacuum, respectively; $\varphi_c$ is contact potential difference.

Knowing the concentration of acceptors, and assuming that all impurities are ionized at room temperature ($p=N_A$), it is possible to determine the resistivity of silicon from the formula for the electrical conductivity of a *p*-type semiconductor [22]

$$\sigma = \frac{1}{\rho} = eN_A\mu_p. \tag{6}$$

Knowing $N_A$, it is possible to determine $W_i$ in the case corresponding to equation (4.1). For this, it is necessary to substitute the $U_{bias}$ corresponding to case (4.1) in equation (5). The difference in the SCR corresponding to cases 4.1 and 4.2 is the diffusion length of the minor charge carriers.

Using the given method of determining the $\rho$ and $L_n$, a table of data parameters for $PD_5$ was obtained (Table 2).

**Table 1.** Values of $\rho$ and $L_n$ each RE of $PD_5$

| Parameter | $RE_1$ | $RE_2$ | $RE_3$ | $RE_4$ |
|---|---|---|---|---|
| $\rho$, kΩ | 19.2 | 19.2 | 13.9 | 14.7 |
| $L_n$, µm | 60 | 80 | 35 | 30 |

As can be seen from Table 2, there is some variation in $\rho$ and $L_n$ of $PD_5$. If we compare the data obtained with the dislocation density in the same PD, we can see that the RE with a higher dislocation density have a lower $L_n$. This confirms the fact that the lifetime of minor charge carriers decreases with increasing dislocation density. It can also be seen from Table 2 that the $L_n$, of the RE are correlated with each other as dark current. It can also be seen that an increase in the dislocation density provokes a degradation of the resistivity. This, in turn, can contribute to the scattering of the $C_{RE}$, since the barrier capacity of a PD is determined by the $N_A$ and, accordingly, the $\rho$ of the Si (7)[21]:

$$C_{RE} = A_{RE}\left(\frac{\varepsilon\varepsilon_0 e N_A}{2(\phi_c - U_{bias})}\right)^{\frac{1}{2}}. \tag{7}$$

As for the serial $PD_6$, no responsivity variation was observed (Fig 6b). However, the $S_{pulse}$ reached saturation at slightly lower reverse bias voltages, which indicates a moderate degree of resistivity degradation. In this case, according to the calculation by the above method $\rho\approx 20.8$ kΩ and $L_n\approx 90$ µm. This photodiode had a much lower defect density and, as a result, slightly better final electrophysical characteristics of silicon, which provided better parameters than the studied defective samples.

## CONCLUSIONS

The effect of dislocations on the parameters of silicon four-quadrant *p-i-n* photodiodes was studied. The following conclusions were made during the research:

1) Mechanical stresses formed in plates formed during growth or mechanical processing of ingots provoke the formation of a high density of dislocations due to stress relaxation during thermal operations.

2) Formative defects are often placed unevenly on the plates and cause the unevenness of the parameters on the responsive elements.

3) The described defects often cross the entire wafer to form recombination centers in the space charge region of the photodiode.

4) The presence of recombination centers reduces the life time and diffusion length of minor charge carriers, as a result of which the parameters associated with the specified characteristics deteriorate.

**ORCID**

**Mykola S. Kukurudziak,** https://orcid.org/0000-0002-0059-1387

**REFERENCES**

[1] K.V. Ravi, *Imperfections and impurities in semiconductor silicon*, (Wiley, New York, 1981).
[2] E. Kamiyama, J. Vanhellemont, K. Sueoka, K. Araki, and K. Izunom, Applied Physics Letters, **102**(8), (2013). https://doi.org/10.1063/1.4793662
[3] M. Hourai, E. Asayama, H. Nishikawa, M. Nishimoto, T. Ono, and M. Okui, Journal of Electronic Materials, **49**, 5110 (2020). https://doi.org/10.1007/s11664-020-08203-w
[4] Y. Pavlovskyy, O. Berbets, and P. Lytovchenko, Physics and Chemistry of Solid State, **22**(3), 437-443 (2021). https://doi.org/10.15330/pcss.22.3.437-443
[5] S. Liu, X. Huang, Y. Wang, M. Xia, Q. Lei, and N. Zhou, Vacuum, **206**, 111533 (2022). https://doi.org/10.1016/j.vacuum.2022.111533
[6] M. Kivambe, B. Aissa, and N. Tabet, Energy Procedia, **130**, 7 (2017). https://doi.org/10.1016/j.egypro.2017.09.405
[7] Q. Lei, L. He, C. Tang, S. Liu, X. He, X. Li, and L. Zhou, Materials Science in Semiconductor Processing, **138**, 106318 (2022). https://doi.org/10.1016/j.mssp.2021.106318
[8] V.M. Lytvynenko, Bulletin of the Kherson National Technical University, **4**(87), 85-90 (2023). https://doi.org/10.35546/kntu2078-4481.2023.4.10
[9] A. Heintz, B. Ilahi, A. Pofelski, G. Botton, G. Patriarche, A. Barzaghi, and A. Boucherif, Nature Communications, **13**(1), 6624 (2022). https://doi.org/10.1038/s41467-022-34288-4
[10] A. Liu, S.P. Phang, and D. Macdonald, Solar Energy Materials and Solar Cells, **234**, 111447 (2022). https://doi.org/10.1016/j.solmat.2021.111447

[11] R. Hirose, T. Kadono, A. Onaka-Masada, R. Okuyama, K. Kobayashi, A. Suzuki, and K. Kurita, Materials Science in Semiconductor Processing, **135**, 106063 (2021). https://doi.org/10.1016/j.mssp.2021.106063
[12] M.S. Kukurudziak, Journal of nano- and electronic physics, **14**(4), 04015 (2022). https://doi.org/10.21272/jnep.14(4).0401
[13] M.S. Kukurudziak, Semiconductor Physics, Quantum Electronics & Optoelectronics, **25**(4), 385 (2022). https://doi.org/10.15407/spqeo25.04.385
[14] M.S. Kukurudziak, Surface Chemistry, Physics and Technology, **14**(2), 182 (2023). https://doi.org/10.15407/hftp14.02.182 (in Ukrainian)
[15] M.S. Kukurudziak, Surface Chemistry, Physics and Technology, **14**(1), 42 (2023). https://doi.org/10.15407/hftp14.01 (in Ukrainian)
[16] M.S. Kukurudziak, East Eur. J. Phys. (2), 311 (2023). https://doi.org/10.26565/2312-4334-2023-2-36
[17] D. Yang, and X. Ma, *Defects and Impurities in Silicon Materials. Handbook of Integrated Circuit Industry* (Springer, Singapore, 2024). https://doi.org/10.1007/978-981-99-2836-1_76
[18] M.S. Kukurudziak, Radioelectronic and Computer Systems, **105**(1), 92 (2023). https://doi.org/10.32620/reks.2023.1.07
[19] E. Sirtl, and A. Adler, Z. Metallk, **119**, 529 (1961). (in German)
[20] L.K. Buzanova, and A.Y. Gliberman, *Semiconductor photodetectors* (Energia, Moscow, 1976). (in Russian)
[21] N.M. Tugov, B.A. Glebov, and N.A. Charykov, *Semiconductor devices: Textbook for universities*, edited by V.A. Labuntsov, (Energoatomizdat, Moscow, 1990). (in Russian)
[22] S.M. Sze, *Physics of semiconductor devices*, (John Wiley & Sons, New York, 1981).

**ВПЛИВ СТРУКТУРНИХ ДЕФЕКТІВ НА ПАРАМЕТРИ КРЕМНІЄВИХ ЧОТИРИКВАДРАНТНИХ *p-i-n* ФОТОДІОДІВ**

**Микола С. Кукурудзяк[a,b]**
[a]*АТ «Центральне конструкторське бюро Ритм», 58032, м. Чернівці, вул. Головна, 244, Україна*
[b]*Чернівецький національний університет імені Юрія Федьковича, 58002, м. Чернівці, вул. Коцюбинського, 2, Україна*

У статті досліджено вплив структурних дефектів, зокрема дислокацій, на електричні та фотоелектричні властивості кремнієвих чотириквадрантних *p-i-n* фотодіодів. Встановлено, що ростові дефекти та дефекти, які утворюються при механічній обробці пластин, можуть перетинати всю підкладку та погіршувати параметри фотодіодів. Це явище особливо негативне через розміщення дефектів в області просторового заряду. У цьому випадку через наявність центрів рекомбінації в області просторового заряду зменшується час життя неосновних носіїв заряду, погіршується темновий струм і чутливість фотодіодів. Часто дефекти розміщені нерівномірно, що провокує нерівномірність параметрів на фоточутливих елементах. Також було побачено, що дислокаційні лінії, які перетинають чутливі елементи та захисне кільце, погіршують опір ізоляції зазначених активних елементів. Запропоновано метод визначення кінцевого питомого опору кремнію та довжини дифузії неосновних носіїв заряду шляхом дослідження форми імпульсу вихідного сигналу.

**Ключові слова:** *кремній; фотодіод; чутливість; точковий дефект; дислокація; темновий струм*

East European Journal of Physics. **2.** 353-357 (2024)
DOI:10.26565/2312-4334-2024-2-42 ISSN 2312-4334

# STRUCTURAL FEATURES OF SILICON WITH TIN IMPURITY

**Sharifa B. Utamuradova, Bakhodir B. Bokiyev, Dilorom S. Pulatova**
*Institute of Semiconductor Physics and Microelectronics at the National University of Uzbekistan, Tashkent, Uzbekistan*
**Corresponding Author e-mail: boqiyevb@gmail.com*
Received April 1, 2024; revised April 22, 2024; accepted May 10, 2024

In this work, samples of single-crystalline silicon doped with tin were studied using X-ray diffraction and electron microscopy. It has been established that at a scattering angle of $2\theta \approx 36.6°$ in the X-ray diffraction patterns of n-Si and Si<Sn> samples, structural reflections (110) of the corresponding $SiO_2$ nanocrystallites with lattice parameters $a = b = 0{,}4936$ нм и c = 0,5212 nm and c = 0.5212 nm, belonging to the hexagonal crystal lattice and space group $P3_21$. The formation of tin nanocrystallites with sizes of 9.1 and 8 nm in the near-surface regions of the Si<Sn> matrix crystal lattice was discovered.
**Keywords:** *Silicon; Tin; X-ray diffraction; Subcrystallite crystal lattice; Nanocrystallite*
**PACS:** 61.72. Ff, 61.72.Qq

## INTRODUCTION

As is known, a number of physical properties of semiconductor materials can change as a result of doping with various doping atoms [1-4]. In this case, it is important that the input atoms are evenly distributed throughout the volume. But with traditional doping methods, in particular, in the process of growing bulk single crystals, it is difficult to control a sufficient distribution of input atoms over the volume. This is why it is especially relevant to study how the input atoms are arranged in the crystal structure [5,6]. In addition, it is known that the degree of mono- and polycrystallinity of the silicon structure depends on the impurity composition, the perfection of the defect structure, the distribution of impurities and the lattice mismatch parameters of the matrix and alloying elements [7-10].

In connection with this, the purpose of this work was to study various structural parameters of Si doped with tin atoms using modern methods of X-ray diffraction studies.

## EXPERIMENTAL TECHNIQUE

The initial material was samples in the form of wafers made of single-crystalline n-type silicon with a resistivity of 40 Ω·cm, grown by the Czochralski method. The main disadvantages of growing single-crystal silicon using the Czochralski method include the increased content in the resulting crystals of background impurities of oxygen and carbon atoms with concentrations of up to $2 \cdot 10^{18}$ $cm^{-3}$ and up to $5 \cdot 10^{16}$ $cm^{-3}$, respectively. Among background impurities, the problem of the presence of oxygen atoms in silicon has remained very relevant for many years [11-14].

Doping silicon with tin atoms was carried out by diffusion from the gas phase at a temperature of 1100°C in quartz ampoules under a vacuum of 1 mTorr for 2 hours, followed by rapid cooling.

The structural and phase states of the samples under study were monitored using an Empyrean Malvern X-ray diffractometer. The OriginPro2019 program was used to determine the peak maximum. X-ray diffraction measurements were carried out in the Bragg–Brentano beam geometry in the scattering angle range $2\theta_b$ = from 10° to 90° continuously at a scanning speed of 0.33 degrees/min with an angular step of 0.0200 (deg).

## RESULTS AND DISCUSSION

In Figure 1a shows the X-ray diffraction pattern of the n-Si sample (ρ=40 Ω·cm), from which it follows that at small scattering angles (in the range $2\theta = 12° \div 20°$) there is a wide and low-intensity diffuse reflection on the X-ray pattern, as well as above the level of inelastic background, structural reflections with different intensities are observed. Typically, low-intensity diffuse reflection is due to the presence on the surface of n-Si samples of amorphous clusters with dimensions of 1÷1.5 nm, consisting of silicon oxide [8]. The silicon oxide layer on the surface of silicon samples reforms over time, so the amorphous layer is usually removed by chemical etching before the process of doping impurity atoms [15].

In the given X-ray diffraction patterns at scattering angles of $2\theta = 28{,}52°$ with d/n = 0.3138 nm and $2\theta = 95{,}2°$ with d/n = 0.1045 nm (n is the serial number of the plane and d is the interplanar distance) there are two structural reflections from lines of a selective nature with a main (111)Si peak with high intensity and a (333)Si peak with weak intensity, respectively. The structure line (333) is the third order of the high-intensity reflection (111). At a scattering angle of $2\theta = 25.68°$, the $\beta$ reflection component (111) is observed. Analysis of the above structural results showed that the surface of the n-Si sample wafers corresponds to the (111) crystallographic orientation.

Splitting of the structural reflection (111) into $\alpha_1$ and $\alpha_2$ components, having the values $I(\alpha_1) = 2I(\alpha_2)$, as well as its half-width (FWHM = $4.1 \cdot 10^{-3}$ rad) and high intensity ($3 \cdot 10^4$ $imp \cdot sec^{-1}$) indicates a high degree of perfection of the lattice of n-Si silicon samples (Fig. 2a).

*Cite as:* Sh.B. Utamuradova, B.B. Bokiyev, D.S. Pulatova, East Eur. J. Phys. 2, 353 (2024), https://doi.org/10.26565/2312-4334-2024-2-42
© Sh.B. Utamuradova, B.B. Bokiyev, D.S. Pulatova, 2024; CC BY 4.0 license

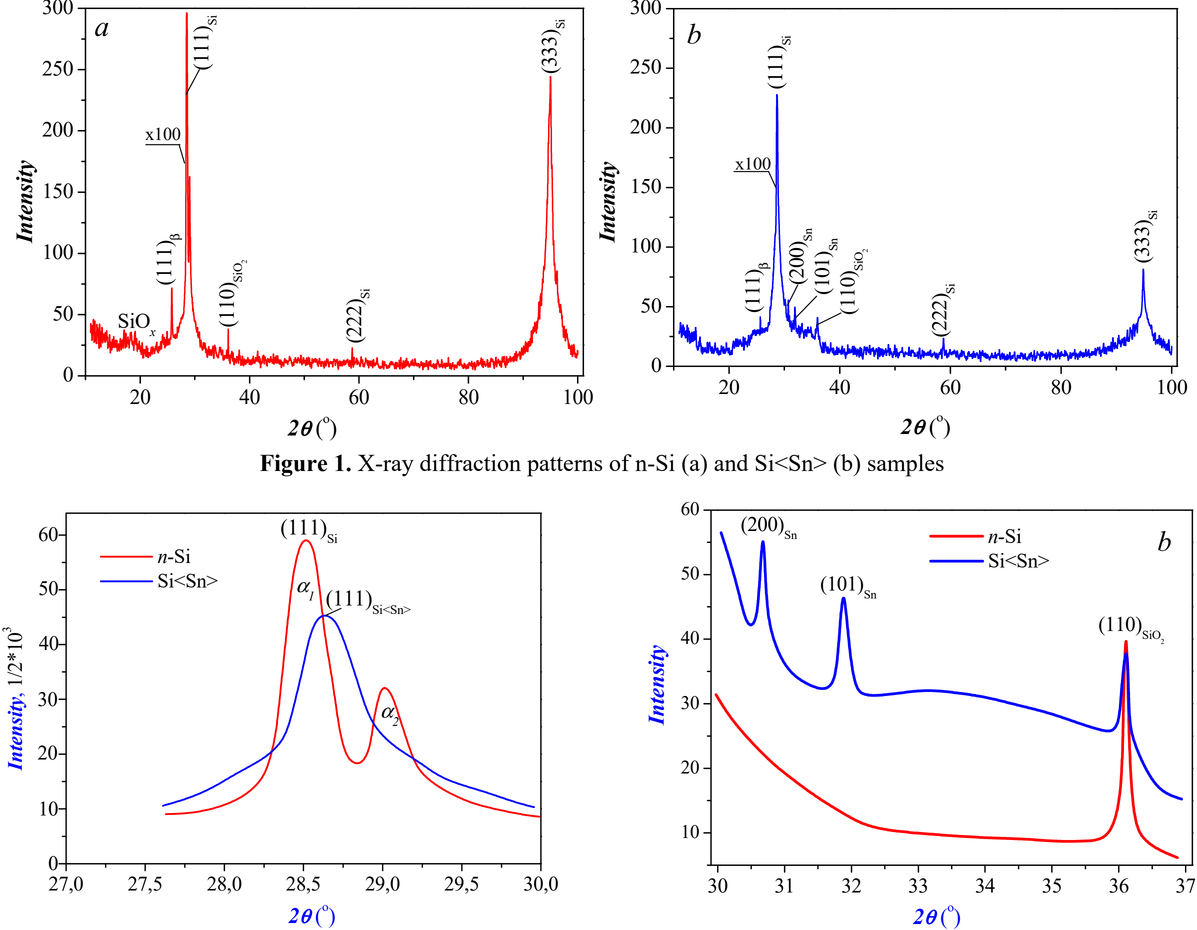


**Figure 1.** X-ray diffraction patterns of n-Si (a) and Si<Sn> (b) samples

**Figure 2.** Shapes of the main (111) selective reflections (a), as well as structural (200), (101) and (110) lines (b) on the X-ray diffraction pattern of n-Si and Si<Sn> samples

From the experimental data of the main reflection (111), it was determined that the average size (L) of subcrystallites (blocks) in n-Si samples is determined by the Selyakov–Scherrer formula:

$$L=K\cdot\lambda/\beta\cdot \mathrm{Cos}\theta, \quad (1)$$

where K is the dimensionless particle shape factor (Scherrer constant, which is equal to 0.94), $\lambda$ is the x-ray wavelength (0.154 nm), $\beta$ is the reflection width (111) at half maximum (in radians) and $\theta$ is the diffraction angle (Bragg angle), and the average size L = 6.5 nm.

Also, the lattice parameter of blocks in n-Si samples was determined from (111) reflections using the extrapolated Nelson-Riley function (x) [15]

$$x = 1/2(\mathrm{Cos}^2\theta/\mathrm{Sin}\theta+\mathrm{Cos}^2\theta/\theta), \quad (2)$$

using the following relationship:

$$y = kx + b, \quad (3)$$

where y is the lattice parameter, k is the slope of the linear trend. When extrapolating x→0 (θ = 90°), the value y = b corresponds to the “true” value of the lattice parameter, the value of which is 0.5439 nm.

In addition, at a scattering angle of 2θ = 58.68° with d/n = 0.1546 nm, the X-ray diffraction pattern of the n-Si sample contains the second (222) Si order of the main structural line (111). In [16], the reason for the appearance of diffraction reflection (222) in an X-ray diffraction pattern in a distorted lattice of single-crystal silicon was reported, and this reflection is a forbidden reflection according to the selection rules. The value is determined to be $15\cdot10^{-4}$ using the ratio I(222)/I(111) and this value is partially greater than $10^{-4}$. This indicates the appearance of an unsaturated bond under a nonuniformly distributed oxygen atom in the silicon lattice. Additional confirmation of the presence of inclusions of oxygen atoms in the silicon lattice is provided by the $SiO_x$ (amorphous) and $SiO_2$ (crystalline) forms formed in locally and defect-prone regions of the n-Si crystal lattice. Diffuse reflection related to the $SiO_x$ form is caused by amorphous phases of silicon oxide [17], and diffraction reflection (110) related to the $SiO_2$ form is observed at a scattering angle of $2\theta \approx 36.6°$ (with $d/n \approx 0.247$ nm) of the X-ray diffraction pattern. This indicates the formation of $SiO_2$ nanocrystallites at the interfaces between blocks in n-Si samples. The average size of these nanocrystallites was experimentally determined

by formula (1), which is 17 nm. The lattice parameter of quartz nanocrystalites at room temperature was also determined from the analysis of experimental results of (110) reflection using the expressions [18]:

$$\frac{1}{d^2(hkl)} = \frac{4}{3}\left[\frac{h^2+hk+k^2}{a^2}\right] + \frac{l^2}{c^2}, \tag{4}$$

$$and\ c = \frac{\lambda}{sin\theta}. \tag{5}$$

Here, taking into account h = 1, k = 1 and l = 0 from reflection (110), the last term of expression (4) is equal to zero, and from this expression a and b are determined by the following relation:

$$a = b = 2d\sqrt{\frac{1}{3}(h^2 + hk + k^2)}. \tag{6}$$

The lattice parameters are a = b = 0.4936 nm and c = 0.5212 nm, respectively, which in turn showed that the unit cell of these nanocrystalites belongs to the hexagonal crystal lattice and space group $P3_21$. Knowing the matrix lattice parameters of silicon and quartz nanocrystalites, it is possible to determine their specific volume, which differs by almost 23%. This, in turn, indicates that the elastic energy associated with structural defects arising at the local boundaries of silicon crystal matrix lattices as a result of the inhomogeneous distribution of oxygen is spent on the formation of nanocrystalites at the interfaces between blocks of n-Si samples. Therefore, a forbidden diffraction reflection of the second order (222) appeared in the X-ray diffraction patterns of n-Si samples under the influence of this process [16]. Low-intensity (222) reflection indicates the presence of minor local defects in the matrix lattices surrounding the formed nanocrystalites. If these nanocrystalites are not formed at the interfaces of blocks of n-Si samples, then in the diffraction pattern there is an expansion of the main structural line (111) and an increase in the second-order structural line (222), as well as defects leading to a change in the level of the inelastic background of the X-ray diffraction pattern, would be formed in the matrix lattice [19].

In Fig. 1-a and Fig. 1-b shows X-ray diffraction patterns of n-Si and Si<Sn> samples, which are very different from each other. Analysis and comparison of these drawings show that the intensity of the main reflection (111) in Si<Sn> samples at a scattering angle of $2\theta = 28.63^\circ$with d/n = 0.3144 nm decreased by 2 times and shifted towards larger angles ($\Delta\theta = 0.11°$), also the appearance of its $\beta$-component was observed at a scattering angle of $2\theta = 25.75^\circ$, respectively. This, in turn, indicates that due to the fact that silicon and tin are isovalent atoms, they are partially interchangeable in the matrix lattice of Si<Sn> samples, since the X-ray scattering intensity is proportional to the atomic number (Z) of the constituent elements [18].

The sufficiently maximum intensity and half-width (FWHM = 9.6 $10^{-3}$rad) of the main reflection (111) means that the Si<Sn> samples have a fairly perfect crystal structure and the direction of the surface of these samples corresponds to the crystallographic orientation (111). From the experimental data of the main reflection (111), it was determined that the lattice parameter of the blocks in the Si<Sn> samples according to formulas (2) and (3), which is equal to $a_{Si<Sn>}$ = 0.5435 nm. The mismatch of the crystal lattice parameters of the blocks in the n-Si and Si<Sn> samples was 0.00037 when determined using the following expression [20]:

$$\xi = 2\frac{a_{Si} - a_{Si<Sn>}}{a_{Si} + a_{Si<Sn>}}. \tag{7}$$

The average block size in Si<Sn> samples, estimated by formula (1) from the experimental results of this reflection, was 29.9 nm. However, although this structural reflex shifts towards larger angles and exhibits its asymmetry, it is not completely separated into its component $\alpha_1$ and $\alpha_2$ emissions (Fig. 2-b). This indicates that, as the authors of [21] note, elastic microdistortions of a growth nature arise during the diffusion of impurity atoms into the silicon crystal lattice in the temperature range 800ºC ÷ 1200ºC. As we noted above, due to the formation of such microdamages in the crystal lattice of Si<Sn> samples, a forbidden second-order reflection of the (222)Si main reflection is observed in the X-ray diffraction pattern at a scattering angle of $2\theta = 58.75^\circ$ with d/n = 0.1570 nm. In addition, the ratio I(222)/I(111) of I(111) intensity to I(222) intensity is $7.8\times10^{-4}$ and this value is 2 times less than the value determined for n-Si samples. This, in turn, indicates that the number of oxygen accumulations in tin-doped silicon samples is two times less than the number of accumulations in the crystalline form of n-Si samples.

In addition, due to the chemical treatment to remove the oxide layer from the n-Si surface before doping with tin atoms, which have the amorphous properties of silicon oxide, no diffusion reflection was observed in the X-ray diffraction patterns of the Si<Sn> samples. However, the authors of [17] showed that oxygen atoms do not have a large effect on the distortion of the silicon crystal lattice, but on the contrary, the formation of localized microdistortions in the silicon crystal lattice occurs due to the difference in the ionic radii of silicon (0.42 nm) and tin (0 .71 nm), located at the nodes. Note that in Fig. 2-a and 2-b, on the right side of the main reflection, a diffusion slope was observed, which, in turn, indicates the formation of stacking faults in the silicon crystal lattice, which are often encountered in many cases. In most cases, due to the difference between the covalent radius of a tin atom (RSn = 1.40Å) and the covalent radius of a silicon atom (RSi=1.14Å), they prefer to be located at nodes at the interfaces of silicon subcrystallites [23]. This, in turn, allows the

formation of new types of small tin nanocrystals of various sizes and crystallographic orientations in these places, preventing the occurrence of a large number of microdistortions in the silicon crystal lattice [24].

In addition, three more structure lines are observed above this diffusion reflection of the X-ray diffraction pattern at scattering angles of $2\theta$= 30.67°, $2\theta$= 31.84° и $2\theta$= 36.57° nm, respectively (see Fig. 2-a and 2-b). These structure lines are caused by tin nanocrystallite phases with crystallographic orientation (200) and (101) between the d/n = 0.2948 nm and d/n = 0.2814 nm planes. Also, a narrower ($1.58\times10^{-2}$rad) reflection (110) with d/n = 0.2469 nm, which belonged to silicon dioxide nanocrystallites with an average size of 14 nm. From these half-width values ($1.65\times10^{-2}$ rad) and ($1.88\times10^{-2}$ rad) (200) and (101) reflections, it was determined that the average sizes of these tin nanocrystallites, calculated by formula (1), were 9.1 nm and 8 nm respectively. This, in turn, indicates that the formation of tin nanocrystallites in the (101) and (200) crystallographic planes occur under the influence of the oriented matrix lattice of Si<Sn> (111) samples. This case leads to an increase in the consistency between tin nanocrystallites and silicon matrix lattices, as well as to an increase in the hardness of samples based on them [22].

In addition, tin nanocrystallites with sizes of 9.1 and 8 nm, formed on the matrix lattice of Si<Sn> samples, can exhibit quantum-size effects, which are of great interest in modern nanotechnologies. Therefore, using the expression

$$\lambda_D = \frac{1}{e}\sqrt{\frac{\varepsilon\varepsilon_0 kT}{n}}. \tag{8}$$

The value of the Debye length ($\lambda_D$) of screening for the samples under study was calculated, which is equal to 13.2 nm. Here, ε is the relative dielectric constant of Si<Sn> samples (ε = 11.7), $\varepsilon_0$ is the dielectric constant, k is Boltzmann's constant, T is temperature, e is the electron charge, n is the concentration of current carriers, in this case equal to $10^{17}$ $cm^{-3}$. The average size of tin nanocrystallites determined from experimental data is less than the Debye electron length.

Thus, we can conclude that tin atoms partially (in low concentrations) exchange places with silicon atoms, and the rest combine in the near-surface regions of the Si<Sn> samples, forming tin nanocrystallites. If tin atoms were replaced by homogeneous silicon atoms in the matrix crystal lattice, then the intensity of the main (111) and its third order (333) reflections should increase. However, in the X-ray diffraction patterns of Si<Sn> samples, a decrease in the intensity of structural reflections (111) and (333), as well as reflections related to tin nanocrystallites in other crystallographic orientations, was observed. This, in turn, indicates that tin atoms accumulate in defective regions of the silicon crystal lattice. Since in these regions of the lattice there is no saturation of the chemical bonds of the constituent atoms, they are considered high-potential nodes and are formed at the boundary sections of blocks belonging to the category of near-surface sections. The authors of the study [25] predicted that since the rate of diffusion of tin atoms through the surfaces and border regions of silicon is twice the rate of bulk diffusion, the penetrating atoms will easily move and accumulate in defective regions of the matrix lattice. Such diffusion processes cause the rapid formation of tin nanocrystallites in defective regions and block interfaces in Si<Sn> samples. The formation of such nanocrystallites at block boundaries in silicon samples may also be due to the fact that $E_{Sn\text{-}Sn}>E_{Si\text{-}Sn}$ и $E_{Sn\text{-}Sn}>E_{Si\text{-}Si}$.

$$\frac{1}{d^2(hkl)} = \frac{h^2+k^2}{a^2} + \frac{l^2}{c^2}, \tag{9}$$

$$and\ c = \frac{1}{\sqrt{3}}\frac{\lambda}{sin\theta}. \tag{10}$$

Here, taking into account that h = 1, k = 0 and l = 0 from reflection (200), the last term of expression (9) is equal to zero, and from this expression a is determined as follows;

$$a = d \cdot h, \tag{11}$$

and the lattice parameters are $a_{Sn}$ = 0.5831 nm and $c_{Sn}$ = 0.3412 nm, respectively. The unit cell of tin nanocrystallites has a body-centered tetragonal system corresponding to the space group $I4_1$/amd.

## CONCLUSIONS

Thus, it was found that in the X-ray diffraction patterns of n-Si and Si<Sn> samples, structural reflections (110) of the corresponding $SiO_2$ nanocrystallites (quartz nanoinclusions) are observed at scattering angles of $2\theta \approx 36.6°$ with sizes of 14 nm and 17 nm in the boundary regions of the samples. It has been established that the lattice parameters of the unit cells of these nanoinclusions belonging to the hexagonal crystal lattice and space group $P3_21$ are a = b = 0.4936 nm and c = 0.5212 nm. It was found that the intensity of the main reflection (111) at a scattering angle of $2\theta$= 28.63° with d/n = 0.3144 nm decreases by 23% and shifts toward larger angles (Δθ = 0.11°) due to a decrease in the parameters of the matrix crystal lattice samples of Si<Sn>, due to the interchangeability of silicon and tin atoms. It has been established that the sizes of tin nanocrystallites are 9.1 and 8 nm in the near-surface regions of the matrix lattice of Si<Sn> sample wafers. The unit cell of tin nanocrystallites has a tetragonal system with lattice parameters $a_{Sn}$ = 0.5831 nm and $c_{Sn}$ = 0.3412, corresponding to the space group $I4_1$/amd.

**ORCID**
**Sharifa B. Utamuradova,** https://orcid.org/0000-0002-1718-1122

**REFERENCES**

[1] B.S. Ahmed, B. Anissa, D. Radouan, N. Al Bouzieh, I.K. Durukan, and N. Amrane, East Eur. J. Phys. (1), 294 (2024), https://doi.org/10.26565/2312-4334-2024-1-26
[2] K.S. Daliev, S.B. Utamuradova, J.J. Khamdamov, and M.B. Bekmuratov, "Structural properties of silicon doped rare earth elements ytterbium," East European Journal of Physics, (1), 375–379 (2024). https://doi.org/10.26565/2312-4334-2024-1-37
[3] K.S. Daliev, S.B. Utamuradova, J.J. Khamdamov, and Z.E. Bahronkulov, "Electrophysical properties of silicon doped with lutetium," Advanced Physical Research, **6**(1), 42–49 (2024). https://doi.org/10.62476/apr61.49
[4] Kh.S. Daliev, and Z.M. Khusanov, East Eur. J. Phys. (1), 366 (2024), https://doi.org/10.26565/2312-4334-2024-1-35
[5] T.V. Kritskaya, V.N. Zhuravlev, and V.S. Berdnikov, "The ability to use an inert gas flow to control the qualitative characteristics of grown silicon single crystals," News from universities. Electronic materials, **22**(3), 158-167 (2019). https://doi.org/10.17073/1609-3577-2019-3-158-167
[6] Kh.S. Daliev, Z.E. Bahronkulov, and J.J. Hamdamov, East Eur. J. Phys. (4), 167 (2023), https://doi.org/10.26565/2312-4334-2023-4-18
[7] R.S. Madatov, A.S. Alekperov, F.N. Nurmammadova, N.A. Ismayilova, and S.H. Jabarov, East Eur. J. Phys. (1), 322 (2024), https://doi.org/10.26565/2312-4334-2024-1-29
[8] K.P. Abdurakhmanov, Kh.S. Daliev, Sh.B. Utamuradova, and N.Kh. Ochilova, "On defect formation in silicon with impurities of manganese and zinc," Applied Solar Energy (English translation of Geliotekhnika), **34**(2), 73–75 (1998). http://www.scopus.com/inward/record.url?eid=2-s2.0-77949325013&partnerID=MN8TOARS
[9] Z.T. Azamatov, M.A. Yuldoshev, N.N. Bazarbayev, and A.B. Bakhromov, "Investigation of Optical Characteristics of Photochromic Materials," Physics AUC, **33**, 139-145 (2023). https://cis01.central.ucv.ro/pauc/vol/2023_33/13_PAUC_2023_139_145.pdf
[10] V.N. Lozovsky, L.S. Lunin, and B.M. Seredin, "Features of silicon doping using the thermomigration method. News of higher educational institutions," Electronic materials, **18**(3), 179-188 (2015). https://doi.org/10.17073/1609-3577-2015-3-179-188
[11] K.A. Ismailov, Z.M. Saparniyazova, G.T. Kudeshova, G.A. Seytimbetova, and F.A. Saparov, East Eur. J. Phys. (1), 327 (2024), https://doi.org/10.26565/2312-4334-2024-1-30
[12] Sh.B. Utamuradova, Z.T. Azamatov, and M.A. Yuldoshev, Russian Microelectronics, **52**, Suppl. 1, S99-S103 (2023). https://doi.org/10.1134/S106373972360022X
[13] K.P. Abdurakhmanov, Sh.B. Utamuradova, Kh.S. Daliev, N.Kh. Ochilova, and Z.O. Olimbekov, "Study of the interimpurity interaction in silicon doped with platinum and iron," Applied Solar Energy (English translation of Geliotekhnika), **34**(2), 71–72 (1998).
[14] S.Z. Zainabidinov, Kh.S. Daliev, K.P. Abdurakhmanov, Sh.B. Utamuradova, I.Kh. Khomidjonov, and I.A. Mirzamurodov, "The influence of the impurities with deep levels on the iron behavior in silicon," Modern Physics Letters B, **11**(20), 909–912 (1997). http://dx.doi.org/10.1142/S0217984997001110
[15] K.V. Ravi, *Imperfections and impurities in semiconductor silicon*, (Wiley, New York, 1981). https://lib.ugent.be/catalog/rug01:001484099
[16] N.A. Hassan, W.H. Albanda, and M.H. Al-Timimi, East Eur. J. Phys. (3), 296 (2023), https://doi.org/10.26565/2312-4334-2023-3-28
[17] Z. He, X. Zhang, X. Wei, D. Luo, H. Ning, Q. Ye, R. Wu, et al., "Solution-Processed Silicon Doped Tin Oxide Thin Films and Thin-Film Transistors Based on Tetraethyl Orthosilicate," Membranes, **12**, 590 (2022). https://doi.org/10.3390/membranes12060590
[18] D. Comedi, O.H.Y. Zalloum, E.A. Irving, J. Wojcik, T. Roschuk, M.J. Flynn, and P. Mascher, "X-ray-diffraction study of crystalline Si nanocluster formation in annealed silicon-rich silicon oxides," Journal of Applied Physics, **99**(2), 023518 (2006). https://doi.org/10.1063/1.2162989
[19] D. Comedi, O.H.Y. Zalloum, E.A. Irving, J. Wojcik, T. Roschuk, M.J. Flynn, and P. Mascher, "X-ray-diffraction study of crystalline Si nanocluster formation in annealed silicon-rich silicon oxides," Journal of Applied Physics, **99**(2), 023518 (2006). https://doi.org/10.1063/1.2162989
[20] C.S.G. Cousins, L. Gerward, and J.S. Olsen, "Multiple diffraction in crystals studied by an X-ray energy-dispersive method," Physica status solidi (a), **48**(1), 113-119 (1978). https://doi.org/10.1002/pssa.2210480115
[21] Y.-H. Miao, H.-Y. Hu, J.-J. Song, R.-X. Xuan, and H.-M. Zhang, "Effects of rapid thermal annealing on crystallinity and Sn surface segregation of $Ge_{1-x}Sn_x$ films on Si (100) and Si (111)," Chinese Physics B, **26**(12), 127306 (2017). https://doi.org/10.1088/1674-1056/26/12/127306
[22] R.A. Puglisi, C. Vecchio, S. Lombardo, S. Lorenti, and M.C. Camalleri, "Charge transport in ultrathin silicon rich oxide/$SiO_2$ multilayers under solar light illumination and in dark conditions," Journal of Applied Physics, **108**(2), 023701 (2010). https://doi.org/10.1063/1.3463381
[23] I. Khidirov, editor, *Neutron diffraction*, (InTech, Rijeka, Croatia, 2012). http://www.intechopen.com/books/neutron-diffraction
[24] G. Will, *Powder Diffraction: The Riyetveld Method and the Two Stage Method of Determine and Refine Crystal Structures from Powder Diffraction Data*, (Springer, New York, 2005).

**ОСОБЛИВОСТІ БУДОВИ КРЕМНІЮ З ДОМІШКАМИ ОЛОВА**

**Шаріфа Б. Утамурадова, Баходір Б. Бокієв, Ділором С. Пулатова**
*Інститут фізики напівпровідників і мікроелектроніки Національного університету Узбекистану, Ташкент, Узбекистан*

У даній роботі методом рентгенівської дифракції та електронної мікроскопії досліджено зразки монокристалічного кремнію, легованого оловом. Встановлено, що при куті розсіювання $2\theta \approx 36.6°$ на дифрактограмах зразків n-Si та Si<Sn> спостерігаються структурні рефлекси (110) відповідних нанокристалітів $SiO_2$ з параметрами ґратки. a = b = 0,4936 нм і c = 0,5212 нм і c = 0,5212 нм, що належать до гексагональної кристалічної ґратки та просторової групи P321. Виявлено утворення нанокристалітів олова розміром 9,1 та 8 нм у приповерхневих областях кристалічної решітки матриці Si<Sn>.

**Ключові слова:** *кремній; олово; рентгенівська дифракція; субкристалітна кристалічна ґратка; нанокристаллiт*

East European Journal of Physics. 2. 358-361 (2024)
DOI:10.26565/2312-4334-2024-2-43 ISSN 2312-4334

# CVC STRUCTURE OF PtSi - Si<Pt>-M IN A WIDE RANGE OF TEMPERATURES

**Abdugafur T. Mamadalimov[a], Makhmudkhodja Sh. Isaev[b], Tokhirjon U. Atamirzaev[c], Shamsiddin N. Ernazarov[d], Mukhtor K. Karimov[e]**

*[a]Institute of Semiconductor Physics and Microelectronics at the National University of Uzbekistan, 20 Yangi Almazar st., Tashkent, Uzbekistan*
*[b]National University of Uzbekistan, Tashkent, Uzbekistan*
*[c]Namangan Engineering-Construction Institute, Namangan, Uzbekistan*
*[d]Tashkent Institute of Chemical Technology, Tashkent, Uzbekistan*
*[e]Urgench State University, Department of Physics, Urgench, Uzbekistan*
**Corresponding Author e-mail: isayevmahmd02@gmail.com*
Received April 4, 2024; revised May 2, 2024; accepted May 11, 2024

In this work the mechanism of current flow during illumination with $h\nu \geq E_g$ in the temperature range of 77÷300 K is considered. It is established that in the PtSi – Si<Pt>-M structure in the temperature range of 77÷270 K the regime of space charge limited currents (SCLC) is realized. The current-voltage characteristics of the structures show areas of linear and quadratic dependences of current on voltage, as well as areas of a sharp increase in current. These features of the current-voltage characteristic are explained by the presence of deep level structures and sticking levels for charge carriers in the base region. From the temperature dependence of the SCLC, the concentration of adhesion levels was determined to be equal to (1.8÷3) $10^{15}$ $cm^{-3}$ and the adhesion factor to be equal to $6.32\cdot10^{-2}$. In the temperature range 77÷115 K at voltages 0.2÷1 V, the current-voltage characteristic obeys the law $J \sim U^n$(n=3÷4), and above U – the law $J \sim U^6$, followed by a transition to the quadratic law.
**Key words:** *Structure; Diffusion; Concentration; Level of Adhesion; Photoconductivity; Trap; Injection; Silicide; Silicon; Platinum*
**PACS:** 33.20.Ea, 33.20.Fb

## INTRODUCTION

Currently, complex theoretical and practical work is being carried out on the research of optical and electro-optical properties of various wide bandgap materials [1-3].

The world's leading research institutes are studying the physical processes occurring in the bulk of monocrystalline silicon after doping with impurities, creating deep levels [4-9]. In such crystals, the surface layer with a thickness of 150-200 microns were considered to be damaged and of no practical interest.

However, for an in-depth study of the process of diffusion doping of silicon with metals and atoms of rare earth elements [10,11], it is relevant to consider such important issues as the physics of the formation of a heavily doped surface and near-surface region, the nature of the formation of metal silicides, which are very different from the metal and semiconductor, as well as the mechanism of current flow through the near-surface region and the bulk part of the crystal [12,13].

Therefore, in this work, the current-voltage characteristics (CVC) were studied through a structure consisting of a near-surface and bulk part of diffusion-doped silicon with platinum atoms.

## EXPERIMENTAL PART

To dope silicon with platinum, single-crystal silicon ingots of p-type KDB-10 grade, grown by the Czochralski method, were used. Their initial parameters are as follows: for p-type silicon, resistivity ρ = 10 Ohm·cm, hole mobility $\mu_p$ = 430 $cm^2$ / V·s, hole concentration $n_p = 1.5\cdot10^{15}$ $cm^{-3}$, oxygen concentration $\leq 1\cdot10^{15}$ $cm^{-3}$.

Samples in the form of a parallelepiped with dimensions of 1.5×5×12 $mm^3$ were cut from single-crystal silicon ingots using a diamond disk. The samples were ground using silicon carbide micropowder M-5, M-10. In order to remove the surface layer damaged during grinding, the samples were degreased in toluene at a temperature 40-50 °C and subjected to chemical etching in a solution of 1HF:5$HNO_3$ for 1÷2 minutes, washed in deionized water and dried at a temperature of no more than 100 °C. Silicon samples were placed in quantities of 3 in quartz ampoules, previously washed in a solution of $HNO_3$÷3HCl and boiled in distilled water [14].

Metal powder of 99.999 purity in an amount of 3÷5 mg was placed into the ampoule. Ampoules with samples and diffusant were evacuated to a vacuum of ~$10^{-3}$ mm Hg ($1.33\cdot10^{-1}$ Pa) and sealed. Then the ampoules were placed in a horizontal oven and annealed at a temperature of 950÷1000 °C for 50 minutes up to 2 hours. Temperature fluctuations in the working area of the furnace did not exceed ±5 °C. After annealing, the samples were quenched by cooling at a rate of 100-150 degrees/s by dropping the ampoules into water and kept to a crystal temperature of T = 15-20 °C. After opening the ampoules, the surface of the samples had p-type conductivity.

Due to the fact that the samples had a surface layer with high conductivity, to eliminate its shunting effect, the samples were ground off on three sides to a depth of about 40-50 μm. Electrical contacts were connected to two opposing

***Cite as:*** A.T. Mamadalimov, M.Sh. Isaev, T.U. Atamirzaev, Sh.N. Ernazarov, M.K. Karimov, East Eur. J. Phys. 2, 358 (2024), https://doi.org/10.26565/2312-4334-2024-2-43
© A.T. Mamadalimov, M.Sh. Isaev, T.U. Atamirzaev, Sh.N. Ernazarov, 2024; CC BY 4.0 license

unpolished highlanders, and measurements were taken on the unpolished surface lying between them while successively removing thin layers. It turned out that the conductivity profiles have two sections: the near-surface area with increased conductivity and the volume area with conductivity close to its own. Parallel measurements of conductivity and the Hall effect [15] at temperatures T=77÷300 K showed that the near-surface layer has p-type conductivity, with a carrier concentration of ~$10^{20}$÷$10^{21}$ cm$^{-3}$ and Hall mobility $\mu_H$=2÷6 cm$^2$/V·s and volumetric – i-type conductivity, with carrier concentration $10^{10}$÷$10^{12}$ cm$^{-3}$ and mobility $\mu_H$=300÷400 cm$^2$/V·s.

The measurement results showed that the near-surface anomalous layer has a carrier concentration of ~$10^{20}$÷$10^{21}$ cm$^{-3}$ and a Hall mobility of 1÷17 cm$^2$/V·s. Calculations have shown that the surface layers of Si<Pt> with a thickness of 1÷5 μm have a specific conductivity of (1.6÷9.9)·$10^3$ (Ohm·cm)$^{-1}$.

## RESULTS AND DISCUSSION

PtSi-Si<Pt>-M structures were fabricated based on diffusion-doped silicon with platinum. The blocking contact was created by applying NiGa or AlGa alloys to the side surface of the base area of the structures or by pressing a metal contact on the same surface. When this structure is formed, the Longini-Green mechanism occurs, which consists in the fact that the base region becomes highly resistive. Therefore, at low temperatures, when the level of thermal generation is low, an analogue of the structure is a dielectric diode.

The current-voltage characteristics of the structure were studied at different temperatures. Carriers injected from the contacts will fill stationary charged centers (SCCs) in the space charge region (SCR) [12]. From the solution of the equation, it follows that the length of the SCR is proportional to $\sqrt{N_{SCC}}$, i.e. with a decrease in the concentration of immobile charged centers ($N_{SCC}$), the length of the SCR increases and, ultimately, the length of the high-resistivity region W decreases. At sufficiently small W, when the base is considered thin, the regime of space charge limited currents (SCLC) will be realized in the structure.

The dark current-voltage characteristic of structures at T = 300 K is linear (Ohm's law is satisfied) throughout the entire range of applied voltage. However, when the temperature of the samples is lowered to T = 77 K in the dark at biases U > 10 V, the value of the dark current decreases to 10÷12 A, which makes it impossible to measure the current-voltage characteristic [13-16]. Therefore, in order to study the injecting properties of contacts, current-voltage characteristics were measured by photoexcitation with hν = 1.4 eV both in the near-contact and in the middle parts of the base region of the structures. In this case, the power of the incident local radiation did not exceed 1÷2 mW.

Figure 1 (curve 1) shows the direct current-voltage characteristic curve and curves 2–5 show a family of reverse current-voltage characteristics in the temperature range T=77÷145 K, and Figure 2 shows the direct current-voltage characteristic (curve 1) and the reverse one (curve 2–6) in the temperature range from 160 K to 300 K. As can be seen from the curves above, at U = 10 V the photocurrent increases with decreasing temperature.

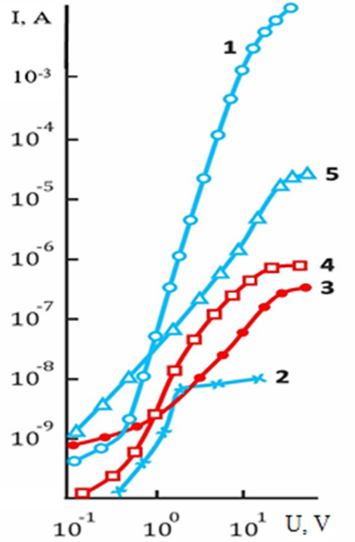


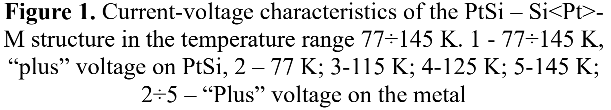

**Figure 1.** Current-voltage characteristics of the PtSi – Si<Pt>-M structure in the temperature range 77÷145 K. 1 - 77÷145 K, "plus" voltage on PtSi, 2 – 77 K; 3-115 K; 4-125 K; 5-145 K; 2÷5 – "Plus" voltage on the metal

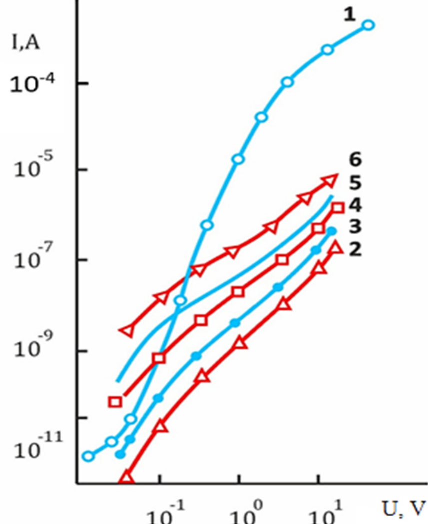


**Figure 2.** Current-voltage characteristics of the PtSi – Si<Pt>-M structure in the temperature range 160÷300 K. 1 - 160÷300 K, "Plus" voltage on PtSi, 2 – 160 K, 3 – 180 K, 4 – 250 K, 5 - 270 K, 6 – 300 K

Starting from a temperature of 250 K and below, a change in the course of the current-voltage characteristic curves is observed: for the curve at T = 250 K, a section J ~ $V^{3.3}$ is observed, followed by a section with a quadratic dependence, and for temperatures below 180 K on the current-voltage characteristic there are sections of a sharp increase in current and quadratic dependence of current on applied voltage. The transition voltage, starting from which the section of sharp increase in current turns into a quadratic section, does not depend on the temperature in the region T = 77÷250 K.

The current-voltage characteristics at T=300 K were almost symmetrical and linear. Under illumination with hν>1.2 eV, an increase in the photocurrent by 5–6 times relative to the dark current is observed in the case when a positive bias is applied to the silicide contact, and approximately 2 times with reverse polarity.

At low temperatures, a current-voltage characteristic characteristic of an SCLC with ohmic, quadratic sections and sections of a sharp increase in current is observed, followed by a transition again to quadratic sections. Another proof of the SCLC mode in such structures is that the electric field with a physical base length of 45 μm (determined from capacitance measurements) at biases of 10÷15 V has a value characteristic of this mode of ~$10^3$ V/cm.

The presence of a vertical section preceding the quadratic section gives grounds to believe that there are monoenergetic levels of attachment for holes located significantly below the quasi-Fermi level F, i.e. condition is met $(F-E_t)/kT>>1$, because up to the voltage of completely filled traps ($U_{CFT}$), all attachment levels for holes are occupied by electrons. In hole high-resistivity silicon, levels below the equilibrium Fermi level are occupied by electrons, i.e. "empty" for holes, so $P_{t,o}=N_t$.

In this case, the concentration of adhesion levels is equal to $(1.8÷3)\cdot10^{15}$ cm$^{-3}$, the adhesion factor is equal to $6.32\cdot10^{-2}$. Traps are sticking levels for holes, and the presence of such sticking levels is evidenced by the fact that long-term relaxation of photoconductivity and residual conductivity, as well as thermally stimulated conductivity, are observed in these structures.o dope silicon with platinum, single-crystal silicon ingots of p-type KDB-10 grade, grown by the Czochralski method, were used. Their initial parameters are as follows: for p-type silicon, resistivity ρ = 10 Ohm·cm, hole mobility $\mu_p$ = 430 cm$^2$ / V·s, hole concentration $n_p = 1.5\cdot10^{15}$ cm$^{-3}$, oxygen concentration $\le1\cdot10^{15}$ cm$^{-3}$.

## CONCLUSION

As a result of the scientific research, we came to the following important scientific conclusions:

1. The current-voltage characteristics of PtSi – Si<Pt>-M structures in the temperature range 77÷300 K were studied.
2. In the range T = 125÷160 K in the voltage range above 1 V, $J \sim U^6$ is observed.
3. In the range T=160 ÷ 250 K, the power-law dependence $J \sim U^6$ turns into $J \sim U^3$ in the voltage range 0.1 – 1 V; in this case, U > 1 V, the quadratic dependence remains.
4. Above 250 K, the direct and reverse branches of the current-voltage characteristic transition to a linear law.

**ORCID**

**Makhmudkhodja Sh. Isaev,** https://orcid.org/0009-0007-9559-5834

## REFERENCES

[1] Sh.B. Utamuradova, Z.T. Azamatov, M.A. Yuldoshev, N.N. Bazarbayev, and A.B. Bakhromov, "Investigations of Nonlinear Optical Properties of Lithium Niobate Crystals," East Eur. J. Phys. (4), 147 (2023), https://doi.org/10.26565/2312-4334-2023-4-15
[2] Sh.B. Utamuradova, Z.T. Azamatov, and M.A. Yuldoshev, Russian Microelectronics, **52**(Suppl. 1), S99-S103 (2023). https://doi.org/10.1134/S106373972360022X
[3] Z.T. Azamatov, M.A. Yuldoshev, N.N. Bazarbayev, and A.B. Bakhromov, "Investigation of Optical Characteristics of Photochromic Materials," Physics AUC, **33**, 139-145. (2023). https://cis01.central.ucv.ro/pauc/vol/2023_33/13_PAUC_2023_139_145.pdf
[4] B.A. Lombo, "Deep levels in semiconductors," S. Can. J. Chem. **63,** 1666 (1985). http://dx.doi.org/10.1139/v85-279
[5] A.A. Lebedev, "Deep level centers in silicon carbide: A review," Semiconductors, **33**(2), 107-130 (1999). https://doi.org/10.1134/1.1187657
[6] K.P. Abdurakhmanov, Sh.B. Utamuradova, Kh.S. Daliev, S.G. Tadjy-Aglaeva, and R.M. Érgashev, "Defect-formation processes in silicon doped with manganese and germanium," Semiconductors, **32**(6), 606–607 (1998). https://doi.org/10.1134/1.1187448
[7] Kh.S. Daliev, Sh.B. Utamuradova, O.A. Bozorova, and Sh.Kh. Daliev, "Joint effect of Ni and Gf impurity atoms on the silicon solar cell photosensitivity," Applied Solar Energy (English translation of Geliotekhnika), **41**(1), 80–81 (2005). https://www.researchgate.net/publication/294234192_Joint_effect_of_Ni_and_Gf_impurity_atoms_on_the_silicon_solar_cell_photosensitivity
[8] K.S. Daliev, S.B. Utamuradova, J.J. Khamdamov, and M.B. Bekmuratov, "Structural properties of silicon doped rare earth elements ytterbium," East European Journal of Physics, (1), 375–379 (2024). https://doi.org/10.26565/2312-4334-2024-1-37
[9] S.B. Utamuradova, S.Kh. Daliev, E.M. Naurzalieva, and X.Yu. Utemuratova, "Investigation of defect formation in silicon doped with silver and gadolinium impurities by raman scattering spectroscopy," East European Journal of Physics, (3), 430–433 (2023). https://doi.org/10.26565/2312-4334-2023-3-47
[10] Kh.S. Daliev, Sh.B. Utamuradova, O.A. Bozorova, and Sh.Kh. Daliev, "Joint influence of impurity atoms of nickel and hafnium on photosensitivity of silicon solar cells," Geliotekhnika, **1**, 85–87 (2005). https://www.researchgate.net/publication/294234192_Joint_effect_of_Ni_and_Gf_impurity_atoms_on_the_silicon_solar_cell_photosensitivity
[11] M.Sh. Isaev, I.T. Bozarov, and A.I. Tursunov, "Investigation of thermally stimulated conductivity of cobalt silicide," E3S Web of Conferences, **402**, 14019 (2023). https://doi.org/10.1051/e3sconf/202340214019
[12] M.Sh. Isaev, T.U. Atamirzaev, M.N. Mamatkulov, U.T. Asatov, and M.A. Tulametov, "Study of the mobility and electrical conductivity of chromium silicide," East European Journal of Physics, (4), 189–192 (2023). http://dx.doi.org/10.26565/2312-4334-2023-4-22
[13] N.A. Turgunov, E.Kh. Berkinov, and R.M. Turmanova, "The effect of thermal annealing on the electrophysical properties of samples n-Si<Ni,Cu>," East European Journal of Physics, (3), 287–290 (2023). https://doi.org/10.26565/2312-4334-2023-3-26
[14] P.R. Berger, G. Gulyamov, M.G. Dadamirzaev, M.K. Uktamova, and S.R. Boidedaev, "Influence of microwave and magnetic fields on the electrophysical parameters of a tunnel diode," Romanian journal of physics, **69**, 609 (2024). https://rjp.nipne.ro/accpaps/594CF41F1C91CCE710E9B3070FF760461CC68693.pdf

[15] J.J. Liou, "Non-quasi-static capacitance of p/n junction space-charge regions," Solid-State Electronics, **31**(1), 81-86 (1998). http://dx.doi.org/10.1016/0038-1101(88)90088-3
[16] S.B. Utamuradova, S.Kh. Daliev, S.A. Muzafarova, K.M. Fayzullaev, "Effect of the diffusion of copper atoms in polycrystalline CdTe films doped with Pb atoms," East European Journal of Physics, (3), 385–390 (2023). https://doi.org/10.26565/2312-4334-2023-3-4

**СТРУКТУРА ВАХ PtSi - Si<Pt>-M В ШИРОКОМУ ДІАПАЗОНІ ТЕМПЕРАТУР**

**Абдугафур Т. Мамадалімов[a], Махмудходжа Ш. Ісаєв[b], Тохірджон У. Атамірзаєв[c], Шамсиддін Н. Ерназаров[d], Мухтор К. Карімов[e]**
[a]*Інститут фізики напівпровідників і мікроелектроніки Національного університету Узбекистану, вул. Янги Алмазара, 20,*
[b]*Національний університет Узбекистану, Ташкент, Узбекистан*
[c]*Наманганський інженерно-будівельний інститут, Наманган, Узбекистан*
[d]*Ташкентський хіміко-технологічний інститут, Ташкент, Узбекистан*
[e]*Ургенчський державний університет, кафедра фізики, Ургенч, Узбекистан*

У роботі розглянуто механізм протікання струму при освітленні з hν≥Eg в інтервалі температур 77÷300 К. Встановлено, що в структурі PtSi – Si<Pt>-M в інтервалі температур 77÷270 К реалізується режим обмежених струмів об'ємного заряду (СКЗ). На вольт-амперних характеристиках конструкцій спостерігаються ділянки лінійної та квадратичної залежності струму від напруги, а також області різкого зростання струму. Ці особливості вольт-амперної характеристики пояснюються наявністю структур глибокого рівня та рівнів прилипання носіїв заряду в базовій області. За температурною залежністю СКЛК визначено концентрацію рівнів адгезії (1,8÷3) ·1015 см-3 і коефіцієнт адгезії 6,32·10-2. В інтервалі температур 77÷115 К при напругах 0,2÷1 В вольт-амперна характеристика підкоряється закону J ~ Un(n=3÷4), а вище U – закону J ~ U6 з наступним переходом до квадратичний закон.

**Ключові слова:** *структура; дифузія; концентрація; рівень адгезії; фотопровідність; пастка; ін'єкція; силіцид; кремній; платина*

East European Journal of Physics. 2. 362-365 (2024)
DOI:10.26565/2312-4334-2024-2-44 ISSN 2312-4334

# STUDY OF THE THERMOELECTRIC PROPERTIES OF CHROME SILICIDES

**Abdugafur T. Mamadalimov[a], Makhmudkhodja Sh. Isaev[b]*, Ismoil T. Bozarov[c], Alisher E. Rajabov[d], Sojida K. Vakhabova[e]**
*[a]Institute of Semiconductor Physics and Microelectronics at the National University of Uzbekistan, Tashkent, Uzbekistan*
*[b]National University of Uzbekistan, Tashkent, Uzbekistan*
*[c]Tashkent Institute of Chemical-Technology, Tashkent, Uzbekistan*
*[d]Urgench branch of Tashkent University of Information Technologies named after Muhammad al-Khwarizmi, Uzbekistan*
*[e]Namangan Engineering-Construction Institute, Namangan, Uzbekistan*
**Corresponding Author e-mail: isayevmahmd02@gmail.com*
Received April 2, 2024; revised May May 2, 2024; accepted May 11, 2024

The temperature dependences of the thermoelectromotive force of chromium mono and disilicides in the temperature range 200°C÷+600°C have been studied. For chromium disilicide, the dependence of the thermopower coefficient (α) on temperature (T) has three sections. Chromium monosilicide is characterized by a smooth increase in thermopower with increasing temperatures up to 200°C, and then its constancy. It was revealed that silicides rich in chromium atoms have lower thermopower values than silicides rich in silicon. The maximum thermo-EMF values of 110 μV/K and 190 μV/K were observed for chromium mono- and disilicides, respectively. It was revealed that for chromium silicides the dependence of the dimensionless parameter Q = Z·T on temperature is linear. The possibility of predicting the technology of synthesis of semiconductor material with optimal thermoelectric properties using the dependence of thermopower on conductivity and the parameter Q on temperature is shown.
**Keywords:** *Silicide; Thermal EMF; Hall Mobility; Doping; Saturation; Electrical Conductivity; Phase Diagram; Temperature Gradient*
**PACS:** 33.20.Ea, 33.20.Fb

## INTRODUCTION

One of the pressing problems of microelectronics is the study of physical processes occurring in the surface and near-surface regions of silicon, diffusion-doped with impurities that create deep levels [1-6]. In the near-surface region of diffusion-doped silicon with chromium atoms, the formation of chromium silicides was revealed.

As is known [7-10], transition metal silicides are becoming the base material for new promising technological schemes of future generations due to their resistance to aggressive environments and high-temperature treatments. Therefore, a comprehensive study of the mechanism by which impurities enter the crystal volume and their interaction with both matrix atoms of the crystal and technological impurities is relevant.

From this point of view, the study of the formation of chromium silicides in the near-surface region of silicon during diffusion doping and the study of their thermal properties is of particular scientific importance in the context of the creation of new materials for micro- and nanoelectronics [11-15].

These materials will be used in thermal converters of spacecraft, in the petrochemical industry, in the energy sector and other industries.

In this regard, in this work, we studied the conductivity distribution profile of diffusion-doped silicon with chromium atoms and studied their temperature dependence of thermopower.

## EXPERIMENTAL PART

To dope silicon with chromium, single-crystal p-type silicon ingots of the KDB-10 brand, grown by the Czochralski method, were used. Their initial parameters: resistivity 10 Ohm·cm, hole mobility 430 $cm^2$/V·s, hole concentration $1.5\cdot10^{15}$ $cm^{-3}$. Chromium powder in an amount of 5 ÷ 6 mg was placed in the ampoule near the crystals. The ampoule with samples and diffusant was evacuated to a vacuum of ~$10^{-3}$ mmHg. and soldered it.

The ampoules were placed in a horizontal diffusion oven and annealed at a temperature of 950-1020°C using laser irradiation for 30 minutes to 2 hours. Temperature fluctuations in the working furnace did not exceed ±5°C. After annealing, the samples were quenched by cooling at a rate of 100-150 K/s by dropping the ampoules into a vessel with water rotating at 33 rpm and kept to room temperature [16-19].

## RESULTS AND DISCUSSION

The temperature dependences of the thermoelectromotive force of chromium silicides were studied in the temperature range -200°C ÷ +600°C, using a classical compensation scheme [20].

The dependence of the thermopower coefficient (α) on temperature for chromium monosilicides showed that α increases linearly with increasing temperature up to 200°C, and then remains constant (Fig. 1).

*Cite as:* A.T. Mamadalimov, M.Sh. Isaev, I.T. Bozarov, A.E. Rajabov, S.K. Vakhabova, East Eur. J. Phys. 2, 362 (2024), https://doi.org/10.26565/2312-4334-2024-2-44
© A.T. Mamadalimov, M.Sh. Isaev, I.T. Bozarov, A.E. Rajabov, S.K. Vakhabova, 2024; CC BY 4.0 license

When studying this dependence for chromium disilicides, three sections were found in the curve: the first section is a section of linear growth of α as temperatures increase to 150℃, the second is a saturation section (temperature range +150℃ ÷ +250℃) and the third is a section of a smooth decrease in α with increasing temperature (+250℃ ÷ +600℃). The first section is explained by the effect of drag of charge carriers by phonons.

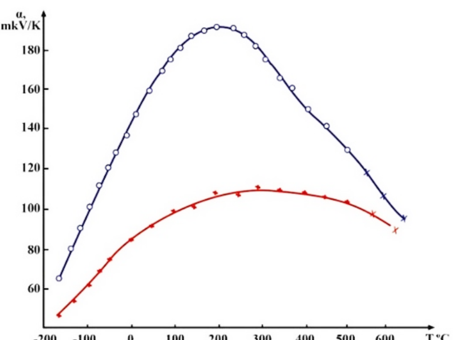


**Figure 1.** Temperature dependence of thermoEMF. 1 – $CrSi_2$; 2 – CrSi

The α(T) dependence for chromium monosilicides is explained by the fact that α increases up to +200℃ due to the effect of hole entrainment by phonons, after 200℃ α remains constant due to the disappearance of the effect of hole entrainment by phonons and due to an increase in the hole concentration and the acquisition of thermal kinetic energy.

The studied crystals are characterized by the fact that silicides rich in chromium have lower thermopower values than silicides rich in silicon. The maximum thermopower values of 1110 μV/K and 190 μV/K were observed for silicides CrSi and $CrSi_2$, respectively. Among the studied silicides, $CrSi_2$ has a linear dependence α(T) and can be used as a material for electronic thermometers and thermogenerators.

From the literature [21-24] it is known that the value of thermopower depends on the temperature difference and the type of material. When heating a metal silicide at high temperatures, the average energy of charge carriers and their concentration will be greater than in the region where the crystal temperature is lower. Consequently, the temperature gradient in such crystals leads to a gradient of the average energy of charge carriers and a gradient of their concentration, as a result of which thermopower arises.

The bell-shaped nature of the thermopower of chromium disilicide is explained by a change in the ratio of the concentration of charge carriers and their mobility in the temperature range of 150℃-250℃. In all other cases, a positive thermopower is observed, which indicates the formation of a negative space charge at the hot end of the crystal.

The measured temperature dependences of α, σ and χ are presented in Figs. 2 and 3.

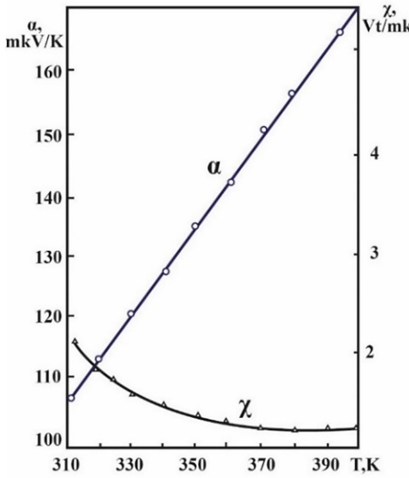


**Figure 2.** Temperature dependence of α and χ

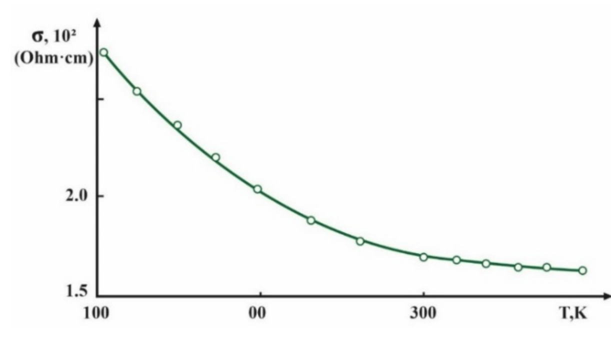


**Figure 3.** Temperature dependence of conductivity

To analyze the obtained thermoelectric properties of the samples, we will use generally accepted criteria.

The parameter Z, as well as the parameters α, ρ and χ, is a single-valued function of temperature, therefore it is practically more convenient to use the dimensionless parameter $Q = Z{\cdot}T$, which is equal to 0.25, where T is the average temperature of the thermoelement branch. The relationship between electrical conductivity (σ) and thermoEMF (α) turned out to be a linearly decreasing function (Fig. 4).

The possibility of obtaining sufficiently high thermopower values in silicides was demonstrated by estimating the ratio of the radii of the silicon atom to the metal atom in the compound. The criterion for this ratio (k) is 0.59. It has been

established that at k <0.59 there is a conventional structure with embedded atoms. At k>0.59, a more complex structure appears that has semiconductor properties, the thermoelectric figure of merit of which can exceed by an order of magnitude the figure of merit of materials with a conventional structure. For chromium silicide k=0.94, which makes it possible to obtain high values of the thermoelectric figure of merit Z.

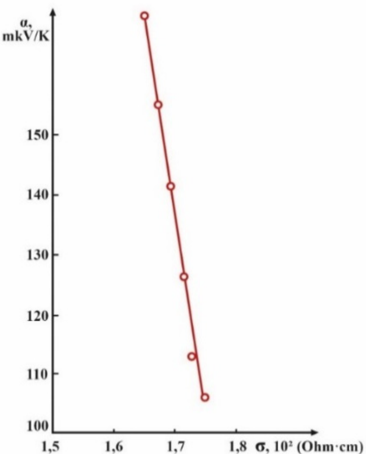


**Figure 4.** Dependence of thermopower on electrical conductivity

The convenience of the diffusion method for producing HCM of both electronic and hole type conductivity lies in the fact that it becomes possible to create the N and P branches of a thermogenerator from a material with identical electrical and thermoelectric properties.

Thus, the diffusion method for producing metal silicides opens up wide possibilities for varying parameters such as electrical conductivity, thermal conductivity and thermopower, and ultimately thermoelectric figure of merit, all of which contributes to the possibility of using chromium silicides as a promising material for thermoelectric converters in solar engineering.

## CONCLUSION

1. Chromium mono- and disilicides were obtained by diffusion doping of silicon.
2. The electrical parameters of chromium disilicide were measured: charge carrier mobility 19 $cm^2$/V s, hole concentration $5.9 \cdot 10^{19}$ $cm^{-3}$, resistivity 1800 μOhm·cm, Hall constant $1.3 \cdot 10^{-2}$ $cm^3$/Kl.
3. Studies of the dependence α (T) for chromium disilicide revealed the formation of three sections: the first section is a section of linear growth of α as temperatures increase (-180°C ÷ + 150°C), the second is a saturation section (-150°C ÷ + 250°C) and the third is a section of smooth decrease α with increasing temperature. Chromium monosilicide is characterized by a smooth increase in thermopower with increasing temperature to 200°C, and then its constancy.
4. It was revealed that for chromium silicides the dependence of the dimensionless parameter Q = Z·T on temperature is linear. The possibility of predicting the technology of synthesis of semiconductor material with optimal thermoelectric properties using the dependence of thermopower on conductivity and the parameter Q on temperature is shown.

## ORCID

**Makhmudkhodja Sh. Isaev,** https://orcid.org/0009-0007-9559-5834

## REFERENCES

[1] S.B. Utamuradova, K.S. Daliev, S.Kh. Daliev, and U.K. Erugliev, "Capacitive spectroscopy of deep levels in silicon with samarium impurity," East European Journal of Physics, (4), 303–306 (2023). https://doi.org/10.26565/2312-4334-2023-4-39
[2] Kh.S. Daliev, Sh.B. Utamuradova, O.A. Bozorova, and Sh.Kh. Daliev, "Joint influence of impurity atoms of nickel and hafnium on photosensitivity of silicon solar cells," Geliotekhnika, **1,** 85–87 (2005). https://www.researchgate.net/publication/294234192_Joint_effect_of_Ni_and_Gf_impurity_atoms_on_the_silicon_solar_cell_photosensitivity
[3] K.P. Abdurakhmanov, Kh.S. Daliev, Sh.B. Utamuradova, and N.Kh. Ochilova, "On defect formation in silicon with impurities of manganese and zinc," Applied Solar Energy (English translation of Geliotekhnika), **34**(2), 73–75 (1998).
[4] M.Sh. Isaev, T.U. Atamirzaev, M.N. Mamatkulov, U.T. Asatov, and M.A. Tulametov, "Study of the mobility and electrical conductivity of chromium silicide," East European Journal of Physics, (4), 189–192 (2023). http://dx.doi.org/10.26565/2312-4334-2023-4-22
[5] N.A. Turgunov, E.Kh. Berkinov, R.M. Turmanova, "Accumalations of impurity Ni atoms and their effect on the electrophysical properties of Si," E3S Web of Conferences, **402**, 14018 (2023). https://doi.org/10.1051/e3sconf/202340214018
[6] Kh.S. Daliev, Sh.B. Utamuradova, O.A. Bozorova, and Sh.Kh. Daliev, "Joint effect of Ni and Gf impurity atoms on the silicon solar cell photosensitivity," Applied Solar Energy (English translation of Geliotekhnika), **41**(1), 80–81 (2005).

https://www.researchgate.net/publication/294234192_Joint_effect_of_Ni_and_Gf_impurity_atoms_on_the_silicon_solar_cell_photosensitivity
[7] K.P. Abdurakhmanov, Sh.B. Utamuradova, Kh.S. Daliev, S.G. Tadjy-Aglaeva, and R.M. Érgashev, "Defect-formation processes in silicon doped with manganese and germanium," Semiconductors, **32**(6), 606–607 (1998). https://doi.org/10.1134/1.1187448
[8] M.Sh. Isaev, A.G. Gaibov, and A.A. Eshkulov, "Investigation of parameters of Schottky diodes based on chromium silicides," Journal of Physics: Conference Series, **1679**(2), 022029 (2020). https://doi.org/10.1088/1742-6596/1679/2/022029
[9] K.S. Daliev, S.B. Utamuradova, I.K. Khamidzhonov, I.K. Mirzairova, Z. Akimova, "Thermally induced deep centers in silicon doped with europium or lanthanum," Inorganic Materials, **37**(5), 436–438 (2001). https://doi.org/10.1023/A:1017556212569
[10] S.B. Utamuradova, S.Kh. Daliev, S.A. Muzafarova, K.M. Fayzullaev, "Effect of the diffusion of copper atoms in polycrystalline CdTe films doped with Pb atoms," East European Journal of Physics, (3), 385–390 (2023). https://doi.org/10.26565/2312-4334-2023-3-4
[11] M.Sh. Isaev, I.T. Bozarov, and A.I. Tursunov, "Investigation of thermally stimulated conductivity of cobalt silicide," E3S Web of Conferences, **402**, 14019 (2023). https://doi.org/10.1051/e3sconf/202340214019
[12] Sh.B. Utamuradova, Sh.Kh. Daliev, E.M. Naurzalieva, X.Yu. Utemuratova. Investigation of defect formation in silicon doped with silver and gadolinium impurities by raman scattering spectroscopy. East European journal of physics, (3), 430-433 (2023). https://doi.org/10.26565/2312-4334-2023-3-47
[13] S.B. Utamuradova, Z.T. Azamatov, M.A. Yuldoshev, N.N. Bazarbayev, A.B. Bakhromov, "Investigations of Nonlinear Optical Properties of Lithium Niobate Crystals," East Eur. J. Phys. (4), 147-152 (2023), https://doi.org/10.26565/2312-4334-2023-4-15
[14] Sh.B. Utamuradova, Z.T. Azamatov, M.A. Yuldoshev, "Optical Properties of $ZnO–LiNbO_3$ and ZnO–LiNbO3:Fe Structures," Russian Microelectronics. **52**(Suppl. 1), S99-S103 (2023). https://doi.org/10.1134/S106373972360022X
[15] Z.T. Azamatov, M.A. Yuldoshev, N.N. Bazarbayev, and A.B. Bakhromov, "Investigation of Optical Characteristics of Photochromic Materials," Physics AUC, **33**, 139-145 (2023). https://cis01.central.ucv.ro/pauc/vol/2023_33/13_PAUC_2023_139_145.pdf
[16] N.A. Turgunov, E.Kh. Berkinov, and R.M. Turmanova, "The effect of thermal annealing on the electrophysical properties of samples n-Si<Ni,Cu>," East European Journal of Physics, (3), 287–290 (2023). https://doi.org/10.26565/2312-4334-2023-3-26
[17] Sh.B. Utamuradova, Kh.J. Matchonov, J.J. Khamdamov, and Kh.Y. Utemuratova, "X-ray diffraction study of the phase state of silicon single crystals doped with manganese," New Materials, Compounds and Applications, **7**(2), 93-99 (2023). http://jomardpublishing.com/UploadFiles/Files/journals/NMCA/v7n2/Utamuradova_et_al.pdf
[18] K.S. Daliev, S.B. Utamuradova, J.J. Khamdamov, and M.B. Bekmuratov, "Structural properties of silicon doped rare earth elements ytterbium," East European Journal of Physics, (1), 375–379 (2024). https://doi.org/10.26565/2312-4334-2024-1-37
[19] K.S. Daliev, Z.E. Bahronkulov, and J.J. Hamdamov, "Investigation of the magnetic properties of silicon doped with rare-earth elements," East European Journal of Physics, (4), 167–171 (2023). https://doi.org/10.26565/2312-4334-2023-4-18
[20] M. Isaev, A. Gaibov, A. Eshkulov, and P. Saidachmetov, "Formation of nanosized films of chromium silicides on silicon surface," Lecture Notes in Networks and Systems, **247**, 1031–1041 (2022). https://doi.org/10.1007/978-3-030-80946-1_93
[21] S.R. Boidedaev, G. Gulyamov, M.O. Qosimova, and M.G. Dadamirzayev, "Influence of deformation and light on the diffusion capacity and differential resistance of the p-n junction of a strong electromagnetic field," AIP Conference Proceedings, **2700**, 050013 (2023). https://doi.org/10.1063/5.0124926
[22] K. Youngsang, L. Andrej, M. Edgar, and R. Pramod, "Temperature dependence of thermopower in molecular junctions," Appl. Phys. Lett. **109**, 033102 (2016). https://doi.org/10.1063/1.4958999
[23] M.K. Karimov, F.O. Kuryozov, S.R. Sadullaev, M.U. Otabaev, and S.B. Bobojonova, "Investigation of defect InP(001) surface by low energy ion scattering spectroscopy," Mater. Sci. Forum, **1049**, 192-197 (2022). https://doi.org/10.4028/www.scientific.net/MSF.1049.192
[24] U.O. Kutliev, M.U. Otabaev, and M.K. Karimov, "Investigation Ne ions scattering from the stepped InP(001)<1̄10> surface," Journal of Physics: Conference Series, **2388**(1), 012092 (2022). https://doi.org/10.1088/1742-6596/2388/1/012092

**ДОСЛІДЖЕННЯ ТЕРМОЕЛЕКТРИЧНИХ ВЛАСТИВОСТЕЙ СИЛІЦИДІВ ХРОМУ**

**Абдугафур Т. Мамадалімов[a], Махмудходжа Ш. Ісаєв[b], Ісмоіл Т. Бозаров[c], Алішер Е. Раджабов[d], Сожида К. Вахабова[e]**
*[a]Інститут фізики напівпровідників та мікроелектроніки Національного університету Узбекистану, Ташкент, Узбекистан*
*[b]Національний університет Узбекистану, Ташкент, Узбекистан*
*[c]Ташкентський хіміко-технологічний інститут, Ташкент, Узбекистан*
*[d]Філія Ташкентського університету інформаційних технологій імені Мухаммеда аль-Хорезмі, Ургенч, Узбекистан*
*[e]Наманганський інженерно-будівельний інститут, Наманган, Узбекистан*

Досліджено температурні залежності термоелектрорушійної сили моно- та дисиліцидів хрому в інтервалі температур -200°C ÷ +600°C. Для дисиліциду хрому залежність коефіцієнта термоЕРС (α) від температури (T) має три ділянки. Для моносиліциду хрому характерне плавне зростання термоЕРС з підвищенням температури до 200°C, а потім її постійність. Виявлено, що силіциди, багаті атомами хрому, мають менші значення термоЕРС, ніж силіциди, багаті кремнієм. Максимальні значення термоЕРС 110 мкВ/К та 190 мкВ/К спостерігаються для моно- та дисиліцидів хрому відповідно. Виявлено, що для силіцидів хрому залежність безрозмірного параметра Q = Z·T від температури має лінійний характер. Показано можливість прогнозування технології синтезу напівпровідникового матеріалу з оптимальними термоелектричними властивостями на основі залежності термоЕРС від електропровідності та параметра Q від температури.

**Ключові слова:** *силіцид; термо-ЕРС; холлівська рухливість; легування; насичення; електропровідність; фазова діаграма; градієнт температури*

EAST EUROPEAN JOURNAL OF PHYSICS. 2. 366-371 (2024)
DOI:10.26565/2312-4334-2024-2-45 ISSN 2312-4334

# STUDY OF SILICIDE FORMATION IN LARGE DIAMETER MONOCRYSTALLINE SILICON

**Abdugafur T. Mamadalimov[a], Makhmudkhodja Sh. Isaev[b], Mukhammadsodik N. Mamatkulov[c], Sardor R. Kodirov[d], Jamshidjon T. Abdurazzokov[e]**
[a]*Institute of Semiconductor Physics and Microelectronics at the National University of Uzbekistan, Tashkent, Uzbekistan*
[b]*National University of Uzbekistan, Tashkent Uzbekistan*
[c]*Tashkent Institute of Chemical-Technology, Tashkent, Uzbekistan*
[d]*Urgench State University, Urgench, Uzbekistan*
[e]*Tashkent Medical Academy, Tashkent, Uzbekistan*
**Corresponding Author e-mail: isayevmahmd02@gmail.com*
Received April 4, 2024; revised May 3, 2024; accepted May 16, 2024

To study the formation of silicides, dislocation-free ingots of single-crystalline silicon with a diameter of 65÷110 mm, grown by the Czochralski method, were used. When studying such silicon samples using electron microscopy, small-angle scattering of $CO_2$ laser radiation, three types of defects were identified: swirl defects, impurity micro inclusions and impurity clouds. It has been shown that silicide inclusions with sizes of 8-20 μm are formed in the near-surface layer of doped silicon, and they decrease linearly deeper into the crystal. The electrical parameters of semiconductor chromium silicide were determined: resistivity 1800 μOhm·cm, thermopower coefficient 180 μV/k, Hall constant $1.2\cdot10^{-2}$ cm$^3$/Kl, hole concentration $6\cdot10^{19}$ cm$^{-3}$, charge carrier mobility 18.6 cm$^2$/V·s, band gap (0.29±0.02) eV.
**Key words:** *Dislocation-Free; Etching; Defects; Swirl; Heterogeneity; Dissolution; Super-Large Circuits; Hardening; Inclusion; Extrapolation*
**PACS:** 33.20.Ea, 33.20.Fb

## INTRODUCTION

Currently, an urgent problem is the study of physical processes occurring both in the bulk and on the surface, and in the near-surface layers of a large-diameter single-crystal semiconductor, in particular, silicon in the process of diffusion doping with impurities that create deep levels (DL) [1-6]. First of all, the need for these studies is due to the fact that in the process of diffusion doping of a semiconductor material—silicon—it is possible to obtain compensated materials with specified electrophysical, photoelectric and optical properties [7-12].

In diffusion-doped silicon crystals, a near-surface layer with a thickness of about ten microns is formed with an impurity concentration that exceeds their solubility by 2÷4 orders of magnitude, and with other electrophysical parameters, namely, high specific conductivity and low mobility in relation to the parameters of the bulk part. In previous works [13-16], studies in doped samples were focused mainly on bulk parts of the crystal obtained by removing the near-surface region, since the near-surface layer was considered to be damaged and not of practical interest.

However, for an in-depth study of the process of diffusion doping of silicon with metals and atoms of rare earth elements, it is necessary to consider such important issues as the physics of the formation of a heavily doped near-surface region, the nature of the formation of metal silicides, which are very different from the metal and semiconductor, as well as the physical and chemical processes occurring in the near-surface region (mutual diffusion, solid-phase reactions, etc.).

It is known that at present, transition metal silicides are becoming the base materials for new, promising technological integrated circuits ((Very Large-Scale Integrated Circuit (VLSI)) of future generations due to their resistance to aggressive environments and high-temperature treatments [17-19].

In particular, transition element silicides can be used to create Schottky barriers and ohmic contacts in integrated circuit technology, serving as gates and interconnects.

In this regard, if we consider the formation of silicides by metallurgical interaction between a metal film and silicon, then subsequent high-temperature heat treatment, which promotes diffusion doping of silicon, leading to the formation of a distribution profile of the concentration of current carriers, requires comprehensive studies of the mechanism of impurities entering the crystal volume and their interaction both with matrix (main) atoms of the crystal, and with technological (background) impurities, as well as with structural defects.

Therefore, the study of silicides in the near-surface region in the process of diffusion doping of silicon is in itself relevant, and the formation of a carrier concentration profile in the near-surface region of silicon doped with impurities that create deep levels opens up ways to create new semiconductor devices.

## EXPERIMENTAL PART

For the study, we used dislocation-free single-crystalline silicon ingots with a diameter of 65÷110 mm, grown by the Czochralski method, with $\rho=10^4$ Ohm·cm, because This method was the first to study such crystals. To convincingly

***Cite as:*** A.T. Mamadalimov, M.Sh. Isaev, M.N. Mamatkulov, S.R. Kodirov, J.T. Abdurazzakov, East Eur. J. Phys. 2, 366 (2024), https://doi.org/10.26565/2312-4334-2024-2-45
© A.T. Mamadalimov, M.Sh. Isaev, M.N. Mamatkulov, S.R. Kodirov, J.T. Abdurazzakov, 2024; CC BY 4.0 license

prove our results, the experiment was carried out first for known crystals. The ingots were cut in cross section into washers. Samples were cut from the washers in the form of a parallelepiped with dimensions of (65÷110)×(20÷25)×(3÷5) $mm^3$.

After grinding, the samples were subjected to chemical etching in a solution in the following composition (weight in %): HF - 36 ÷ 30, $CgO_3$ - 15 ÷ 18, water - the rest. Etching was carried out in a closed vessel for 8÷10 minutes. at a temperature of 80-100 ℃.

Studies of high-purity non-heat-treated dislocation-free silicon samples using electron microscopy, X-ray microanalysis and small-angle scattering of $CO_2$ laser radiation revealed that three types of defects were found in them: swirl defects, impurity micro inclusions and impurity clouds.

Swirl defects are generated by a heterogeneous mechanism and are arranged in layers. The concentration of such defects is $10^6$-$10^8$ $cm^{-3}$. By selecting the cooling rate when growing silicon, you can get rid of this type of defects [20].

The second type of defect is an impurity micro inclusion includes impurities of carbon, calcium, phosphorus, chlorine, aluminum, sodium and some others. Micro inclusions have sizes from fractions of a micron and higher and a concentration of ~$10^7$ $cm^{-3}$. It is assumed that these impurities are captured by the growing single crystal from the melt. In a high-purity crystal that is undersaturated in impurities included in the micro inclusions, their partial dissolution can occur. In this case, slowly diffusing impurities will form clusters around the inclusions with a size of about 10 microns. Such local areas with an increased concentration of dissolved impurities are called impurity clouds [21]. Such defects were detected by small-angle scattering of $CO_2$ laser radiation with λ=10.6 μm.

Thus, the proposed methods for monitoring the level of silicon homogeneity by the presence of microdefects in the structure can be used in the production of large-diameter dislocation-free silicon, from which ultra-large circuits and semiconductor devices are created.

The method of small-angle scattering of $CO_2$ laser radiation was used to determine silicide islands in the surface layer of diffusely doped silicon with manganese, chromium and cobalt. The samples were made from p-type silicon of the KDB-10 brand at a diffusion temperature of 1040-1100 ℃ for 20-120 minutes. The samples were hardened by cooling at a rate of 100-120 ℃/s with the ampoules being dropped into water. To identify silicide islands, five of the six sides of the parallelepiped were polished to a depth of 50-100 μm. On the remaining face, measurements were taken as a layer 3-5 μm thick was removed from the surface. Measurements showed that silicide inclusions with sizes of 8-20 microns are formed in the near-surface layer. The determination of silicide inclusions by the small-angle scattering method is based on light scattering caused by the deviation from the average value of the dielectric constant Δε for the crystal. At λ=10.6 μm, the value of Δε for a charge carrier accumulation is three orders of magnitude greater than for a neutral impurity accumulation with the same concentration. It is assumed that Δε for silicide islands is mainly due to holes. Inhomogeneity such as impurity clouds scatters light at small diffraction angles θ~λ/a, where a is the characteristic size of the cloud. According to the Rayleigh-Gans theory [22], the scattered light flux per unit solid angle is determined by the expression:

$$\boldsymbol{I} = (\boldsymbol{\theta}) = \boldsymbol{WCL}|\boldsymbol{G}|^2 \quad (1)$$

where: W is the initial light flux in the crystal, C is the concentration of scattering centers, L is the thickness of the sample, G(θ) is the integral over the volume of an individual inhomogeneity, the form of which depends on the polarization of light.

The nature of the dependence of the intensity of small-angle scattering of laser radiation I (normalized to the power of the incident beam and to the thickness of the sample) on the scattering angle θ makes it possible to establish the radial profile and size “a” of the silicide inclusion: the intensity Io extrapolated to θ = 0 serves as a characteristic of the total amount of electrically active impurity in silicide clouds.

## RESULTS AND DISCUSSION

In Fig. 1. The dependence of the size of the silicide inclusion at three points of the crystal on the thickness of the layer removed from the crystal surface is shown. It can be seen that the sizes of silicide inclusions decrease linearly deeper into the crystal.

In Fig.2. The dependence of the concentration of silicide inclusions on the distance (into the crystal) is shown. From Fig. It can be seen that on the surface of a crystal with a thickness of ~3 μm, silicide inclusions are saturated, i.e. a continuous film is formed. At depths from 3 to 30 μm, the concentration of inclusions decreases smoothly.

It has been established that the concentration of silicide inclusions in the near-surface region of the crystal depends on the type of substrate, the amount of diffusant, the diffusion temperature and the quenching rate.

The electrical properties of chromium disilicide were determined: band gap (0.29±0.02) eV, resistivity 1800 μOhm·cm, thermoEMF coefficient 180 μV/Kl, Hall constant $1.2\cdot10^{-2}cm^3$/Kl, hole concentration $6\cdot10^{19}$ $cm^{-3}$, charge carrier mobility 18.6 $cm^2$/V·s, ZT = 0.25.

The experimental results obtained show that Cr, Mn, Co in silicon have increased reactivity: metal phases of chromium, manganese and cobalt are not detected on the surface of the doped crystals. Mono- and di-higher metal silicides are formed on the surface in the case of diffusion doping of silicon from the gas phase. The amorphous phase was observed in the surface layer with a thickness of 3-10 μm. At a depth of 10-50 μm, various silicides were observed in different

samples: for Si<Mn>, predominantly higher manganese silicide was observed, for Si<Cr> - chromium mono and disilicides, and for Si<Co> - predominantly cobalt disilicide. When removing a layer from the surface of samples with a thickness of more than 50 microns, silicides of the above metals were not detected.

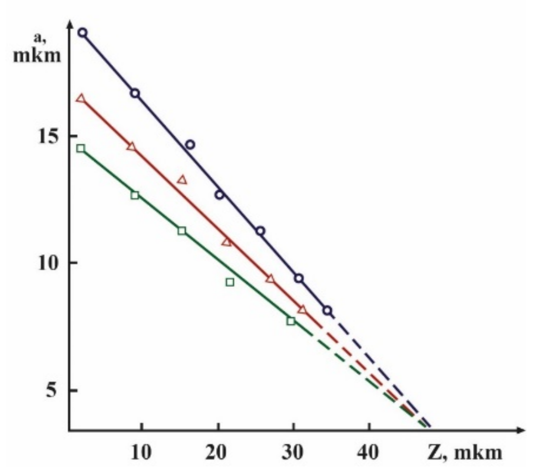


**Figure 1.** Dependence of the size of various silicide inclusions on the crystal depth

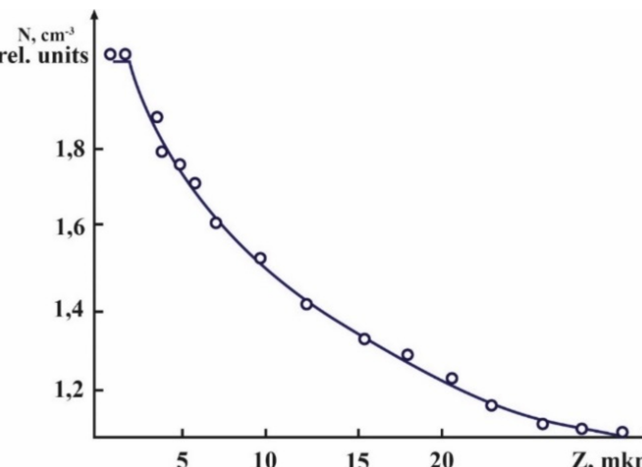


**Figure 2.** Dependence of the surface concentration of silicide inclusions on the crystal depth

The formation of cobalt silicides on polycrystalline silicon by direct implantation of metals was studied in the work of M. Kozicki [23]. Co ions with an energy of 150-350 keV (at a dose of $7 \cdot 10^{16}$ - $7 \cdot 10^{17}$ $cm^{-2}$) were implanted into single-crystal silicon wafers. After implantation, the sample was annealed at a temperature of 950 ℃ for 10-20 s. The properties of Si silicide layers were studied using Rutherford inverse scattering, X-ray diffractometry, and other methods.

A study of the kinetics of growth of the silicide phase along a cross section of samples in the case of annealing of deposited manganese on silicon showed that the dependence of the thickness of the silicide layer (W) on the annealing time (t) is parabolic (Fig. 3.). At lower values of t, this dependence is violated (Fig. 3, section AB), which is apparently associated with limiting the reaction rate of silicide formation. The layers are formed in thickness proportional to the square root of time (section BC). The thickness of the silicide layer W formed during time t is determined by the expression

$$\boldsymbol{W} = \{[\boldsymbol{B} \cdot \mathbf{exp}\,(-\boldsymbol{E_a}/\boldsymbol{kT}]\}\boldsymbol{t^{1/2}} \quad (2)$$

where B is a constant, $\boldsymbol{E_a}$ is the average activation energy of the growth process, k is Boltzmann's constant, T is the absolute temperature.

In the formation of the CoSi and $Co_2Si$ layer, the same $\boldsymbol{t^{1/2}}$ dependence of phase growth was also established. And in the case of $CrSi_2$, a linear dependence on time was discovered, suggesting interaction with a rate determined by the state of the interface. The value of the diffusion coefficient D can be calculated from the slope of the time dependence lines W.

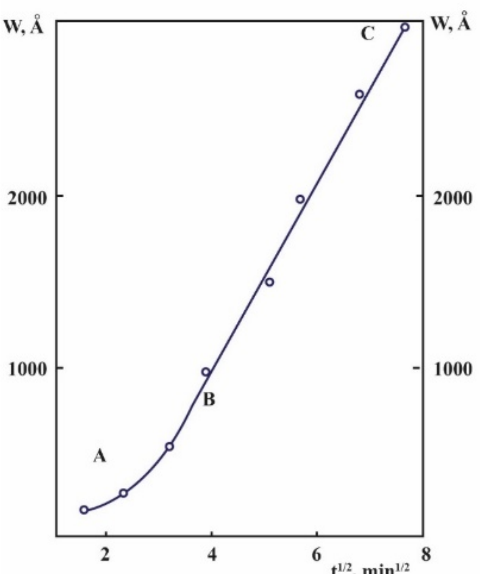


**Figure 3.** Dependence of the HCM layer thickness on annealing time.

The activation energy of the phase formation process can be determined from the dependence of the diffusion coefficient on the inverse temperature, i.e. according to Arrhenius plots [24]. The activation energies are 1.5 eV for $CrSi_2$, 1.5 eV for $Co_2Si$, 1.9 eV for CoSi, and 1.4 eV for $MnSi_{1.75}$. Analysis of the results obtained shows that during the formation of silicides, silicides rich in metal atoms are first formed, and then metal monosilicides, in the case of diffusion doping of silicon from the gas phase. And in the case of metal-sputtered silicon, a metal silicide enriched with the latter is formed at the interface between silicon and metal, after thermal annealing.

It should be noted that oxygen lines are observed in the spectrum during thermal annealing, which is the $Me_2O_3$ compound. Analysis of the results showed that the surface of the deposited metal during temperature annealing is covered with a thin layer of $Me_2O_3$, which plays the role of a diffusion barrier for oxygen from the annealing atmosphere.

The formation of the annealing phase of silicides during thermal annealing obeys the rule of the formation of nuclei at the metal-semiconductor interface. This rule is based on the postulate that initially the interface is a metal-glass with a concentration close to the low-temperature eutectic. However, the experimental setup used is not able to show the existence of such an intermediate layer in reality. There is no exact mechanism for the nucleation of metal silicides yet, but it can be represented by the growth of metal grains and the diffusion of silicon atoms into a polycrystalline film of chromium (or manganese, cobalt) mainly along the grain boundaries. This behavior of silicon was observed in the case of iron-silicon interaction. Ryan et al. suggest that the growth of silicide when depositing pure metal on silicon creates equilibrium conditions by lowering their interfacial energy.

Botha and Kritzinger [25] studied the diffusion mechanism in the formation of nickel, cobalt and platinum silicides using traces of radioactive silicon. They created thin-film structures on Si(100) substrates using electron-beam heating. Radioactive $^{31}Si$ (half-life 2.62 hours), obtained by irradiating pure natural Si in a nuclear reactor, was washed in organic solvents, etched in a 10% solution of hydrogen fluoride, after which it was deposited on Si by evaporating the source. Between layers of radioactive Si with thicknesses of 500 Å and 700 Å, layers of metal (Pt, Ni, Co) with thicknesses of 1000 Å and 1600 Å were deposited. After this, annealing was carried out at $10^{-6}$ Pa to form silicides. The profiles were studied using layer-by-layer HF sputtering using Rutherford backscattering and Geiger-Muller methods. During the growth of NiSi, diffusion of the metal was detected, while during the growth of CoSi and PtSi, predominantly Si diffuses. The $Co_2Si$ transition occurs predominantly during Si diffusion along grain boundaries, while PtSi is formed from $Pt_2Si$ both during Si diffusion at grain boundaries and through the vacancy diffusion mechanism. After nucleation, a reaction of the form $Me + 2Si \rightarrow MeSi_2$ occurs, occurring at the $MeSi_2$ – Me boundary.

The growth of silicides is limited by three factors:

1. The presence of surface silicon atoms;
2. Transfer of silicon atoms through an already formed $MeSi_2$ layer;
3. Reaction at the interface.

In the temperature range studied, an increase in the thickness of the $MeSi_2$ layer either leads to a decrease in the growth rate or the second factor is limiting.

The lack of formation of metal silicides at temperatures below ~400 ℃ is explained by the increasing difficulty of releasing silicon atoms from its covalent bond. At temperatures above ~400 ℃, phonons can provide the necessary energy to liberate a silicon atom.

Finally, when the growth temperature of the silicide decreases, the Si-$MeSi_2$ interface becomes rougher and rougher, so that the exchange across the surface increases, which can explain the observed time dependence of $t^{1/2}$ in the case of the growth of manganese and cobalt silicides.

## CONCLUSION

As a result of the scientific research, we came to the following important scientific conclusions:

1. Based on the study of surface morphology by electron and IR microscopy, the formation of impurity accumulations, which represent the second phase on the surface of diffusion doped silicon with atoms of manganese, chromium and cobalt, has been established. The sizes of the clusters were determined, reaching up to 30-40 μm on the surface and decreasing deeper into the crystal. Qualitative and quantitative analysis showed that atoms of the doped atom and silicon are present on the surface of the crystals under study. Some crystals exhibit a granular structure, which is explained by the diffusion condition.
2. By studying the kinetics of growth of the silicide phase along a cross section of samples, it was shown that during the formation of silicides CoSi, $Co_2Si$, $CoSi_2$, MnSi, $MnSi_{1.75}$, $MnSi_2$, there is a quadratic dependence of the layer thickness on the annealing time, and for silicides CrSi and $CrSi_2$ there is a linear dependence. The activation energies of phase formation for the studied silicides were determined and are 1.4-1.9 eV.
3. It has been shown that the formation of silicide nuclei at the silicon-metal interface begins with the decomposition of silicon atoms at the grain boundaries of the deposited metal layer. In this case, metal disilicides are formed. It has also been shown that the formation of Cr, Mn, Co silicides occurs at temperatures above 400℃.
4. Using the method of small-angle $CO_2$ laser scattering, the formation of silicide inclusions with dimensions of 8÷20 μm in the near-surface region with a thickness of 3÷40 μm in samples of diffusion-doped silicon with manganese, chromium and cobalt was established. The determination of such inclusions is based on the deviation of their dielectric constant from the average value for the crystal.

5. The dependence of the size of silicide inclusions and their concentration on the thickness of the removed layer (depth profile) was studied. A decrease in the size of silicide inclusions with depth of the crystal has been established, which makes it possible to study the dynamics of growth of the silicide layer.

**ORCID**
**Makhmudkhodja Sh. Isaev,** https://orcid.org/0009-0007-9559-5834

**REFERENCES**

[1] L. Wang, J. Liu, Y. Li, G. Wei, Q. Li, Z. Fan, H. Liu, et al., "Dislocations in Crystalline Silicon Solar Cells," Advanced Energy and Sustainability Research, **5**(2), 2300240 (2024). https://doi.org/10.1002/aesr.202300240
[2] K.P. Abdurakhmanov, Sh.B. Utamuradova, Kh.S. Daliev, S.G. Tadjy-Aglaeva, and R.M. Érgashev, "Defect-formation processes in silicon doped with manganese and germanium," Semiconductors, **32**(6), 606–607 (1998). https://link.springer.com/article/10.1134/1.1187448
[3] Kh.S. Daliev, Sh.B. Utamuradova, O.A. Bozorova, Sh.Kh. Daliev, "Joint effect of Ni and Gf impurity atoms on the silicon solar cell photosensitivity," Applied Solar Energy (English translation of Geliotekhnika), **41**(1), 80–81 (2005). https://www.researchgate.net/publication/294234192_Joint_effect_of_Ni_and_Gf_impurity_atoms_on_the_silicon_solar_cell_photosensitivity
[4] K.P. Abdurakhmanov, Kh.S. Daliev, Sh.B. Utamuradova, and N.Kh. Ochilova, "On defect formation in silicon with impurities of manganese and zinc," Applied Solar Energy (English translation of Geliotekhnika), **34**(2), 73–75 (1998).
[5] A.A. Lebedev, "Deep level centers in silicon carbide: A review," Semiconductors, **33**(2), 107-130 (1999). https://link.springer.com/article/10.1134/1.1187657
[6] Sh.B. Utamuradova, Kh.J. Matchonov, J.J. Khamdamov, and Kh.Y. Utemuratova, "X-ray diffraction study of the phase state of silicon single crystals doped with manganese," New Materials, Compounds and Applications, **7**(2), 93-99 (2023). http://jomardpublishing.com/UploadFiles/Files/journals/NMCA/v7n2/Utamuradova_et_al.pdf
[7] Kh.S. Daliev, Z.E. Bahronkulov, and J.J. Hamdamov, "Investigation of the Magnetic Properties of Silicon Doped with Rare-Earth Elements," East Eur. J. Phys. (4), 167-171 (2023). https://doi.org/10.26565/2312-4334-2023-4-18
[8] Z.T. Azamatov, Sh.B. Utamuradova, M.A. Yuldoshev, and N.N. Bazarbaev, East Eur. J. Phys. (2), 187-190 (2023), https://doi.org/10.26565/2312-4334-2023-2-19
[9] S.B. Utamuradova, Z.T. Azamatov, M.A. Yuldoshev, N.N. Bazarbayev, and A.B. Bakhromov, "Investigations of Nonlinear Optical Properties of Lithium Niobate Crystals," East Eur. J. Phys. (4), 147 (2023), https://doi.org/10.26565/2312-4334-2023-4-15
[10] N.A. Turgunov, E.Kh. Berkinov, and R.M. Turmanova, "The effect of thermal annealing on the electrophysical properties of samples n-Si<Ni,Cu>," East European Journal of Physics, (3), 287–290 (2023). https://doi.org/10.26565/2312-4334-2023-3-26
[11] Sh.B. Utamuradova, Z.T. Azamatov, and M.A. Yuldoshev, "Optical Properties of ZnO–LiNbO$_3$ and ZnO–LiNbO$_3$:Fe Structures," Russian Microelectronics, **52**(Suppl. 1), S99–S103 (2023). https://doi.org/10.1134/S106373972360022X
[12] Z.T. Azamatov, M.A. Yuldoshev, N.N. Bazarbayev, and A.B. Bakhromov, "Investigation of Optical Characteristics of Photochromic Materials," Physics AUC, 33, 139-145 (2023). https://cis01.central.ucv.ro/pauc/vol/2023_33/13_PAUC_2023_139_145.pdf
[13] E.V. Astrova, V.B. Voronkov, V.A. Kozlov and A.A. Lebedev, "Process induced deep-level defects in high purity silicon," Semiconductor Science and Technology, **13**(5), 488(1998). https://doi.org/10.1088/0268-1242/13/5/008
[14] K.S. Daliev, S.B. Utamuradova, I.K. Khamidzhonov, I.K. Mirzairova, and Z. Akimova, "Thermally induced deep centers in silicon doped with europium or lanthanum," Inorganic Materials, **37**(5), 436–438 (2001). https://link.springer.com/article/10.1023/A:1017556212569
[15] S.B. Utamuradova, S.Kh. Daliev, S.A. Muzafarova, and K.M. Fayzullaev, "Effect of the diffusion of copper atoms in polycrystalline CdTe films doped with Pb atoms," East European Journal of Physics, (3), 385–390 (2023). http://dx.doi.org/10.26565/2312-4334-2023-3-41
[16] M. Schulz, "Determination of deep trap levels in silicon using ion-implantation and CV-measurements," Appl. Phys. (4), 225-236 (1974). https://link.springer.com/article/10.1007/BF00884233
[17] Kh.S. Daliev, Sh.B. Utamuradova, J.J. Khamdamov, and Z.E. Bahronkulov, "Electrophysical properties of silicon doped with lutetium," Advanced Physical Research, **6**(1), 42-49 (2024). http://dx.doi.org/10.62476/apr61.49
[18] M.Sh. Isaev, T.U. Atamirzaev, M.N. Mamatkulov, U.T. Asatov, and M.A. Tulametov, "Study of the mobility and electrical conductivity of chromium silicide," East European Journal of Physics, (4), 189–192 (2023). https://doi.org/10.26565/2312-4334-2023-4-22
[19] A.Kh. Kasymov, and M.Sh. Isaev, "Thermoelectric properties of manganese silicide for thermoelectric converters of solar energy," Applied Solar Energy (English translation of Geliotekhnika), **33**(1), 54–58(1997).
[20] K.S. Daliev, S.B. Utamuradova, J.J. Khamdamov, and M.B. Bekmuratov, "Structural properties of silicon doped rare earth elements ytterbium," East European Journal of Physics, (1), 375–379 (2024). https://doi.org/10.26565/2312-4334-2024-1
[21] N.A. Turgunov, E.Kh. Berkinov, R.M. Turmanova, "Accumalations of impurity Ni atoms and their effect on the electrophysical properties of Si," E3S Web of Conferences, **402**, 14018 (2023). https://doi.org/10.1051/e3sconf/202340214018
[22] C. Argentin, M.J. Berg, M. Mazur, R. Ceolato, and J. Yon, "Assessing the limits of Rayleigh–Debye–Gans theory: Phasor analysis of a biosphere," Journal of Quantitative Spectroscopy and Radiative Transfer, **264**, 107550 (2021). https://doi.org/10.1016/j.jqsrt.2021.107550
[23] M. Kozicki, "Formation and oxidation of implanted cobalt silicides on polycrystalline-silicon," in*: Electrical Engineering. 1988 Proceedings - Fifth International IEEE VLSI Multilevel Interconnection Conference*, (Santa Clara, CA, USA), pp.198-204.
[24] D.G. Truhlar, and A. Kohen, "Convex Arrhenius plots and their interpretation," PNAS, **98**(3), 848-851 (2001). https://doi.org/10.1073/pnas.98.3.848
[25] A.P. Botha, S. Kritzinger, and R. Pretorius, "Self-diffusion of silicon in thin films of cobalt, nickel, palladium and platinum silicides," Thin Solid Films, **141**(1), 41-51 (1986). https://doi.org/10.1016/0040-6090(86)90317-2

**ДОСЛІДЖЕННЯ СИЛІЦИДОУТВОРЕННЯ В МОНОКРИСТАЛІЧНОМУ КРЕМНІЇ ВЕЛИКОГО ДІАМЕТРА**

**Абдугафур Т. Мамадалімов[a], Махмудходжа Ш. Ісаєв[b], Мухаммадсодік Н. Маматкулов[c], Сардор Р. Кодиров[d], Джамшиджон Т. Абдураззоков[e]**

[a]*Інститут фізики напівпровідників та мікроелектроніки Національного університету Узбекистану, Ташкент, Узбекистан*
[b]*Національний університет Узбекистану, Ташкент, Узбекистан*
[c]*Ташкентський хіміко-технологічний інститут, Ташкент, Узбекистан*
[d]*Ургенчський державний університет, Ургенч, Узбекистан*
[e]*Ташкентська медична академія, Ташкент, Узбекистан*

Для дослідження утворення силіцидів використовували бездислокаційні злитки монокристалічного кремнію діаметром 65÷110 мм, вирощені методом Чохральського. При дослідженні таких зразків кремнію методом електронної мікроскопії, малокутового розсіювання випромінювання CO2-лазера виявлено три типи дефектів: завихрені дефекти, домішкові мікровключення та домішкові хмари. Показано, що в приповерхневому шарі легованого кремнію утворюються силіцидні включення розміром 8-20 мкм, які лінійно зменшуються вглиб кристала. Визначено електричні параметри напівпровідникового силіциду хрому: питомий опір 1800 мкОм·см, коефіцієнт термоЕРС 180 мкВ/к, стала Холла $1{,}2\cdot10^{-2}$ см$^3$/Кл, концентрація дірок $6\cdot10^{19}$ см$^{-3}$, рухливість носіїв заряду 18,6 см$^2$/В. ·s, ширина забороненої зони (0,29±0,02) еВ.

**Ключові слова:** *бездислокаційний; травлення; дефекти; завихрення; гетерогенність; розчинення; надвеликі схеми; зміцнення; включення; екстраполяція*

East European Journal of Physics. 2. 372-379 (2024)
DOI:10.26565/2312-4334-2024-2-46 ISSN 2312-4334

# COMPARISON OF 2D AND 3D P-N JUNCTION DIFFERENTIAL CONDUCTANCE AND DIFFUSION CAPACITANCE

**Muhammadjon G. Dadamirzaev, Mamura O. Kosimova*, S.R. Boydedayev, Azamat S. Makhmudov**
*Namangan Engineering-Construction Institute, Namangan 160103, Uzbekistan*
**Corresponding Author e-mail: omamuraqosimova@gmail.com*
Received April 9, 2024; revised April 27, 2024; accepted May 15, 2024

In the fabrication of 3D p-n junctions, doping or surface modification caused by ion injection changes the electrical properties and crystal structure of the semiconductor. In addition, as the size of the semiconductor device decreases, various quantum effects are gradually appearing in them. This shows that the scope of application of classical device theory is now limited. In recent years, two-dimensional (2D) materials with amazing atomically fine properties have attracted great interest. The electrostatic field properties of some 2D p-n junctions, such as WS2, $MoS_2$, $MoSe_2$, $WSe_2$, and black phosphorus (BP), open the door to new possibilities for semiconductors. Changes in the diffusion capacitances and differential conductance's of 2D p-n junctions under the influence of an microwave field, and the diffusion capacitances and differential conductance's of 2D and 3D p-n junctions the change of conductivities under the influence of microwave field is compared.
**Keywords:** *p-n-junction; Diffusion capacitance; Differential conductance; Microwave field; 2D dimensional materials*
**PACS:** 85.30. Kk

## INTRODUCTION

p-n-junction rectifiers consisting of two types of semiconductors [1], photodetectors [1-5], photovoltaics [6-10], and light-emitting diodes [11-12] are the basis of electronic and optoelectronic devices. In the fabrication of 3D p-n junctions, doping or surface modification caused by ion injection changes the electrical properties and crystal structure of the semiconductor. In addition, as the size of the semiconductor device decreases, various quantum effects are gradually appearing in them. This shows that the scope of application of classical device theory is now limited.

In recent years, two-dimensional (2D) materials with amazing atomically fine properties have attracted great interest. The electrostatic field properties of some 2D p-n junctions, such as WS2, $MoS_2$, $MoSe_2$, $WSe_2$, and black phosphorus (BP), open the door to new possibilities for semiconductors [9,13-18]. Using light as an external field to diodes provides many additional advantages. For example, light can be sent from a distance. This is of great importance for modern integrated optoelectronic connection circuits that are precisely controlled, fast switching and consume very little energy [19-25].

In [26], the Poisson equation for a 2D p-n junction is combined with the drift-diffusion and continuity equations and the Shockley equation for an ideal current-voltage characteristics is proposed. Fig. 1 shows the geometric scheme of a 2D p-n junction. This structure is formed by the combination of p and n types at x=0 and lies in z=0 plane, the structure along the y axis is large enough, so the effect of this direction on the properties is considered.

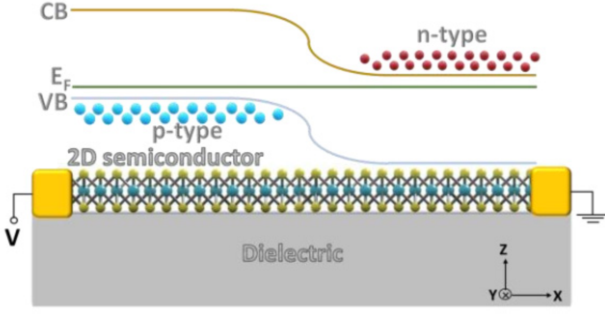


**Figure 1.** Geometric scheme of 2D p-n junction [26]

Fig. 2 shows the quasi-Fermi levels and energy states obtained in the authors' numerical model for the physical structure of a 2D p-n junction in thermodynamic equilibrium. At equilibrium, φ increases through the filling layer, while at nonequilibrium, φ decreases or increases depending on the direction of the voltage.

In addition, in this work, the recombination and generation processes in the effective depletion layer (EDL) are significantly deviated from the ideal, and the capacitances and conductance of the 2D p-n junction are considered. The

*Cite as:* M.G. Dadamirzaev, M.O. Kosimova, S.R. Boydedayev, A.S. Makhmudov, 2024; East Eur. J. Phys. 2, 372 (2024), https://doi.org/10.26565/2312-4334-2024-2-46
© M.G. Dadamirzaev, M.O. Kosimova, S.R. Boydedayev, A.S. Makhmudov, 2024; CC BY 4.0 license

barrier and diffusion capacities for the structure in the non-equilibrium state were analyzed. The barrier capacity was calculated by the following expression:

$$C_б = \frac{2\pi\varepsilon_{эфф}}{8G}. \quad (1)$$

Diffusion capacity calculated by this expression:

$$C_{df} = \frac{2qn_i(L_p + L_n)\exp\left(\frac{qU}{kT}\right)}{2kT}. \quad (2)$$

Using these expressions, capacitance plots are presented based on the authors' numerical model for a silicon-based 3D p-n junction and a 2D monolayer $MoS_2$.

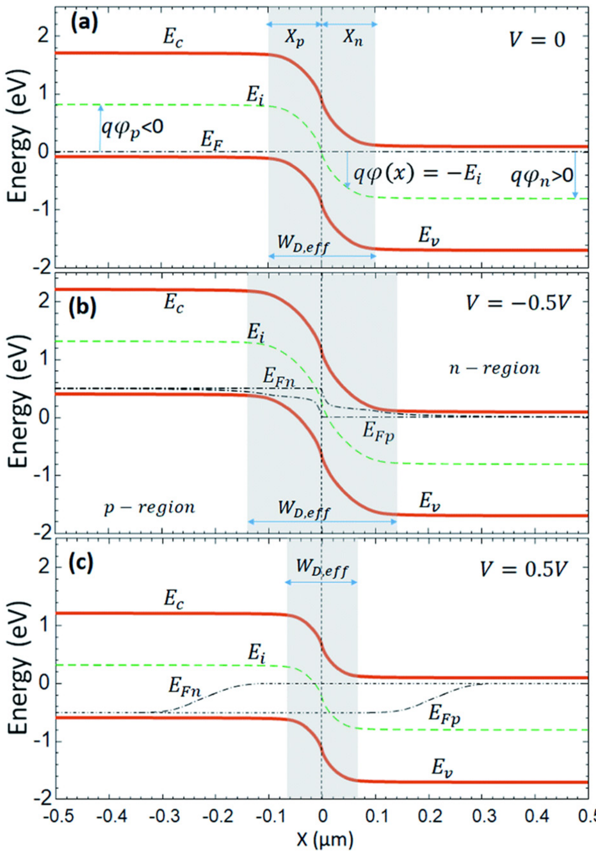


**Figure 2.** Zone diagram of 2D p-n junction in thermodynamic equilibrium state (a); in the reverse direction (b) and in the forward direction (c) [26]

However, in the above-mentioned studies, the changes of diffusion capacities and differential conductivities of 2D p-n junctions due to external influences have not been sufficiently studied, and the differences between 3D and 2D p-n junctions' graphs of changes of diffusion capacities and differential conductivities as a result of external influences are not compared.

The purpose of the work is to analyze the change of diffusion capacities and differential conductivities of 2D and 3D p-n junctions as a result of external influences.

## COMPARISON OF 2D AND 3D p-n JUNCTION DIFFERENTIAL CONDUCTANCE

The differential conductivity of a p-n junction in 3D size is determined by the following relation [27]:

$$G = \frac{eI_s}{kT}\exp\left(\frac{eU}{kT}\right) \quad (3)$$

Differential conductance of p-n junction in 2D size using the expressions presented in the work [27], we get the following formula:

$$G = \frac{q^2 n_i^2}{kTN_d}\left(\frac{D_p}{L_p} + \frac{D_n}{L_n}\right)\exp\left(\frac{qU}{kT}\right), \quad (4)$$

here, $n_i = g_{2D}kT\exp\left(-\frac{E_g}{2kT}\right)$, $L_n = L_p = \sqrt{D_{n(p)}\tau_{n(p)}}$, $D_{n(p)} = \frac{kT\mu_{n(p)}}{q}$, $E_g = 1.8eV$, $\mu_n = \mu_p = 50\frac{sm^2}{Vs}$, $\tau_n = \tau_p = 3\cdot10^{-10}s$, $n_i = 9.9\cdot10^{-3}sm^{-2}$.

From the expressions (3) and (4), 2D and 3D p-n junction differential conductivities were compared (Fig. 3).

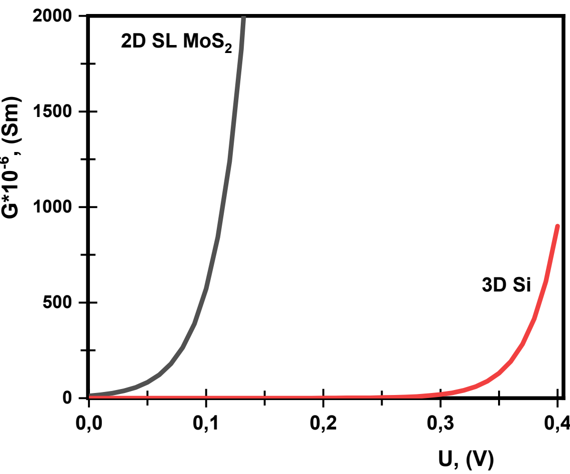


**Figure 3.** Rate dependence of p-n junction differential conductance in 2D and 3D dimensions

Fig. 3 shows the voltage dependence of the differential conductance of a 2D and 3D p-n junction. The obtained results show that the differential conductance of the 3D p-n junction is smaller than the differential conductance of the 2D p-n junction. This shows that the 2D p-n junction is more efficient than the 3D p-n junction.

Electrons and holes in a 3D p-n junction are not heated under the influence of a weak microwave field, and if only the perturbation of the potential barrier height is taken into account, we have the following expression for the differential conductance of the p-n junction [28]:

$$G = \frac{eI_s}{kT}e^{-\frac{e(U+U_1-\phi_0)}{kT}}. \quad (5)$$

We have the following expression for the differential conductance of a 2D-sized p-n junction under the influence of a weak microwave field:

$$G = \frac{q^2n_i^2}{kTN_d}\left(\frac{D_p}{L_p}+\frac{D_n}{L_n}\right)\exp\left(\frac{q(U+U_1-\phi)}{kT}\right). \quad (6)$$

Using expressions (5) and (6), it is possible to compare the differential conductivities of 2D and 3D p-n junctions located in a weak microwave field (Fig. 4).

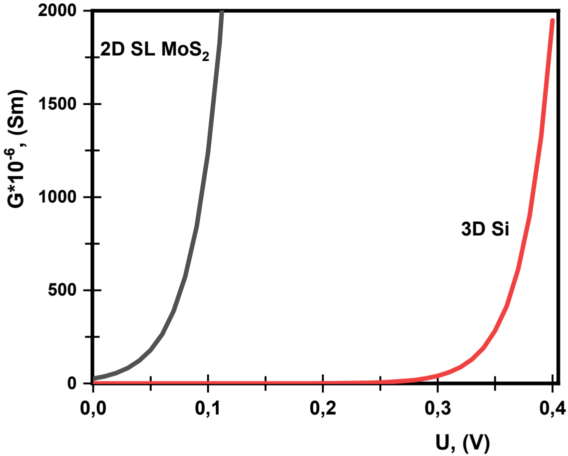


**Figure 4.** Dependence of applied voltage of the differential conductance of 2D and 3D p-n junctions located in a weak microwave field

Fig. 4 shows the voltage dependence of the differential conductance of a 2D and 3D p-n junction located in a weak microwave field. The obtained results show that the 3D p-n junction differential conductance located in the microwave is smaller than the 2D p-n junction differential conductance. This shows that a 2D p-n-junction located in a weak microwave field is more efficient than a 3D p-n-junction.

We have the following expression for the differential conductance of a 3D-dimensional p-n junction under the influence of a strong microwave field:

$$G = \left( \frac{kT}{eI_e} \sqrt{\frac{T}{T_e}} e^{\left( \frac{e(\phi_0 - U - U_1)}{kT_e} - \frac{e\phi_0}{kT} \right)} + \frac{kT}{eI_h} \sqrt{\frac{T}{T_h}} e^{\left( \frac{e(\phi_0 - U - U_2)}{kT_h} - \frac{e\phi_0}{kT} \right)} \right)^{-1} . \quad (7)$$

We have a differential expression for the differential conductance of a 2D-sized p-n junction under the influence of a strong microwave field:

$$G = \frac{q^2 n_i^2}{kTN_d} \left( \frac{D_p}{L_p} + \frac{D_n}{L_n} \right) \left( \sqrt{\frac{T}{T_e}} \exp\left(\frac{q(\phi - U - U_1)}{kT_e} - \frac{q\phi}{kT}\right) + \sqrt{\frac{T}{T_h}} \exp\left(\frac{q(\phi - U - U_2)}{kT_h} - \frac{q\phi}{kT}\right) \right)^{-1} . \quad (8)$$

Using expressions (7) and (8), it is possible to compare the differential conductivities of 2D and 3D p-n junctions located in a strong UHF field (Fig. 5).

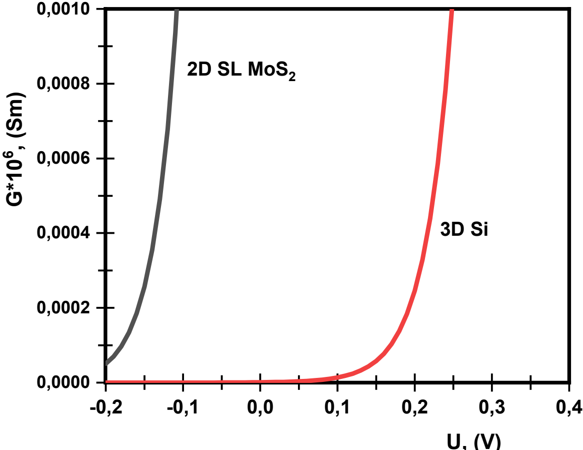


**Figure 5.** Dependence of differential conductance of 2D and 3D p-n junctions located in a strong microwave field on applied voltage

Figure 5 shows Dependence of differential conductance of 2D and 3D p-n junctions located in a strong microwave field on applied voltage. The obtained results show that the differential conductance of a 3D-sized p-n junction located in a strong microwave field is small compared to the differential conductance of a 2D-sized p-n junction. This shows that the 2D p-n junction located in a strong microwave field is more efficient than the 3D p-n junction.

Using the expressions (4), (6) and (8), the variation of the 2D p-n junction differential conductance without the influence of the microwave field, under the influence of the weak and strong UHF field is shown in Fig. 6.

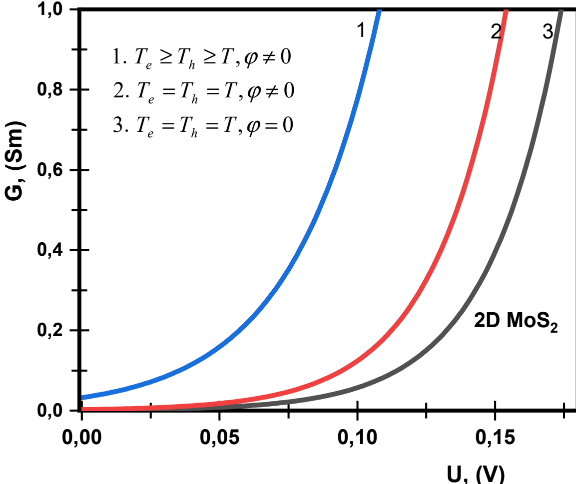


**Figure 6.** Variation of the differential conductance of a 2D p-n junction under the influence of a strong microwave field

From the obtained results, it can be seen that the differential conductance of the 2D-sized p-n junction increases under the influence of a strong microwave field.

## COMPARISON OF DIFFUSION CAPACITIES OF 2D AND 3D p-n JUNCTIONS

For 3D-dimensional p-n junction diffusion capacitance [28]

$$C = \frac{\tau e I_s}{2kT} e^{-\frac{eU}{kT}}, \tag{9}$$

using the expression, its graph on a logarithmic scale can be obtained (Fig. 7).

The diffusion capacity of a 2D p-n junction is determined by the following relation [27]:

$$C = \frac{q^2 n_i^2 \left(L_n + L_p\right)}{2kTN_d} \exp\left(\frac{qU}{kT}\right). \tag{10}$$

The graph of expressions (10) and (11) on a logarithmic scale is shown in Figure 8.

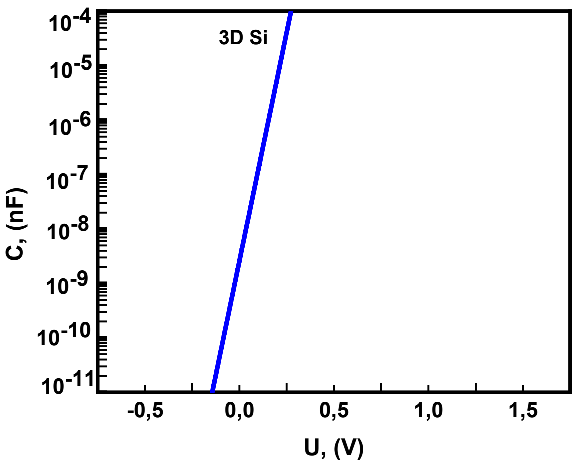


**Figure 7.** Voltage dependence of the diffusion capacitance for a 3D p-n junction

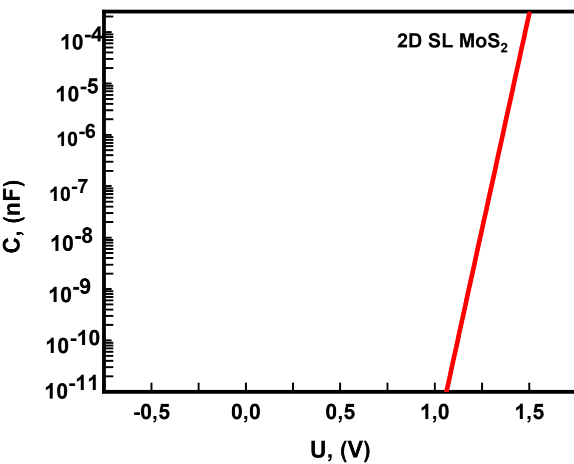


**Figure 8.** Voltage dependence of diffusion capacity for 2D monolayer SL $MoS_2$

We compare the diffusion capacities of p-n junctions in 3D and 2D sizes from a theoretical point of view (Fig. 10).

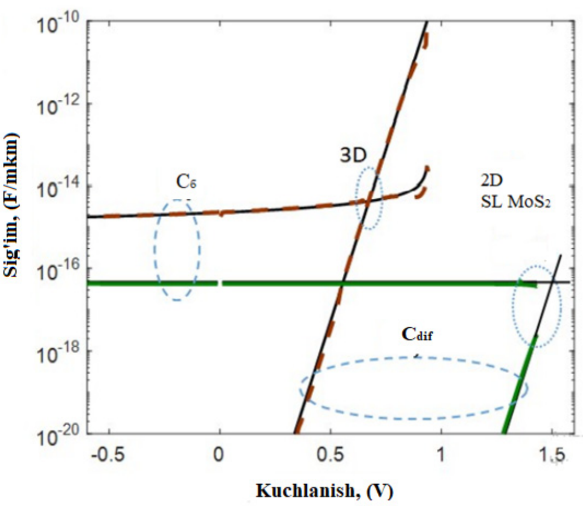


**Figure 9.** Comparison of barrier and diffusion capacities for silicon-based 3D p-n junction and 2D monolayer $MoS_2$ [26]

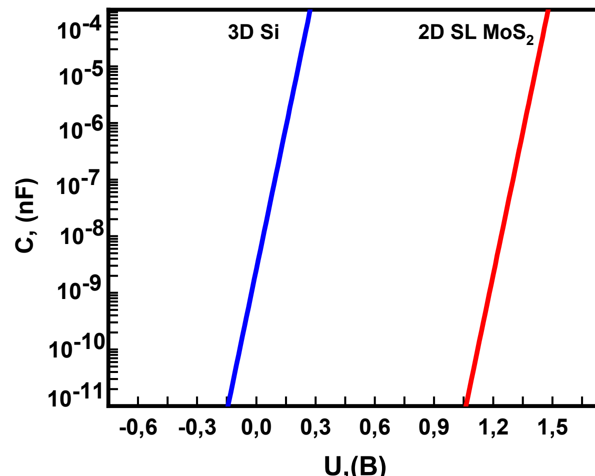


**Figure 10.** Voltage dependence of p-n junction diffusion capacitance in 3D and 2D dimensions

As can be seen from Figures 9 and 10, the theoretical calculations and experimental results show that the diffusion capacity for 2D monolayer SL $MoS_2$ is larger than the 3D Si diffusion capacity.

Electrons and holes in a 3D p-n junction are not heated under the influence of a weak microwave field, and we have an expression for the diffusion capacity of a p-n junction when only the perturbation of the potential barrier is obtained [29]:

$$C = \frac{eI_s\tau}{2kT} e^{-\frac{e(U+U_1-\phi)}{kT}} . \tag{11}$$

2D single-layer SL $MoS_2$ diffusion capacitance, assuming equal electron and hole lifespan when the potential barrier height is perturbed, that is, considering that $\tau_n = \tau_p = \tau$, we have the following expression for the diffusion capacity of a 2D monolayer SL $MoS_2$:

$$C = \frac{q^2 n_i^2 \tau}{2kTN_d}\left(\frac{D_p}{L_p} + \frac{D_n}{L_n}\right)\exp\left(\frac{q\left(U + U_1 - \phi\right)}{kT}\right) . \tag{12}$$

Using the expression (11) and (12), it is possible to obtain a graph of the applied voltage dependence of the 2D and 3D p-n junction diffusion capacitances located in a weak microwave field (Fig. 11).

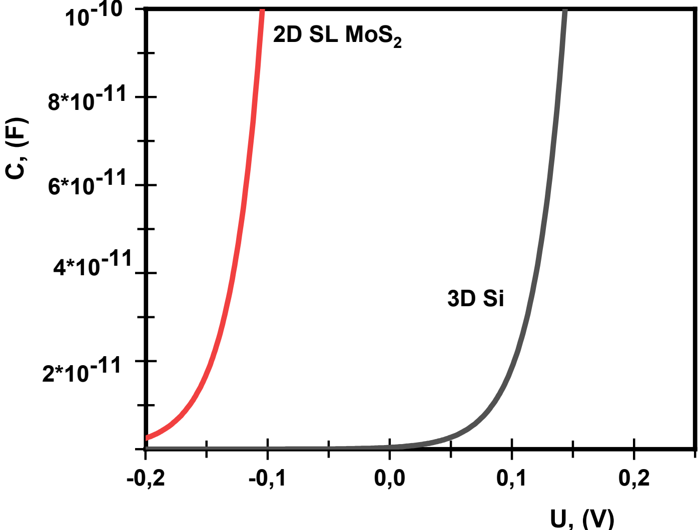


**Figure 11.** Dependence of the applied voltage of the 2D and 3D p-n junction diffusion capacitance located in a weak microwave field

As can be seen in Fig. 11, the theoretical calculations show that the diffusion capacity for 2D single-layer SL $MoS_2$ in the weak microwave field is greater than the 3D Si diffusion capacity.

We have the following expression for the differential conductance of a 3D-dimensional p-n junction under the influence of a strong microwave field:

$$C = \left(\left(\frac{kL_e\sqrt{TT_e}}{e^2 D_e n_p} e^{\frac{e(\phi_0 - U_1 - U)}{kT_e} - \frac{e\phi_0}{kT}}\right) + \left(\frac{kL_h\sqrt{TT_h}}{e^2 D_h p_n} e^{\frac{e(\phi_0 - U_2 - U)}{kT_h} - \frac{e\phi_0}{kT}}\right)\right)^{-1} \frac{\tau}{2} . \tag{13}$$

Electrons and holes in a 2D p-n junction are heated under the influence of a strong microwave field, taking into account the perturbation of the potential barrier height, the lifespan of electrons and holes are equal, that is, considering that $\tau_n = \tau_p = \tau$ , in 2D size we have the following expression for the diffusion capacity of monolayer SL $MoS_2$:

$$C = \frac{q^2 n_i^2 \tau}{2kTN_d}\left(\frac{D_p}{L_p} + \frac{D_n}{L_n}\right)\left(\sqrt{\frac{T}{T_e}}\exp\left(\frac{q(\phi - U - U_1)}{kT_e} - \frac{q\phi}{kT}\right) + \sqrt{\frac{T}{T_h}}\exp\left(\frac{q(\phi - U - U_2)}{kT_h} - \frac{q\phi}{kT}\right)\right)^{-1} . \tag{14}$$

Using the expression (13) and (14), it is possible to obtain a graph of the applied voltage dependence of the diffusion capacity of a single-layer SL $MoS_2$ in 2D and 3D dimensions located in a strong microwave field (Fig. 12).

It can be seen from Fig. 12 that the diffusion capacity for 2D monolayer SL $MoS_2$ located in a strong microwave field is greater than the 3D Si diffusion capacity.

Using the expressions (10), (12) and (14), the variation of the 2D p-n junction diffusion capacitance under the influence of the microwave field is shown in Fig. 13.

The obtained results show that the 2D p-n junction diffusion capacity increases under the influence of a strong microwave field.

**Figure 12.** Dependence of the applied voltage of the 2D and 3D p-n junction diffusion capacitance located in a strong microwave field

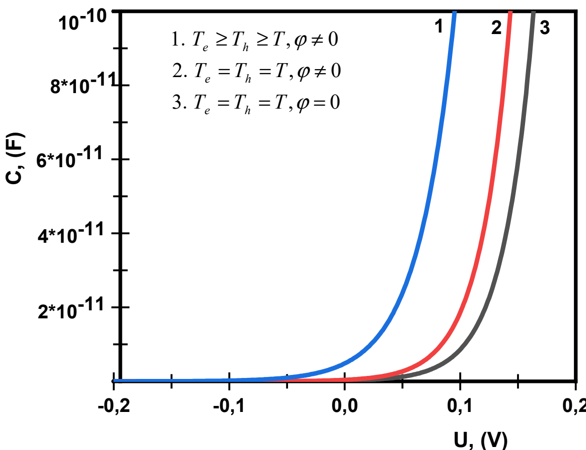


**Figure 13.** Voltage dependence of the diffusion capacity for a 2D single-layer SL $MoS_2$ in a strong microwave field

## CONCLUSIONS

– The differential conductance of a 3D p-n junction is smaller than the differential conductance of a 2D p-n junction.
– The differential conductance of a 3D-dimensional p-n junction located in a weak and strong microwave field is small compared to the differential conductance of a 2D-dimensional p-n-junction. This shows that the 2D p-n junction located in weak and strong microwave field is more efficient than the 3D p-n junction.
– Theoretical calculations show that the diffusion capacity for 2D single-layer SL $MoS_2$ in both weak and strong microwave fields is greater than that of Si in 3D.
– The differential conductance and diffusion capacity of the 2D-sized p-n junction also increase under the influence of a strong microwave field.

**ORCID**
**Muhammadjon G. Dadamirzayev,** https://orcid.org/0000-0001-8258-4617
**Mamura O. Kosimova,** https://orcid.org/0000-0002-0759-5890; **Azamat S. Makhmudov,** https://orcid.org/0009-0001-1189-8202

## REFERENCES

[1] T. Yang, B. Zheng, Z. Xu, T. Wang, C. Pan, J. Zou, X. Zhang, et al., “Van der Waals epitaxial growth and optoelectronics of large-scale $WSe_2/SnS_2$ vertical bilayer p–n junctions,” Nat. Commun. **8,** 1906 (2017). https://doi.org/10.1038/s41467-017-02093-z
[2] Z. Lou, Z. Liang, and G. Shen, “Photodetectors based on two dimensional materials,” Journal of Semiconductors, **37**(9), 091001 (2016). https://doi.org/10.1088/1674-4926/37/9/091001
[3] G. Gulyamov, U.I. Erkaboev, and A.G. Gulyamov, “Shubnikov–de Haas Oscillations in Semiconductors at the Microwave-Radiation Absorption,” Adv. Cond. Matter Phys. **2019**, 3084631 (2019). https://doi.org/10.1155/2019/3084631
[4] R. Cheng, D. Li, H. Zhou, C. Wang, A. Yin, S. Jiang, anf X. Duan, “Electroluminescence and Photocurrent Generation from Atomically Sharp $WSe_2/MoS_2$ Heterojunction p–n Diodes,” Nano Letters, **14**(10), 5590–5597 (2014). https://doi.org/10.1021/nl502075n
[5] H. Yuan, X. Liu, F. Afshinmanesh, W. Li, G. Xu, J. Sun, and Y. Cui, “Polarization-sensitive broadband photodetector using a black phosphorus vertical p–n junction,” Nature Nanotechnology, **10**(8), 707–713 (2015). https://doi.org/10.1038/nnano.2015.112
[6] F. Wang, L. Yin, Z.X. Wang, K. Xu, F.M. Wang, T.A. Shifa, and J. He, “Configuration-Dependent Electrically Tunable Van der Waals Heterostructures Based on $MoTe_2/MoS_2$,” Advanced Functional Materials, **26**(30), 5499–5506 (2016). https://doi.org/10.1002/adfm.201601349
[7] G. Gulyamov, G. Majidova, F. Muxitdinova, and S. Madumarova, “Changes in diodes with a pn-transition under the influence of microwave radiation,” AIP Conference Proceedings, **2700**(1), 050008 (2023). https://doi.org/10.1063/5.0126385
[8] G. Gulyamov, F. Mukhitdinova, and G. Majidova, “Changing the Voltage of the p-n Junction in a Magnetic Field,” e-Journal of Surface Science and Nanotechnology, **21**(4), 273-277 (2023). https://doi.org/10.1380/ejssnt.2023-047
[9] M.M. Furchi, A. Pospischil, F. Libisch, J. Burgdörfer, and T. Mueller, “Photovoltaic Effect in an Electrically Tunable van der Waals Heterojunction,” Nano Letters, **14**(8), 4785–4791 (2014). https://doi.org/10.1021/nl501962c
[10] F. Wang, Z. Wang, K. Xu, F. Wang, Q. Wang, Y. Huang, and J. He, “Tunable GaTe-$MoS_2$ van der Waals p–n Junctions with Novel Optoelectronic Performance,” Nano Letters, **15**(11), 7558–7566 (2015). https://doi.org/10.1021/acs.nanolett.5b03291
[11] C.H. Lee, G.H. Lee, A.M. van der Zande, W. Chen, Y. Li, M. Han, and P. Kim, “Atomically thin p–n junctions with van der Waals heterointerfaces,” Nature Nanotechnology, **9**(9), 676–681 (2014). https://doi.org/10.1038/nnano.2014.150
[12] Y.J. Zhang, T. Oka, R. Suzuki, J.T. Ye, and Y. Iwasa, “Electrically Switchable Chiral Light-Emitting Transistor,” Science, **344**(6185), 725–728 (2014). https://doi.org/10.1126/science.1251329
[13] A. Pospischil, M. Furchi, and T. Mueller, “Solar-energy conversion and light emission in an atomic monolayer p-n-diode,” Nature Nanotech. **9,** 257–261 (2014). https://doi.org/10.1038/nnano.2014.14

[14] J.S. Ross, P. Klement, A.M. Jones, N.J. Ghimire, J. Yan, D.G. Mandrus, T. Taniguchi, et al., "Electrically tunable excitonic light-emitting diodes based on monolayer $WSe_2$ p–n junctions," Nature Nanotechnology, **9**(4), 268–272 (2014). https://doi.org/10.1038/nnano.2014.26
[15] M. Buscema, D.J. Groenendijk, G.A. Steele, H.S.J. van der Zant, and A. Castellanos-Gomez, "Photovoltaic effect in few-layer black phosphorus junctions defined by local electrostatic gating," Nature Communications, **5**(1), 4651 (2014). https://doi.org/10.1038/ncomms5651
[16] D. Li, M. Chen, Z. Sun, P. Yu, Z. Liu, P.M. Ajayan, and Z. Zhang, "Two-dimensional non-volatile programmable p–n junctions," Nature Nanotechnology, **12**(9), 901–906 (2017). https://doi.org/10.1038/nnano.2017.104
[17] J.-W. Chen, S.-T. Lo, S.-C. Ho, S.-S. Wong, T.-H.-Y. Vu, X.-Q. Zhang, Y.-D. Liu, et al., "A gate-free monolayer $WSe_2$ p-n-diode," Nature Communications, **9,** 3143 (2018). https://doi.org/10.1038/s41467-018-05326-x
[18] Z. Ni, L. Ma, S. Du, Y. Xu, M. Yuan, H. Fang, D. Yang, et al., "Plasmonic Silicon Quantum Dots Enabled High-Sensitivity Ultrabroadband Photodetection of Graphene-Based Hybrid Phototransistors," ACS Nano, **11**(10), 9854–9862 (2017). https://doi.org/10.1021/acsnano.7b03569
[19] D. Xiang, T. Liu, J. Xu, J.Y. Tan, Z. Hu, B. Lei, Y. Zheng, et al., "Two-dimensional multibit optoelectronic memory with broadband spectrum distinction," Nature Communications, **9**(1), 2966 (2018). https://doi.org/10.1038/s41467-018-05397-w
[20] Z. Hai, M.K. Akbari, Z. Wei, D. Cui, C. Xue, H. Xu, P.M. Heynderickx, et al., "Nanostructure-induced performance degradation of $WO_3{\cdot}nH_2O$ for energy conversion and storage devices," Beilstein Journal of Nanotechnology, **9**, 2845–2854 (2018). https://doi.org/10.3762/bjnano.9.265
[21] U.I. Erkaboev, G. Gulyamov, J.I. Mirzaev, and R.G. Rakhimov, "Modeling on the temperature dependence of the magnetic susceptibility and electrical conductivity oscillations in narrow-gap semiconductors," International journal of modern physics B, **34**(07), 2050052 (2020). https://doi.org/10.1142/S0217979220500526
[22] J.O. Island, S.I. Blanter, M. Buscema, H.S.J. van der Zant, and A. Castellanos-Gomez, "Gate Controlled Photocurrent Generation Mechanisms in High-Gain $In_2Se_3$ Phototransistors," Nano Letters, **15**(12), 7853–7858 (2015). https://doi.org/10.1021/acs.nanolett.5b02523
[23] G. Gulyamov, U.I. Erkaboev, R.G. Rakhimov, and J.I. Mirzaev, "On temperature dependence of longitudinal electrical conductivity oscillations in narrow-gap electronic semiconductors," Journal of Nano-and Electronic Physics, **12**(3), (2020). https://doi.org/10.21272/jnep.12(3).03012
[24] E. Wu, Y. Xie, J. Zhang, H. Zhang, X. Hu, J. Liu, Ch. Zhou, et al., "Dynamically controllable polarity modulation of $MoTe_2$ field-effect transistors through ultraviolet light and electrostatic activation," Science Advances, **5**(5), eaav3430 (2019). https://doi.org/10.1126/sciadv.aav3430
[25] B.W.H. Baugher, H.O.H. Churchill, Y. Yang, and P. Jarillo-Herrero, "Optoelectronic devices based on electrically tunable p-n-diodes in a monolayer dichalcogenide," Nature Nanotechnology, **9**(4), 262–267 (2014). https://doi.org/10.1038/nnano.2014.25
[26] F.A. Chaves, P.C. Feijoo, D. Jiménez, "The 2D p-n-Junction Driven Out-of-Equilibrium," Nanoscale Advances, **2**, 3252-3262 (2020). https://doi.org/10.1039/D0NA00267D
[27] R.A. Smith, *Semiconductors*, first ed. (Cambridge University Press, 1959).
[28] G. Gulyamov, M.G. Dadamirzaev, and M.O. Kosimova, "Comparison of parameters of two-dimensional (2D) and three-dimensional (3D) pn-junction diodes," Romanian Journal of Physics, **68**, 603 (2023). https://rjp.nipne.ro/2023_68_1-2/RomJPhys.68.603.pdf
[29] G. Gulyamov; M.G. Dadamirzayev; M.O. Qosimova; and S.R. Boydedayev, "Influence of deformation and light on the diffusion capacity and differential resistance of the p-n junction of a strong electromagnetic field," AIP Conference Proceedings, **2700**, 050013 (2023). https://doi.org/10.1063/5.0124926

## ПОРІВНЯННЯ ДИФЕРЕНЦІАЛЬНОЇ ПРОВІДНОСТІ ТА ДИФУЗІЙНОЇ ЄМНОСТІ 2D І 3D P-N ПЕРЕХОДУ

**Мухамаджон Г. Дадамірзаєв, Мамура О. Косимова, С.Р. Бойдедаєв, Азамат С. Махмудов**
*Наманганський інженерно-будівельний інститут, Наманган 160103, Узбекистан*

Під час виготовлення тривимірних p-n-переходів легування або модифікація поверхні, викликана ін'єкцією іонів, змінює електричні властивості та кристалічну структуру напівпровідника. Крім того, у міру зменшення розмірів напівпровідникового приладу в них поступово виникають різноманітні квантові ефекти. Це показує, що сфера застосування класичної теорії пристроїв зараз обмежена. Останніми роками великий інтерес викликають двовимірні (2D) матеріали з дивовижними атомарно тонкими властивостями. Властивості електростатичного поля деяких 2D p-n-переходів, таких як WS2, MoS2, MoSe2, WSe2 і чорний фосфор (BP), відкривають двері для нових можливостей для напівпровідників. Порівняно зміни дифузійної ємності та диференціальної провідності двовимірних p-n-переходів під впливом НВЧ-поля та дифузійних ємностей і диференціальної провідності двовимірних та тривимірних p-n-переходів під впливом НВЧ-поля.

**Ключові слова:** *p-n-перехід; дифузійна ємність; диференціальна провідність; мікрохвильове поле; двовимірні матеріали*

EAST EUROPEAN JOURNAL OF PHYSICS. **2.** 380-383 (2024)
DOI:10.26565/2312-4334-2024-2-47 ISSN 2312-4334

# INFLUENCE OF DIFFERENT TYPES OF RADIATION ON THE CRYSTAL STRUCTURE OF SILICON MONOCRYSTALS n-Si

**Sharifa B. Utamuradova[a], Dilmurod A. Rakhmanov[a]*, Afsun S. Abiyev[b,c,d]**
*[a]Institute of Semiconductor Physics and Microelectronics at the National University of Uzbekistan, 20 Yangi Almazar st., Tashkent, 100057, Uzbekistan*
*[b]Innovation and Digital Development Agency, Baku AZ-1073, Azerbaijan*
*[c]Khazar University, Az1096, Baku, Azerbaijan*
*[d]Western Caspian University, Baku, AZ1001, Azerbaijan*
**Corresponding Author e-mail: dilmurod-1991@bk.ru*
Received February 23, 2024; revised May 6, 2024; accepted May 8, 2024

In this work, the influence of alpha particles, protons and gamma rays on the crystal structure and structural characteristics of n-type silicon (n-Si) single crystals was studied using X-ray diffraction. N-type silicon (KEF-40) was used for the study. The samples were irradiated with protons with a dose of $9\times10^{14}$ cm$^{-2}$ with an energy of 600 keV and a current of 1÷1.5 μA, irradiated with alpha particles with a dose of $6\times10^{14}$ cm$^{-2}$ with an energy of 800 keV and a current of 0.5÷1 μA and γ− $^{60}$Co quanta with a flux intensity of ~ $3.2\times10^{12}$ quantum/cm$^2$·s. Based on the results of X-ray diffraction analysis, it was established that distortions, vacancies and amorphization of lattice parameters that arose after irradiation lead to an increase in lattice parameters.
**Key words**: *Monocrystal; Silicon; Irradiation; Alpha particles; Proton; Gamma quantum; X-ray diffraction*
**PACS:** 78.30.Am

## INTRODUCTION

In recent years, scientists around the world have paid great attention to research into the electrical properties and structure of semiconductors. Because the basis of modern microelectronics is semiconductor materials and various device structures based on them. Today, in the context of the rapid development of technology and technology, the creation of sensitive and resistant to external influences devices with wide application possibilities and completely new semiconductor materials that can serve as the basis for them is considered one of the urgent tasks [1-3].

In the technological processes of manufacturing semiconductor devices, semiconductor materials are subjected to various mechanical, thermal, and radiation influences. These effects, in turn, can lead to a noticeable change in the initial parameters of semiconductor materials [4,5].

Irradiation of silicon with protons and alpha particles leads to the formation of primary point radiation defects in the crystal – vacancies and associated interstitial silicon atoms (Frenkel pairs), which are generated along the ion path as a result of the development of cascades of collisions of ions with atoms of the crystal lattice. During irradiation at room temperature, especially created pairs of Frenkel disappears as a result of reciprocal annihilation, and the isolated components of the pairs, in the process of their movement, cooperate with each other and with impurity atoms of the crystal, creating more complex and stable secondary radiation defects. Secondary defects are subsequently transformed, for example, when exposed to temperature, complex complexes can decompose into components [6-7].

The main aim of this work is to investigate the effect of various types of radiation on changes in the crystal structure and structural characteristics of n-type silicon single crystals using X-ray diffraction.

As is known [8], X-ray analysis is based on the Wulff–Bragg equation, which relates the interplanar distance (d), angle of incidence of X-rays (θ) and wavelength (λ):

$$\lambda=2d\sin\theta. \quad (1)$$

The main advantages of X-ray diffraction analysis are that the solid body itself is examined in an unchanged state and the result of the analysis is the direct determination of the substance or its components. X-rays examine the crystal, just the connection itself. Moreover, in the case of polymorphic bodies, X-rays make it possible to distinguish individual modifications characteristic of a given substance. To study a substance, a very small amount is required, which is not destroyed during the analytical operation [9,10]. A crystalline substance of a certain chemical composition as a result of any physical impact (mechanical, thermal) can greatly change its properties. For the most part, this is due to a change in the crystal structure (phase transformation) or distortion of this structure under the influence of external forces or internal stresses. Diffraction methods make it possible to detect the slightest changes in the state of the atomic lattice of a crystal that are not detected by other methods.

***Cite as:*** Sh.B. Utamuradova, D.A. Rakhmanov, A.S. Abiyev, East Eur. J. Phys. 2, 380 (2024), https://doi.org/10.26565/2312-4334-2024-2-47
© Sh.B. Utamuradova, D.A. Rakhmanov, A.S. Abiyev, 2024; CC BY 4.0 license

## EXPERIMENTAL PART

For the experiments, n-type silicon (KEF-40) was used, grown by the Czochralski method. The resistivity of these samples is 40 Ohm cm. The concentration of phosphorus dopant in the original n-Si single crystals was $7.3\times10^{13}\div7.1\times10^{15}$ cm$^{-3}$.

These samples were first divided into group 3 and irradiated with alpha particles, protons and gamma rays. Samples of the first group were irradiated with alpha particles with an energy of 800 keV, a current of 1÷1.5 μA and a dose of $6.0\times10^{14}$ cm$^{-2}$. The samples were irradiated using the EG-5 electrostatic accelerator in the FLNP, JINR.

Samples of the second group were irradiated with protons with an energy of 600 keV at a current of 1÷1.5 μA with a dose of $9\times10^{14}$ cm$^{-2}$. The samples were irradiated using the SOKOL EG-2 electrostatic accelerator at the Research Institute of Semiconductor Physics and Microelectronics. The samples of the third group were irradiated at room temperature with $^{60}$Co γ quanta with a flux intensity of ~ $3.2\times10^{12}$ quantum/cm$^2$·s.

Investigating of n-Si samples before and after irradiation with various types of radiation source were carried out on X-ray diffractometer with a Miniflex 300/600 goniometer and a D/teX Ultra2 detector. CuKα1 radiation was used, wavelength λ = 1.541 Å, with an accelerating 15 mA current and 40 keV voltage on the X-ray tube. Diffraction measurements were carried out in the Bragg–Brentano beam geometry in the $2\theta$ range from 5° to 60° continuously with a scanning speed of 10 degrees/min and an angular step of 0.02°.

## RESULTS AND DISCUSSIONS

The influence of various radioactive methods on the structural properties of Si mono crystal was investigated. To investigate the effect of radioactivity on the structural properties of single crystals after irradiation the analysis was carried out using the X-ray method. As a result of research, it has been seen that the change of crystal lattice parameters was basically the same. Change of characteristics was studied by the Rietveld method [11], Table 1. The measurements of the material used in the experiment before and after irradiation are shown [12]. It was revealed that, after irradiation, an increase in the value of the dimensions of the lattice constant is observed. The largest jump occurred after proton irradiation.

**Table 1.** Crystal lattice parameter values determined by the Rietveld method

| Name | Type of radiation | Space group | a (Å) | V (Å)$^3$ | Reliability Factors |
|---|---|---|---|---|---|
| **Si** | initial | F d -3 m | 5.42989 (8) | 160.093 (4) | Rp: 9.4 Bragg: 10.2 Rf: 15.0 |
| **Si** | alpha | F d -3 m | 5.43184 (10) | 160.266 (5) | Rp: 10.1 Bragg: 11.0 Rf: 15.1 |
| **Si** | gamma | F d -3 m | 5.43368 (10) | 160.429 (5) | Rp: 10.2 Bragg: 11.0 Rf: 15.0 |
| **Si** | proton | F d -3 m | 5.43636 (14) | 160.666 (7) | Rp: 10.4 Bragg: 11.2 Rf: 15.3 |

After refining with the FullProf program, it was found that the diffraction peak is *(111)* indexed. In the initial state of the sample, the diffraction peak itself is at an angle of $2\theta=28.4473°$ has shown (Fig. 1). Depending on the type of effect after alpha, gamma and proton radiation, the lattice of the crystal $\Delta a_\alpha=0.00195°$, $\Delta a_\gamma=0.00379°$ and $\Delta a_p=0.00647°$ changes in parameter $2\theta$ to *28.4270°, 28.4368°* and *28.4127°* respectively caused a shift to the left. In Fig. 2. The shift is clearly observed.

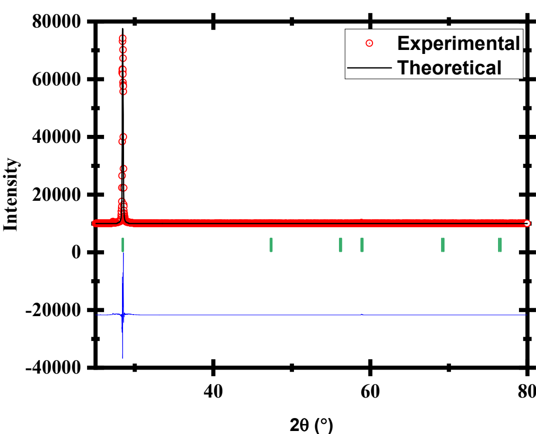


**Figure 1.** Pre-irradiation X-ray spectrum of a Si mono-crystal

In order to see how the lattice parameters in the crystals change depending on the type of irradiation, the ratio of the lattice parameters before and after the irradiation was looked at. Increasing the value of the lattice parameters shows

a sharper change in the volume $V/V_0$. It can be said with certainty that after exposure to radiation, the process of amorphization and defect formation in the crystal structure increased dramatically. Since the amount of distribution of such disorders throughout the crystal increased after irradiation, it led to an increase in the value of the lattice volume parameter.

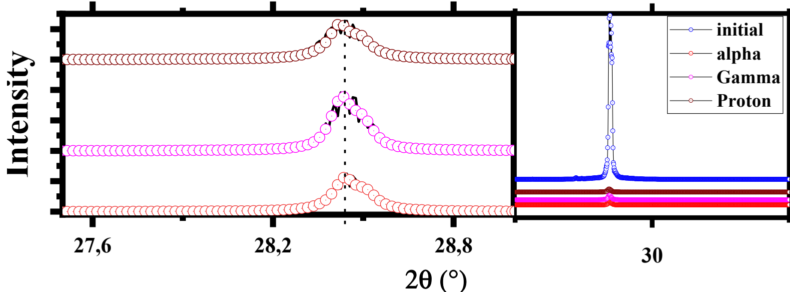


**Figure 2.** Shift of X-ray diffraction peaks after different types of radioactive effects

It can also be clearly seen that the changes caused by defects and lattice distortions after proton irradiation had the greatest effect on the values of the lattice parameters, and the smallest in alpha irradiation in Fig. 3.

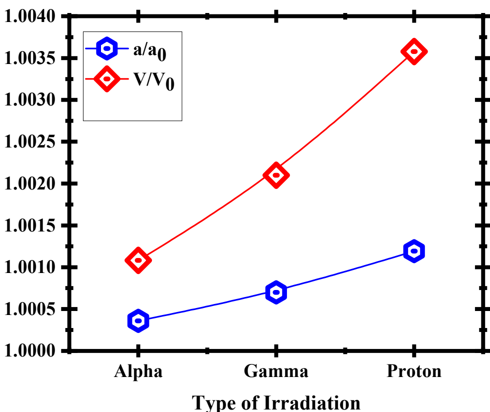


**Figure 3.** Characteristics of changes in lattice parameters after different types of irradiations

The crystal had a very long ordered structure before irradiation. After irradiation, this regularity decreased dramatically. By the method of integration of diffraction peaks (similarly as in this articles [13,14]), it was determined how much this change changes in which radiation. Calculations show that after alpha, gamma and proton irradiation, the long-range order in the crystal is reduced by 98.09%, 97.17%, and 97.92%, respectively. This is due to the inability of the crystal to maintain its regular structure after irradiation.

The authors [15] work with alpha-irradiated silicon monocrystalline samples with energy of 5.4 MeV. They wrote that when studying irradiated silicon samples, the presence of thin amorphized layers was observed near the surface of the samples. Irradiation of silicon with alpha particles with an energy of 5.4 MeV with doses in the range from $4\times10^{10}$ to $8\times10^{11}$ particles/cm$^2$ can lead to the development in the near-surface region of a compensating layer caused by excess concentrations of A-centers and complexes based on vacancies, including divacancies.

In [16], using high-resolution X-ray diffraction analysis, the transformation of radiation defects in n-type silicon crystals irradiated with protons was studied. It was shown that the proton-irradiation of silicon structures with energy of 100, 200 or 300 keV respectively with a dose of $2 \times 10^{16}$ cm$^{-2}$ causes the creation of a amorphous layer 2.4 μm thick with a large crystal parameters. The layer is formed at the same time with the congestion of its own radiation defects, such as vacancies and interstitial ones.

From those results [15, 16], it can be assumed that irradiation of a silicon single crystal with various types of radiation leads to the formation of radiation defects, the creation of amorphous layers and the deterioration of the crystalline structure of silicon samples.

## CONCLUSION

The response of the Si crystal to all applied radioactive influences was similar regardless of the type of irradiation. From the results of the X-ray diffraction experiment, it was found that the distortions, vacancies and amorphization that occurred after the irradiation of the lattice parameters led to an increase in the lattice parameters. After the theoretical calculations, it was found that the increase of the lattice parameters of the crystal is up to 0.12% after proton irradiation. Disruption of the long-range regularity of the lattice due to the influence of radiation shows itself in different values depending on the type of radiation. The results show that the long order of the crystal is destroyed by more than 98 % under the influence of alpha rays. From this, we can conclude that the main reason for the increase in the size of the lattice

is the vacancies created by different types of effects, and it is assumed that as the duration of the effect changes during irradiation, these vacancies are grouped and covered in a cluster shape.

**Conflict of Interest**
The authors declare that there is no conflict of interest regarding the publication of this paper.

**ORCID**
**Sharifa B. Utamuradova,** https://orcid.org/0000-0002-1718-1122; **Dilmurod A. Rakhmanov**, https://orcid.org/0000-0003-1275-5999
**Afsun S. Abiyev,** https://orcid.org/0009-0009-9377-7567

**REFERENCES**

[1] Sh.B. Utamuradova, Sh.Kh. Daliev, D.A. Rakhmanov, S.F. Samadov, and A.S. Doroshkevich, "Investigation of Radiation Defect Formation of Irradiated n-Si<Pt>," Advanced Physical research, **5**(3), 183-191 (2023). http://jomardpublishing.com/UploadFiles/Files/journals/APR/V5N3/7.Utamuradova.pdf
[2] V.A. Kozlov, and V.V. Kozlovskiy, "Doping of semiconductors with radiation defects when irradiated with protons and alpha particles. Review," Physics and technology of semiconductors, **35**(7), (2001). http://journals.ioffe.ru/articles/viewPDF/37060 (in Russian)
[3] Sh.B. Utamuradova, Sh.Kh. Daliev, A.V. Stanchik, and D.A. Rakhmanov, "Raman spectroscopy of silicon, doped with platinum and irradiated by protons," E3S Web of conferences, **402**, 14014 (2023). https://doi.org/10.1051/e3sconf/202340214014
[4] Sh.B. Utamuradova, Sh.Kh. Daliev, D.A. Rakhmanov, A.S. Doroshkevich, V.A. Kinev, O.Yu. Ponamareva, et al., "IR – spectroscopy of n-Si<Pt> irradiated with protons," Advanced Physical research, **5**(2), 73-80 (2023). http://jomardpublishing.com/UploadFiles/Files/journals/APR/V5N2/Utamuradova_et_al.pdf
[5] N.A. Turgunov, E.Kh. Berkinov, and D.X. Mamajonova, "Decay of Impurity Clusters of Nickel and Cobalt Atoms in Silicon under the Influence of Pressure," Journal of Nano- and Electronic Physics, **13**(5), 05006 (2021). https://doi.org/10.21272/jnep.13(5).05006
[6] Sh.B. Utamuradova, D.A. Rakhmanov, A.S. Doroshkevich, I.G. Genov, P.L. Tuan, and A. Kirillov, "Processes of defect formation in silicon diffusionally doped with platinum and irradiated with protons," Eurasian physical technical journal, **20**(3), 35-42 (2023). https://doi.org/10.31489/2023No3/35-42
[7] Sh.B. Utamuradova, A.V. Stanchik, and D.A. Rakhmanov, "X-Ray Structural Investigations Of n-Si<Pt> Irradiated with Protons," East Eur. J. Phys. 2, 201 (2023). https://doi.org/10.26565/2312-4334-2023-2-21
[8] Z.T. Azamatov, M.A. Yuldoshev, N.N. Bazarbayev, and A.B. Bakhromov, Physics AUC, **33**, 139-145 (2023). https://cis01.central.ucv.ro/pauc/vol/2023_33/13_PAUC_2023_139_145.pdf
[9] Kh.S. Daliev, Z.E. Bahronkulov, J.J. Hamdamov, East Eur. J. Phys. 4, 167 (2023), https://doi.org/10.26565/2312-4334-2023-4-18
[10] Sh.B. Utamuradova, A.V. Stanchik, D.A. Rakhmanov, A.S. Doroshkevich, and K.M. Fayzullaev, "X-ray structural analysis of n-Si<Cr>, irradiated with alpha particles," New materials, compounds and applications, **6**(3), 214 (2022). http://jomardpublishing.com/UploadFiles/Files/journals/NMCA/V6N3/Utamuradova_et_al.pdf
[11] H.M. Rietveld, A Profile Refinement Method for Nuclear and Magnetic Structures. J. Appl. Cryst. **2**, 65 (1969). https://doi.org/10.1107/s0021889869006558
[12] S. Stefanoski, M.C. Blosser, and G.S. Nolas, "Pressure Effects on the Size of Type-I and Type-II Si-Clathrates Synthesized by Spark Plasma Sintering," Crystal Growth & Design, **13**, 195, (2013). https://doi.org/10.1021/cg3013443
[13] A.S. Abiyev, E.M. Huseynov, and R.F. Hashimov, "Gamma radiation-induced alterations in nanocrystalline titanium nitride (TiN) particles: A structural perspective," Radiation Physics and Chemistry, **218**, 111638 (2024). https://doi.org/10.1016/j.radphyschem.2024.111638
[14] S.F. Samadov, A.S. Abiyev, A.G. Asadov, N.V.M. Trung, A.A. Sidorin, O.A. Samedov, E.P. Popov, et al., "Investigating the crystal structure of ZrB2 under varied conditions of temperature, pressure, and swift heavy ion irradiation," Ceramics International, **50**(2), Part B, 3727-3732 (2023). https://doi.org/10.1016/j.ceramint.2023.11.125
[15] O.V. Skalyauh, Ph.D. Thesis, Ulyanovsk, (2005). https://www.dissercat.com/content/defektoobrazovanie-v-kremnii-pri-obluchenii-alfa-chastitsami-s-energiei-54-mev
[16] N.M. Bogatov, L.R. Grigorian, A.I. Kovalenko, F.A. Kolokolov, and L.S. Lunin, "Influence of Radiation Defects Induced by Low-Energy Protons at a Temperature of 83 K on the Characteristics of Silicon Photoelectric Structures," Semiconductors, **54**, 196 (2020). https://doi.org/10.1134/S1063782620020062

**ВПЛИВ РІЗНИХ ВИДІВ ВИПРОМІНЮВАННЯ НА КРИСТАЛІЧНУ СТРУКТУРУ МОНОКРИСТАЛІВ КРЕМНІЮ n-Si**

**Шаріфа Б. Утамурадова[a], Ділмурод А. Рахманов[a], Афсун С. Абієв[b,c,d]**
*[a]Інститут фізики напівпровідників і мікроелектроніки Національного університету Узбекистану, 100057, Ташкент, Узбекистан, вул. Янги Алмазар, 20*
*[b]Агентство інновацій та цифрового розвитку, Баку AZ-1073, Азербайджан*
*[c]Хазарський університет, Az1096, Баку, Азербайджан*
*[d]Західнокаспійський університет, Баку, AZ1001, Азербайджан*

У цій роботі методом рентгенівської дифракції досліджено вплив альфа-частинок, протонів і гамма-випромінювання на кристалічну структуру та структурні характеристики монокристалів кремнію n-типу (n-Si). Для дослідження використовували кремній N-типу (KEF-40). Зразки опромінювали протонами дозою $9\times10^{14}$ см$^{-2}$ з енергією 600 кеВ і силою струму 1÷1,5 мкА, опромінювали альфа-частинками дозою $6\times10^{14}$ см$^{-2}$ з енергією 800 кеВ і струмом 0,5÷1 мкА та квантами γ– $^{60}$Co з інтенсивністю потоку ~ $3{,}2\times10^{12}$ квант/см$^2$·с. За результатами рентгеноструктурного аналізу встановлено, що спотворення які виникли після опромінення, вакансії та аморфізація параметрів ґратки призводять до збільшення параметрів ґратки.
**Ключові слова:** *монокристал; кремній; опромінення; альфа-частинки; протон; гамма-квант; рентгенівська дифракція*